Hydroxide Catalysis and Indium Bonding Research for the Design of Ground-Based Gravitational Wave Detectors

Margot Hensler Phelps

BA

Submitted in fulfilment of the requirements for the degree of

Doctor of Philosophy

School of Physics and Astronomy
College of Science and Engineering
University of Glasgow

May 2018

Table of contents

List of tables

List of figures

Acknowledgements

I would like to thank my supervisors, Sheila Rowan, Jim Hough and Marielle van Veggel for their help and guidance throughout my PhD. I have learned so much from all of you. Additionally, I would also like to thank Liam Cunningham, for all his help with ANSYS and in the lab. While I moved here a little over three years ago only knowing a couple people, I immediately felt like I was a part of a large family. The coffee time camaraderie made it possible to get to know the group, and the many adventures organised by Gail Penny made it possible to get to know Scotland as well. My fellow denizens of 253, past and present, livened up the Kelvin Building experience, and many a lunchtime discussion. To them and to the larger IGR family as a whole, thank you for giving me this experience, its one I will look back on with fondness. The friendships formed during this PhD made it possible to endure all its stresses. In particular, thanks to Stuart and Mariela, Jessica Dassow, Ray and Mallory, and Monifa for so many good memories over these last three years. Mostly, thank you for your friendship.

I would also like to thank past supervisors and mentors, who all played important roles for me during my journey through the field of physics. During my stay at Caltech; Norna Robertson, Calum Torrie, Dennis Coyne, Eric Gustofson, Rich Abbott and Melody Araya all offered support, encouragement and wise advice which guided me on my path when I was unsure. I owe the deepest gratitude to the late Debbie Jin, who hired me as an undergraduate freshman to work in her group's labs at JILA when I had nothing to offer but excitement. There I stayed for the next four years. Debbie taught me how to think like an experimental physicist, and made me believe I could become one. No matter how busy she was, she made time to patiently explain physics to me, then pushed me from my comfort zone and challenged me to succeed. Without her guidance I would have given up long ago. My family (and extended family), of course, deserves the deepest gratitude. My grandparents, parents, and brother have forever been my constant and patient cheerleaders no matter how far away they are or how many Thanksgivings I miss. I love you all so much. To my brother, Mitchel, thank you for showing genuine interest in my research, your intelligent and insightful questions during our discussions always helped me think of things in different ways. To my Mom, I can't thank you enough. You are the one I come to when I don't know what to do, and your strength, friendship, wise advice, and unfailing support has made all the difference to me throughout my life. Thanks also to Jan and Larry Shepherd, Patricia Flint-Lacey, and Phil and Cecily Abel for academic, and/or financial, and/or moral support. To my fiance, Jan-Simon Hennig, you came into my life when I least expected it, and I couldn't be happier. I've spent much of the last three years side by side with you, whether we were fixing experiments in a physics lab or travelling to distant countries. I love you, and I hope to spend many more years side by side.

Preface

This thesis is an account of work carried out at the Institute for Gravitational Research (IGR) at the University of Glasgow from October 2014 to March 2018. It is an account of work done by the author, except where explicit references are made to the contributions of others.

The aim of this thesis is to develop and characterise the properties of hydroxide catalysis bonds and indium bonds between oxides or oxidisable materials for implementation in constructing the mirror suspensions of future ground-based gravitational wave detector designs. The work in this thesis was carried out with the supervision of Prof. Jim Hough, Prof. Sheila Rowan, and Dr. Marielle van Veggel.

In Chapter 1 an overview of gravitational wave (GW) sources, detectors, and the detections that have been made to date is given, to put the research into GW detector development in context.

In Chapter 2 different bonding techniques are explained, especially those that could be considered for use in the suspensions of GW detectors. Information on the advantages and disadvantages to each approach in the context of GW detectors is also summarised.

In Chapter 3 the relationship between the tensile strength of hydroxide catalysis bonded c-plane sapphire substrates and their curing time is studied. Bonds were made and strength tested by the author following the training and supervision of Dr. Marielle van Veggel. The characterisation of the sapphire substrates prior to bonding was carried out by the author with advice from Dr. Liam Cunningham. Mr. John Davidson assisted the author during strength testing.

The tensile strength measurements of the bonds reported in this study were made by the author and compared with past tensile strength results of bonded sapphire, measured by Dr. Douglas, a PhD student at the time, and with fused silica results from other IGR members collected between 2009 and 2014.

In Chapter 4 the effect of crystal orientation on the tensile strength of hydroxide catalysis bonded sapphire is studied. The author bonded a-a and m-m plane sapphire samples of the same geometry and using the same bonding procedures as the c-c plane bonds presented in Chapter 3. The author let the samples cure at room temperature for 4 weeks and strength tested them. The breaking stress results of the strength test were then compared to the breaking stress results of the 4 week old c-c plane bonds in the previous chapter. Mr. John Davidson assisted the author during strength testing.

In Chapter 5 a technique to measure non-destructively the Young's modulus of hydroxide catalysis bonds between silica and sapphire substrates is developed. This was achieved by sending ultrasonic pulses through bonded samples, and characterising the reflections from the bond interfaces. The Young's modulus of the bonds was extracted by analysing the

amplitude of the pulses that were reflected from the embedded bond layers. A Bayesian analysis of the bonded fused silica data was also completed, and the results of both approaches was compared.
The ultrasonic measurements in this experiment were carried out by the author at the Institute of Thin Films, Sensors, and Imaging, University of the West of Scotland with the help of Dr. David Hughes.
The derivation of the mathematical equations necessary to model the phase and amplitude of an acoustic pulse reflected from a thin embedded hydroxide catalysis bond was carried out by the author with guidance from Prof. Jim Hough. Dr. Chris Messenger led the development of a Bayesian analysis model used by the author to analyse the bonded fused silica data from this chapter.
The author prepared the samples for SEM measurements of the bond thickness with the guidance of Dr. Marielle van Veggel; cutting, polishing, and coating the bonded samples with gold. Dr. Jamie Scott led the SEM measurements, assisted by the author and Dr. Marielle van Veggel. A TEM sample with known layers made by Mr. Martin Hart was used as a calibration sample by the author, Dr. Jamie Scott and Dr. Marielle van Veggel.
In Chapter 6 the thermal noise of bonded test masses is modelled using the new bond Young's modulus value that was gained in the previous chapter. The FE modelling was done by the author in collaboration with Dr. Cunningham and Dr. Haughian. The author used FE modelling in ANSYS to investigate the mechanical loss of a fused silica cylinder with an off-centre bond using a model previously developed by Dr. Haughian. The author also used FE modelling in ANSYS to investigate the strain energy stored in hydroxide catalysis bonds on a realistic test mass, using models based on models previously developed by Dr. Liam Cunningham. A new ear geometry was proposed for the upgrade to aLIGO, A+. Its geometry was designed by Dr. Cunningham with input from Dr. Marielle van Veggel, Prof. Jim Hough, Prof. Sheila Rowan, Prof. Hammond, and the author. Dr. Liam Cunningham used this prototype ear design to model the thermal noise of a A+ prototype test mass, with input from the author.
In Chapter 7 a number of possible approaches to develop indium bonding procedures for use in cryogenic GW detectors are investigated. The author developed two promising approaches, and all sample preparation, indium bonding, and strength testing of the bonds were conducted by the author. Mr. John Davidson assisted the author during strength testing. The crystal structures of two indium coated samples prepared by the author were measured at the University of the West of Scotland by Prof. Stuart Reid and Mr. Sean Macfoy. Mr. Jan-Simon Hennig assisted the author in constructing the compression jig for the IGR induction heater.
Additionally, the work carried out by the author at the ICRR in Tokyo as a part of the EliTEs exchange was under the supervision of Dr. Kieran Craig and Dr. Kazuhiro Yamamoto.

Summary

In 2015, a gravitational wave (GW) signal from a binary black hole merger passed through the arms of the US-based Advanced LIGO (aLIGO) interferometers, resulting in the first direct detection of gravitational waves. This long-awaited observation made worldwide news one hundred years after Einstein first predicted the existence of GWs in 1916. Since the first detection, four more binary black hole inspiral events have been detected, as well as the ground-breaking GW observation of a binary neutron star inspiral. To detect these signals, ground-based GW detectors like aLIGO and the French-Italian detector, Advanced Virgo, need to be sensitive to changes in separation of close to 10^{-19} m between freely suspended test masses spaced up to 4 km apart. This has always been a challenge to achieve, thus 50 years of technological developments were needed to make these first detections possible.

Following the first observations of coalescing black holes and neutron stars, it is essential to pursue technological advancements that improve the sensitivities of ground-based detectors. Doing so will increase the signal-to-noise ratio of future detectors, which will allow for the better extraction of astrophysical source parameters. Observing more types of astrophysical sources, and at greater distances from the Earth will further the field of GW astronomy. One such area of advancement is to pair the operation of detectors at cryogenic temperatures with improvements in mirror and suspension design, with the aim of improving sensitivities by lessening the effects of thermal noise. Fused silica, currently used for the mirror substrates and suspension fibre elements in all detectors that operate at room temperature, cannot be used in detectors that operate at cryogenic temperatures due to its unfavourable thermo-mechanical properties. Thus a change of mirror substrate and suspension material is necessary for the construction of cryogenic detectors. There are two promising candidates for cryogenic mirrors and suspension elements, sapphire and silicon. Currently one cryogenic detector, the Japan-based KAGRA observatory, is under construction using sapphire as a material for its mirrors and some suspension elements. Other future detectors currently in the design phase, such as the Einstein Telescope (ET) in Europe and Voyager, in the USA may use silicon or sapphire material in their mirror suspensions.

In all ground-based detectors the test masses are supported in multi-stage pendulum suspensions, where the last stages are quasi-monolithic. In the quasi-monolithic stage, the test masses are suspended from penultimate masses via fibres, welded to an interface piece, or "ear". Currently these ears are connected to the test masses using a method called hydroxide catalysis bonding, which creates a strong, low noise joint. This bonding technique has been used successfully in room temperature detectors for 17 years. This thesis details research into hydroxide catalysis bonding, with a focus on its use to create cryogenic crystalline

suspensions for future ground-based detectors. The use of indium as an alternative bonding technology for joints in low temperature crystalline suspensions is also investigated. The aim of this study is to research possible ways to implement indium bonding into suspension design along with hydroxide catalysis bonds to create a more versatile and easily repairable system. This work was completed with the aim of investigating novel ways of implementing bond techniques into GW detectors, and studying their material properties. The breaking stress and stability of different bond technologies were investigated, as well as their thermal noise levels and impact on overall detector sensitivity. The majority of substrate materials used in this thesis were sapphire and silicon, as these are the two materials of choice for use in future cryogenic detectors. Measurements of the Young's modulus of hydroxide catalysis bonds between fused silica were also completed and used to model the thermal noise contribution of bonds in a prototype test mass for the possible room temperature upgrade to aLIGO, A+.

In Chapter 1 an overview of the field of gravitational wave research is given. An explanation of GW sources and a history of the different types of ground-based GW detectors are summarised here, with a focus on Michelson-type interferometric detectors, used to make the first direct GW detections. The noise sources that affect the sensitivity of interferometric detectors are also reviewed.

In Chapter 2 there is a summary of several different bonding techniques that could be considered for making joints between the test masses and suspension elements of GW detectors. The mechanisms of bond formation as well as the advantages and disadvantages to each approach are covered, especially in the context of the requirements for use in a GW detector. Finally hydroxide catalysis and indium bonding are introduced as possible techniques to join the suspension and mirror elements in GW detectors.

In Chapter 3 the breaking stresses of hydroxide catalysis bonds between c-plane sapphire substrates as a function of time is studied. The aim of this experiment is twofold. The breaking stress of bonds that have been allowed to cure for shorter lengths of time is investigated to gain insight into the chemical processes of the bonds as they develop. Additionally, it is crucial to know the breaking stress over longer periods of curing time to be assured that they will not fail in the long term. In fact, this study found that hydroxide catalysis bonded sapphire shows an initial drop in breaking stress, which then levelled off at 15-16 MPa. These results agree with similar trends found in shorter curing time tests on sapphire and fused silica completed in the past.

In Chapter 4 the effect of crystal orientation on the tensile strength of hydroxide catalysis bonded sapphire is investigated. Specifically, the breaking stress of bonds between a-a and m-m planes of sapphire jointed with hydroxide catalysis bonds is studied, using samples of the same geometry and jointed using the same bonding procedures as those presented in Chapter 3. These samples were allowed to cure at room temperature for 4 weeks, then the

samples were strength tested. The breaking stresses were recorded and compared with the breaking stress results of c-c plane sapphire, also cured for 4 weeks at room temperature, reported in the previous chapter.

In Chapter 5 a non-destructive technique of measuring the Young's modulus of hydroxide catalysis bonds between silica and between sapphire is developed. This approach uses acoustic pulses from an ultrasonic transducer transmitted through the bonded samples, and the portion of the acoustic wave that is reflected back from the embedded bond layer is recorded and studied. The bond Young's modulus was extracted from the data by analysis of the amplitudes of the acoustic pulses reflected from the bonds. A Young's modulus value of 15.3 ± 5.2 GPa for hydroxide catalysis bonded sapphire and 21.5 ± 6.6 GPa for bonded fused silica was found with this approach. A Bayesian analysis model of the reflected acoustic signal and the underlying noise background was developed to analyse the low SNR signals of bonds between fused silica. A value of $18.5 \pm^{2.0}_{2.3}$ GPa, with a 90% confidence range was found with this approach, agreeing well with the results from the pulse amplitude analysis.

In Chapter 6 the new Young's modulus value found in Chapter 5 is used to assess the mechanical loss and thermal noise budgets of hydroxide catalysis bonds in different mirror suspension geometries. Two room temperature test masses were modelled; a bonded aLIGO mass and a bonded prototype test mass, of a design suitable for use in A+. Three different cryogenic masses were also modelled; first a sapphire KAGRA mass, followed by a prototype sapphire ET mass, and a prototype silicon ET mass. The thermal noise budgets of the bonds in all of these cases were found to be below the anticipated technical noise requirement for bonds, which is based on each detector's current design sensitivity curves. This indicates that hydroxide catalysis bonds are suitable for use in current detectors and for the design of future ones.

In Chapter 7 different approaches to creating indium bonding procedures for use in cryogenic ground-based detectors are studied. Hybrid suspension designs that utilize both indium and hydroxide catalysis bonding are being considered in cryogenic detector designs such as KAGRA or ET. It is proposed that the hydroxide catalysis bonds would be used to fix the test masses to the suspension elements. This takes advantage of their high breaking stress under shear and peeling, as has been successfully demonstrated in the past for room temperature detectors such as Virgo, aLIGO, or the Germany-based detector GEO600. Indium's low tensile strength means it cannot be used as a joint under tensile or shear load. However it is being considered for use in compressive joints, such as between the fibres and ears or between the fibres and blade springs. This would be done for contingency reasons, since indium can be de-bonded and re-bonded relatively easily, whereas hydroxide catalysis bonds cannot. In the event of a fibre break or a test mass upgrade, the whole bonded test mass assembly could be removed by de-bonding the indium bond interface. It could then be replaced by re-bonding it, making it a good option for future cryogenic mirror suspensions.

Two indium bonding approaches are investigated, diffusion bonding and induction bonding. In both cases the substrates used were polished silicon, and the indium layers between them were made with different combinations of thin thermally deposited films and foils. The tensile strength and a post-break visual inspection of the indium bonds were used as a standard by which to judge bond quality and repeatability.

Chapter 1

The beginnings of gravitational wave astronomy

1.1 Introduction to gravitational waves

The existence of gravitational waves (GW) was first predicted by Einstein in 1916, indicated by the existence of wave solutions to the field equations in his General Theory of Relativity [1]. Since they were first predicted, the effects of GWs were observed by Hulse and Taylor [2]. They made very accurate measurements of the evolution of the orbit of the binary pulsar system PSRB1913+16, showing that the system was losing orbital energy consistent with the emission of GW radiation. While these results were groundbreaking, they weren't yet a direct observation of GWs.

In the 1960's, scientists began developing instruments aimed at the direct detection of GWs, with systems such as resonant bar detectors. These systems were composed of massive aluminium cylinders designed to detect passing GWs as a vibration at the resonant frequency of the bar [3]. Due to the noise limitations and narrow frequency range of the bar detectors, most GW detector approaches starting in the 1970's involved the use of Michelson-type laser interferometers instead of bar detectors. The first interferometric detectors were built around the world beginning in the early 1990s, with the initial LIGO detectors in the USA, initial Virgo in Italy, GEO600 in Germany and TAMA in Japan [4–7]. Since then, general improvements to interferometer design have led to advanced ground-based detectors with increasingly higher sensitivities, such as the advanced LIGO (aLIGO) and advanced Virgo detectors [8, 9].

Finally, in 2015, a gravitational wave signal from a binary black hole merger passed through the arms of the aLIGO interferometers, resulting in the first ever direct detection of gravitational waves [10]. This long-awaited detection made the news worldwide one hundred years after Einstein first predicted the existence of GWs in 1916 [1], and resulted in the 2017

Nobel Prize in Physics being awarded to three key members of the LIGO Scientific Collaboration; Kip Thorne, Rai Weiss and Barry Barish. Since that first detection there have been four more binary black hole inspiral events detected, most recently in August 2017 when the two aLIGO detectors were joined by the advanced Virgo detector in Italy, greatly enhancing the sky localisation of the GW events [11–14].
Only three days after the three detectors observed a binary black hole inspiral in August 2017, the GW signals from a binary neutron star inspiral were detected [15], launching the beginnings of multi-messenger GW astronomy. In two years the GW community has not only confirmed the existence of GWs, but has opened a new window onto our universe and gained previously unattainable knowledge of astrophysical sources. A new era of gravitational wave astronomy has begun.

1.2 Gravitational wave radiation

According to the laws of mass conservation, monopolar GW radiation is not possible. Dipolar radiation is possible in systems where there exists two possible signs, such as positive and negative charges in the case of electromagnetism. In the case of gravitation, there is only positive mass. Therefore dipolar radiation of GWs is also not possible, as it would violate the law of conservation of momentum. Thus the lowest order of GWs that is physically possible is quadrupole radiation, produced by the asymmetric acceleration of mass [16]. For quadrupolar radiation there are two possible orthogonal wave polarisations at 45°

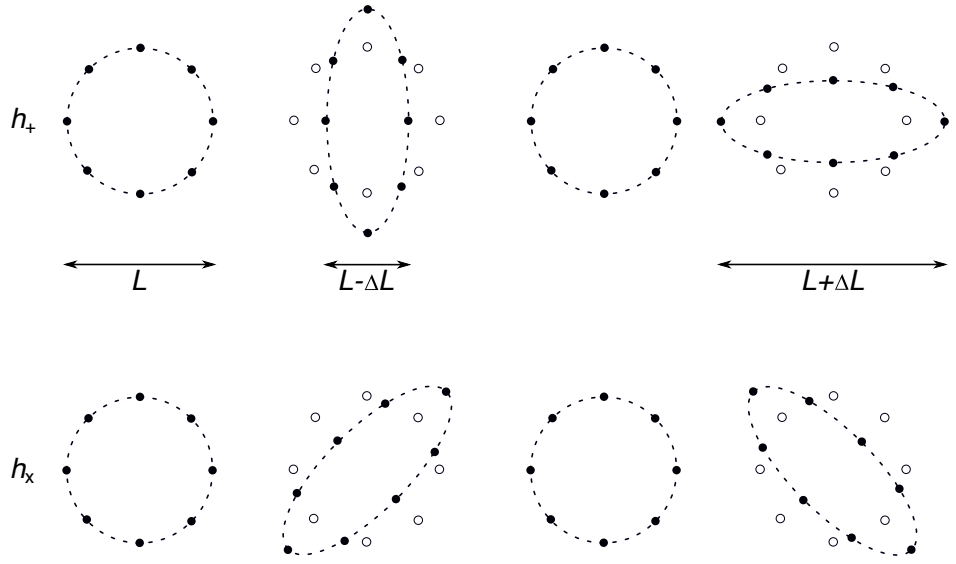

Figure 1.1: Strain effect of a GW propagating normal to the plane of paper acting on a ring of particles. The ring is squeezed in one direction and stretched in the orthogonal direction by ΔL. This schematic shows both possible GW polarisations, h_+ and h_x.

to each other, of amplitude h_+ and h_x. These waves propagate as distortions in space-time

which can be measured as fluctuating strains in space. A visual representation of the strain effect of GWs of both polarisations, h_+ and h_x, as they pass through a ring of particles can be found in Figure 1.1.
Gravitational waves can be thought of as ripples in the curvature of space-time that travel at the speed of light [17]. Such ripples propagating normal to the plane of this page would cause a change in the separation, ΔL, between two adjacent masses with an initial separation L. If a GW with amplitude h and optimal polarization is incident on these two masses, it would produce the following strain relationship [16].

$$\mathrm{h} = 2 \cdot \Delta\mathrm{L}/\mathrm{L} \tag{1.1}$$

All interferometric ground based detectors operate by measuring this strain in some way. However, as the gravitational constant is so small, the effect that GWs have on matter is very weak. Even the most energetic events in the universe such as the coalescence of two massive black holes produce relatively low strain amplitudes as they pass through the Earth, of order $h \approx 10^{-20}$ or lower[10]. Thus attempts to observe them have taken many years of technological advancements to produce detectors with the necessary sensitivities.

1.3 Sources of gravitational waves

GW radiation spans a wide range of frequencies, with different sources emitting signals in different frequency bands, shown in Figure 1.2. Ground-based detectors aim to operate in the frequency band of 10-7000 Hz [16], to detect signals from sources such as merging neutron star binaries and stellar mass black holes. Other types of detectors are proposed to operate in different frequency bands, such as LISA, a space-based detector designed to detect lower frequency sources such as super massive binary black hole systems [18].
In general, sources of GWs can be categorised into different types depending on their signal type. Transient, continuous, and stochastic sources are explained here.

1.3.1 Transient sources

Transient sources emit short duration and highly intense GW signals. These signals may result from violent astronomical events such as supernovae and coalescing compact binary systems, which are discussed in this section.

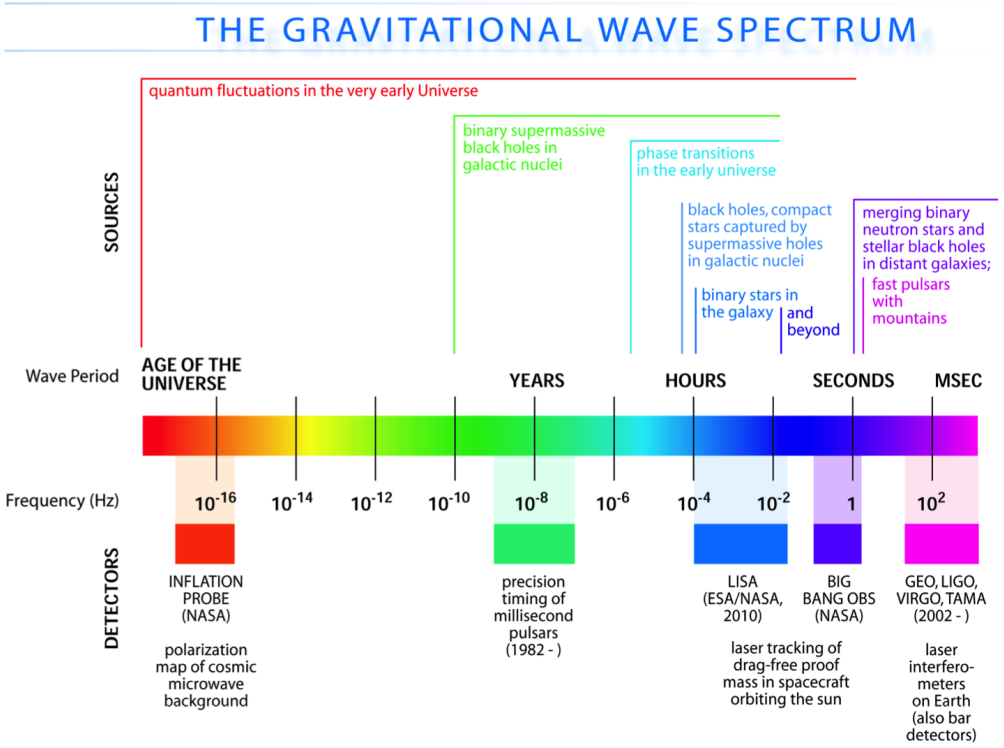

Figure 1.2: Spectrum of GW sources and types of detectors (credit:NASA).

Supernovae

Massive stars gradually build up heavier and heavier elements in layers around their core during their lifetime, with lighter elements in the outer shells and denser ones at the centre. Once the star's dense core exceeds $\approx 1.4 M_{\odot}$ (1.4 solar masses), the star will experience runaway internal nuclear reactions and experience core collapse. This is defined as the Chandrasekhar limit. During collapse, the lighter outer shells of the star bounce off the denser core, and at this point the implosion turns into a massive explosion [19]. This phenomenon has long been studied by astronomers, as in its final death-throes a star can emit brightly and suddenly in the electromagnetic spectrum. In fact "new star" is where the name supernovae is derived from.
In the case of an asymmetric core collapse, the massive amount of energy of the explosive supernovae is not all released as electromagnetic radiation. In this case some of it can be released in the form of gravitational radiation. Such events are expected to be rare however. If Earth was 10 kpc away from a star that went supernova then the strain seen at Earth would be somewhere in the range of $h \approx 10^{-21}$ [20].

Compact binary systems

After going supernova, the cores of these massive stars are predicted to form either black holes or neutron stars, depending on the initial starting mass of the star. When a star is

between $\approx 10M_\odot$ and $\approx 29M_\odot$, the core will then collapse to form a new and extremely dense star. These objects have been compressed so much during collapse that while their radii measure in the tens of kilometres, their mass can exceed twice that of our Sun. These stars approach the density of atomic nuclei and some models suggest they are mostly comprised of neutrons. Thus they are called neutron stars [19].
Similarly, if a star is initially $\gtrsim 29M_\odot$ in total mass, it is expected to form a black hole after the collapse of its core.
The strain signal from the collapse of a compact binary system can be written as [21]

$$h \approx 1 \times 10^{-23} \left(\frac{m_{tot}}{M_\odot} \right)^{2/3} \left(\frac{\mu}{M_\odot} \right) \left(\frac{f}{100\,\mathrm{Hz}} \right)^{2/3} \left(\frac{100\,\mathrm{Mpc}}{r} \right) \tag{1.2}$$

where the total mass of the system is $m_{tot} = m_1 + m_2$, and the reduced mass is $\mu = \frac{m_1 m_2}{m_1 + m_2}$. The distance from the Earth to the source is r and the frequency of the gravitational radiation emitted from the system is f. The exact amplitude of these signals depends on how massive each star or black holes in the binary is. However, as these compact binary systems are made up of the most massive and dense objects in our universe, the inspiral and merger of such a system can produce GW signals with very high amplitudes, on the order of $h \approx 10^{-19}$ [16].
The coalescence of compact binary star systems, including both black holes and neutron stars, is a promising area of GW astronomy. Little is known about black holes in particular; although massive and energetic they do not emit measurable energy in the form of electromagnetic (EM) radiation. Thus GW astronomy can provide unique information about these sources that is not possible to get from EM astronomy alone. In fact, the first detection of GWs from a binary black holes inspiral was the first time black holes had been directly observed [10].
There are three main stages of a coalescing binary system; the inspiral, the merger, and the ringdown [10]. These stages can be seen in the observed signal from the first GW detection in Figure 1.3.

When two compact objects which orbit a common centre of mass draw closer together, their orbital frequency increases and they begin to spiral in towards each other. This is observed as an increase in the frequency of GWs being emitted from the binary system, and is called an inspiral. This source frequency increases until the two objects meet and merge together, releasing a huge amount of energy. The amplitude of the signal also increases, reaching a maximum at the point where the two compact objects merge. During the merger, the two compact objects, either black holes, neutron stars or a combination of both, combine to form a single compact object which then rings down and settles to a constant state. In the case of the first detection in Figure 1.3 two black holes, $36^{+5}_{-4} M_\odot$ and $29 \pm 4 M_\odot$ in size, released $3 \pm 0.5 M_\odot$ of energy in the form of GWs as they coalesced into

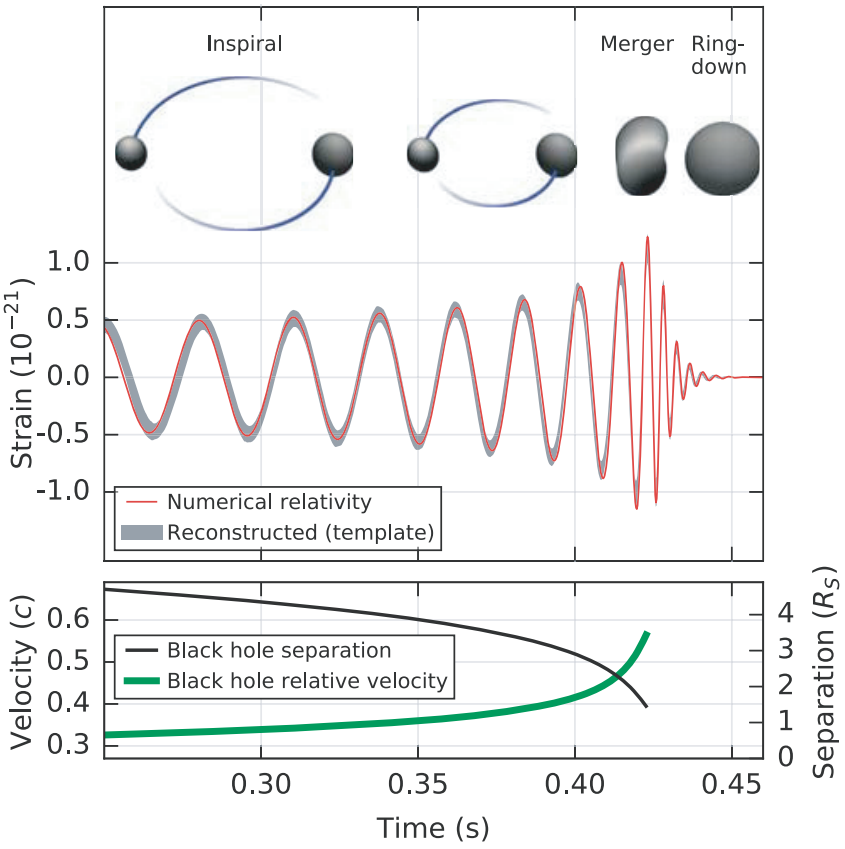

Figure 1.3: Detection of GWs from a binary black hole merger [10]

one black hole of $62 \pm 4 M_\odot$.

A GW signal from a binary neutron star inspiral was observed in August 2017, the first detection of its kind. Each star's mass was in the range of $1.17 M_\odot - 1.6 M_\odot$, where the total mass of the system was $2.74^{+0.04}_{-0.01} M_\odot$. Although there were three detectors online, the two aLIGO detectors and the advanced Virgo detector, the signal was present in only the two aLIGO detectors. The absence of signal in the advanced Virgo detector provided valuable extra information on where in the sky the source was located, narrowing the sky localisation to 28 ° (90 % probability). This merger had a luminosity distance of 40^{+8}_{-14}Mpc, also making it the closest and most precisely localized GW signal yet detected [15].

In addition to GWs, signals in the electromagnetic spectrum produced by this neutron star merger were detected in over 70 different observatories. A gamma ray burst named GRB 170817A, was first observed by Fermi-GBM, who then alerted the GW community to the possibility of a GW source [22]. This burst, which actually happened 1.7 s after the GW signal was measured in our detectors, was also verified by INTEGRAL [23]. Follow-up observations in collaboration with the wider electromagnetic astronomy community led to several important breakthroughs, a selection of which are shown in Figure 1.4. The as-

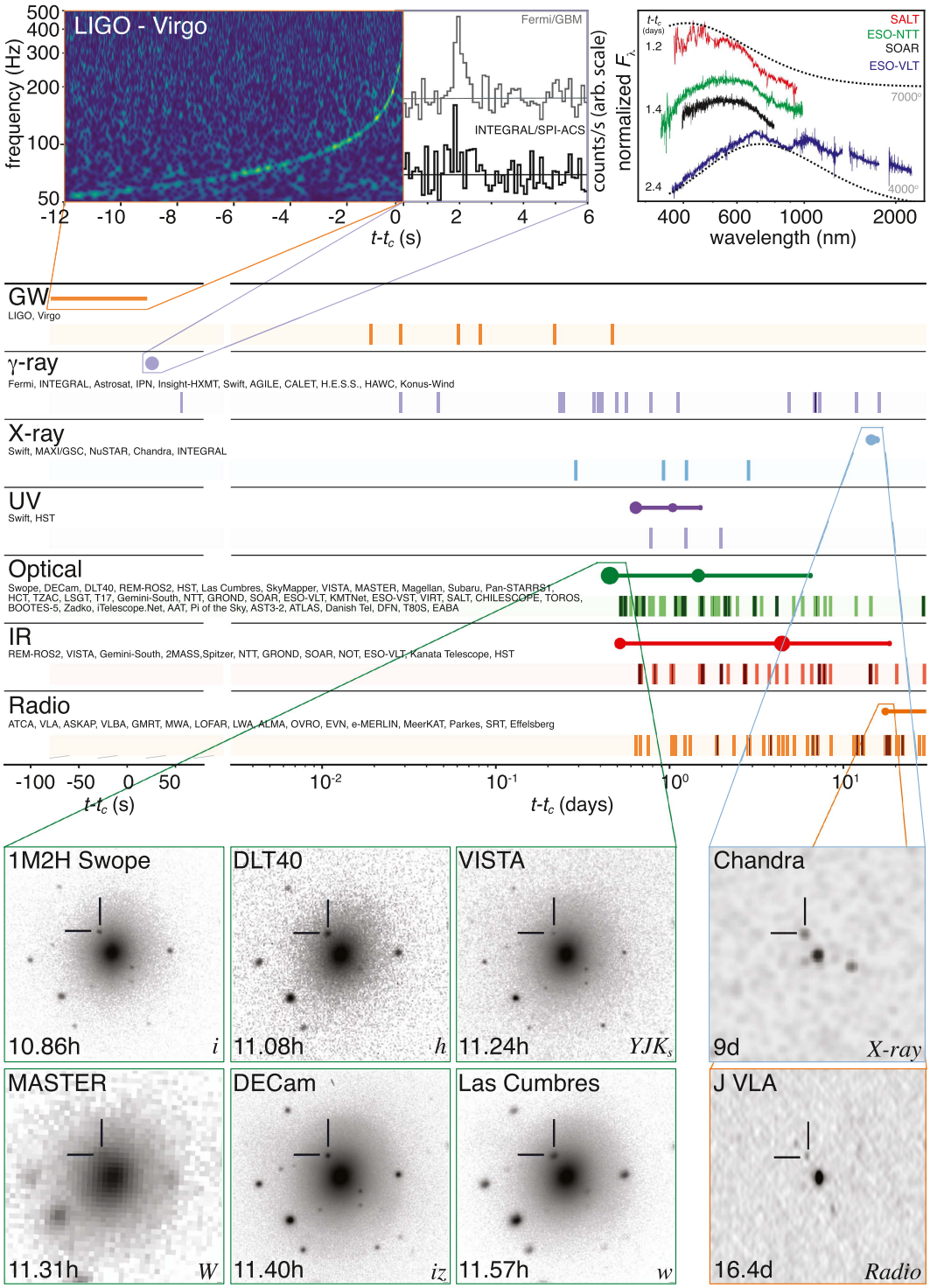

Figure 1.4: Results of multi-messenger GW astronomy from binary neutron star merger GW170818. The gravitational wave signal is shown alongside its electromagnetic counterparts, over a period of about two weeks after the event [22].

sociation of these two events not only provided compelling evidence of the link between gamma ray bursts and neutron star mergers, it also confirmed that GWs travel at the speed of light, in accordance with Einstein's General Theory of Relativity.

The neutron star merger rate could be calculated as $R = 1540^{+3200}_{-1220}\,\mathrm{Gpc}^{-3}\,\mathrm{yr}^{-1}$, from O1 and

O2 data [15].
An independent measurement (or so-called standard candle measurement) of the Hubble constant, a quantity which represents the local expansion rate of the Universe, was also made using the distance to the binary neutron star merger from the GW signal combined with the recession velocity inferred from the electromagnetic data of the same event. The Hubble constant was determined to be $H_0 = 70^{+12.0}_{-8.0}\,\mathrm{km\,s^{-1}\,Mpc^{-3}}$, which is consistent with existing measurements while being completely independent of them [24].
The observed electromagnetic counterparts indicated the signature of a kilonova, a phenomenon by which the leftover material from the neutron star collision is blown far out into space. Labelled AT 2017gfo, this kilonova that is thought to have followed the neutron star merger produced and ejected about $0.5\mathrm{M}_\odot$ of heavy elements, such as gold and platinum [25]. Counterpart observations across the electromagnetic spectrum including X-ray, ultraviolet, optical, infra-red, and radio waves that originated in the same area of the sky were witnessed by over 70 observatories worldwide, definitively marking the beginning of multi-messenger GW astronomy.

1.3.2 Continuous sources

There are sources in our universe that constantly produce GWs. However the amplitude of these is much smaller than the violent coalescence of black holes and neutron stars, and was out of the range of sensitivity of ground-based detectors until aLIGO and Virgo [16, 26].

Pulsars

Rotating neutron stars emit beams of electro-magnetic radiation at radio frequencies from their magnetic poles. If these poles are oriented towards the Earth at any point in the rotation of the star, they will been observed as a periodically pulsing radio source, much like the light from a lighthouse. These pulsed radio sources were discovered in 1967 and were named pulsars [27].
Pulsars that have some degree of asymmetry in their shape can release energy in the form of GWs as well as electro-magnetic radiation. GW radiation that is emitted by pulsars in this way could have a strain described by [28]

$$h = \frac{16\pi^2 G}{c^4}\frac{\epsilon I_{zz} f_{rot}^2}{r} \tag{1.3}$$

once it reaches the Earth. Here r is the distance from the detector, c is the speed of light, G is the gravitational constant, f_{rot} and I_{zz} are the frequency of the pulsar's rotation and its

moment of inertia. The last term, $\epsilon = \frac{I_{xx}-I_{yy}}{I_{zz}}$ is the equatorial ellipticity of the star, which could be related to distortion from the magnetic field, but is not usually well known. Defining the upper limit of energy from pulsars released as GWs and developing algorithms to search for these continuous signals is an active area of research within the GW community [26], with recent analysis of aLIGO data pointing towards strain amplitudes of $\approx 10^{-25}$ for these sources [29].

X-ray binaries

Neutron stars can exist in binary systems with ordinary stars. In this case the gravitational well of the dense neutron star gradually pulls mass away from its companion star. The angular momentum of the neutron star will increase as more mass is accreted from the other star. X-rays can be emitted during mass accretion, which leads these systems to be called x-ray binaries [16]. As the angular momentum of the neutron star increases, the star may become unstable and its rotation become non-axisymmetric. At the point where rotation is non-axisymmetric, gravitational waves can be emitted. Neutron stars of this type are called Wagoner stars [30]. The gravitational radiation of this source is estimated to have a strain amplitude of

$$h = 3 \times 10^{-27} \left(\frac{1\,\mathrm{kpc}}{r} \right) \left(\frac{1\,\mathrm{kHz}}{mf} \right)^{1/2} \left(\frac{\mathcal{L}_\gamma}{10^{-8}\mathrm{erg/cm^2/\,sec}} \right)^{1/2} \tag{1.4}$$

where m is the mode number, $f = 500 \pm 300$Hz is the frequency of the rotation of the star, r the distance away from the Earth, and $\mathcal{L}_\gamma$ is the x-ray flux, which indicates the accretion rate of the Wagoner star [30]. The strain of these sources could be as high as $h \approx 10^{-22}$, depending on the accretion rate, distance, and the unpredictable internal viscosity of the neutron star.

Gravitational radiation could be emitted by low-mass x-ray binaries via a few possible mechanisms. If the matter accreted by the neutron star is confined by its magnetic field to a mountain at the magnetic pole, then GWs would be produced [31]. Alternatively, instabilities in the star driven by accretion could lead to a steady emission of GWs [32, 33]. It is possible that the rotational speed of neutron stars in low mass x-ray binary systems is limited by the accreted angular momentum being radiated in the form of GWs, possibly due to asymmetrical heating of the neutron star as it pulls matter from its companion, creating a quadrupole moment [34]. In these cases, GWs emitted from x-ray binaries such as x-ray source Sco X-1 could be detected by ground-based detectors [35].

Stochastic background

The superposition of GWs from events all across the Universe creates a stochastic background of GWs, including GWs produced in the Big Bang at the end of the Inflationary Period, or anisotropies in space-time arising from quantum gravitational processes in the early Universe [36]. The stochastic background is made up of all these sources, and would be random in distribution and roughly constant in amplitude. More understanding is needed of what the frequencies and strain amplitudes of this source would be, however GWs from the early universe as well as the anisotropy of the stochastic background could be studied in LISA's detection band [36, 37]. It is possible that the aLIGO detectors could detect signals from the stochastic background, and in doing so gain information on its polarisation [38].

1.4 Resonant bar GW detectors

Efforts to directly detect GWs began in the 1960's with the development of resonant bar detectors. These detectors were composed of room temperature aluminium cylinders, isolated from the ground vibrations of the surrounding environment. A passing GW would produce spatial strains in such a bar, which was postulated to make it vibrate at its resonant frequency of 1657 Hz [3]. A belt of piezos, mounted around the middle of the bar was designed to transform the strain from a GW passing through the bar into an electric signal [39].

In 1969 Weber reported coincident GW measurements between two bar detectors. Since these two bars were situated 1000 km apart, the probability for accidental occurrence from local sources was very small [40]. This report spurred the construction of more resonant bar detectors, which unfortunately were not able to replicate these measurements of GWs. Although the room temperature resonant bar detector approach was largely superseded in the 1970s in favour of more sensitive detector designs, it served to pioneer the field of GW detectors.

As technologies improved and interest in the field grew, some new resonant bar detectors were cooled to cryogenic temperatures, achieving sensitivities of $10^{-20}\sqrt{\text{Hz}}$ with a band width of 100 Hz in comparison to the $10^{-19}\sqrt{\text{Hz}}$ strain sensitivity of room temperature resonant bars. AURIGA was the last detector of this type in operation [41]. Two spherical mass detectors, MiniGRAIL and the Mario Schenberg Detector were also constructed. Their spherical geometry allows the measurement in five more degrees of freedom, compared to only one in a bar detector. They were operated at a bandwidth of 60 Hz, and although the achievement of such performance has not been reported, they were designed to measure strains of $10^{-21}\sqrt{\text{Hz}}$ at 3000 Hz [42, 43].

1.5 Interferometric GW detectors

Beginning in the early 1970s laser interferometer technology had advanced and the first Michelson-type interferometric detectors were constructed [44]. While resonant bar detectors are only sensitive in a narrow frequency range close to their resonant frequency; interferometric detectors can be designed to have much wider bandwidths, and lower noise levels.

All GW detectors can be imagined simply as systems that are capable of measuring the fluctuating strains in space-time caused by GW radiation. One such system would be two free masses, separated by a well monitored distance L, that would measure strain amplitudes, h, as was defined in equation 1.1 where $h = 2 \cdot \Delta L/L$. Interferometric GW detectors work on this basic principle, with their sensitivity defined by this strain equation. By splitting a coherent light source (i.e. laser) along two perpendicular paths of equal length L, and recombining them as shown in Figure 1.5 it is possible to measure very small differences in optical path length by comparing the phase difference of the laser light after it is recombined.

GWs passing through the interferometer will shorten or lengthen one of the arms with

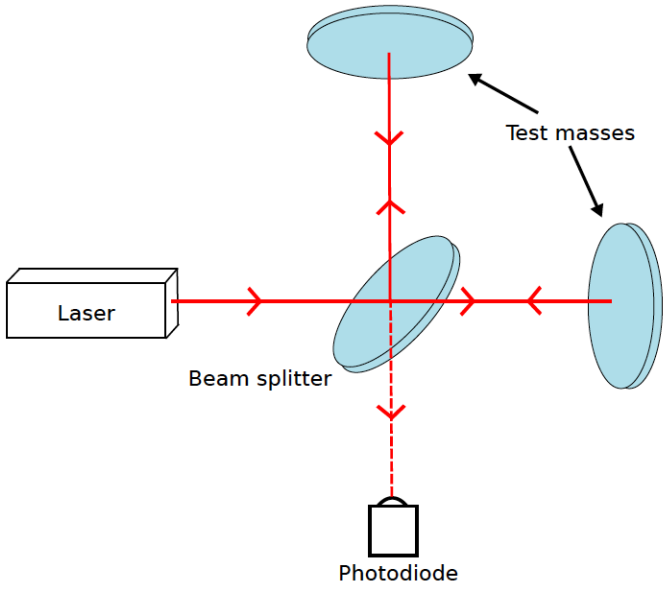

Figure 1.5: Schematic of simple Michelson interferometer.

respect to the other, to an extent determined by the source's direction of incidence with respect to the detector's arms and the GW polarisation. This results in a phase difference between the light in the two arms on recombining and thus a change in the detected intensity of the interference pattern at the interferometer output.

The arm length of interferometric detectors greatly affects their overall sensitivity, the maximum occurring when the time for which the laser light is stored within the interferometer arms is equal to half the GW's period. In this ideal case, the light takes a quarter of the

period of the GW to travel from the beam splitter to the end test masses. Hence the light would reach the end test masses at maximum displacement by passing GWs.
For a GW source at $f = 100\,\text{Hz}$ the arms of the detector would ideally be 750 km in length [45]. In reality this proves to be impractical on Earth, due to its curvature and other environmental constraints. Thus different interferometric techniques were developed to increase the optical path length of the detectors and their sensitivities without physically increasing their arm lengths.

1.5.1 Fabry-Perot cavities

One optical technique that increases the sensitivity of GW detectors involves the use of Fabry-Perot cavities. The use of such cavities in prototype GW detectors was developed in Glasgow in the 1980s [46]. Fabry-Perot cavities are created by placing partially transmissive input test masses (ITMs) after the beam splitter in both arms of the interferometer. Laser light enters the cavities through the partially transmissive ITMs and is reflected back and forth between each ITM and the highly reflective end test mass (ETM) in each arm. In this configuration the laser beams overlap and the optical path length is effectively lengthened.

1.5.2 Power recycling

Power recycling is a technique used to increase the power of the laser light incident on the detector's beamsplitter [47, 48]. A partially transmissive optic is placed in the beam path between the laser and the beam splitter which forms an additional cavity with the interferometer. The light reflected back from the power recycling mirror cancels with the signal from the beamsplitter towards the laser, as in Figure 1.6. The interferometer is then operated at a "dark fringe", meaning that the laser light from its arms completely destructively interferes at the beam splitter, as it propagates towards the photodetector. This increases the stored laser power within the interferometer, thus increasing the sensitivity of the detector by reducing the levels of shot noise, which is explained in more detail in Section 1.6.2.

1.5.3 Signal recycling

Signal recycling is similar in concept to power recycling, only this time a partially transmissive optic is placed in between the beam splitter and the photodiode instead of in between the beam splitter and the input laser [48]. Again the detector is operated at a dark fringe, where any relative motion of the test masses will change the relative phase of the laser light and a non-zero signal will be seen instead of the null signal of the dark fringe. When

a non-zero signal is present, the laser light from the interferometer will pass through the beam splitter and be partially returned by the signal recycling mirror, thereby allowing the output signal to build up. The peak frequency sensitivity of the detector can be altered by changing the placement of the signal recycling mirror. This means the detector can be effectively tuned to be more sensitive to GWs from different sources.

1.5.4 Interferometric GW detector layout

Most Michelson-type interferometer GW detector share a few key elements. The aLIGO detectors, for example, operates under vacuum with a pre-stabilized Nd:YAG laser with a wavelength of 1064 nm as a light source [8]. This laser injects 20 W into the interferometer, which is increased via use of a power-recycling cavity prior to the beamsplitter [49]. After

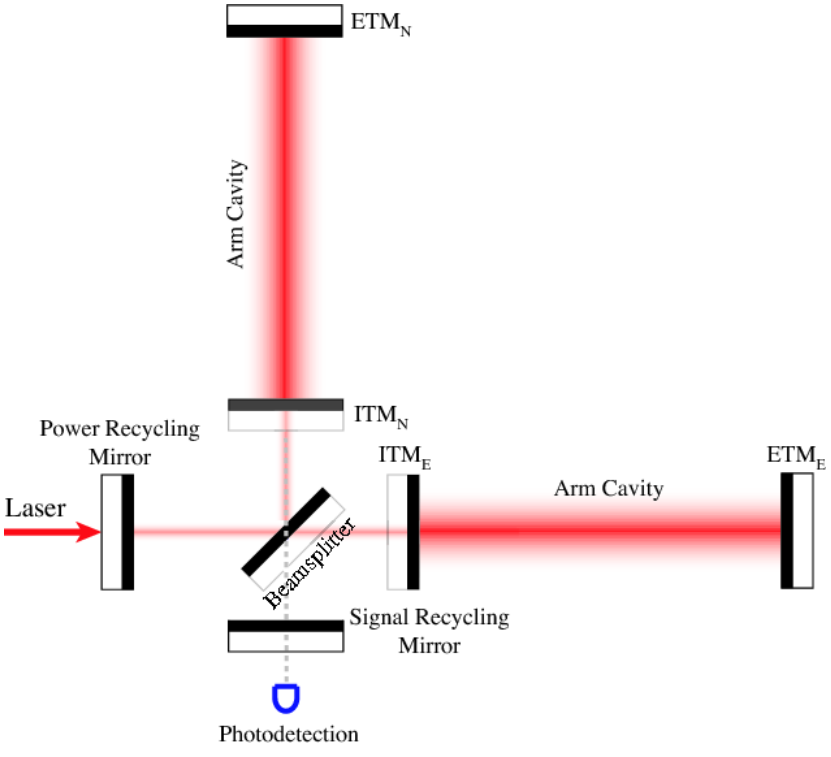

Figure 1.6: Michelson interferometer layout, with signal and power recycling and Fabry-Perot cavities

being split into the two arms of the detector, the light builds up in both Fabry-Perot cavities, then returns to the beamsplitter and registered as an output signal by the photodetector, shown in Figure 1.6. Here a signal recycling mirror again increases detector sensitivity. Changes in the phase difference between the two returning laser beams reflect a departure from perfectly matched arm lengths. Such changes can be caused by local strains in space-time created by a passing gravitational wave [50].

The mirror suspensions are isolated from environmental and technical noise sources using

a variety of techniques [16]. The noise sources that have the most impact on detector sensitivity are explained in the next section, along with the techniques used to mitigate them.

1.6 Noise sources in GW detectors

For a detector to reliably measure such small changes in distance, it must be isolated as much as possible from all environmental effects that cause movement. Thus ground-based GW systems face an extensive list of environmental and technical noise sources that limit their performance. The most significant noise sources that limit the current detectors are seismic noise [51], shot noise [52], radiation pressure noise [53], Newtonian noise [54], and suspension and mirror thermal noise [55]. Each noise source impacts detector sensitivity in different frequency bands, and is addressed in different ways. An example showing the predicted level of each noise source and how each contributes to the sensitivity curve of the aLIGO observatories is shown in Figure 1.7.

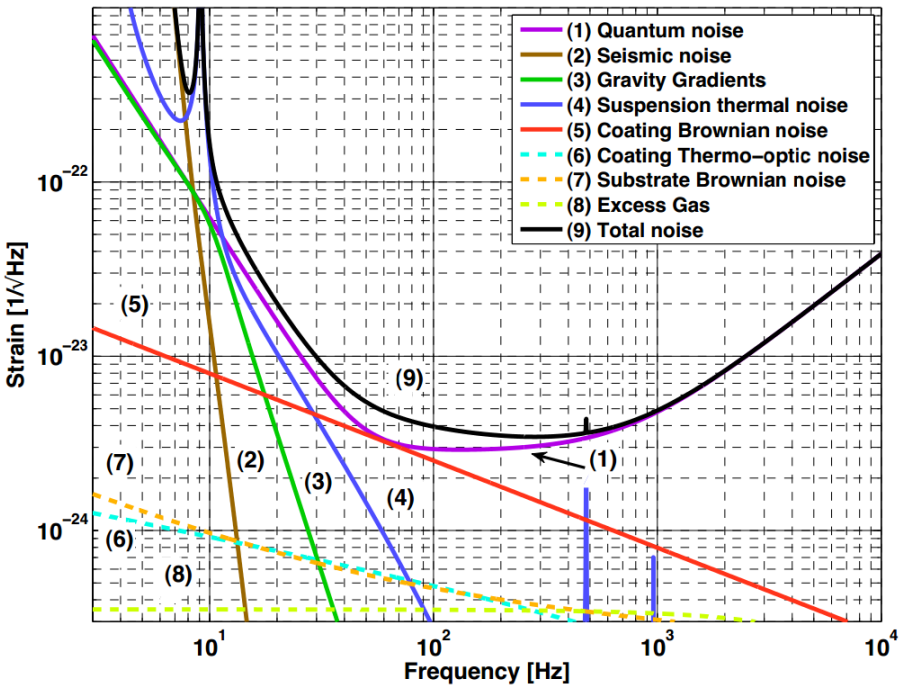

Figure 1.7: Impact of noise sources on a ground-based GW system's sensitivity curve (aLIGO) [56]

1.6.1 Seismic noise

Seismic noise includes the environmental vibrations felt by the mirrors and is most dominant at frequencies of around 1-10 Hz [51]. The sources and amplitudes of seismic noise are

location and time specific and more variable than other more fundamental sources, which means the frequency of seismic noise is also variable and unpredictable. Vibrations caused by a far away earthquake, a logging truck on a nearby highway, and everything in between impact the detectors as sources of seismic noise. The overall levels of seismic noise vary by geographical location. For a relatively quiet place the noise (at a frequency f) is $\approx 10^{-7} \times f^{-2}\mathrm{m}/\sqrt{\mathrm{Hz}}$ [51]. For a gravitational wave to be detected the maximum displacement of each test mass must be $< 3 \times 10^{-20}\mathrm{m}/\sqrt{\mathrm{Hz}}$ in all three directions at 30 Hz [51]. This means the seismic noise in the horizontal direction must be reduced by at least a factor of 10^{10} at 30 Hz. Due to the Earth's curvature, seismic noise in the vertical direction can couple to the horizontal axis, so though requirements are most strict along the horizontal axis, seismic isolation must be applied in all three directions.

The best way to limit this source is to isolate the mirrors from the surrounding environment

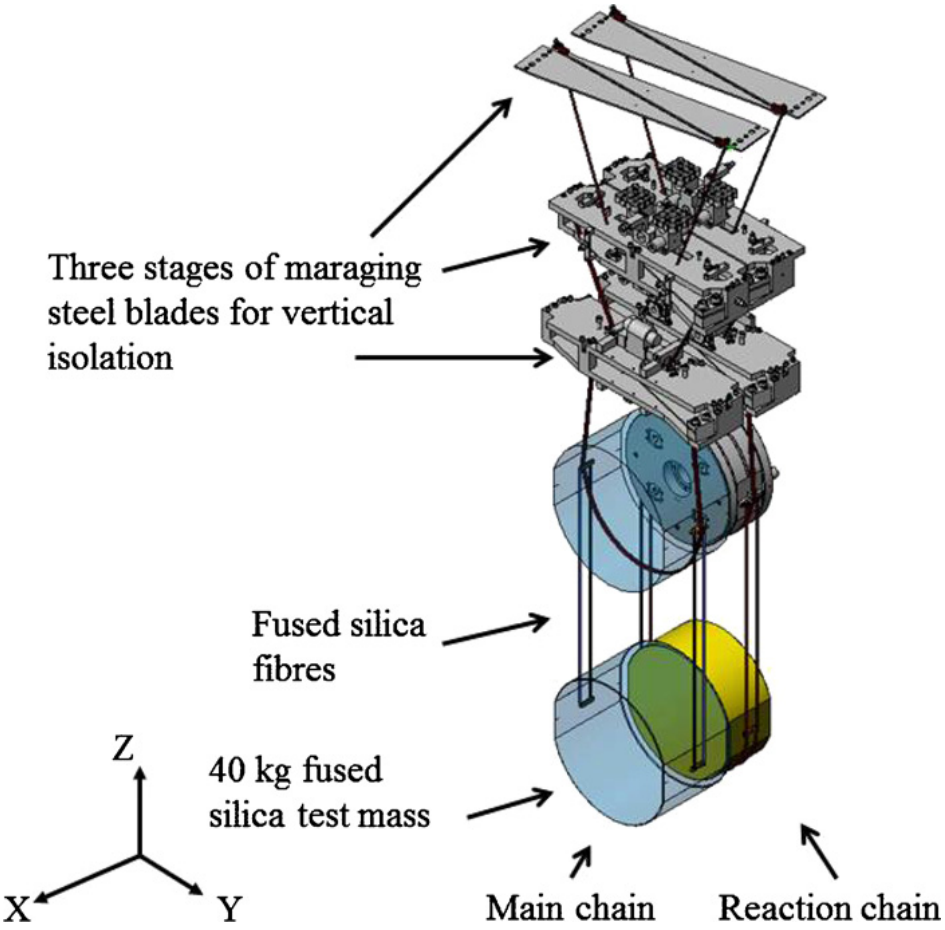

Figure 1.8: aLIGO QUAD multi-stage pendulum suspension, where the bladesprings provide three stages of vertical isolation and the four stage pendulum provides four stages of horizontal isolation. [57].

as far as is possible. In particular, horizontal seismic noise can be mitigated by suspending the test masses as pendulums. This attenuates the effects of ground motion above the resonant frequency, f_0, of the pendulum by $\approx -f_0^2/f^2$ for a single stage pendulum. Thus

the test masses are suspended in multi-stage pendulum suspensions, where each additional stage offers a further degrees of isolation [56]. For example, in the aLIGO detectors such multi-stage pendulums include the use of cantilever springs to limit vertical motion of the test masses, and are fixed to seismic pre-isolation tables, as shown in Figure 1.8 [57].

1.6.2 Quantum noise

Two quantum noise sources have to be considered in GW detector design; photon shot noise, and radiation pressure noise. Photon shot noise is an effect that is due to the discrete nature of photons. The independent and random distribution of photons is measured by photodiodes as a Poisson distribution [52]. A similar effect is found in electronics, where the discrete nature of electric charge can result in electronic shot noise [58].
Vacuum fluctuations between optics and the photodiodes in detectors cause random events which is interpreted as shot noise. This effect becomes dominant at frequencies on the order of a few hundred hertz.
Additional effects from technical noise sources can worsen the level of apparent shot noise, such as the efficiency of photodiodes used. These should be as efficient as industry can provide, but will never fully reach 100 %.
Therefore, shot noise is a limiting factor to detector sensitivity. Assuming a photodiode that has 100 % quantum efficiency, the absolute limit in a Michelson-type interferometer can be represented as [16]

$$h_{shot}(f) = \left(\frac{1}{L}\right)\left(\frac{\hbar c \lambda}{2\pi P_{in}}\right)^{1/2} \tag{1.5}$$

where L is the interferometer arm length, $\hbar$ is the reduced Planck's constant, c is the speed of light, λ is the laser wavelength and P_{in} is the laser power. Equation 1.5 shows that photon shot noise levels can be reduced by increasing the laser power in the interferometer.
Radiation pressure noise occurs when the photons from the laser are reflected from the test mass optics and in doing so transfer momentum from the photons to the optic, which acts as a force on the face of the optic. The random distribution of the photons reflected from the optic leads to a fluctuating force on its face, causing it to change position. This movement leads to a phase change when the beams are recombined. The radiation pressure noise in a Michelson-type interferometer is given by [16]

$$h_{rp}(f) = \left(\frac{1}{mf^2 L}\right)\left(\frac{\hbar P_{in}}{2\pi^3 c \lambda}\right)^{1/2} \tag{1.6}$$

where m is the mass of the optic (test mass in this case), f is the frequency, L is the interferometer arm length, $\hbar$ is the reduced Planck's constant, P_{in} is the input laser power, c is the speed of light and λ is the laser wavelength. From equation 1.6 it can be seen that radiation pressure noise has the greatest effect at the lowest frequencies and that it's effect increases with increasing laser power.

Although this effect is small, the interferometer must be sensitive to extremely small changes in distance to detect GWs. Thus radiation pressure noise must be mitigated. This source has the greatest effect at very low frequencies, increases with increasing laser power, and decreases with increasing mass of the optic it acts upon. For example, one of the reasons the 40 kg optics in aLIGO are so large is to counter-act the effects of radiation pressure noise [8].

Quantum noise sources such as shot noise and radiation pressure noise are not correlated sources in Michelson-type interferometers without signal recycling and so can be combined in quadrature to give the total optical readout noise of a detector, as in

$$h_{o.r.n}(f) = \sqrt{h^2_{shot}(f) + h^2_{rp}(f)}. \tag{1.7}$$

Photon shot noise can be reduced by increasing laser power, and radiation pressure noise can be reduced by reducing laser power, shown in equations 1.5 and 1.6. Thus an optimal power level exists where each noise source is minimised, where $h_{shot} = h_{rad}$. Plugging this optimal power value P_{opt} into equation 1.7 attains a level of lowest possible quantum noise,

$$h_{SQL}(f) = \frac{1}{\pi f L}\sqrt{\frac{\hbar}{m}}. \tag{1.8}$$

This sensitivity limit is known as the standard quantum limit (SQL) and is consistent with the Heisenberg Uncertainty Principle [52, 53].

Techniques are being investigated to extend the sensitivities of GW detectors past the SQL. These are known as quantum non-demolition (QND) techniques. One such technique is to measure the speed (and with it the momentum) of test masses instead of monitoring their position as most currently operating detectors do. Instruments emplying this technique are called "speedmeters", and are expected to outperform an equivalent Michelson-type interferometer at low frequencies due to reduced quantum radiation pressure noise [59]. A proof of concept Sagnac speedmeter experiment is currently in its commissioning phase at the University of Glasgow [60].

Another QND technique called "squeezing" was proposed in the early 1990's [53] and has since then been developed to reduce shot noise via manipulating or "squeezing" the states of laser light in order to reduce vacuum fluctuations and overall quantum noise. First tested on a large scale in GEO 600 [61], it is proposed to be a part of the A+ upgrade to the aLIGO

detector and is also proposed be a fundamental part of future detectors [62].

1.6.3 Newtonian noise

Newtonian noise, also called gravity gradient noise, is dominant at low frequencies under 10 Hz [51]. This source is created by density perturbations from moving terrestrial masses such as vehicles and clouds. These density perturbations exert a direct gravitational pull on the test masses, changing their position as the sources move. It cannot be fully mitigated on the surface of the earth and so effectively provides a lower limit to current ground-based detectors [63]. Next generation detectors such as KAGRA [64] and ET [65] are being built underground to reduce the effects of gravity gradient noise. Space based detectors such as LISA are not exposed to the effects of terrestrial gravity gradient noise, which will allow them to observe lower frequency sources than ground-based detectors [45].

1.6.4 Thermal noise

Thermal noise in interferometric detectors arises from thermally driven motion of the mirror suspensions, or other thermodynamical fluctuations which may impart a phase change to the laser beam as it probes the mirror's position. An important component of this is Brownian motion, which was first quantified by Einstein in 1905 for a particle as an energy of $\frac{1}{2}\mathrm{k_B T}$ per degree of freedom, where $\mathrm{k_B}$ is Boltzmann's constant and T is temperature [66]. It is now well understood that dissipative systems such as mechanical oscillators will exhibit spontaneous thermal fluctuations in displacement as described by the fluctuation-dissipation theorem [55, 67].
This theorem relates the power spectral density due to a fluctuating driving force, $S_F(\omega)$, of a mechanical system to the dissipative, or real, part of the system's impedance, $\mathbb{R}[Z(\omega)]$. This is represented as [55, 67]

$$S_F(\omega) = 4k_B T \mathbb{R}[Z(\omega)] \tag{1.9}$$

where k_B is Boltzmann‘s constant, and T is the temperature. Considering a force, F, that acts on an object causing a velocity v of this object, the mechanical impedance can then be defined as F/v. Using this, the fluctuation-dissipation theorem can be expressed as the power spectral density of thermal displacement, $S_x(\omega)$,

$$S_x(\omega) = \frac{4k_B T}{\omega^2} \mathbb{R}[Y(\omega)] \tag{1.10}$$

where $Y(\omega) = 1/Z(\omega)$ is the mechanical admittance. Therefore, noise in the form of the amplitude spectral density of thermal fluctuations can be calculated from the real part of

the mechanical admittance of a system, $\mathbb{R}[Y(\omega)]$.
A number of different external sources can contribute to thermal noise in a detector. Gas damping from air molecules is one possible source [68], or recoil damping where energy can be dissipated from the suspension to the support structure [68]. Frictional losses from contact points of the suspension and/or test masses rubbing together also contributes to external sources of dissipation [69]. However, external damping effects such as these are intentionally minimized in the design of gravitational wave detectors, i.e. by operating under vacuum to minimize gas damping [16].
After external sources are mitigated, the internal damping in the materials that make up the test mass and suspension elements must also be addressed. Internal damping arises from anelastic behaviour, where the strain response in a material is not instantaneous when a stress is applied [70]. An ideal elastic material would obey Hooke's law such that a strain would be produced instantly in response to an external force, or stress. Conversely, the phase lag between the stress and the strain in anelastic materials, has a finite relaxation time. For example, a periodic stress of angular frequency ω that is applied to a material will induce a periodic strain. In an anelastic material this periodic strain will have the same angular frequency, ω, as the applied stress, but it will also have a phase lag, ϕ. This ϕ is known as the mechanical loss angle, or the mechanical dissipation factor of a material [71].
The resonant modes of the pendulum suspensions in a GW detector can be modelled as damped harmonic oscillators that obey Hooke's law. This law relates a force F to a displacement x, depending on a spring constant, k,

$$F(\omega) = -kx \tag{1.11}$$

For materials that do exhibit anelastic properties, but the phase lag is very small, are called low loss systems where $\phi(\omega) << 1$. This can be introduced into Hooke's law as an imaginary part of the spring constant k,

$$F_{\text{spring}}(\omega) = -k\,(1 + i\phi(\omega))\,x \tag{1.12}$$

Thus the equation of motion for a harmonic oscillator of mass m, with a phase lag (i.e. mechanical loss) $\phi(\omega)$, that experiences an internal driving force due to thermal sources can be written as

$$F_{\text{thermal}}(\omega) = m\ddot{x} + k\,(1 + i\phi(\omega))\,x. \tag{1.13}$$

This can be expressed in terms of velocity, using complex notation ($e^{i\omega t}$),

$$F_{\text{thermal}}(\omega) = i\omega m\dot{x} - i\frac{k}{\omega}\,(1 + i\phi(\omega))\,\dot{x}. \tag{1.14}$$

Now it is possible to obtain an expression for impedance, which is the force divided by velocity,

$$\mathcal{Z}(\omega) = i\left(\omega m - \frac{k}{\omega}\right) + \frac{k}{\omega}\phi(\omega). \tag{1.15}$$

Recalling that the mechanical admittance was defined as one over the mechanical impedance, the admittance can now be calculated as

$$\mathcal{Y}(\omega) = \frac{1}{\mathcal{Z}(\omega)} = \frac{-i\left(\omega m - \frac{k}{\omega}\right) + \frac{k}{\omega}\phi(\omega)}{\left(\omega m - \frac{k}{\omega}\right)^2 + \left(\frac{k}{\omega}\phi(\omega)\right)^2} \tag{1.16}$$

Now considering that $\omega_0^2 = \frac{k}{m}$, the real part of the admittance can be simplified and used,

$$\Re\left\{\mathcal{Y}(\omega)\right\} = \frac{\omega_0^2\phi(\omega)\frac{\omega}{m}}{\left(\omega_0^2 - \omega^2\right)^2 + \left(\omega_0^2\phi(\omega)\right)^2} \tag{1.17}$$

Finally the admittance can be used in the fluctuation-dissipation theorem to obtain the power spectral density of thermal motion

$$S_x(\omega) = \frac{4k_B T}{\omega^2}\Re\left\{\mathcal{Y}(\omega)\right\} \tag{1.18}$$

$$= \frac{4k_B T}{m\omega}\frac{\omega_0^2\phi(\omega)}{\left(\omega_0^2 - \omega^2\right)^2 + \left(\omega_0^2\phi(\omega)\right)^2} \tag{1.19}$$

Considering angular frequencies, ω, that are close to the resonant frequency, ω_0, it can be seen that this form of $S_x(\omega)$ would be proportional to $1/\phi(\omega_0)$. Thus for materials that exhibit low levels of anelasticity, i.e. have a low mechanical loss and small ϕ, the dissipation peak would be tall and narrow and centred around the resonant frequency, ω_0. The levels of thermal noise at frequencies away from this narrow resonant peak would be low. A larger loss angle would result in a shallower, broader peak, and an increase in off-resonant thermal noise.

Thermal noise is a limiting noise source in the most sensitive frequency band of current ground-based detectors, 10-100 Hz, thus its mitigation is important for their performance [56]. Mechanical loss in the mirrors and suspensions of GW detectors is particularly detrimental, as it causes displacements of the front faces of the test masses [72]. Thus, low mechanical loss materials are chosen to construct the suspensions and test masses, in order to mitigate the effect of this noise source on detector performance.

Statistical temperature fluctuations in the suspension elements and test masses result in a type of thermal noise called thermoelastic noise [71, 73]. These fluctuations cause local expansion or contraction depending on the thermal expansion coefficient of the material.

Thermorefractive noise is caused by small local fluctuations in the refractive index of the

test mass mirrors which is caused by local temperature fluctuations [74]. These fluctuations in the refractive index alter the phase of the laser light as it passes through them. The thermoelastic and thermorefractive noise contributions of GW optics together are called thermo-optic noise [75].

The mechanical dissipation of the optical coatings, suspensions, and mirror substrates in each case make contributions to the thermal noise present in GW detectors. The thermal noise of optical coatings is split up between Brownian and thermo-optic noise, which impacts the detector at different sensitivities as can be seen in Figure 1.7. The bulk material of the test mass substrates has Brownian and thermo-optic noise associated with it as well. The first incarnations of the LIGO and Virgo detectors used wire loops that ran on the underside of the test masses as a suspension approach [4, 5]. However the high internal loss of the wire itself and the higher external frictional losses between the wire and the masses led to other suspension approaches being explored. Fused silica suspension fibres were first explored in the GEO600 interferometer, implemented to create a quasi-monolithic test mass suspension [6].

Extensions of this low mechanical loss fibre design were eventually implemented in ground-based detectors such as aLIGO, advanced Virgo, and KAGRA [8, 9, 64]. The fibres consist of fused silica for room temperature detectors or sapphire and silicon for cryogenic detectors. Though the fibres themselves have lower loss than metal wires, there are additional sources of thermal noise in them that have mechanical considerations. For example, in a quasi-monolithic suspension of aLIGO design, fused silica fibres and low loss interfaces are used in the last suspension stage, as seen in Figure 1.9. In this configuration, contributions

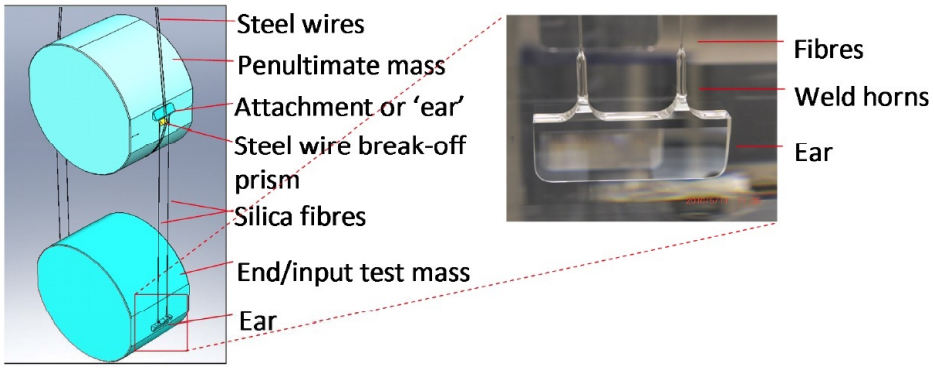

Figure 1.9: Quasi-monolithic suspension with hydroxide catalysis bonds

to thermal noise can come from the mechanical loss of the welded connection at the top of the interface ear on the test mass and the fibre. Additionally, the thermoelastic loss due to the bending of the fibre [71], the fibre's surface loss [76], and in the case of thicker fibres, the bulk loss, are all thermal noise sources which are mitigated by bulk material choice and design geometry [76].

These last stage fibres between the penultimate mass and the test mass must be fixed to

the masses by using a jointing technique that is both strong enough to safely suspend the $\geq 40\,\mathrm{kg}$ test masses and also comprises material of suitable low mechanical loss [77].
This thesis will focus on studies of properties of this jointing technique, which is called hydroxide catalysis bonding.
The spectral density of thermal noise (at frequency f), $S_x(f)$, of test masses with hydroxide catalysis bonds is discussed in Chapter 6. The thermal noise contribution of these bonds and their impact to the overall thermal noise budgets of various detectors will also be discussed in detail in that chapter.

1.7 Detector status and outlook

Currently there are four operational interferometric GW detectors around the world, GEO600 in Germany [6], Virgo in Italy [9] and two LIGO observatories in the United States [8]. These observatories will soon be joined by the not-yet-completed cryogenic detector, KAGRA, in Japan [64]. A third room temperature detector of LIGO design, LIGO India, is planned to be constructed in India. The network of these observatories is shown in Figure 1.10.

More sophisticated cryogenic detectors such as the Einstein Telescope [78] and Voyager

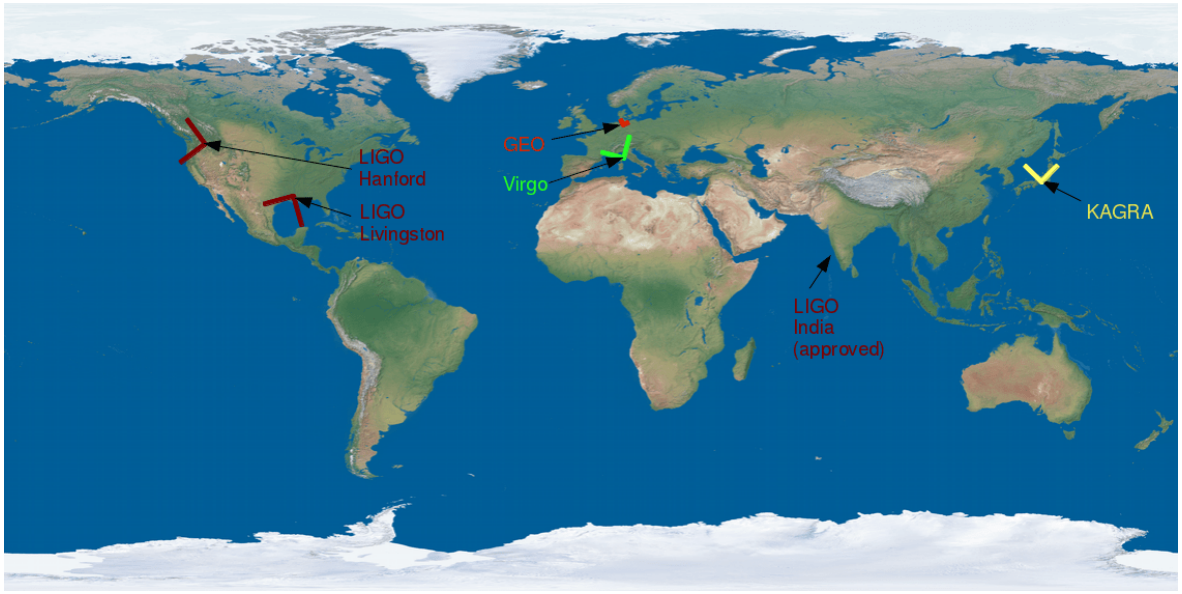

Figure 1.10: Network of ground-based GW detectors (credit: the Virgo collaboration)

[62], are currently in the early stages of design and development, and will greatly improve the sensitivity of the worldwide network when they join it. A comparison of the sensitivities of current and proposed ground-based detectors are shown in Figure 1.11.

Planned space based detectors such as LISA [45], currently planning to launch in 2034,

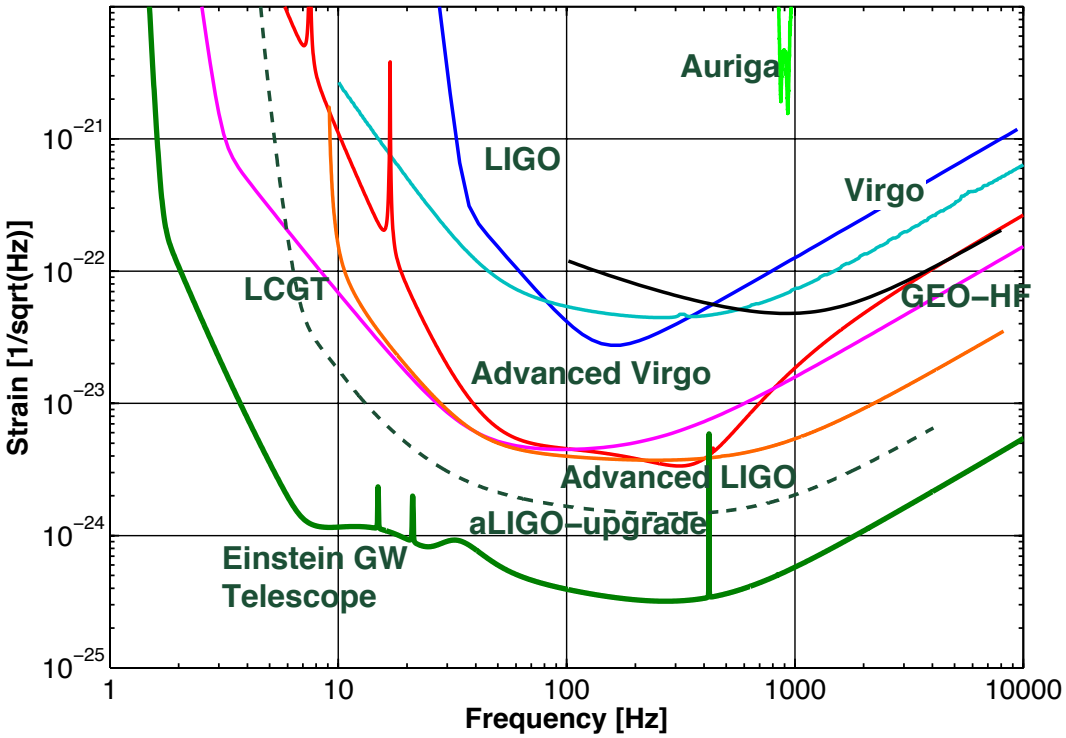

Figure 1.11: Ground-based detector design strain sensitivities, where LCGT has been renamed the KAGRA detector, and the ET GW Telescope includes both the ET-LF and the ET-HF detectors [79].

will be able to detect GW sources in frequency bands unattainable by ground-based systems due to gravity gradient noise limitations on Earth [54]. The successful launch of the LISA Pathfinder mission in early 2015 has made positive progress towards putting interferometric GW detectors into space.

Newer ground-based GW detectors, such as KAGRA, ET, and Voyager, seek to increase sensitivity by operating at cryogenic temperatures to reduce thermal noise [62, 64, 65]. Operating in the cryogenic regime necessitates the use of optical substrate and optical interface materials with suitable thermo-mechanical properties at low temperatures. For systems that operate at room temperature fused silica is an excellent substrate material, with hydroxide catalysis bonds creating reliably strong joints between fused silica substrates [80]. Unfortunately, fused silica's broad dissipation peak at low temperatures makes it a poor choice for the suspensions and test masses of cryogenic detectors[81, 82]. At present, sapphire and silicon are the two favoured materials for optical and suspension components in third generation cryogenic detectors.

Mono-crystalline sapphire is being used in the KAGRA interferometer [64], with silicon test masses more likely to be used in detectors such as ET and Voyager [62, 83]. Thus the majority of this thesis is focussed on bonding techniques between silicon or sapphire substrates, with the design of crystalline suspensions in future cryogenic gravitational wave detectors in mind.

Chapter 2

Introduction to bonding techniques

All the materials that make up a GW detector have to be carefully selected to optimise detector sensitivity. As was discussed in the previous chapter the closer a component is to the face of the test masses the more important its material properties become. In this chapter different jointing techniques will be investigated, with a focus on the selection of the jointing technologies used between the test masses and suspension components of GW detectors. For these interfaces, joint material characteristics such as low mechanical loss, high tensile strength, vacuum compatibility, and in some cases high thermal conductivity are required.

The test mass must be fixed to its suspension element, or ear, in a way that keeps the thermal noise of the test mass system down to within an acceptable level, as defined by the design sensitivity of each detector. This joint must not outgas any volatile solvents, as this would contaminate the GW detector suspensions and vacuum system. For cryogenic detectors, this material must also have a high enough thermal conductivity to allow heat to be extracted from the test mass up through the suspension elements and out of the system when cooling to cryogenic temperatures. A high tensile strength is also required for all GW detectors, as this is the interface that holds the test mass in suspension.

The benefits and downsides of a number of different bonding techniques typically used in different industries are outlined here, and an explanation of which ones can be used in GW detectors is given.

2.1 Epoxy

The most common way of creating a bond between two materials is to use some sort of epoxy or glue. There is a vast array of different types of epoxy/glue adhesive available, most of them fitting into two main categories, reactive or non-reactive [84]. Reactive adhesives, such as two part epoxies, involve a chemical reaction as the adhesive cures. These

approaches result in chemical reactions, forming either ionic, covalent or hydrogen bonds. Non-reactive adhesives such as polyvinyl acetates (PVAs) set as solvents leave the adhesive or as it cools, as in the case of hot glue. These non-reactive bonds adhere via electrostatic forces such as the Van der Waals force [84].
Most epoxy and glue adhesives release volatile solvents and elements and thus they are are not vacuum compatible [85], and so cannot be considered for use in GW detectors. However there are a few ultra-high vacuum (UHV) compatible epoxies to consider, such as Masterbond EP-30-2 [86], which has been used in GW detectors for some interfaces such as magnet standoffs or to fix metal prisms onto smaller, less critical optics in the aLIGO detector. Although it is UHV compatible, EP-30-2 still creates relatively thick joints, tens of microns at the thinnest. This results in unacceptably high, but unknown, thermal noise level as more energy is stored in the thicker bonds. Thus it cannot be used for an interface where thermal noise levels are important.
Additionally, adhesives such as epoxies or glue usually have a very narrow range of operating temperatures centred around room temperature, outside of which they become brittle and fail [87]. One adhesive, Masterbond EP29LPSP [86], is low outgassing and can be used at cryogenic temperatures. However the interface of a cryogenic detector must have a high thermal conductivity in order to extract heat from the the test mass through the suspension fibres. As the EP29LPSP epoxy has a very low thermal conductivity [86], this rules it out for use in these joints. This rules out the use of adhesives in general in cryogenic detectors. Most adhesives create relatively thick joints to create reliable bonds, on the order of tens of microns to millimetres [88, 89].

2.2 Cold welds

Two metallic surfaces of the same type, from which all surface contaminants have been removed, will chemically bond to each other when contacted together at room temperature. This process is called cold welding [90]. This has caused mechanical problems in the past for satellites which have all lubricants removed for space travel [91], as in the antenna deployment of the Galileo mission [92]. Similarly it must be avoided during the assembly of clean mechanical parts for GW detectors, which is averted by designing the mechanical systems with dissimilar materials at all interfaces, such as using nuts of one type of metal and bolts of another type.
However, cold welding can be used to fix together two metals of the same type in a deliberate way that have had all oils, grease, and contaminants removed from their surface. This process that can occur at room temperature and with very little applied pressure. This process is commonly used to create vacuum seals with indium metal [93].
Most optic and suspension elements in GW detectors consist of non-metallic materials,

such as fused silica, sapphire, or silicon which cannot be cold welded together. As such, cold welding of these interfaces would only be possible after the addition of an appropriate metal layer between them, such as indium.

2.3 Diffusion bonds

Solid-state diffusion bonding occurs when the atoms of two solid, metallic surfaces intermingle over time under contact at elevated temperature and high pressures. This process can happen between similar or dissimilar metals, typically at temperatures of 50-70% of the metal's melting temperature [94]. As it involves the diffusion of atoms between two metal surfaces, it does not require extra material other than the metal already present in order to create the joint. Phases of a diffusion bond are shown in Figure 2.1 [95]. Diffusion bonding

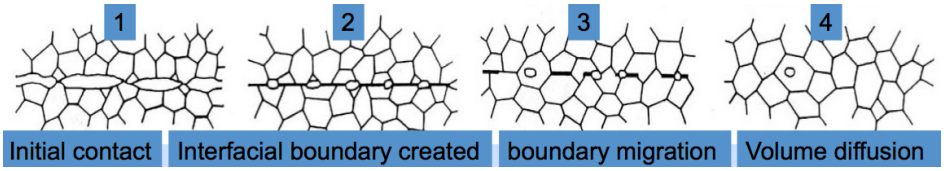

Figure 2.1: Phases of diffusion bond formation between two metals [95].

is often used in metalworking [94].
Similar to cold welding, diffusion bonding in the final stage of a GW detector suspension would only work with the addition of metal layers in between the non-metallic optics and their suspension interfaces.
Some non-metallic materials can be bonded together in a similar fashion to diffusion bonding, i.e. without the use of an interface. The direct bonding of silicon is one approach. In this case a bond can be made by first contacting very clean, very flat silicon surfaces together. Then the silicon can be heated up to 1000 °C to create a bond [96], or it can be etched and bonded under vacuum at room temperature [97]. Optical contacting of materials such as fused silica is another jointing approach which does not require the use of additional interface material, which is discussed in Section 2.6.

2.4 Indium as a bond material

Indium has the unique property of being a very malleable metal; it has a very low Young's modulus of 10-13 GPa and starts deforming plastically at very low stresses. It also has a low melting point 157 °C [98]. It can bond easily to other metals to form alloys, as well as to non-metallic materials such as glass, quartz and metallic oxides; either covalently at room temperature or at slightly elevated temperatures [99, 100]. It's thermal conductivity is fairly

high, 81.8 $W\,m^{-1}\,K^{-1}$. At standard temperatures and pressures, indium has a face-centred tetragonal crystal structure. Below 3.4 K indium becomes a superconductor [101].
Indium has many industrial uses, particularly in the semi-conductor industry. It is used as low temperature solder, and in an indium tin oxide (ITO) alloy it forms transparent conductive coatings for use in various electronic applications [102, 103]. It is also used for ultra-high vacuum (UHV) seals for room temperature and cryogenic systems, due to its high thermal conductivity, vacuum compatibility, and low melting point [93, 98, 104–106]. Due to its low melting point indium is a malleable metal making it easy to work with at room temperature, but it is not recommended for use at high temperatures. For future GW detectors that operate in the cryogenic to room temperature regime, indium could be a good choice of bond material for compressive joints.
Indium can be found in many different forms depending on the desired application, including thin films, solder wires, thin and thick foils, and alloys [99, 102, 103, 106, 107]. One approach to creating a bond with pure indium metal is called bump bonding where bumps of indium are brought into contact and pressed together [105]. In doing so the indium is plastically deformed and cold welds to itself at room temperature.
Another technique is to use indium foils or thin evaporated indium films as a layer of bond material [107]. Using thin indium layers is not as straightforward as bump bonding, since indium forms an oxide layer immediately on contact with air which inhibits a cold weld and thus prevents a bond from happening. In the case of bump bonding there is a large amount of pure indium metal that easily breaks the outer shell of oxide when pressed together. In the case where there is a smaller amount of metal underneath an oxide layer, steps need to be taken to either prevent the oxide from forming or to remove it immediately before jointing the metal.
Due to the low tensile strength of indium and low melting point, indium bonds are not suitable for use at elevated temperatures (above 80-100 °C) or under tensile loads. Indium was considered for use in the suspension design for the GEO detector, but was not selected due to the concern that the indium layers may creep during vacuum bakeouts. In the aLIGO detector, indium was incorporated into suspension design as a UHV compatible solder to create the Electrostatic Drive connections in the reaction chains of the mirror suspensions [108]. For GW detectors operating in the cryogenic regime, a hybrid suspension design utilizing both indium and hydroxide catalysis bonding has been proposed [64, 78]. Some research into indium bonds for cryogenic detectors has been done, with the results suggesting this approach could yield bonds with acceptable thermal conductivity and mechanical loss [109, 110]. This will be discussed further in Chapter 7.

2.5 Glass frit bonds

Glass frit bonding can be used to join materials of the same or similar coefficient of thermal expansion as glass. To create a frit bond, first a paste of glass particles and organic binders is applied between the desired bond surfaces, for example two silicon wafers. The wafers are compressed together and a bond is formed by heat cycling to temperatures of up to 450 °C [111].
This approach can yield strong, hermetically sealed bonds, and is used to construct micro-electro-mechanical (MEMs) devices such as gyroscopes and accelerometers or seal optical windows [112]. However, while strong, frit bonds are composed of a matrix of glass particles and organic binders and as such are assumed to be high thermal noise joints. Also, they can only be used to bond systems that can be heat cycled up to 450 °C while under pressure. This is unsuitable for GW detector mirrors, as their optical coatings cannot be heated up to such high temperatures.

2.6 Optical contacts

Optical contacting is one way of bonding two surfaces together without the use of extra jointing material. The two surfaces are stuck together via intermolecular forces, mostly Van der Waals, and possibly hydrogen bonds and dipole-dipole interactions [113]. In order for these forces to be strong enough to hold two interfaces together, they both have to be very close together and well matched. Therefore, a peak-to-valley (PV) flatness on the order of 1 nm is required for the intermolecular forces to cause the surfaces to actually stick together[113]. Any contamination on the bond surfaces would also keep an optical contact from forming, and as such this type of jointing has to be done in a specialised cleanroom with substrates that are very flat and also have had all contaminants removed from their surfaces.
If the requirements for substrate properties can be met, optical contacting can be a useful method of fixing clean components together. It is an optically clear and highly precise technique that is often used to fix together optical components used at room temperature [114]. A joint that connects a test mass to the suspension element interface (ear) in a ground-based detector must have a high tensile strength. The tensile strength of optical contact bonds is not well defined in the literature. As the dominant forces behind most optical contacts are Van der Waals in nature it can be assumed the strength of optical contacts are mostly due to this phenomenon, with some sources reporting breaking stresses of 1.4 MPa [114]. Although some report strengths that approach those of the bulk material that is fixed together, glass for example, this would assume perfectly clean and perfectly flat surface conditions [113], with the strength reducing drastically with greater substrate separation.

A bonding technique that can be performed in a non-specialised cleanroom and that produces reliably strong bonds between the test mass and ear is necessary for the construction of GW detectors. For optical contacts to work for this interface the side of the test mass and the ear would have to be polished to 1 nm PV flatness over the entire surface. Both surfaces would also have to be completely pristine, any contaminants preventing an optical contact would have to be removed. Due to the large sizes of the test masses, 40 kg in the case of aLIGO, the ears that fix them to the suspension elements also have a minimum possible size, with the aLIGO ears having a surface area of 120 cm^2 [57]. Therefore, in practice it is almost impossible to achieve the required flatness and surface cleanliness over the whole interface that is required for an optical contact bond of this size. The cleanliness of the interfaces would not be certain, even in a cleanroom. Also, assuming a tensile strength of 1.4 MPa from the literature, the strength of an optical bond would be too low to safely suspend test masses. Additionally, optical contacts do not survive at low temperatures [115] and so are not suitable for space-based or cryogenic ground-based GW detectors.

2.7 Hydroxide catalysis bonds

Hydroxide catalysis bonding is a method of creating chemical bonds between oxides or oxidisable materials with an aqueous hydroxide solution, and has been the preferred technique for creating the necessary quasi-monolithic optic and suspension systems for current and future ground-based GW detectors [9, 57, 116]. Initially patented by Gwo at Stanford in 1998 [115, 117] for use in the Gravity Probe B mission, it has since been used in many different applications [80]. Hydroxide catalysis bonds create strong, thin bonds of order 15 MPa and 100 nm that can be precisely aligned to within 10 µrad, optically clear, vacuum compatible and used at cryogenic temperatures [80]. This makes it an ideal way of assembling low thermal noise quasi-monolithic optical suspensions in ground based GW detectors or to create precisely aligned optical assemblies for space based GW detectors [118].
In ground-based detectors hydroxide catalysis bonds were first used in GEO600 to create strong and low noise interfaces to the mirror suspensions [116]. Now the technique is used extensively to attach the ears to the core optics in the Virgo, aLIGO, and KAGRA suspensions [9, 57, 64]. These bonds were also used to align and bond the low noise fused silica optical components of the LISA Pathfinder [80] to its Zerodur optical bench, and are proposed for use in future full-scale space GW missions [45, 119].
This bonding approach depends on the formation of silicate networks, explained in the following sections for sapphire and fused silica substrates. Thus it follows that the most straightforward class of bondable materials are silica based ones, such as fused silica, glass, and glass ceramic composites such as Zerodur [115]. In the case of non-silica materials con-

sidered for use in cryogenic mirror suspension, such as sapphire or silicon, it is necessary to investigate the bond properties between these material types as well. Bonding non-silica based material is possible because silicate like networks can be attached to oxide materials as well as silica based ones. Sapphire, or Al_2O_3, is such an oxide, and hydroxide can in theory etch such materials and form bonds, particularly if aided by colloidal silicate ions already present in the bond solution [120].
Sodium silicate solution can also used to bond silicon. If the hydroxide solution touches the pure silicon it will form hydrogen gas, which counteracts silicate formation and would push the bonds apart [121]. Thus for bonding silicon, an oxide layer, SiO_2, must be added to the pure silicon. This necessary oxide layer can be deposited via electron beam sputtering or ion beam sputtering, or growing it as a thermal oxide by heating the silicon substrates to 1000 °C [122]. A SiO_2 layer no thinner than 100 nm is ideal, providing an appropriate oxide layer to which the silicate network of the bond can attach [121].

2.7.1 Formation of hydroxide catalysis bonds between fused silica

Hydroxide catalysis bonding works by forming silicate networks between two bond surfaces [115]. These two surfaces must have the ability to form silicate networks, or attach covalently to them. To get the strongest joints the substrates to be bonded must have well matched surface figures and be clean of particulates, polishing compounds and hydrocarbons. The bonding process is carried out in a cleanroom to keep contaminants out of the bond. The bond itself is created in three main steps: etching by hydration, polymerization and dehydration. A short description of the reaction for bonding silica to silica is given below, the chemistry of which is described more extensively in the original patent by Gwo [117].
1. Etching by hydration: The substrate surface is flooded with an aqueous hydroxide solution. The hydroxide ions in the solution etch the surface, liberating silica which forms $Si(OH)_5^-$. In this process the number of hydroxide ions decreases which causes the pH of the solution to drop.

$$SiO_2 + OH^- + 2H_2O \rightarrow Si(OH)_5^- \tag{2.1}$$

2. Polymerization: As the surfaces are hydrated, the OH^- ions and the pH of the bond solution decreases, silicate ions dissociate and siloxane chains are formed between the bond surfaces.
First dissociation:

$$Si(OH)_5^- \rightarrow Si(OH)_4 + OH^- \tag{2.2}$$

Then the formation of siloxane chains and water occurs:

$$2\mathrm{Si(OH)_4} \rightarrow \mathrm{(HO)_3SiOSi(OH)_3} + \mathrm{H_20} \tag{2.3}$$

3. Dehydration: In the final step of the bond process, the water leaves the bond, and the bond strength settles.
The bonds tend to set within minutes but take weeks to become thinner and fully cured [117]. The initial settling time can be used to precisely align optical components before permanent placement. If the bond quality is poor, they can be de-bonded within a day of bonding. Actual settling and curing times depend on the type and concentration of OH solution and substrate type [123].

2.7.2 Formation of hydroxide catalysis bonds between sapphire

Although sapphire is chemically different to silica and is difficult to etch, the steps in the bonding process are very similar to that of bonded silica. In this case, a hydroxide only bond solution can etch the alumina bond surfaces, however a silicate-like network cannot be formed on the alumina surfaces at a reasonable rate. Thus the sapphire surfaces are hydrated with a silicate rich hydroxide solution, in order to speed the creation of a stronger joint, where the free alumina ions attach to the silicates in solution, forming a 3D aluminosilicate network. This sodium silicate solution is used in the study outlined in Chapter 3 and Chapter 4.
First the alumina ions are freed from the surface in the etching stage of bond formation. The sapphire surface is flooded with an aqueous hydroxide solution. The hydroxide ions in the solution interact with the sapphire surface in a few ways, one of which is explained here. First the alumina ions are freed from the surface by the hydroxide.

$$\mathrm{Al(OH)_3(s)} + \mathrm{OH^-(aq)} \rightarrow \mathrm{Al(OH)_4^-(l)} \tag{2.4}$$

Then the $Al(OH)_4^-$ ions can begin bond formation via the dimerization process.

$$2\mathrm{Al(OH)_4^{-2}} \rightarrow \mathrm{(HO)_3^{-2}AlOAl(OH)_3^{-2}} + \mathrm{H_20} \tag{2.5}$$

As the pH drops, the silicate ions form a silicate like network. The alumina ions in solution will chemically react with this silicate network, as the Al atoms replace some of the Si atoms

a 3D aluminosilicate network is formed.

$$Si(OH)_4 + Al(OH)_4^- \rightarrow (HO)_2AlOSi(OH)_3 + H_20 + OH^- \quad (2.6)$$

A detailed explanation of these chemical reactions for the formation of hydroxide catalysis bonded sapphire is given by Elliffe [124].
As for fused silica the bonds tend to set within minutes but take weeks to months for the water to fully leave the bonds [117]. The settling time of bonds between different types of substrate material can be different and is investigated in detail in Chapter 3.

2.8 Summary of bonding techniques

Bond technique	Contribution to thermal noise	tensile strength	Operating temperatures	UHV compatible	required flatness
Epoxy/Glue	high,variable**	high, variable	210-500 K*	most no*	none
Indium bonds	low for L$\leq$10 µm	low	0-300 K	yes	variable
Glass frit bonds	high**	high,variable	variable	yes	none
Optical contacts	$\approx$bulk material	$\leq$1.4 MPa[114]	300 K	yes	1 nm
Hydroxide catalysis	very low	$\geq$15 MPa	0-500 K	yes	$\lambda/10$

Table 2.1: Comparison of bonding techniques considered for use in GW detectors. *There are a few epoxies available from Masterbond that are UHV compatible and have better than average optical clarity, (EP30-2), and one thermally insulating glue that can be used at cryogenic temperatures, (EP29LPSP) [86]. **Assumed levels of thermal noise based on the joint thickness.

Bonds with properties such as high thermal conductivity, low mechanical loss (and thus small effect on thermal noise) and high tensile and compressive strengths are necessary to join the test masses to their suspension elements in GW detectors. The comparison between the bonding techniques that could be considered for use in GW detectors is shown in Table 2.1. Here it can be seen that epoxy and glue adhesives are not applicable. For most of the adhesives this is due to the resulting thickness of the joints, the narrow range of operating temperatures, and non-UHV compatibility. For Masterbond EP30-2, which is UHV compatible, the thickness of the joints it creates would result in unacceptably high thermal noise levels to allow its use in low thermal noise test mass to ear interfaces. Masterbond EP29LPSP, which can be used at cryogenic temperatures, also has poor thermal conductivity, which would prevent the necessary extraction of heat from the test mass through the suspension elements, as well as creating bonds of the order of tens of microns at the thinnest.
Glass frit bonds, while UHV compatible and having high tensile strengths, are not suited for cryogenic temperatures. They are also lossy materials due to their composition of glass

and binder materials. Additionally, the pressure and high temperature thermal cycling necessary for frit bonding would not suit an optically coated test mass and ear. Diffusion bonds can only be used to fix metals together, which would not work with the fused silica, sapphire, or silicon test masses. Due to their ability to form strong, low noise, UHV compatible interfaces the only approach that satisfies all the requirements at room temperature [115] and cryogenic temperatures [120] are hydroxide catalysis bonds.

In addition to hydroxide catalysis bonds, indium bonds could be considered for use in GW detectors. While their tensile strength is too low to be used in a high tensile or shear stress bond, they could be used in compressive joints. The development of reliable and practical procedures for indium bonding in cryogenic mirror suspensions that retain the desirable jointing properties in Table 2.1 is required. Approaches to achieve this type of bonding with thin evaporated layers and foils of indium on silicon substrates are discussed in Chapter 7. Methods of creating indium bonds in-situ at a detector are investigated as well.

To attain the desired sensitivities the observatories are being redesigned and upgraded using the knowledge gained from previous generations of detectors to improve the sensitivity levels by controlling noise sources to a greater degree. Hydroxide catalysis bonding is one such technology that proved to be a successful integration in GEO600 and a valuable upgrade to the Advanced LIGO, Advanced Virgo, and KAGRA detectors.

Different aspects of bond properties and approaches for GW detectors, with an emphasis on bonding crystalline silicon, and sapphire suspensions for future detectors is investigated in this thesis. First, a study on how the curing time of hydroxide catalysis bonds between sapphire substrates influences their tensile strength was investigated in Chapter 3 and compared with past results of bonded fused silica. In Chapter 4 the breaking stress of bonds between m-m and a-a plane sapphire was studied and compared to the breaking stress of bonded c-c plane sapphire from the previous chapter. A better understanding of the Young's modulus of hydroxide catalysis bonds in the cases of fused silica and sapphire is discussed in Chapter 5. This value is then used in Chapter 6 to calculate more accurate thermal noise levels of bonds in different detector geometries and compare them to detector requirements. Lastly in Chapter 7 the development of procedures to integrate indium bonds into future cryogenic ground based GW detectors is discussed.

Chapter 3

Influence of curing time on hydroxide catalysis bonded sapphire

3.1 Introduction

Due to their noise and thermal conductivity performance at low temperatures, sapphire and silicon are the top two choices of bulk material for optics in cryogenic ground based detectors. This chapter will focus on the hydroxide catalysis bonding of sapphire substrates, using sodium silicate solution. The strength of these bonds is tracked as a function of curing time. Currently hydroxide catalysis bonded sapphire suspensions are a part of the first cryogenic ground based detector, KAGRA [64]. Consequently they could potentially be employed as part of the design for future cryogenic detectors such as ET and Voyager[65]. Therefore it is necessary to know how strong these bonded materials are, and how stable their strength is over time. Similar curing time experiments of hydroxide catalysis bonded fused silica were researched prior to their integration into room temperature detectors such as GEO600, VIRGO, and Advanced LIGO [9, 57, 116]. However, as shown in Chapter 2, there are differences in the chemistry of how a hydroxide catalysis bond forms between sapphire compared to their formation between silica or silicon substrates. Thus it is necessary to investigate how bonds between materials for cryogenic detectors such as sapphire develop as a function of curing time.

Previous research on the hydroxide catalysis bonding of sapphire for use in cryogenic GW detectors suggested that the tensile strength of the bonds was not adversely affected by cryogenic temperatures, or thermal cycling from room temperature to cryogenic temperatures [120, 125]. Some results indicated higher bond tensile strengths at curing times of 2 to 4 weeks followed by a small decrease at 8 and 12 week curing times[126]. A decrease in strength as a function of curing time was unexpected behaviour, so to investigate whether the drop in strength was a statistical variation or something related to the chemistry of age-

ing bonds, a longer follow-up curing time experiment was envisaged and will be discussed in this chapter. Bond curing times from 1 week to longer term curing times of 8, 12, and 30 weeks are investigated here. Curing times of less than 2 weeks were included to probe the gaps in knowledge of how a sapphire bond initially forms. A longer curing time of 30 weeks was also chosen to gain valuable information on the strength and lifetime of any assembled cryogenic sapphire suspensions in which hydroxide catalysis bonds are used. The content of this chapter has been prepared for publication as *The influence of curing time on the strength of hydroxide catalysis bonds between fused silica, sapphire, and silicon* in [127]. The sapphire and fused silica results in this paper are explained in greater detail in this chapter in order to include a greater degree of context and understanding, especially in the areas of surface characterisation and general bond procedure. The conclusion presented here is the same as in [127].

3.2 Method

3.2.1 Characterisation of substrate surfaces prior to bonding

One hundred and forty polished sapphire samples were procured from Impex [128] in 2015, a large number in order to attain statistical tensile strength results over a long period of time. All individual samples had dimensions 5 mmx5 mmx20 mm. The c-axis, shown in Section 4.1, was normal to the bond plane, all bond surfaces were in the c-plane. Upon arrival the samples were visually inspected for defects, and a subset was measured with callipers near the bond surface to ensure they matched the tolerances outlined in the quoted drawing, shown in Figure 3.1. All samples were within dimension tolerance, measuring 5x5 mm $\pm$0.05 mm. The samples were given serial numbers by scribing them with a diamond scribe on the long polished 5x20 mm face at the time of visual inspection and dimensional checks.

Further characterisation of the bond surface substrates included flatness measurements of every bond surface. Thus peak-to-valley (PV) flatness measurements were taken of each of the one hundred and forty bond surfaces on a ZYGO GPI XP/D interferometer [129]. Knowing the exact surface profile over the entire 5 mm by 5 mm bond area is necessary to ensure the absence of peaks or unusual surface topography that could result in low quality hydroxide catalysis bonds. The substrate PV flatness requirement for sodium silicate hydroxide catalysis bonds is $\lambda/10$ over 95% of the bond surface, where $\lambda/10$ is 63.3 nm or less. One of these measurements is shown in Figure 3.2 as an example of an acceptable bond surface flatness.

All bond surfaces were measured three times, with the average of each of these measurements shown in Figure 3.3. The average PV flatness of all surfaces was 45.8 nm, with a standard deviation of 18.3 nm. A few of the surfaces had a PV flatness that exceeded

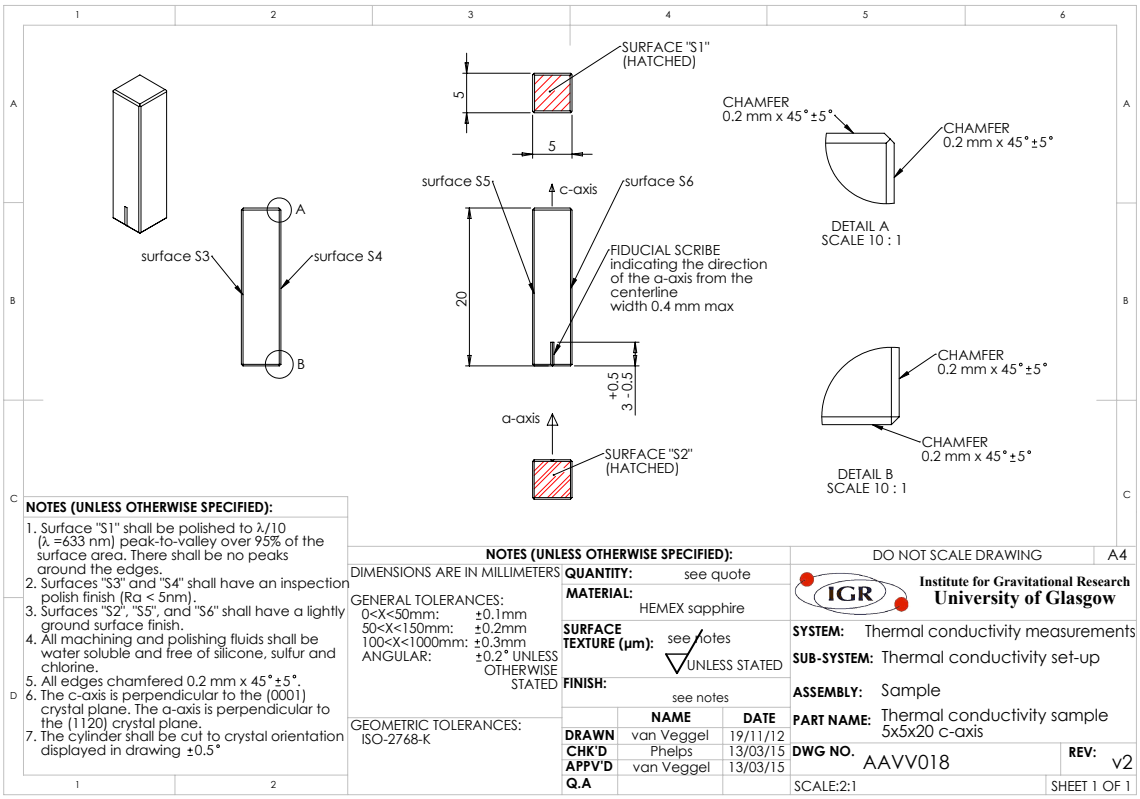

Figure 3.1: Sapphire block sample geometry CAD drawing

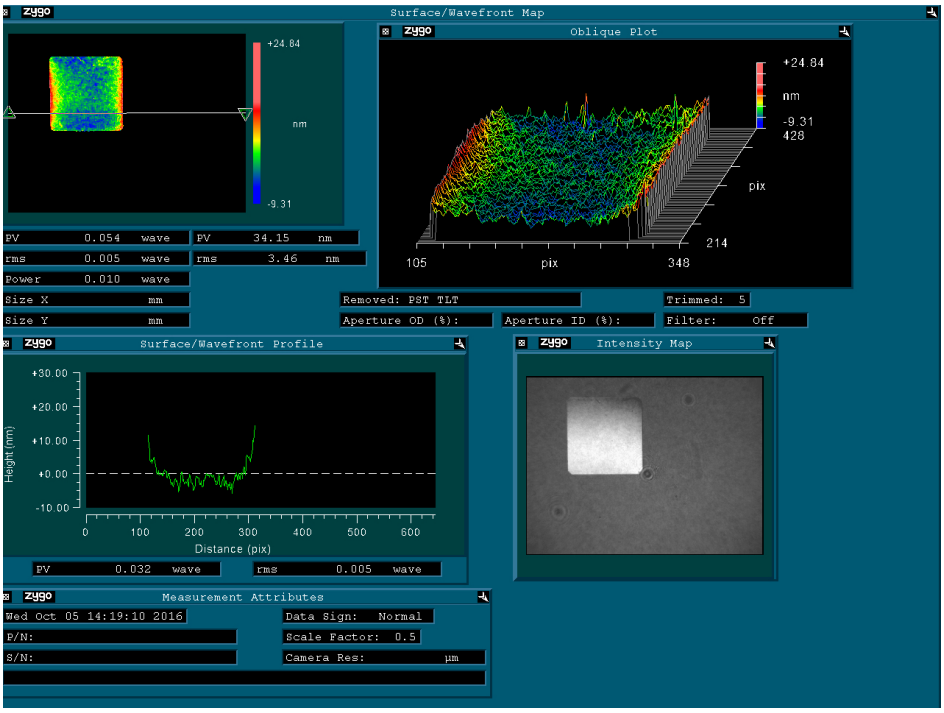

Figure 3.2: PV flatness map of a typical 5x5 mm sapphire sample, produced with Zygo software [129]

63.3 nm. In these cases the surfaces profiles were uniformly convex or concave, with no edge peaks and so were accepted for this test, while tracking any correlation of breaking

strength to abnormal flatness.

Only one sample had a serious surface defect, which was a non-removable scratch as

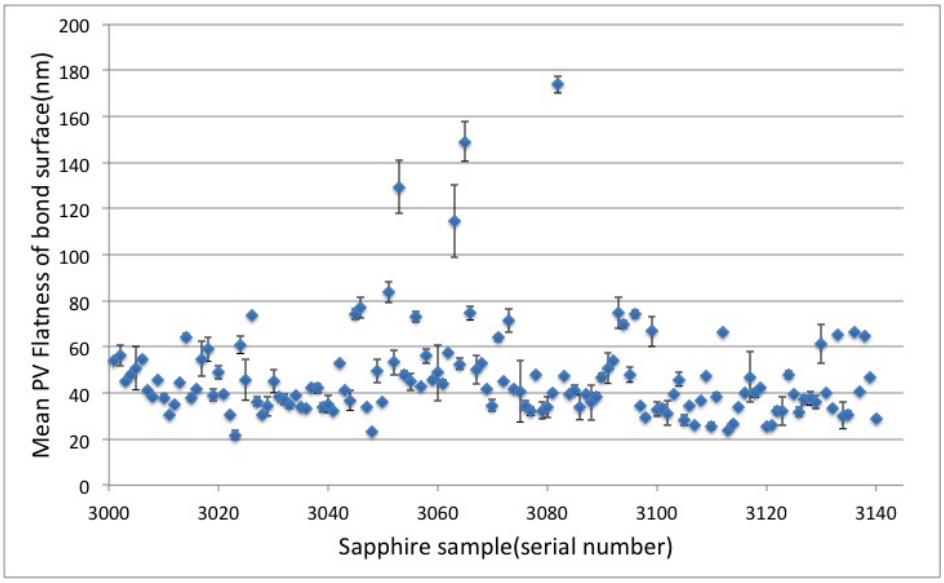

Figure 3.3: PV flatness of all 5x5 mm sapphire samples

shown in Figure 3.4. Four other samples with serial numbers 3003, 3013, 3133, and 3138 had small point defects that could not be removed with a cerium oxide cleaning. If these samples were the surfaces to be bonded in a real GW detector it would not be advisable to use them due to the possibility of a poor bond due to surface defects. For this study, however, it was decided to spread the samples out between all sets and closely monitor them.

Global flatness of a bond surface is one of the most important surface characteristics, for a hydroxide catalysis bond to form between two substrates they must have a minimal surface mismatch. It is possible to bond ground fused silica surfaces together if they are flat enough, thus the micro-roughness of the substrates is less important than global flatness. However, the micro-roughness must also be good enough overall to provide well matched bond surfaces [118]. With this in mind two other bond surface requirements, micro-roughness and chamfer measurements, of these samples were also measured. It is possible that peaks of substrate material form at the edges during polishing which can impact the global flatness. Therefore the addition of a chamfer on the bond surface after the polishing stage is specified to get rid of possible edge peaks.

Chamfer dimension measurements and micro-roughness measurements were completed for approximately 30 of the samples chosen at random. Chamfer dimensions were measured on a Hitachi TM 1000 tabletop Scanning Electron Microscope (SEM)[130]. The chamfer requirement was a width of 200 µm, cut at an angle of 45±5°. The chamfers were measured on either side of each of the sample's corners, for a total of 8 measurements per bond surface. They were 177 µm on average for all positions, with a standard deviation of 42 µm. An example of sample 3003 is shown in Figure 3.5. The chamfer width, averaged over all 8

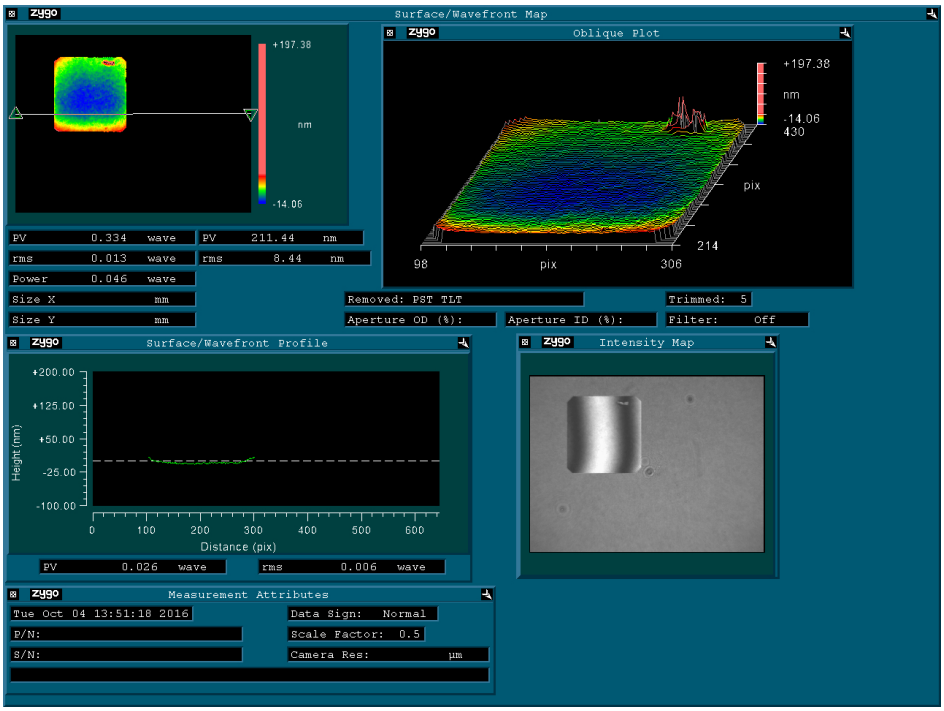

Figure 3.4: PV flatness map of scratched 5x5 mm sapphire sample, showing scratch in upper right corner of sample. Produced with Zygo software [129]

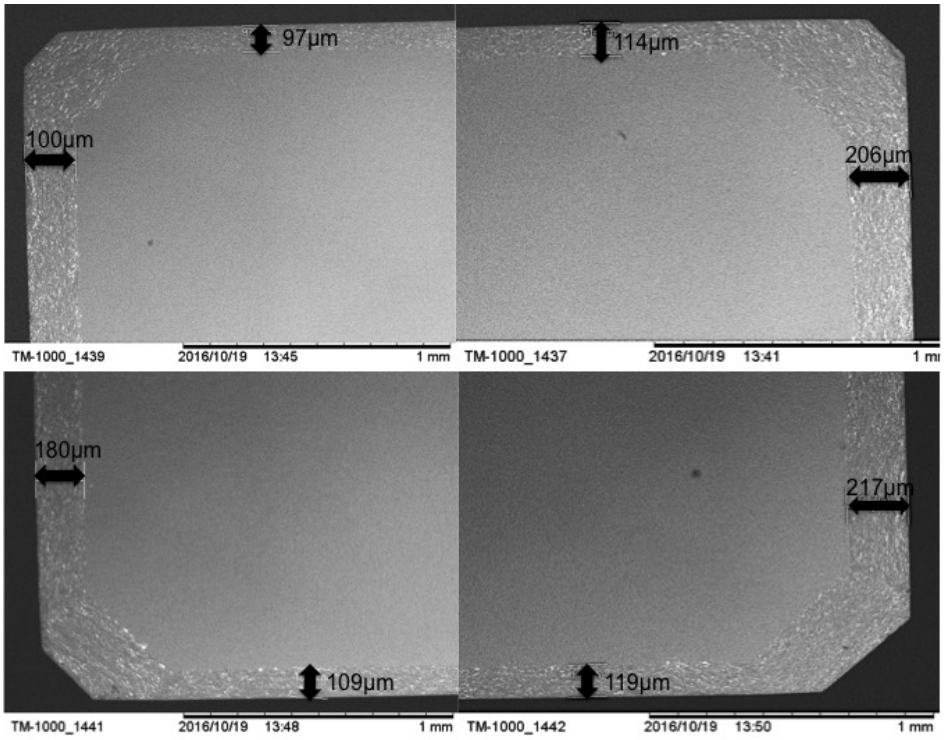

Figure 3.5: Chamfer measurements of c plane sapphire bond surface sample 3003 using a Hitachi SEM [130]

positions per surface for each sample measured, is shown in Figure 3.6.

Similarly, a subset of sapphire samples was also selected to have the micro-roughness of

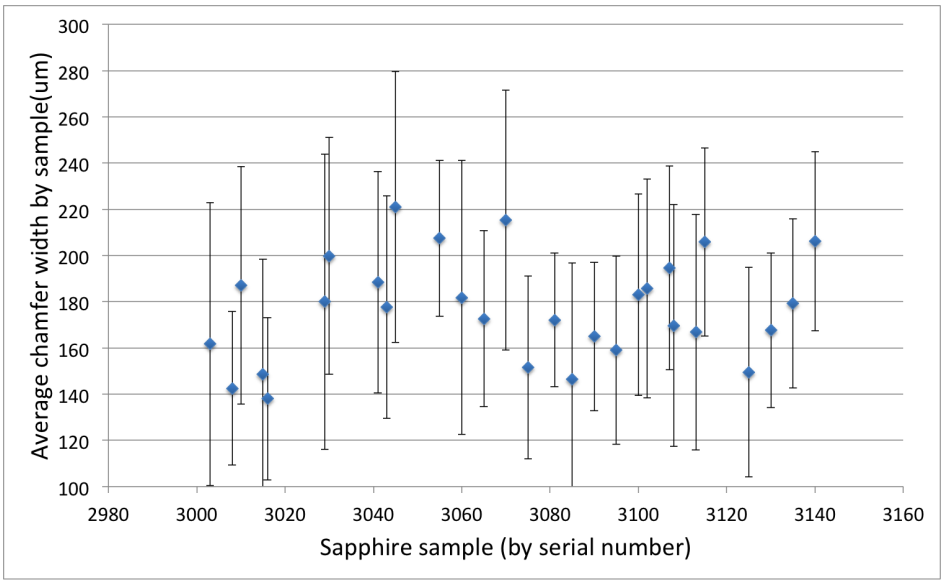

Figure 3.6: Average chamfer widths of a subset of c-plane sapphire bond surfaces

their bond surfaces measured, using a Wyko NT1100 white light interferometer[131]. This was to check that the sample's Ra roughness (Ra referring to the average deviation from the mean) requirement of 5 nm rms was met. The average value of Ra roughness at a central location on the bond samples measured was 3.79 nm, with a standard deviation of 0.84 nm as can be seen in Figure 3.7. An example of a typical sapphire surface micro-roughness

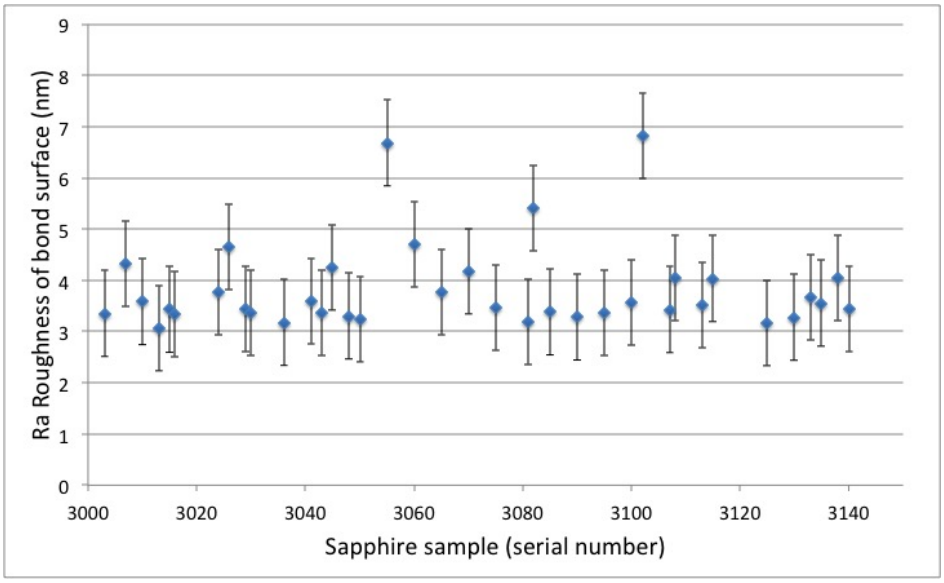

Figure 3.7: Ra roughness of a subset of 5x5 mm sapphire samples

measurement is shown in Figure 3.8.

Once the bond surfaces were characterised and it was verified that they meet the requirements for flatness, micro-roughness, overall dimensions, and chamfer dimensions they were ready to begin the bond process. The first step in the bond process was to clean and

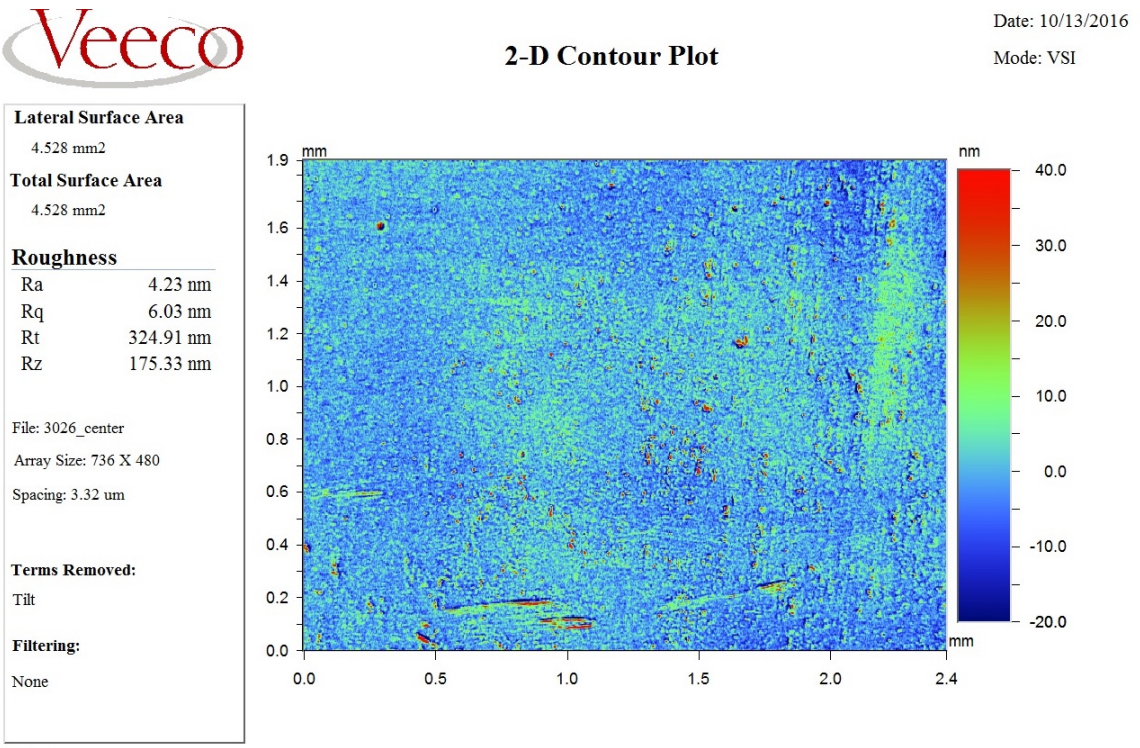

Figure 3.8: Micro-roughness measurement of c plane sapphire sample 3026

prepare the surfaces for bonding.

3.2.2 Substrate bond surface preparation

A very clean substrate surface that is hydrophilic and free from contaminants is necessary to create a good quality hydroxide catalysis bond [118]. Different approaches have been used to attain such surface quality in addition to cerium oxide cleaning, such as exposure to ozone or acid solutions. However the cerium oxide clean remains the most reliable approach[132]. As such the cleaning procedure used in this chapter and now viewed as standard for hydroxide catalysis bonded substrates is the one developed for joining the Advanced LIGO ears to the penultimate masses and test masses [133]. Reverse osmosis (RO) water was used to clean the substrates to be bonded and to make the bond solution, as the cleanest form of water available, without ions, salts or contaminants is needed to produce good quality bonds. De-ionised (DI) and RO water refers to water that has had its ions (i.e its charge carriers) removed. Thus its quality is described in units of Ω. 18 MΩ is considered the standard for good quality RO water for the creation of hydroxide catalysis bonds [133]. The following procedure was used for bond surface preparation in past hydroxide catalysis bond research. Using the same approach in this study will allow the results to be more comparable to past curing time test results. The primary steps of the full procedure are as follows. All are to be performed in a clean room.

1. Rinse sample and Anticon gold wipe (or equivalent cleanroom wipe) with 18 MΩ reverse osmosis (RO) water.
2. Apply a paste of cerium oxide and RO water to the sample and rub with the wipe for 30 seconds to a minute, not allowing the paste to dry on the surface.
3. Rinse the sample and gloves to remove the cerium oxide.
4. Get a new wipe and repeat steps 2 and 3 for a total of two times.
5. Rinse the sample and gloves under RO water until no cerium oxide remains.
6. Apply a paste of sodium bicarbonate and RO water to the sample with a new wipe, rub for 30 seconds to remove traces of cerium oxide.
7. Repeat step 6 once more.
8. Get a new wipe and fully rinse the sample and gloves.
9. Rinse the sample in spectroscopic grade methanol(>99.9%), keeping the bond surface up and away from glove fingertips.
10. Wipe sample dry, starting with bond surface and moving away from it.
11. Cover with a new dry wipe until ready to bond.

This procedure ensures the bond surfaces are hydrophilic and free of particulates and organic residue.

3.2.3 Bonding procedure

The bonding procedure that was used here follows the aLIGO hydroxide catalysis bond procedure [133]. Sodium silicate solution was used in all cases, to allow the bond strength to be compared with previous studies of sodium silicate bonded fused silica and sodium silicate bonded sapphire [126].

1. First prepare the bonding solution. Start with an off the shelf sodium silicate, Na_2SiO_3, Sigma Aldrich 338443-1L 10.6% NaOH, 26.5% SiO_2 by weight (or equivalent). Do not use if over one year has passed since procurement.
2. Pour 2 ml of sodium silicate solution into a 15 ml centrifuge tube. Put the lid on and return the rest of the sodium silicate solution to the chemical cabinet.

3. Slowly drip 18 MΩ RO water into the centrifuge tube, diluting the sodium silicate solution until there is 14 ml in total.

4. Close the tube and shake vigorously for 1 minute.

5. Open mixed solution and carefully pour some into three small 1.5 ml centrifuge tubes.

6. Place equidistant around the centre of the centrifuge, close and spin for 30 s.

7. Pour 2/3 of the solution of 2 of the tubes into the outer part of a medical filter [133]. (Leaving 1/3 behind will also leave behind large particulates.) Only fill the filter until it reaches the stepped edge, otherwise there is too much solution for the filter to effectively handle.

8. Press the inner part of the filter straight down until a click is heard, thereby filtering the solution.

9. Wipe down a clean area under a flow bench and change gloves.

10. Use a 2-20 µL variable volume pipette with tip ejector such as Eppendorf 200 to set the amount of solution to suit the bond area. The aLIGO procedure recommends 0.8 µl cm^{2-1} for small bond areas. Set the pipette to a value calculated from the surface area of the bond samples.

11. Gather the samples to be bonded. Wipe the bond surface with a new clean room wipe soaked in spectroscopic grade methanol (>99.9%) and inspect in a bright light source, like a fibre optic light, for surface defects or contamination.

12. Insert the pipette into a clean tip, being careful not to touch the clean tip to any surface.

13. Slowly insert the clean tip into the medical filter tube of bond solution, only far enough to have the tip under the solution surface. Withdraw solution and place carefully onto the first bond surface. The pipette should be close but not touching.

14. Carefully place the second bond surface onto the first.

15. Remove the pipette tip and close the medical filter of bond solution.

16. Inspect the bonded interface.

For bonded fused silica the bond will immediately look mostly transparent. However, in the case of bonded sapphire the index mismatch between bond solution and sapphire is greater. This means the bond will look more reflective to start, and then more transparent over time as the bond cures and water leaves the bond. In all cases, take note of any bubbles

that are visible in the bond, both right after bonding. The bonds can be checked in intervals of 1-2 hours during the first day, then twice a day for a few days afterwords. If the bond has visible contaminants in it then it is advisable to de-bond immediately. It is advisable to de-bond and re-bond if there are bubbles that take up 5% or more of the total bond area, especially if the large bubbles do not move towards the edges over a 3-4 hours. De-bonding can be done up to 8 hours after the initial bond is formed. The samples can be carefully de-bonded under RO water, re-cleaned, and re-bonded as per the above procedure.
To get statistical results over the broadest range of curing time possible with the amount of procured samples it was decided to test the bond strengths at 1 week, 2 weeks, 4 weeks, 8 weeks, 12 weeks, and 30 weeks. Batches of 20 samples were cleaned and bonded as per the procedure above between November 2016 and January 2017, to attain 10 bonds per set. The timing of each bonded set allowed the strength testing of 1, 2, 4, 8, and 12 week old bonds to be conducted on the same day, February 1st 2017. One set of 20 samples, bonded and set aside for a 30 week cure, was then strength tested on September 20th 2017.

3.2.4 Tensile strength testing

The tensile strength of each hydroxide catalysis bonded sapphire sample was measured using a four-point bending test, following the mechanical testing standard outlined in ASTM C1161-13 [134]. This procedure is an industry standard to test the flexural strength of brittle materials such as fused silica and so has been used in the GW community as a standard to assess the tensile strength of hydroxide catalysis bonded fused silica, sapphire, and silicon for GW detectors [121, 122].
A Zwick-Roell 200 kN machine [135], with a 25 kN load cell was used in this study. The schematic on the right side of Figure 3.9 shows how the force was applied to the bonds. A jig was specially made to hold and apply force to bonded samples as in the schematic, a picture of the actual jig is on the left of Figure 3.9. The metal foot of the jig was clamped into the top of the strength tester and carefully aligned to the bottom part of the mount in order to provide straight and equally distributed force onto the bonded samples. Then the foot was lowered down to the top of the bonded sample, contacting it via two metal rods a distance l apart. The sample sat on two metal rods below it, a distance L apart. This ensured the even distribution of force to the bonded sample via four line contacts.
The loading arm of the machine provided the necessary force, F, on the bond interface. The starting point of the test was defined by pressing down on the bond sample with a user defined pre-load, in this case it was 1 N. The speed at which the loading arm moved was also user defined, in this case it was 2 mm/minute for all hydroxide catalysis bonded sapphire samples. The force at which each bond broke was recorded. The broken samples were then removed from the strength tester and the bond surfaces inspected. Different characteristics

of the bond surface post-break such as non-uniformities in the bond, damage to substrates, and bond layer discolourations were photographed and recorded to see if any correlations between tensile strength and bond interface appearance could be made.

The equation for the tensile strength of the bond, using the maximum recorded breaking

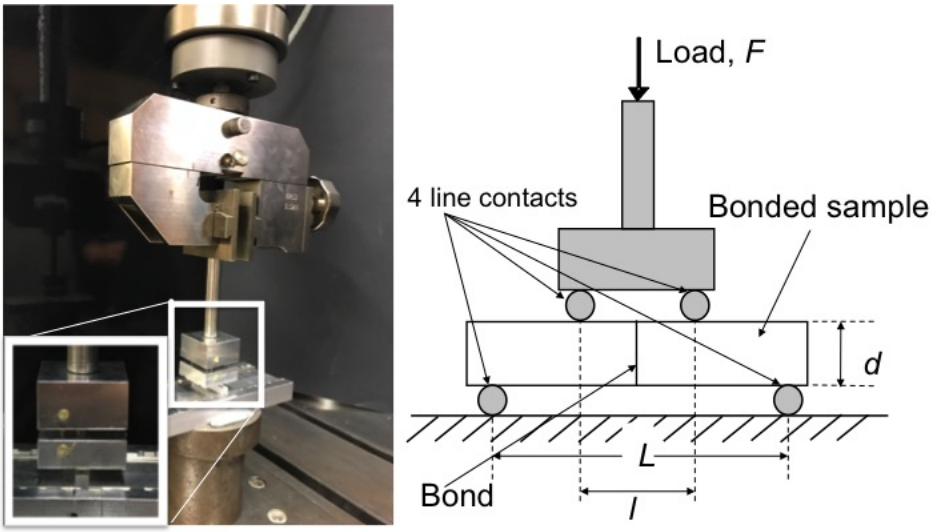

Figure 3.9: On the left is a hydroxide catalysis bonded sapphire in strength tester, on the right is the schematic for the same set-up.

force registered is [121]

$$\sigma_{max} = \frac{3(L - l)F}{2bd^2} \tag{3.1}$$

where F is the force at break, L is the distance between the sample supports, l the distance between the rod contacts of the pressure foot, b is thickness and d the width of the bonded sample as shown in the schematic in Figure 3.9. For this study, L=34 mm ±0.1 mm, l=20 mm ±0.1 mm, and b=d=5 mm ±0.05 mm.

3.2.5 Mechanisms of water bonds and their contribution to hydroxide catalysis bond strength

The contribution of water to the initial strength of hydroxide catalysis bonds is investigated here. After the polymerisation stage of hydroxide catalysis bonds, the bond interface is full of siloxane chains and water. The water then leaves the bond during the last dehydration stage. It is at this point between the polymerisation stage and the end of the dehydration stage that we see the drop in tensile strength, so it is of interest to review how the presence of H_2O molecules could lead to an initially higher bond strength.

The positive and negative charges in H_2O molecules are not distributed uniformly, which leads to the water molecules having large dipole moments. The negative end of one water molecule will orient itself to be close to the positive end of another nearby water molecule.

This dipole-dipole attraction is weaker than that of covalent or ionic bonds. However in liquid water where the molecules are close together these bonds form between neighbouring hydrogen and oxygen atoms of adjacent water molecules. This process is called cohesion [136].

When H_2O molecules come in contact with a surface they can bond to it via hydrogen bonds, in a process called adhesion. The level of adhesion depends on what characteristics the surface has. The substrates used in hydroxide catalysis bonds in GW detectors are very clean, hydrophilic, $\lambda/10$ flat surfaces. The hydrophilicity of both the sapphire and fused silica surfaces encourages the quick spread of water and creation of hydrogen bonds between the substrates and the water molecules. This property by itself indicates a high level of adhesion occurs in the initial stages of bonding [137]. The cleanliness and flatness of all the bond substrate types will also increase the creation of hydrogen bonds, unimpeded by surface features or contaminants that would prevent bonds. In the case of fused silica, its SiO_2 molecules are also polar. This means water will readily adhere to it, the oxygen atoms on the fused silica surface form hydrogen bonds with H_2O molecules, as shown in Figure 3.10. Sapphire, Al_2O_3, also has oxygen molecules that can form hydrogen bonds

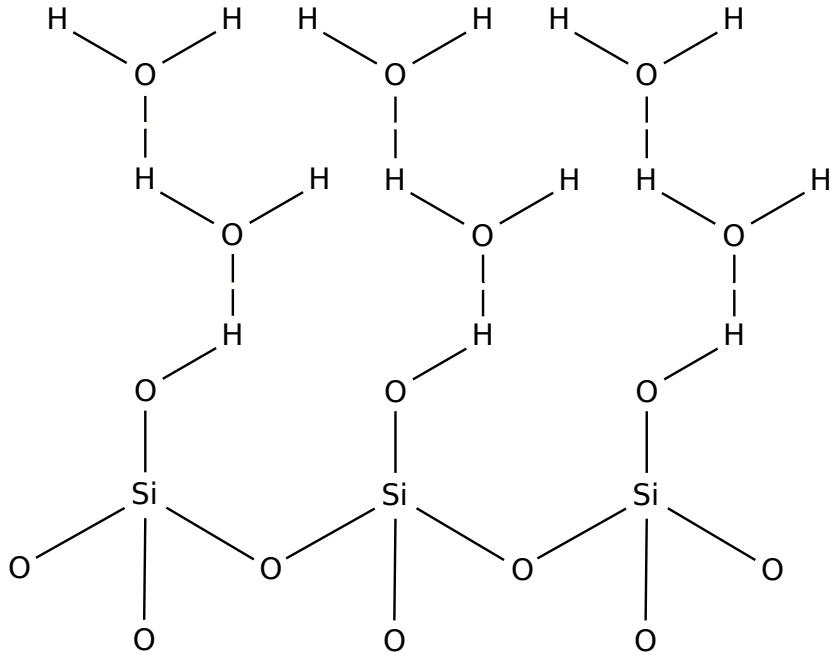

Figure 3.10: Hydrogen bonds between water molecules and a fused silica surface. Hydrogen bonds indicated by dashed line, covalent bonds by a solid line.

with water. However if the sapphire substrate is a pristine and unbroken crystal the oxygen atoms are bound tightly within the crystal lattice and it cannot form hydrogen bonds as readily as fused silica [138]. However, sapphire substrates are mechanically polished during manufacturing, and additionally prior to bonding using cerium oxide. This mechanical polish breaks up the connections between alumina molecules across the surface. This polish step is thought to allow the hydroxide catalysis bond to free aluminium atoms from the

Al_2O_3 substrate in order to form aluminosilicate networks, and would also allow water to permeate the partially broken Al_2O_3 connections to form hydrogen bonds with the oxygen atoms. In most cases fused silica is also cerium oxide cleaned before bonding, which may also increase bonds between the water molecules and free oxygen atoms on the fused silica surface.

In the literature, a correlation between hydrogen bonds and improved compressional strength and torsional modulus of rigid-rod polymers has been shown [139], as well as the importance of water in hydrogen bond formation between paper fibres that produces the highest breaking length and tear resistance compared to other tested solvents [136]. For hydroxide catalysis bonded fused silica and hydroxide catalysis bonded sapphire, how much the hydrogen bonds add to the overall bond strength is difficult to predict, as the bond solution is made up of not only water but also sodium silicate. The siloxane chains (or aluminosilicate networks) that form lattices between the substrates during the bonding process must form alongside, and interact with, the water molecule's hydrogen bonds. Thus, how the two mechanisms contribute to the overall bond strength is intertwined.

The water leaves the hydroxide catalysis bond via evaporation to air and diffusion through the substrates it is attached to, as outlined in Section 2.7. It would be expected that there would be a difference in how these bonds evolve over time between substrates of different materials, as water diffuses into different materials at different rates. Here we will look at the diffusion of water through amorphous fused silica and through single crystal sapphire. Both the fused silica substrates and the sapphire substrates were mechanically polished using cerium oxide prior to bonding, which is assumed to increase the permeability of both the materials.

Most research on the rates of water diffusion in materials are based on infra-red optical absorption measurements of the materials, at temperatures of 400 celsius or higher, since it is difficult to measure the effects at lower temperatures. The lowest temperature that was found was the diffusion of water into glass at 400 °C [140].

Water diffusion through single crystal sapphire is presumed to happen along dislocations [138]. The number of dislocations and thus the rate of diffusion depends on the crystal plane orientation and the state of the surface layer in contact with the bond solution. In this case the bond surface was c-plane sapphire, with the mechanical cerium oxide polish increasing the number of dislocations on the surface.

The rates of water diffusion through fused silica are also dependent upon temperature. However the mechanism of movement is the same at all temperatures in that the water molecules move through the silica, reacting with it as they go and forming stationary hydroxyl, HOSi, as follows [141]

$$\mathrm{Si{-}O{-}Si} + \mathrm{H_2O} \longrightarrow \mathrm{Si(OH)} + \mathrm{HOSi} \tag{3.2}$$

Even with the increase in dislocations via a mechanical polish the diffusion rate of water through bulk sapphire would be much slower than through fused silica[138, 141]. In all cases, the water evaporates over time and as such the additional bonds between the water molecules and the bond substrates would be seen to weaken and eventually disappear, while the silicate lattices continue to form and strengthen and the bond strength levels off and stabilises. In the case of hydroxide catalysis bonded sapphire, the presence of a water bond would be expected to decrease in strength much more slowly than a water bond between fused silica due to a slower diffusion rate. The rates of bond strength settling times between these two different substrates is compared in the next section.

3.3 Results and analysis

These results include the tensile strengths of all bonds where more than 80% of the bond interface did not have any visible contaminants or air bubbles, which will be referred to here as "bond quality better than 80%". All samples were cleaned with cerium oxide, and bonded with 1:6 sodium silicate and 0.8 µl/cm^2 as per the procedures above and cured at room temperature.

All of the bonded samples except one, with serial numbers 3050/3051, had bond quality better than 80%. The tensile strength of nine substrates that exceeded specified flatness, roughness, or number of visible surfaces defects, are shown in Figure 3.11. The sample

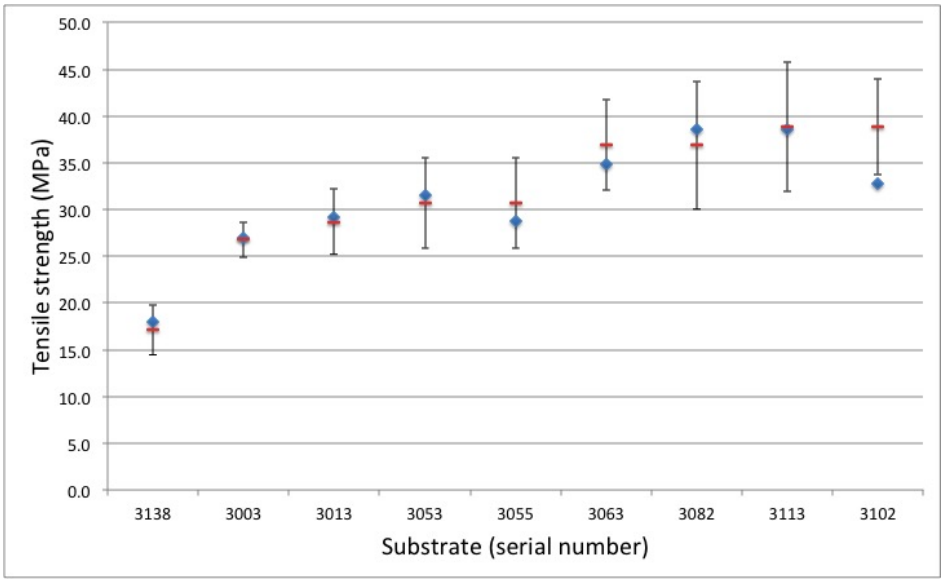

Figure 3.11: Breaking strength of individual hydroxide catalysis bonds in blue diamonds where one substrate had high flatness, roughness, or surface defects. The average breaking strength and standard deviation of the batch that the sample was in is shown in orange bars for comparison.

with the worst scratch on it, 3082, had a breaking strength of 38.6 MPa in the 2 week set

where the average strength for that set was 36.9 MPa. Similarly the rest of the 9 samples that did not meet a roughness, flatness, or defect requirement were all within the average tensile strength and standard deviation of the batch they were in, and thus could not be correlated to an abnormally low breaking strength. This is seen in Figure 3.11.

The 1, 2, 4, 8, 12, and 30 week old curing time results from this study are shown in Fig-

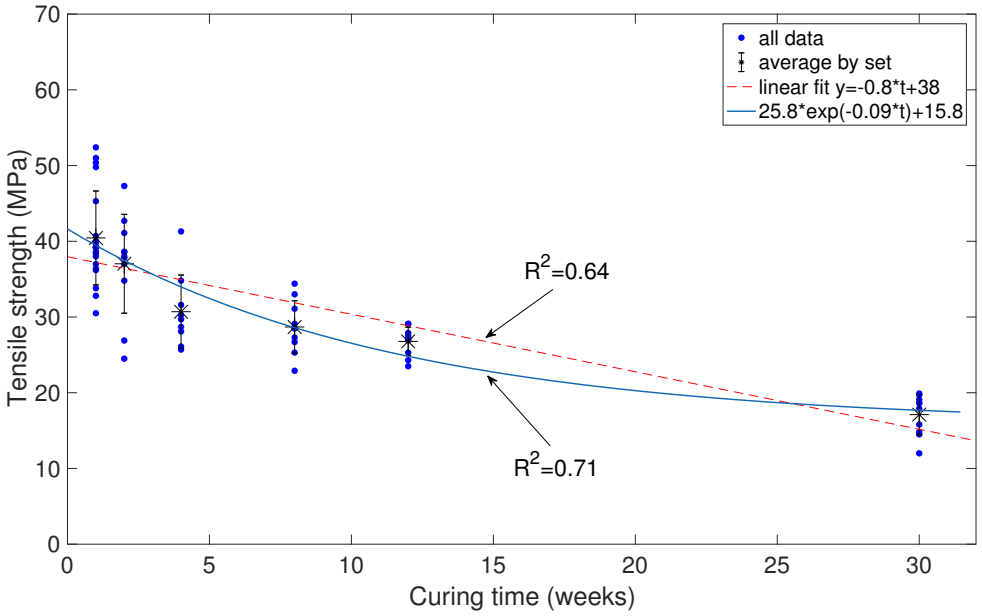

Figure 3.12: Strength of hydroxide catalysis bonded c plane sapphire as a function of curing time. M.Phelps results

ure 3.12, where the data are fit against linear and exponential models.

The initial drop in bond strength was concerning; if the hydroxide catalysis bond strength drops too low over time it could become a concern for suspended optics system failure. The $R^2 = 0.64$ value of the linear fit, $y = -0.8t + 38$, and the $R^2 = 0.71$ value of exponential fit, $y = 25.8 \cdot \exp(-0.09t) + 15.8$, suggest the exponential fit is a better match for the data. The linear fit could be used as a worst case scenario suggesting that the bond strength would drop to zero in 38 weeks, where the exponential fit suggests the strength will level off at 15-16 MPa.

The 1, 2, 4, 8, and 12 week old 2017 breaking stress results proved to be in reasonable agreement with those produced in 2014-2015 by R. Douglas. Both sets of data show a slight drop in bond strength from one week to 12 weeks, with the addition of the 30 week results from 2017. All data are plotted with linear and exponential fits in Figure 3.13.

To compare the hydroxide catalysis bonded sapphire results found in this study data to hydroxide catalysis bonded fused silica, the tensile strength results of sodium silicate bonds between fused silica substrates over time from past studies were plotted and fitted to an exponential as well, in Figure 3.14.

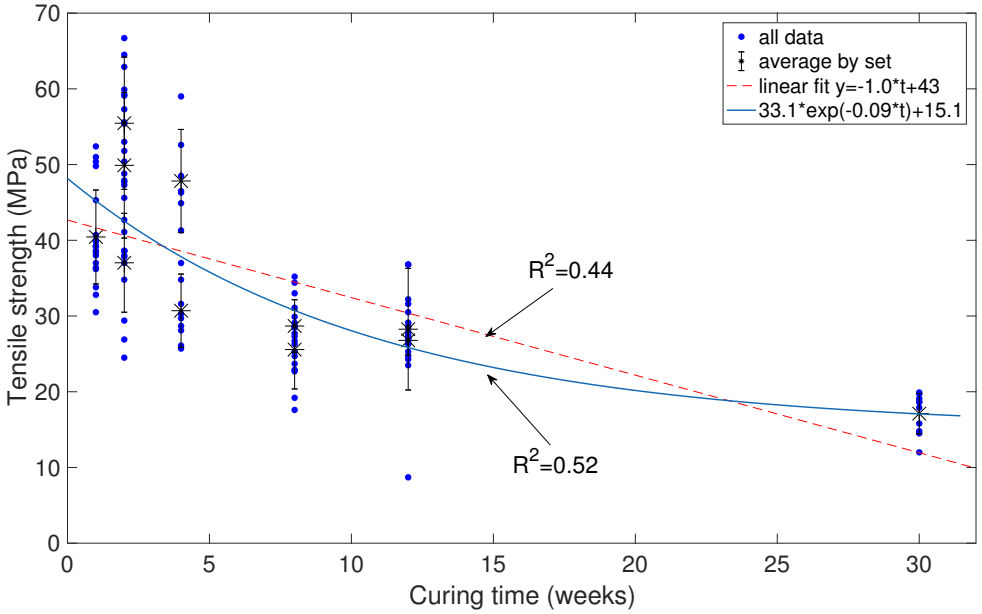

Figure 3.13: Strength of hydroxide catalysis bonded c plane sapphire over time. M.Phelps and R. Douglas 2014-2017 combined results

It is proposed here that the initially higher bond strength of hydroxide catalysis bonded

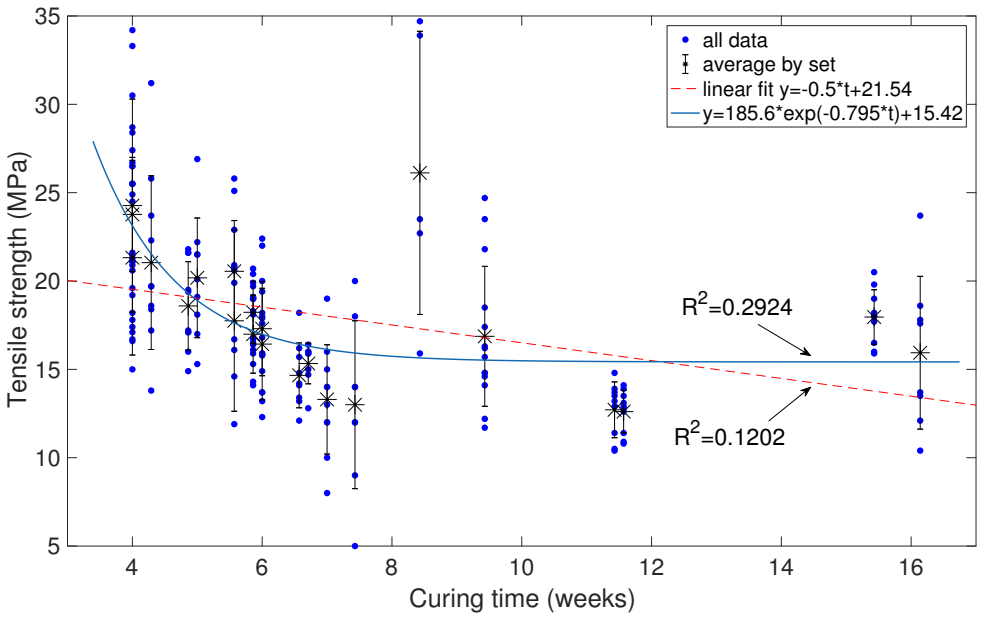

Figure 3.14: Combined curing time tensile strength results of hydroxide catalysis bonded fused silica sets made between 2009-2014.

fused silica and sapphire seen in both Figure 3.14 and Figure 3.13 is due to the presence of water forming additional hydrogen bonds between itself and the substrate surfaces, which decreases as the water evaporates and the silicate lattices stabilises.

3.4 Conclusions and recommendations

The tensile strength results of both the hydroxide catalysis bonded fused silica and the hydroxide catalysis bonded sapphire show an initial drop in strength, though at different rates, and levels off at 15-16 MPa. It should be noted that this hydroxide catalysis bonded fused silica data were collected over many years by different users and different types of fused silica substrates, and volumes of sodium silicate solution so while the fits are both not as close to the data, they still follow a similar trend. Most importantly, as we know that hydroxide catalysis bonded fused silica has been a part of GW detector suspensions for longer than seventeen years without failing [6], as such this comparison indicates hydroxide catalysis bonded sapphire suspensions should also level off to a strength of around 15 MPa instead of failing altogether.

The requirement for the tensile strength of hydroxide catalysis bonds in a cryogenic sapphire detector such as KAGRA is 1 MPa [142], so a level off at 15 MPa would be more than acceptable, leaving a safety factor of 15.

How the tensile strength of hydroxide catalysis bonded sapphire and bonded silicon develops over curing time periods of years could also be investigated for completeness. Further investigation into the exact role that water plays in hydroxide catalysis bond formation could also be pursued.

Chapter 4

The strength of hydroxide catalysis bonds between sapphire of m and a crystal orientations

4.1 Introduction

Sapphire, or Al_2O_3, is an anisotropic crystalline material made up of alumina and oxygen atoms. How the alumina and oxygen atoms order themselves in the hexagonal crystal lattice is different depending on the plane orientation, which is shown in Figure 4.1 [143]. Sap-

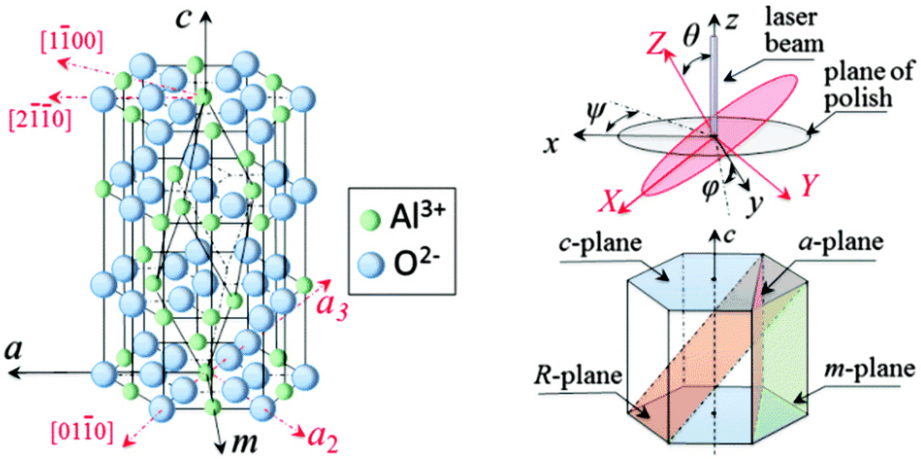

Figure 4.1: On the left, alumina and oxygen atoms in the a, m, and c sapphire planes. On the top right an example of how a laser beam should be oriented with respect to the c-axis to avoid birefringent effects. The planes of sapphire are shown in the diagram below it in the bottom right.

phire exhibits birefringent behaviour. This means that different polarisations of light will see different effective indices of refraction within the material, and be refracted through it at different angles. For a GW detector with a laser source and a sapphire optic, this difference

in refraction between source polarisation would be a serious source of optical distortion. Thankfully, sapphire does not exhibit this birefringent effect along all crystal planes. A light source that shines through the crystal parallel to the c-axis, indicated by the arrow coming out of the top of Figure 4.1, will not be distorted by sapphire's crystal structure. However, if the direction of the light source is changed to pass perpendicular to the a, m, or r-planes, it would be refracted due to the birefringent nature of the crystal structure at those orientations [143]. Therefore, in cryogenic GW detectors that have sapphire test masses and suspension elements, the c-axis must align with the laser beam of the detector, as this will not produce any birefringent effects which would induce optical noise. This defines the optical faces of sapphire test masses to be in the c-plane orientation.
However, the hydroxide catalysis bond interfaces may be between any number of different sapphire planes. Thus the strength of bonds between sapphire of different orientations and temperatures has been an active area of research. The breaking stress over time at room temperature of c-plane to c-plane bonds was reported in the previous chapter to have breaking stresses that settle to 15 MPa for bonds cured for 7 months. Additionally, in the literature the shear strength of c-c, c-a, and c-m bonds has been investigated at cryogenic temperatures. These were also found to have suitably high tensile strengths, averaging 23 MPa for 4 week old bonds [125].
While c-c plane bonds as well as cross-axis bonds of c-a and c-m had been measured previously, the breaking stress of bonds between a-a and m-m plane sapphire had not. Thus the breaking stress of m-m and a-a plane bonds were studied here, after a curing time of 4 weeks at room temperature.
The a plane and m plane were focussed on as more probable crystal planes for a test mass to ear interface where the test mass face was defined to be in the c-plane.

4.2 Method

For this study 44 samples of 5 mm×5 mm×20 mm sapphire rods were procured from Impex [128], half of which had the bond surface in the a-plane and the other half in the m-plane. All samples were characterised, cleaned, and bonding solution prepared following the same bond procedure as in Chapter 3 for the c-c plane curing time tests. The PV flatness of the a-plane bond surfaces was measured to be 30 ± 5 nm, and 33 ± 5 nm for the m-plane bond surfaces. A 0.1 µL volume of 1:6 sodium silicate solution to RO water was used for all bonds. Only the crystal orientation that was bonded was different between procedures carried out in this chapter and the previous chapter.
All samples were cured for 4 weeks and then their breaking stresses recorded following the same tensile strength test procedure outlined in Chapter 3. This was done with the aim of making direct comparisons of m-m and a-a data with previous breaking stress results of c-c

sapphire bonds cured for 4 weeks at room temperature.

4.3 Results and discussion

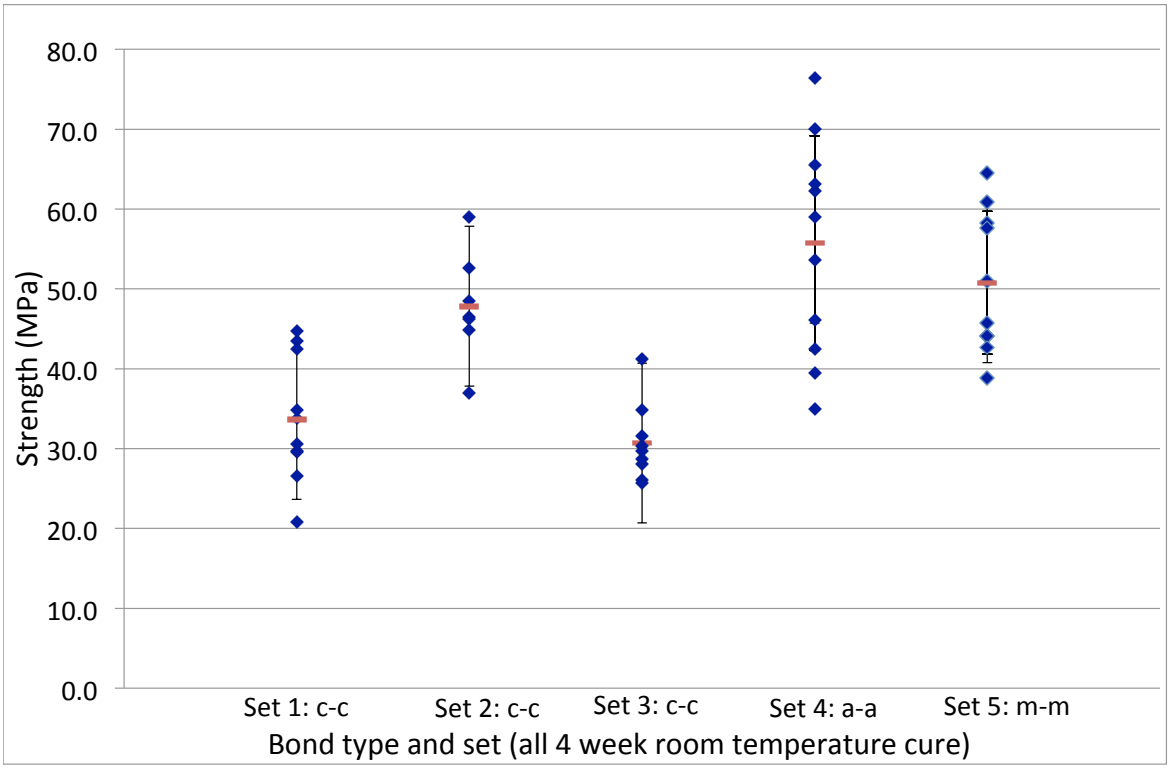

Figure 4.2: Tensile strength comparison of c-c plane, a-a plane and m-m plane bonds cured for 4 weeks.

The comparison of 4 week old bonds between c-c, a-a, and m-m plane sapphire is shown in Figure 4.2. The average breaking stress of the a-a plane bonds was found to be 56 $\pm$ 13 MPa and the average of the m-m plane bonds was 51 $\pm$ 9 MPa. The averages of the three sets of c-c plane sapphire bonds in Figure 4.2 were 31 $\pm$ 5 MPa, 48 $\pm$ 7 MPa, and 34 $\pm$ 8 MPa.
The breaking stress results obtained in this chapter are also plotted in Figure 4.3 along with c-c plane results of varying ages to indicate how their average breaking stress compares to bonds of other ages. The averages of the a-a and m-m plane bonds were slightly higher than those of 4 week old c-c plane bonds, however they are still within error, as shown in Figure 4.2 and Figure 4.3.
Interestingly, the majority of the sapphire substrates in this study were damaged during strength testing. 8 of the 11 a-a plane bonds and 5 of the 11 m-m bonds broke along one or both of the sapphire substrates (as well as the bond interface). Conversely, all of the c-c plane bonds reported in Chapter 3 (over 100 bonds) broke along the bond interfaces only, leaving the substrates intact. Similarly, the majority of the cryogenic cross axis tests of

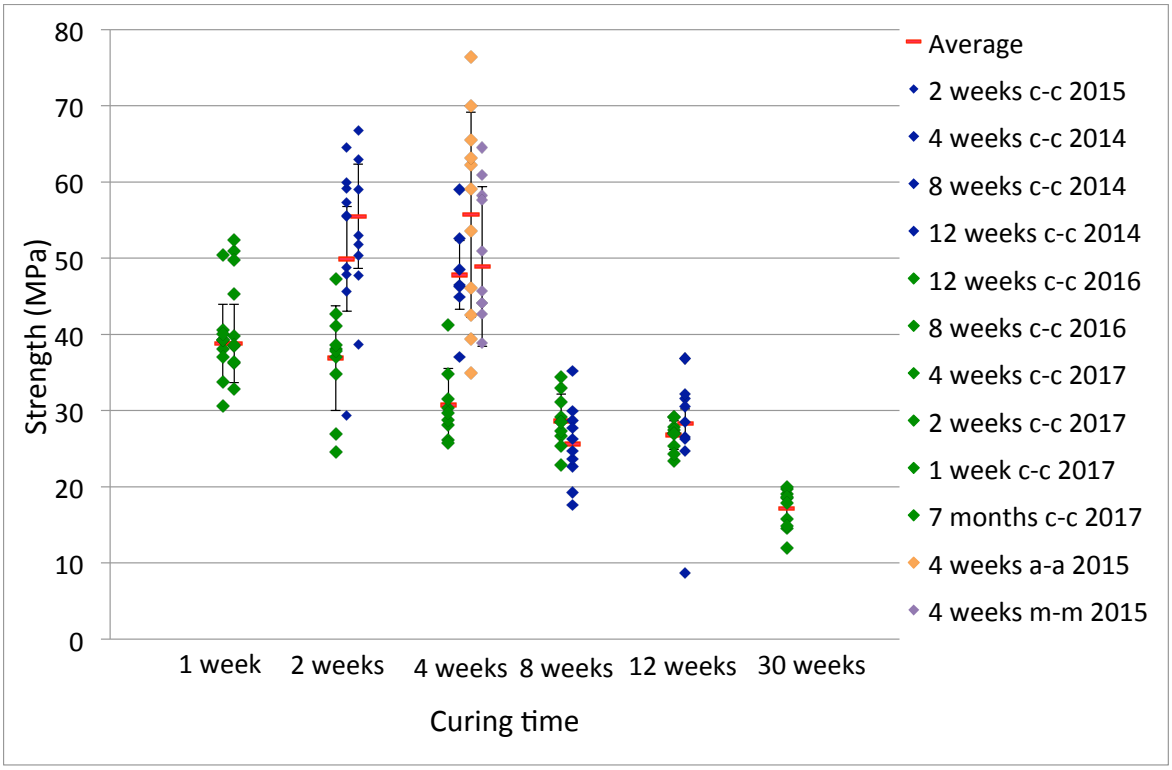

Figure 4.3: Tensile strength comparison of 4 week old a-a plane and m-m plane to c-c plane bonds of varying ages.

bonded c-a and c-m planes broke across the bond interface, with reported substrate damage in only 4 of the 54 samples [125].

Sapphire does not exhibit strong cleavage in general along its crystal planes. Its basal plane (parallel to c-plane), with interchanging O-Al-Al-O-Al-O layers, has no conditions for cleavage to occur. In other planes, such as $(10\bar{1}1)$, there are weaker O-O bonds which could allow for some cleavage [143]. This could be the reason for seeing a higher percentage of substrate damage in this study when compared to bonds made between c-plane sapphire.

Comparing the average breaking stress results of hydroxide catalysis bonds between sapphire of different crystal orientations it can be seen that while there may be differences in the type of break and the extent of damage to the substrates, bonds between the a-a, m-m, and c-c plane sapphire compared here were found to be sufficiently strong to be used in typical mirror suspensions. Hydroxide catalysis bonds can be considered for bonding different planes of sapphire together without a compromise in strength.

Chapter 5

Measuring the Young's modulus of hydroxide catalysis bonds

5.1 Introduction

Hydroxide catalysis bonds are currently a core technology for all operating room temperature ground-based detectors, and as such their material properties have to be well understood. In particular, it is necessary to know material properties such as density, Poisson ratio, and Young's modulus that are used in thermal noise calculations, which is explained in detail in Chapter 6. The density of hydroxide catalysis bonds has been previously calculated [144] and the Poisson ratio is assumed to be the same as fused silica, indicated by some mechanical loss models [145]. The Young's modulus, however, is challenging to characterise due to the bonds being very thin and poorly accessible.

The Young's modulus, or elastic modulus, is the ratio of stress to strain in a material. This ratio shows how easily a material deforms and how it will respond to stress[146].

Measurements of the Young's modulus of materials are often carried out with methods involving direct contact of the material in question. Measurements of bulk materials can be made by deforming the material elastically by bending or extending, while measuring the force applied and the deformation of the material [146]. From this information the Young's modulus can be determined. For smaller samples and thin coatings, nano-indentation as well as atomic force microscopy (AFM) measurements are used [124, 147]. AFM and nano-indentation both operate by directly contacting a test material with a sensitive probe. The probe measures the material's response to an applied force in terms of the vertical distance travelled, effectively measuring the amount a material is deformed.

In the case of hydroxide catalysis bonds, measuring the Young's modulus with any of the techniques above is inherently difficult. The bond is by default strongly adhered to two larger rigid substrates, and is also very thin, usually of order 60 nm [77, 148].

Past attempts at measuring the Young's modulus of hydroxide catalysis bonds by nano-indentation or AFM have included the use of chemical etches or mechanically cutting though bonded samples to expose the bond for nano-indentation [124]. The concern with direct contact methods is that they could change the properties to be measured as the bond is exposed during sample preparation. For example, a chemical etch could weaken the bond or change its chemical composition as it etches the substrate away, and slicing through the bonded substrates could easily weaken or shatter the bond material left behind. In addition, the thin bond presents difficulties as it pushes the edge of resolution of most nano-indentation probes [124].
There is one single measurement of a sodium silicate bond available in the literature, a value of 7.9 GPa with no known statistical errors [148]. In this measurement the bond was altered to make it artificially thick to allow for a nano-indentation measurement. This value has been used in calculations of thermal noise arising from the bonds for aLIGO in the past[77]. As the sensitivity of detectors improves it is necessary to obtain more accurate values for the bond properties since they are used in the construction of the detector mirror suspensions, and contribute to the overall thermal noise budget of the detectors. Here a non-destructive method of measurement is investigated, using acoustic pulses at ultrasonic frequencies that do not require alteration or destruction of the bonds. This measurement technique and the results are outlined in this chapter, as well as two analysis approaches to extract the Young's modulus of the bond from the measured data. In Chapter 6, the impact of the new Young's modulus values on thermal noise budgets of GW detectors is discussed.

5.2 Theory of ultrasonic measurements

Ultrasonic waves, or ultrasound, are sound waves produced at frequencies higher than the upper audible limit of human hearing, in the 20 kHz to high GHz range [149]. The transmission and reflection of ultrasonic waves through materials is used as a non-destructive method of probing hidden properties in many different fields. Though most familiarly it is used in medicine to safely image the interior of the human body; it also has many industrial applications as well, such as looking for unseen welding flaws inside manufactured parts [149]. Ultrasonic pulses can also be used to measure material properties such as the Young's modulus [150]; hence, this technology was considered as a non-destructive means to determine the Young's modulus of hydroxide catalysis bonded samples.
An acoustic wave signal that passes from one medium to another can be expressed in terms of the acoustic impedance of each medium. Upon encountering a change in the medium type, part of the signal will be reflected and the rest transmitted. Equation 5.1 shows the relationship between the fraction of the amplitude of a wave travelling through medium

one and reflecting off medium two, where Z_i is the characteristic acoustic impedance of the medium passed through by an acoustic wave.

$$R_{2,1} = \left| \frac{Z_2 - Z_1}{Z_1 + Z_2} \right| \tag{5.1}$$

$Z_i = \rho_i \cdot v_i$ where v is the acoustic velocity, and ρ the density of the medium. The acoustic impedance Z is calculated as $Z_{air} = 331.4$ m/s·1.225 kg/m^3 = 406 Rayls and $Z_{silica} = 5931$ m/s·2200 kg/m^3 = $1.3 \cdot 10^7$ Rayls. The equation for the reflection of a silica-to-air interface is as follows.

$$R_{\text{silica,air}} = \left| \frac{Z_{\text{air}} - Z_{\text{silica}}}{Z_{\text{silica}} + Z_{\text{air}}} \right| = \left| \frac{331.4 - 13 \cdot 10^6}{331.4 + 13 \cdot 10^6} \right| = 0.99 \tag{5.2}$$

In practice the amplitude of the input signal cannot be measured directly in the experimental set-up described in the next section, as the input peaks include a number of additional noise sources such as electronic noise, damping inside the transducer, and edge effects from contacting the sample's surfaces. Thus as the amplitude of the back reflection is assumed to be 99% of the incident wave, it is used as a proxy for the input signal scaled by 100/99. Since the above equation applies to waves passing from one medium to another, not through layered mediums, a different equation is needed to quantify a reflection from a thin bond interface [149].

An expression for an acoustic pulse reflected from a thin layer between two much thicker materials that takes into account the layer thickness is needed to calculate the reflected signal from the hydroxide catalysis bond. To determine it the technique outlined in Physical Acoustics [151] was followed. An equation for R_{bond} was derived from the complex pressure amplitudes of incident waves, $P_{\text{incident}} = Ae^{i(\omega t - kx)}$ and reflected waves, $P_{\text{reflect}} = Be^{i(\omega t + kx)}$. Applying acoustic impedance continuity boundary conditions at the start and end of the layer, $x = 0$ and $x = L$, between two substrates of the same material type such that $Z_1 = Z_3$ the following is obtained

$$R_{\text{bond}} = \frac{i(\frac{Z_2}{Z_1} - \frac{Z_1}{Z_2}) \sin(k_2 L)}{2\cos(k_2 L) + i(\frac{Z_2}{Z_1} + \frac{Z_1}{Z_2}) \sin(k_2 L)} \tag{5.3}$$

where Z_1 is characteristic acoustic impedance of the first and third medium, in this case the substrate material, Z_2 is the characteristic impedance of the second medium, in this case the bond material. L is the bond thickness and k_2 is the wave number for the bond medium.

For cases where $\lambda_{acoustic} \gg L$, the quantity $k_2 L$ is very small, and thus $\sin(k_2 L) \approx k_2 L$ and $\cos(k_2 L) \approx 1 - \frac{(k_2 L)^2}{2}$ by way of the small angle approximation. This applies to the experiment outlined in this chapter, as $\lambda_{acoustic} \approx 50\,\mu$m and the thickness of the hydroxide

catalysis bonds are of order $L \approx 50\,\text{nm}$. This approximation simplifies the equation to:

$$R_{\text{bond}} = \frac{i(\frac{Z_2}{Z_1} - \frac{Z_1}{Z_2})k_2 L}{2(1 - \frac{(k_2 L)^2}{2}) + i(\frac{Z_2}{Z_1} + \frac{Z_1}{Z_2})k_2 L} \tag{5.4}$$

Similarly the L and L^2 terms in the denominator can be approximated to be zero for small values of $k_2 L$, and so the denominator is ≈ 2, which gives the following form of the equation.

$$R_{\text{bond}} = i\left[\frac{Z_2}{Z_1} - \frac{Z_1}{Z_2}\right]\frac{k_2 L}{2} \tag{5.5}$$

The general equation for acoustic impedance is $Z = \rho \cdot v$ where v is the acoustic velocity and ρ the density of the medium. The Young's modulus is the value of interest in this experiment. Therefore the acoustic velocity is expressed as a function of the Young's modulus of the material, E, and its density, ρ, where $v = \sqrt{\frac{E}{\rho}}$. Thus Z can be expressed as

$$Z_j = \rho_j \cdot \sqrt{\frac{E_j}{\rho_j}} = \sqrt{\rho_j E_j} \tag{5.6}$$

Additionally, if the densities of the bond material and the substrate materials are not equal then the following form of R_{bond} is used, where the wave number k is also expressed in terms of acoustic velocity and the frequency of the acoustic source, i.e the ultrasonic transducer, $k_2 = \frac{2\pi}{\lambda_2} = \frac{2f\pi}{v_2}$. Simplifying all these terms gives the following form of R_{bond}.

$$R_{\text{bond}} = i\left[\sqrt{\frac{E_2\rho_2}{E_1\rho_1}} - \sqrt{\frac{E_1\rho_1}{E_2\rho_2}}\right]\sqrt{\frac{\rho_2}{E_2}}\pi f L \tag{5.7}$$

The density of hydroxide catalysis bonds was calculated in prior experiments to be the same as fused silica [144]. Thus for hydroxide catalysis bonded fused silica the impedance terms simplify to ratios of the Young's modulus of fused silica, E_1, and of hydroxide catalysis bonds, E_2, as $\frac{Z_1}{Z_2} \approx \sqrt{(\frac{E_2}{E_1})}$.

$$R_{\text{bond}} = i\left[\sqrt{\frac{E_2}{E_1}} - \sqrt{\frac{E_1}{E_2}}\right]\sqrt{\frac{\rho_2}{E_2}}\pi f L \tag{5.8}$$

Using the different forms of R_{bond} in Equation 5.3, 5.4 and Equation 5.8 to calculate what the reflection coefficient would be from a hydroxide catalysis bond between fused silica substrates at f =12 MHz, all three equations give the same value for R_{bond} for bond thickness values of nanometres to a few microns. For L =7 µm and higher, the reflection coefficients calculated from these three equations differ by $< 2\%$ as the small angle approximations

made to arrive at Equation 5.8 become less true for larger L values. Realistic bond thickness values are of order 100 nm or less, for which the calculated R_{bond} results are the same for Equation 5.3, 5.4 and Equation 5.8.
To analyse hydroxide catalysis bonded sapphire or indium bonded silica, where the densities of the bonds are different from the substrate densities Equation 5.7 must be used, for hydroxide catalysis bonded fused silica the density of the bond and substrate material are the same, so Equation 5.8 is used.

5.3 Method of ultrasonic reflection measurement

The ultrasonic measurements in this experiment were made using a transducer that was contacted with glycerine to one side of a bonded substrate doublet. The majority of samples measured were two fused silica substrates with a hydroxide catalysis bond in the middle. However one sample was made up of two sapphire substrates with a hydroxide catalysis bond in the middle, and three indium bonded fused silica samples were also measured.
The glycerine gel was used to improve the acoustic coupling between the transducer and the sample. Several types of transducers were tried, with different operating frequencies and damping levels. Attempts to achieve an operating frequency range of 20 MHz to 50 MHz were made by depositing a ZnO film directly to the sample to act as the transducer. However the film was not optimised and the signal was overwhelmed by high frequency noise sources from the rest of the lab.
The transducer that had the best combination of damping and high SNR was the Sonatest SLIH 10-10 transducer [152], with a centre frequency of 12 MHz and a bandwidth of 6 MHz to 15 MHz. This was used for the rest of the study.
The transducer is powered by a JSR Ultrasonics DPR300 pulser/receiver control box [153], which sends out an ultrasonic pulse that travels through the fused silica, and is reflected back to the transducer from the embedded hydroxide catalysis bond and the rear face of the sample. The DPR300 control box settings were as follows. High-pass: 15 MHz, low-pass: 5 MHz, relative gain: 30 and 6, prf rate: 8, pulse amplitude: 1, damping: 8.
A schematic of the set-up is shown in Figure 5.1. The first reflection is from the bonded interface, the second from the silica to air boundary on the other side of the sample. Both reflected signals are received back by the same transducer that sent the pulse. The reflected signals are then viewed and captured on a 200 MHz oscilloscope, averaged 4096 times to attain the data. Measurements are repeated an average of 10 times per transducer location to allow an estimation of error to be made.

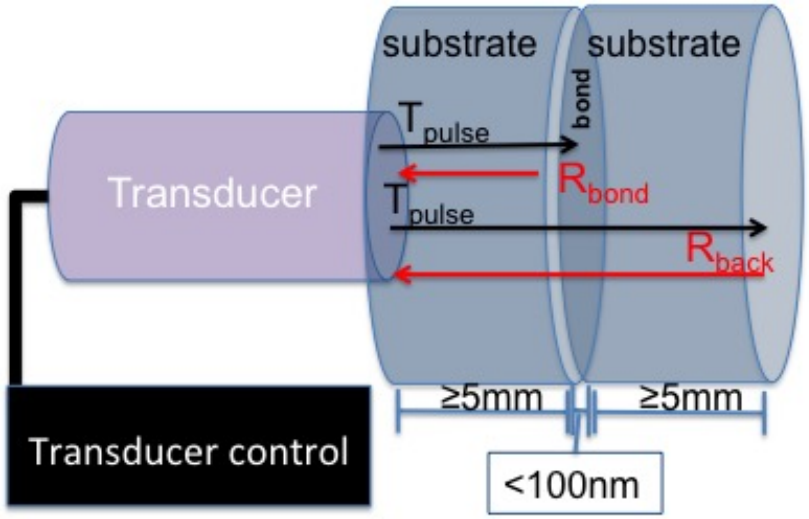

Figure 5.1: Experimental setup schematic

5.4 Measurements of hydroxide catalysis bonded fused silica

Hydroxide catalysis bonded fused silica is currently in use in all room temperature detectors, so updating the knowledge of its Young's modulus was the first priority of this experiment. Thus this study focussed on fused silica samples bonded with 1:10 and 1:6 sodium silicate solution in RO water. The transducer diameter, 10 mm, meant the bonded sample had to be at least this size or bigger to measure them. Fused silica discs, of 25 mm diameter or larger and 6 mm thick were used. An un-bonded fused silica cylinder calibration sample was measured as well. Of the hydroxide catalysis bonded fused silica samples, some had small air bubbles trapped in the bond. The air bubbles have a very high impedance mismatch with the fused silica substrates compared to hydroxide catalysis bonds and the resulting reflected signal was increased by several orders of magnitude, as can be seen in Figure 5.2.

Given their strong signal, the air bubbles were initially used as landmarks to indicate that the measured reflected signal was indeed from the bond interface. Moving over the bubble caused an increase in reflected signal amplitude and moving away from it caused the signal to decrease in amplitude but still remain in the same position and phase. After this initial check the bonded samples that had air bubbles in them were not included in the analysis, as the air bubbles greatly influenced the bond signal, even when the transducer was near but not directly over an air bubble. Only the highest quality bonded fused silica samples were used in the final analysis, the characteristics of which are detailed in Table 5.1. A fused silica cylinder with no bond in it, of the same length as the majority of the bonded discs, 12 mm was used as a reference sample, with its reflection data is shown in Figure 5.3 and Figure 5.4. The reference sample was also used to double-check the speed of sound though

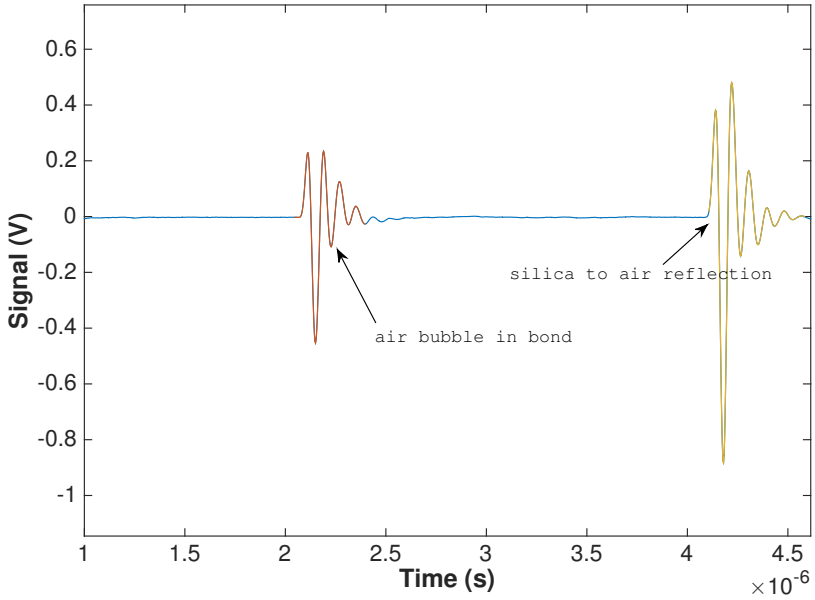

Figure 5.2: Acoustic pulse reflected from air bubble in hydroxide catalysis bonded fused silica

Sample	Transducer Position	Sodium Silicate to RO water ratio	Diameter x Length (mm)
1	top	1:6	25x12
1	bottom	1:6	25x12
1	center	1:6	25x12
1	left	1:6	25x12
1	right	1:6	25x12
2	center	1:6	25x12
3	center	1:6	25x12
4	center	1:6	50x10
5	center	1:6	50x24
6	center	1:10	50x10

Table 5.1: Characteristics of hydroxide catalysis bonded fused silica samples

bulk silica, calculated by $v_{sound} = 2 \cdot d/\delta t$. Here δt was measured to be 4.273 ± 0.002 μs and $d = 12.5 \pm 0.2$ mm, giving $v_{sound} = 5851 \pm 93$ m/s, compared to known values of 5896 m/s for bulk fused silica and 5760 ms for thin rods[151]. Finally in Figure 5.5 and Figure 5.6 there is an example of the acoustic pulse reflection data of a hydroxide catalysis bonded fused silica sample. In Figure 5.5 the signal from the bond interface is shown in the middle, and the larger reflection from the silica-to-air interface is on the right. The zoomed in portion of the bulk silica in Figure 5.4 shows the noise background and is visibly different to the bond reflection signal at the same position within the bonded sample, shown in Figure 5.6. Here an ultrasonic pulse comes out of the transducer, travels through the fused silica, and is reflected back to the transducer first from the bonded interface and second from the silica to air boundary on the other side of the sample, shown in Figure 5.5.

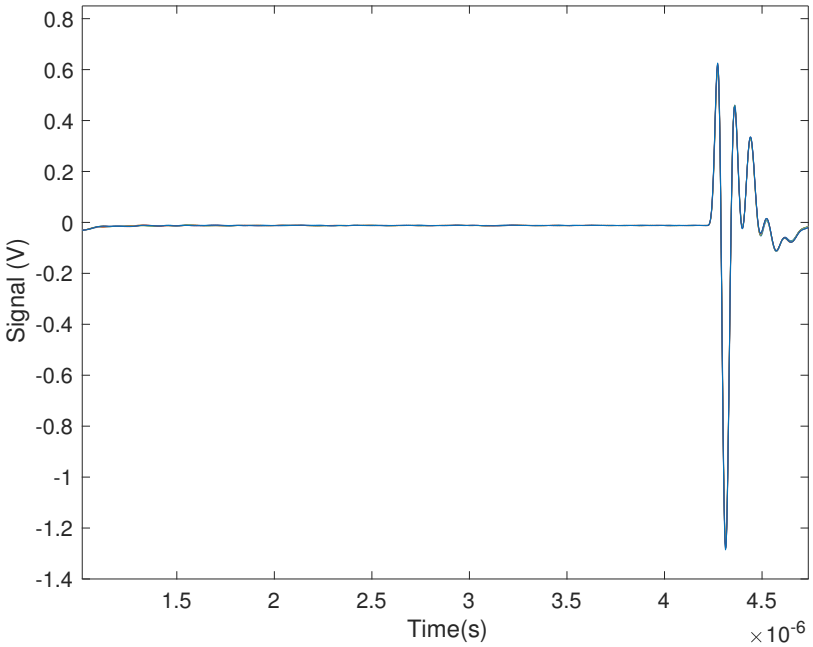

Figure 5.3: Acoustic pulse reflected from the 12 mm long silica cylinder used as a reference sample.

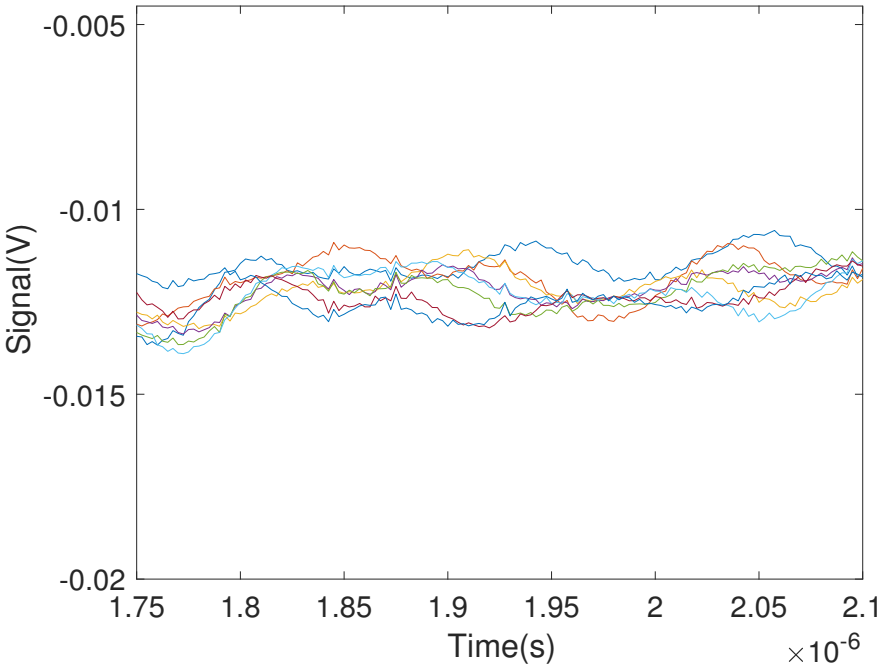

Figure 5.4: Zoom in of 12 mm long silica cylinder reference sample (middle).

5.4.1 SEM thickness measurements of bonds between fused silica

One of the variables that is needed to calculate the bond's Young's modulus from the reflected acoustic pulse is its thickness. Measurements of other bonded samples have been shown to be in the range of 10 nm to 100 nm [77, 148]. However, the exact thickness was

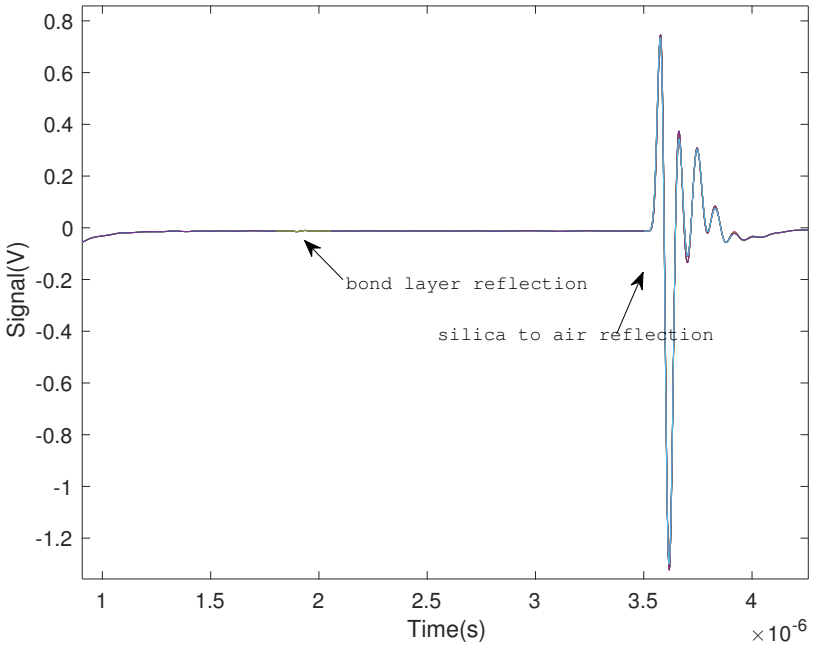

Figure 5.5: Acoustic pulse reflected from 10 mm long hydroxide catalysis bonded fused silica sample.

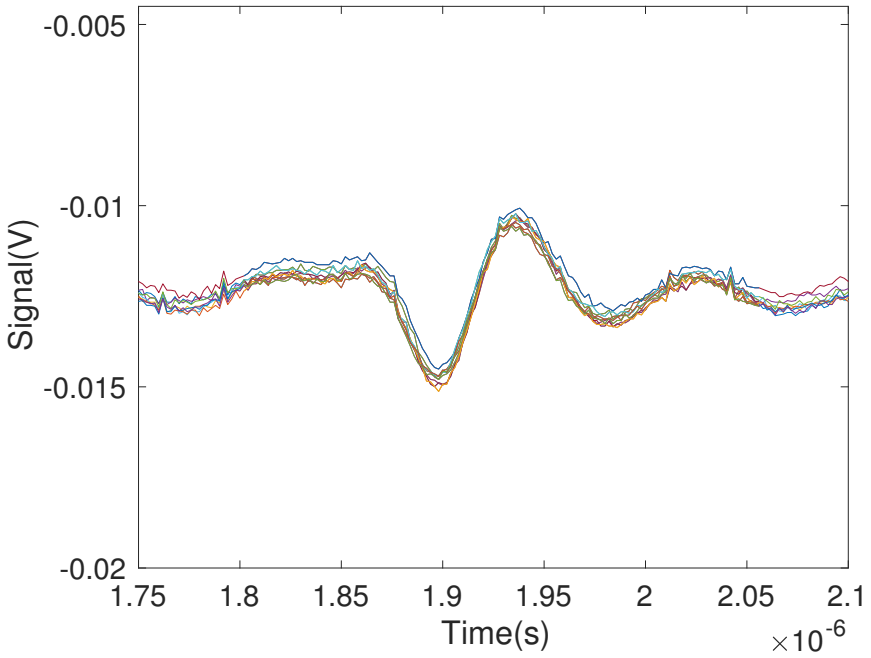

Figure 5.6: Zoom in of acoustic pulse reflected from a 10 mm long hydroxide catalysis bonded fused silica sample.

not known for these samples. To measure them directly, the bonded samples were imaged using a FEI Nova 200 Dual beam FIB system scanning electron microscope(SEM) [154] at Glasgow University.

In order to measure the sample bond thickness with an SEM, the bonded fused silica discs

were cut into slices of 2 mm to 3 mm wide with a Logitech model 15 disc saw [155] with a diamond rimmed steel blade, after all ultrasonic measurements were complete. See Figure 5.7 for a diagram of sample preparation. The slices were serialised after cutting and

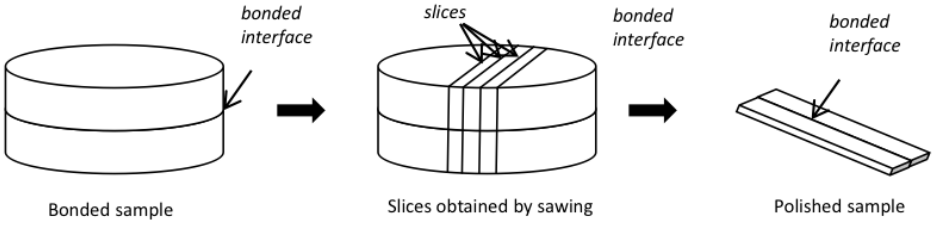

Figure 5.7: Preparation of bonded samples for SEM imaging

prior to polishing so that thickness measurements could later be mapped to each physical location on the sample.

After the samples were cut they were fixed with Glycol Phthalate bonding wax (Logitech 0CON-324 [155]) onto a steel chuck and polished with a PM5 Logitech Polisher [155]. The samples were polished across the bond first with 600 grit silicon carbide, then with 9 µm aluminium oxide, then with 3 µm aluminium oxide, and finally with SF polishing suspension [155]. The silicon carbide and aluminium oxide powders are mixed with water prior to polishing. After this polish regime, the surface roughness of the silica is a few nanometres rms, as measured on a Wyko NT110 white light interferometer [131].

The last step prior to imaging the samples in the SEM is to deposit a thin layer of gold on the surface with an Emitech K950X thermal evaporator [156]. This is necessary in order to make the silica samples more conductive and reduce charging from the electron beam during SEM imaging, which can greatly reduce the measurement accuracy if not addressed. The polished samples are placed in the bottom of the evaporator and a 2 mm diameter ball of pure gold wire (Sigma-Aldrich 310980 [157]) is loaded into a tungsten basket. After pumping down to 1×10^{-4} mbar, the current through the basket is increased to 18 A for 12 seconds to evaporate the gold, before turning it down to 0 A.

Even with a thin layer of gold on the surface, charging of the fused silica and hydroxide catalysis bonds is a problem when the electron beam is focussed down onto the surface. This makes it difficult in general to get accurate measurements of the bond thickness. Using the SEM's Everhart-Thornley detector [158] mode of measuring the secondary electrons gives images with the best contrast. However, obtaining an accurate measurement requires careful technique. The general procedure is to first scribe small fiducial lines through the gold layer with a tweezer tip across the bond to serve as location markers while in the SEM, and also to uncover some of the bond. The samples are then mounted on double-sided copper tape, electrically grounding the samples to the SEM mount, on a stage inside the SEM as shown on the left side of Figure 5.8.

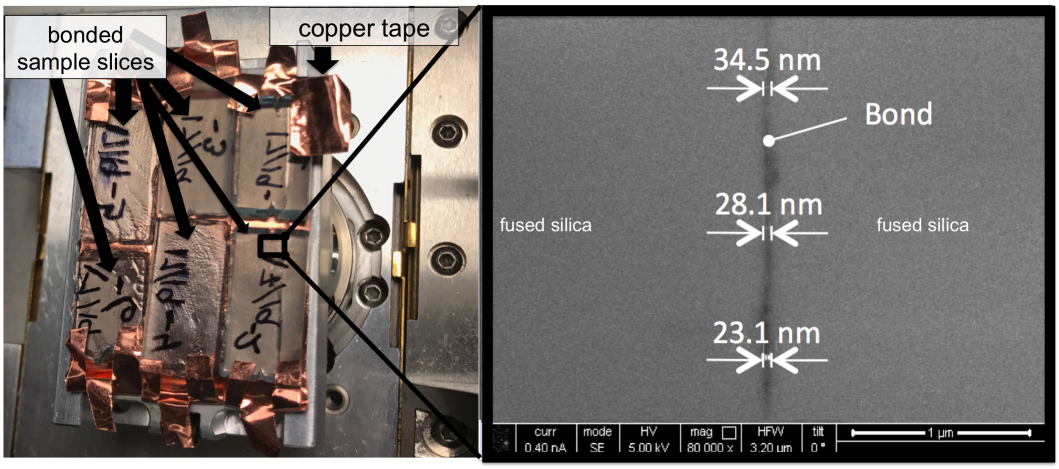

Figure 5.8: On the left, sections of a bonded fused silica sample prepared for measurement by cutting across the bond as in Figure 5.7, and secured with copper tape to prevent charging. The bond is very thin so is not visible by eye. On the right an SEM image taken of the bond in one of the sections at 80000x magnification.

A TEM sample consisting of a silica substrate with a bilayer coating of amorphous silicon and SiO2 was used as a calibration sample in the SEM. This sample has known layer thicknesses of 112.9 nm ±1.6 nm of aSi and 300.9 nm ±2.3 nm of SiO2. Verifying these layer thicknesses in the SEM at the same time as the bonded samples were measured was done as a reference measurement, shown in Figure 5.9.

After pumping down the SEM with the samples inside to below 1×10^{-5} bar of vacuum, the

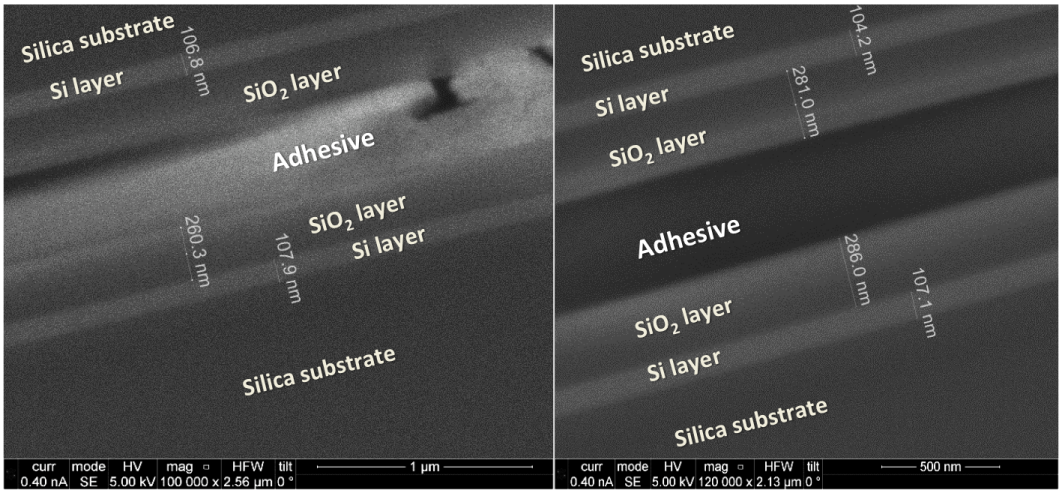

Figure 5.9: SEM images of the calibration sample at 100,000x and 120,000x magnification showing the silicon and SiO2 layers. Adhesive included to strengthen the sample for thinning it for TEM management.

fiducial closest to one edge of the first sample was focussed on as in Figure 5.10. The bond inside the fiducial is not covered by gold and thus will give the most accurate measurement if the image can be taken before the sample starts to charge, as in the right of Figure 5.10.

Ideally, a bond thickness measurement is taken inside each fiducial scribed on the sample before moving on to the next one. Ideal measurements with a minimum of charging look like the right side of Figure 5.8.

A magnification of 50,000x to 120,000x must be used to take a reasonably accurate measure-

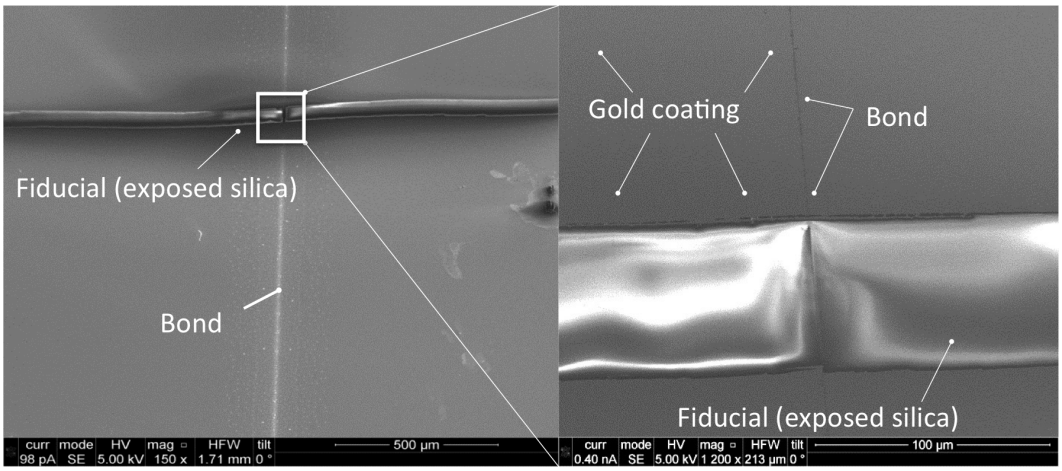

Figure 5.10: SEM images of a bonded sample. On the left an image of the bond, with a zoom-in of fiducial line scribed in gold is on the right, with the exposed bond. Minimal surface charging.

ment of the nanometre thick bonds. There are a few different ways an image can be taken, depending on how much charging the sample exhibits. Ideally, a full resolution image of the bond inside one of the scribed fiducial lines is taken. This takes around 10 seconds to capture, during which time the surface charging is increasing. As a result, these images can end up with the bond line looking distorted in places. However the overall bond thickness seems to still be accurate. Another option is to take a faster and lower resolution image, which can be used if the image distorts too much during a full resolution picture. A third approach is to take a measurement of the bond where it is still coated with the gold. This approach is not recommended as the gold layer is being measured as well as the bond, meaning the bond thickness can be greatly overestimated and inaccurate when compared to measurements made inside a scribed fiducial line. Due to charging effects and poor contrast, measurement accuracy was restricted overall to approximately ± 20 nm.

Measurements along each slice were taken, and the results were combined and linearly interpolated to produce a map of the hydroxide catalysis bond thickness across each sample, as in Figure 5.11. The surface plot maps were used to calculate an average bond thickness. The standard deviation on the thickness was calculated for each location where the transducer contacted the sample during ultrasonic measurements. All values are shown in Table 5.2. The values in Table 5.2 were used in the Bayesian analysis model and the pulse amplitude analysis model to extract the Young's modulus of a bond between fused silica substrates, as explained in Section 5.8.1 and Section 5.8.2.

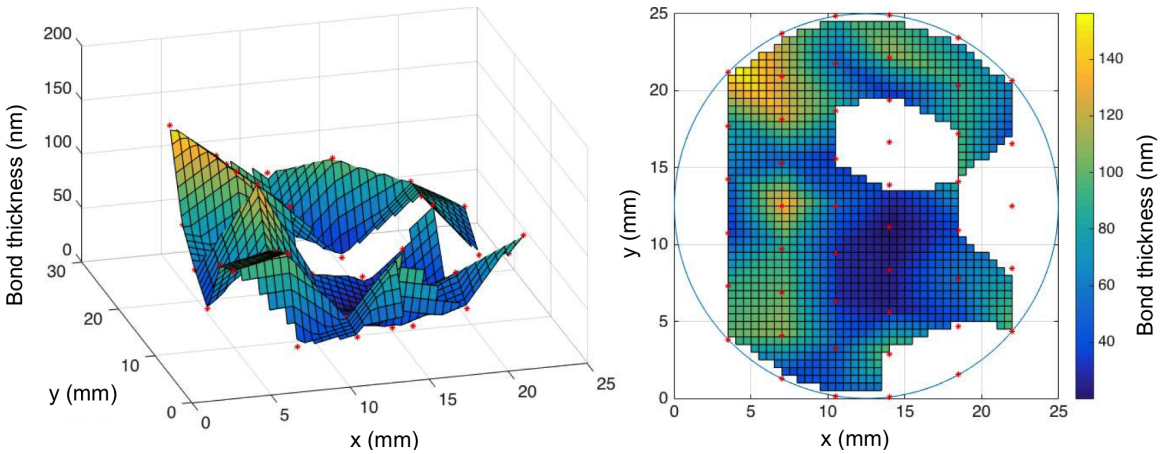

Figure 5.11: Surface plots of the bond thickness measured across a bonded fused silica sample

Sample	Transducer Position	Average L_{bond} (nm)	Standard deviation (nm)
1	top	57	33
1	bottom	40	28
1	center	32	10
1	left	75	38
1	right	71	23
2	center	31	7
3	center	36	9
4	center	50	30
5	center	57	12
6	center	96	42

Table 5.2: Bonded fused silica samples average bond thickness with error

5.5 Measurements of hydroxide catalysis bonded sapphire

Ultrasonic measurements of a sodium silicate hydroxide catalysis bonded sapphire sample are shown in Figure 5.12. There is a greater impedance mismatch between hydroxide catalysis bonds and sapphire than there is between fused silica and hydroxide catalysis bonds. Due to the higher percentage of the incoming acoustic pulse reflecting off the bond, there is a higher signal-to-noise ratio for measurements of hydroxide catalysis bonded sapphire than for bonded silica. This allows the use of the simpler pulse amplitude analysis method approach explained in Section 5.7.1 for the hydroxide catalysis bonded sapphire data. An example of an acoustic pulse measurement of bonded sapphire is shown in Figure 5.13. One 10 mm long, 50 mm diameter sapphire sample bonded with sodium silicate solution was measured. The noise background is different for bonded sapphire than for bonded silica, with some repeated high frequency pulses visible in the data in Figure 5.13. The data was analysed with the pulse amplitude analysis model to extract the bond Young's modulus,

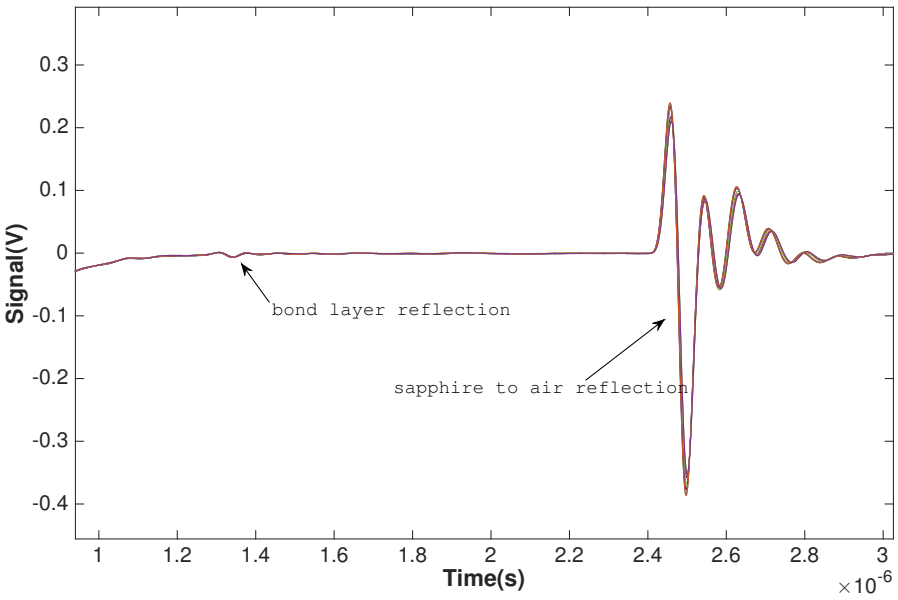

Figure 5.12: Acoustic pulse reflections from a 1:6 sodium silicate 10 mm long hydroxide catalysis bonded sapphire sample, 10 datasets.

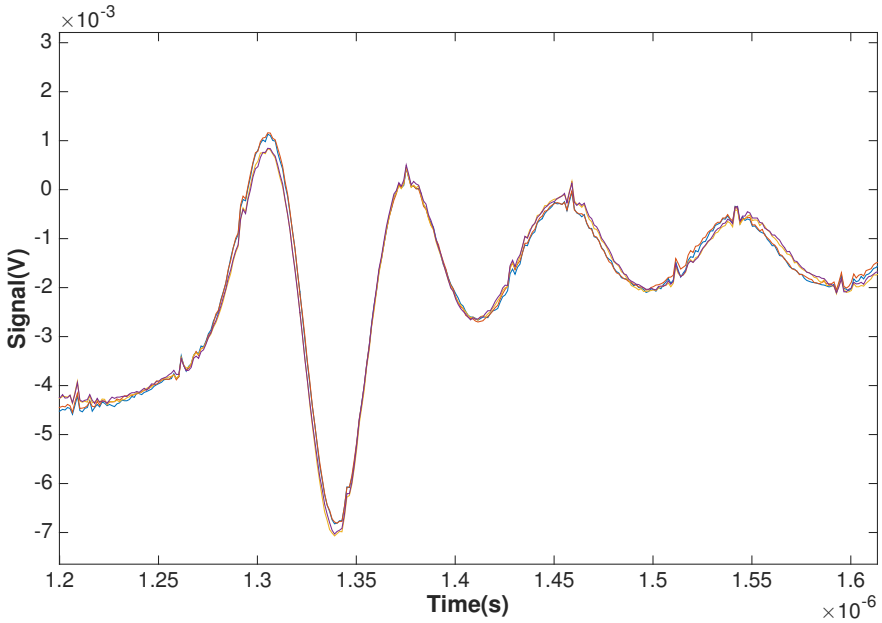

Figure 5.13: Zoom in of an acoustic pulse reflected from a 10 mm long, 50 mm diameter sapphire sample bonded with sodium silicate solution.

the results are in Section 5.8.1.

5.6 Measurements of indium bonded fused silica

Ultrasonic measurements were also performed on fused silica discs bonded with indium layers of different thicknesses and deposition types. In this case, the impedance mismatch between fused silica and indium is even larger than between sapphire and hydroxide catalysis bonds. The signal-to-noise ratio for measurements of indium bonded silica is thus also very high, and the simpler pulse amplitude analysis method is used.

The substrates of the first sample were prepared by cleaning two fused silica discs with solvents in an ultrasonic bath, 5 minutes each of acetone, isopropanol, and methanol. The indium layer consisted of a 50 μm thick indium foil which was etched with dilute hydrochloric acid to remove the indium oxide. It was also rinsed with DI water to quench the acid, followed by methanol to get rid of the water and finally dried with clean nitrogen gas and cold welded between the two silica substrates. The thickness of this foil was measured after etching to have a thickness in this case of 49.19 ± 0.05 μm with an Energy Dispersive X-ray Fluorescence Spectrometer (EDXRF) [159]. The acoustic pulse reflections of this sample's indium-silica and silica-air interfaces are shown in Figure 5.14.

Only the amplitude of the reflection from this indium bond layer and Equation 5.3 was used to extract the bond's Young modulus, as the indium layers of thickness 41.0 ± 0.5 μm and 50 μm were too thick to use the R_{bond} expression which depends on the small angle approximation, Equation 5.8. Using Equation 5.3, the measured thickness value and the measured ultrasonic reflection, the Young's modulus of this sample's indium layer was calculated to be approximately 1 GPa.

The known value of bulk indium is 10-13 GPa [105], making the measured value of 1 GPa far too low to come from only bulk indium. Unfortunately, both non-bond surfaces of the fused silica substrates were ground glass, which made it difficult to see characteristics of the bond layer in between them. However, careful re-inspection of the bonded sample revealed that while it did not have any large air bubbles trapped in the indium layer, it did have small air bubbles all across the indium layer. The amplitude of the reflected pulse is impacted significantly by air bubbles in the indium layer. While the amount of air in the layer is not known the error can be estimated by assuming that the majority of the pulse was reflected from a silica-to-air interface in the worst case scenario. This would set a lower bound of 0 GPa.

Two more indium bonded fused silica samples were produced, trying for an air bubble free layer. These were made by thermally depositing a thin layer of indium directly to the fused silica substrates in an evaporator [156], with the aim of stopping air bubbles from being trapped between the substrates and the indium. Four substrates were solvent cleaned in an ultrasonic bath, 5 minutes each of acetone, isopropanol, and methanol following the same procedure as was used to make the first indium bonded sample. They were then dried with

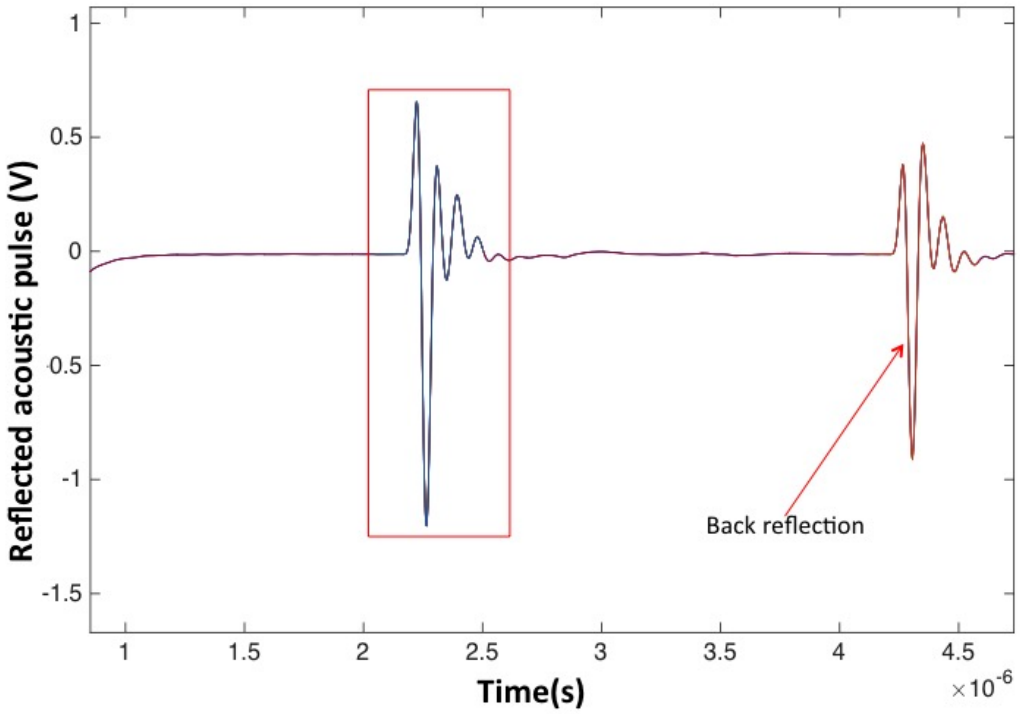

Figure 5.14: Reflected acoustic signal from 50 µm thick indium foil cold welded between 6 mm thick silica discs

clean nitrogen gas and placed bond side up in the evaporator. An indium layer 350-400 nm thick, as measured via EDXRF [159], was thermally deposited onto them under vacuum. The coated samples were etched with dilute hydrochloric acid to remove any indium oxide that had grown on the deposited coating. They were also rinsed with RO water to quench the acid, followed by methanol to get rid of the water and finally dried with clean nitrogen gas.

Two of the four samples were cold welded together immediately after drying with nitrogen gas, resulting in an final indium layer of 750 ± 50 nm. An additional 50 µm indium foil was acid etched along with the last two coated fused silica samples, it was cold welded between the two remaining samples directly after drying. The etched foil was measured to have a thickness of 40.5 ± 0.5 µm with the EDXRF, for a total indium layer thickness of 41.0 ± 0.5 µm.

After the two samples were cold welded together an additional step of heating them under pressure was done to drive the air out of the bond interfaces. This was done by placing the samples on a hotplate, then placing lead weights on them and heating the hotplate up to 160 °C for 1 hour. The weights corresponded to 1 MPa of pressure.

Ultrasonic measurements were then taken on both indium bonded fused silica samples, as well as the fused silica reference sample. The reflected pulses from the thinner indium layer, the thermally evaporated film only, are shown in Figure 5.15. Since the indium layer reflects

a much higher percentage of the incoming ultrasonic pulse, the reflection of the silica-to-air interface from the bonded sample cannot be used as the input pulse, as too much of it was already reflected by the indium layer. The silica-to-air reflected pulse from the un-bonded fused silica cylinder is used instead, and plotted in green in Figure 5.15 and yellow in Figure 5.16 on top of the bonded sample data for reference. The ultrasonic measurements of the

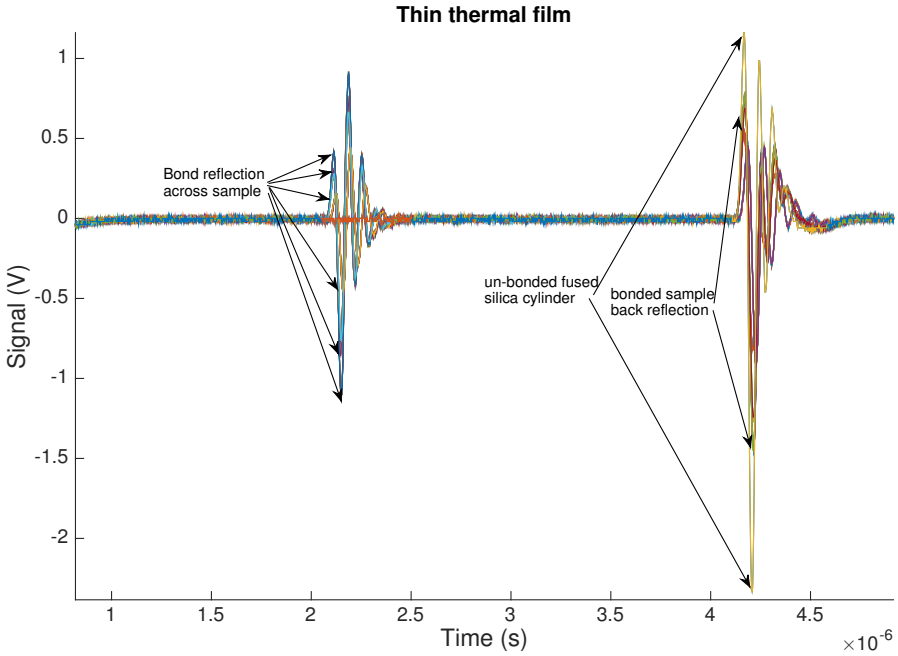

Figure 5.15: Ultrasonic pulses reflected from a 800 nm thick indium layer between 6 mm thick silica discs

third indium bonded sample, made with both indium foil and thermally evaporated indium coating, is shown in Figure 5.16 Data from both new samples were analysed with a similar Matlab code based on the reflection coefficient equation as the first indium bonded sample. This time the small angle approximation that allowed us to solve for E_2 is not possible, as the requirements of $\sin(\theta) \approx 0.244$ and $\cos(\theta) \approx 0.644$ are not satisfied for indium layers of $< 5\mu m$, and so the full equation for R_{bond} in Equation 5.3 is used to quantify the measured value for E_2. This approach does not take into account the many sources of experimental noise, due to the fact that the largest sources of error, such as such how many air bubbles are in the indium layer, are unknown. Thus the error on these numbers is unknown and most likely quite high. For the first bonded sample the Young's modulus of the thin thermally evaporated indium layer was calculated to be 0.8 GPa. For the second bonded sample, with two thermally evaporated layers and a 40 µm indium foil in between, the Young's modulus of was measured to be 5.9 GPa. Remembering that the Young's modulus of bulk indium is 10-13 GPa, these measured values were too low to be from bulk indium only.

A few different things could be contributing to bringing down the Young's modulus values. Still having a contribution from air bubbles throughout the bond will drastically increase

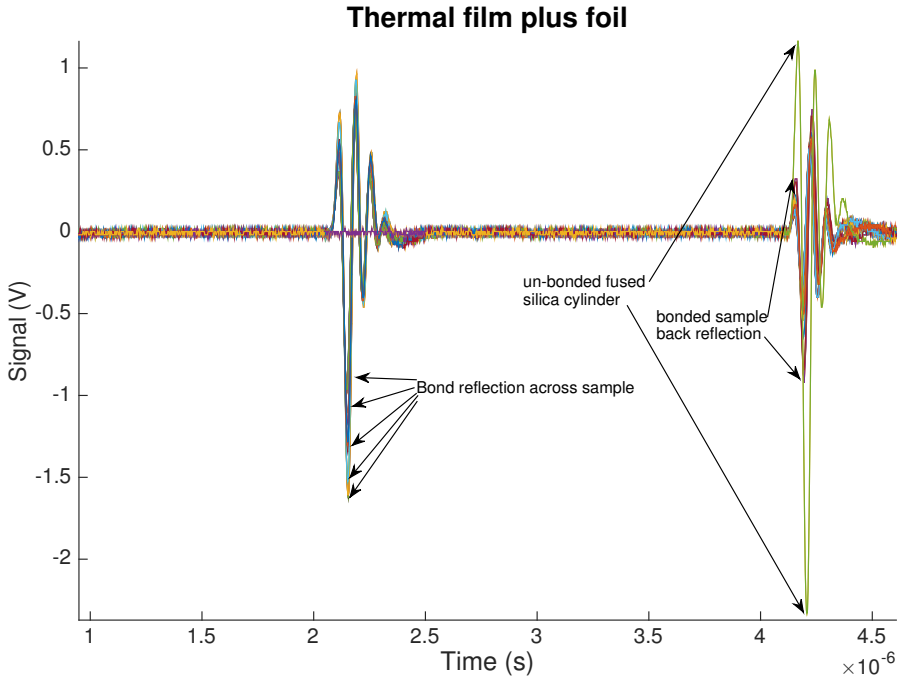

Figure 5.16: Ultrasonic pulses reflected from a41 µm thick thermally deposited indium between 6 mm thick silica discs

the amplitude of the reflected pulse, and thus drastically decrease the Young's modulus calculated from this artificially large reflected signal. If there were no air bubbles in these two bonded samples then the amplitude of the reflected pulse would be constant over the whole sample. This is not the case however. The amplitude of the silica-to-air reflection of the fused silica reference sample ranged from $1.88 - 1.91 V_{pp}$ with an average and standard error of $1.888 \pm 0.005 V_{pp}$ measured at different locations across the surface. For comparison the amplitude of the reflected signal from the thin indium layer varied from 0.88 to 2.01 V_{pp} across the sample, with an average of $1.4 V_{pp}$ and the thermal film plus foil went from 1.67 to 2.57 V_{pp} across the sample with an average of $2.1 V_{pp}$. The differences in amplitude of the reflected signal from the bond interface was dependent on transducer position on both samples. The difference between sample positions the reflected signal amplitudes are pointed out in Figure 5.15 and Figure 5.16.

Another main contributor is that the thin layer of indium that was deposited via thermal evaporation does not necessarily have the same material properties as bulk indium does. Viewed under a microscope the indium foil and the deposited indium layer have visibly different appearances, seen in Figure 5.17 the foil has a smooth and highly reflective surface while the thin film has a non-reflective and porous appearance. Material properties such as density and Young's modulus of thin thermally deposited films are different from their bulk material values. For example the Young's modulus of bulk chromium is 245-285 GPa and thermally deposited thin film chromium is 140 GPa [161]. The visual inspection of the

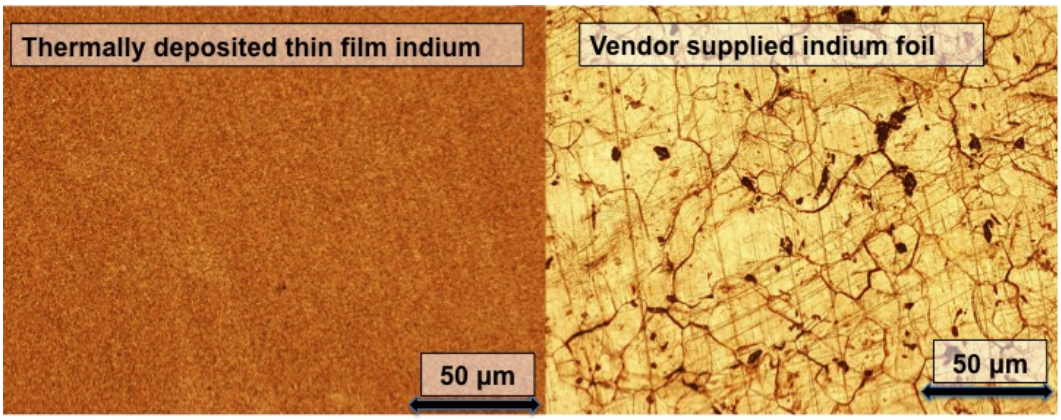

Figure 5.17: Thermally deposited thin film indium on the left, 50 µm foil on the right. Both imaged with a Nomarski microscope [160].

deposited layer compared with the foil, along with the different deposition types and the low value of measured Young's modulus suggests that the thermally deposited thin indium film do have different material properties. The density of the thin film may also be lower than of bulk indium, which could account for the porous appearance.

5.7 Extracting the Young's modulus of hydroxide catalysis bonds

5.7.1 Extracting the Young's modulus of bonds via pulse amplitude analysis

The Young's modulus of the bonds measured in this chapter can be extracted by analysing the amplitude of the acoustic pulses reflected from the bond interface and the silica-to-air interface. This method is explained in this section. Starting with the approximate expression for R_{bond} in Equation 5.7, re-iterated here as Equation 5.9,

$$R_{\text{bond}} = i\left[\sqrt{\frac{E_2\rho_2}{E_1\rho_1}} - \sqrt{\frac{E_1\rho_1}{E_2\rho_2}}\right]\sqrt{\frac{\rho_2}{E_2}}\pi f L \tag{5.9}$$

where it is assumed that the Young's modulus of the bond, E_2, will be some fraction of the Young's modulus of fused silica, E_1 =72 GPa, and write $E_2 = \alpha E_1$ where α is a scalar value. Re-arranging to solve for α can be expressed as

$$\alpha^2\left[\left(\frac{\rho_2}{\rho_1}\right) - \frac{R_{\text{bond}}^2 E_1}{(\pi f L)^2\rho_2}\right] - 2\alpha + \left(\frac{\rho_1}{\rho_2}\right) = 0 \tag{5.10}$$

and solving this quadratic for α gives

$$\alpha = \frac{1 \pm \sqrt{\frac{R_{\text{bond}}^2 E_1 \rho_1}{(fL\pi)^2 \rho_2^2}}}{(\frac{\rho_2}{\rho_1}) - \frac{R_{\text{bond}}^2 E_1}{(fL\pi)^2 \rho_2}} \tag{5.11}$$

Finally, given $E_2 = \alpha \cdot E_1$, the Young's modulus of a hydroxide catalysis bond can be expressed in terms of known constants $\pi, f, \rho_1, \rho_2, E_1$ and measured values of reflection coefficient R_{bond} and bond thickness L.

$$E_2 = E_1 \cdot \frac{1 \pm \sqrt{\frac{R_{\text{bond}}^2 E_1 \rho_1}{(fL\pi)^2 \rho_2^2}}}{(\frac{\rho_2}{\rho_1}) - \frac{R_{\text{bond}}^2 E_1}{(fL\pi)^2 \rho_2}} \tag{5.12}$$

All three types of bonded samples (hydroxide catalysis bonded fused silica, hydroxide catalysis bonded sapphire, and indium bonded fused silica) measured in this study were analysed with this approach. Due to the different levels of impedance mismatch in the three kinds of samples, the SNR of the bond signal in each case was different. In the cases of hydroxide catalysis bonded sapphire and indium bonded fused silica, the bond signal-to-noise ratio was high enough that only the pulse amplitude analysis method outlined in this section was used. For hydroxide catalysis bonded fused silica however, the impedance mismatch between silica and silicate bond is much smaller, which also reduced the bond signal-to-noise ratio. In this case, the results from using the pulse amplitude analysis were not very accurate because of the low SNR, and so a Bayesian analysis model was also developed to analyse the bonded fused silica samples. The Bayesian analysis model is explained in section 5.7.2, and the results of both analysis approaches are compared in section 5.8.2.

5.7.2 Extracting the bond Young's modulus via Bayesian analysis

A Bayesian analysis of the hydroxide catalysis bonded fused silica data was performed in which the signal model is a function of R_{bond}, described by Equation 5.8, with a time offset Δt representing the unknown start time of the bond signal with reference to t_0, an arbitrarily defined time near the centre of the timeseries where the bond signal is expected to be situated.

The noise model contains two main components. The first component is low frequency noise which was intrinsic to the sample and the sample location being analysed. The same realisation of this low frequency noise is found in repeated measurements of the same sample and attributed to reflections from the sample boundaries. This component has a red spectrum, i.e. higher power at low frequencies.

The second noise component has an approximately white spectrum, i.e. uniform power in frequency and dominates the former noise component at high frequency. It is assumed each measurement contains an independent noise realisation for this component and this source is attributed to electronics noise. These noise component Power Spectral Densities (PSDs) were estimated from segments of data taken before and after the bond signal and averaged over all datasets taken at the same sample and sample position. The blue and green regions before and after the bond signal in Figure 5.18 indicate the data segments where the noise components are estimated from, with the combined PSD shown in white. The reflected bond signal, $\boldsymbol{R}$, is found in the red region.

The PSD components as a function of frequency are plotted in Figure 5.19. By averaging

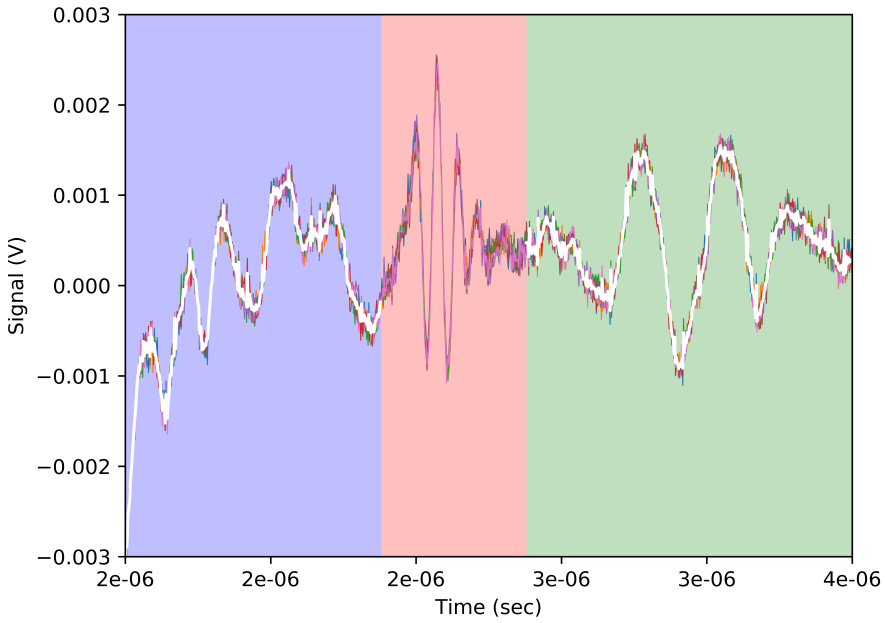

Figure 5.18: Reflection signal of a bond between fused silica substrates, as a function of time. The different coloured regions indicate the location of the noise components in blue and green on the outsides, or of the bond signal in the middle in red.

the timeseries data the high frequency noise is subdued and an estimate of the low frequency noise PSD can be made, $\boldsymbol{P}^{\mathrm{l}}$. Subtracting the averaged timeseries from each dataset leaves the white noise components from which the white noise PSD, $\boldsymbol{P}^{\mathrm{w}}$ can be estimated. Since the effect of the low-frequency noise source is to introduce a repeatable low-frequency signal, this is modelled as an additional signal component with corresponding unknown parameters. The specific realisation of this noise within the bond signal is not known a-priori so this noise signal is parameterised in the frequency domain assuming that each discrete frequency bin has an unknown phase ϕ_j and a known amplitude governed by the estimated low frequency PSD. Only the first 15 frequency bins are used since this is the region over which the low frequency noise power exceeds that of the white noise. These parameters

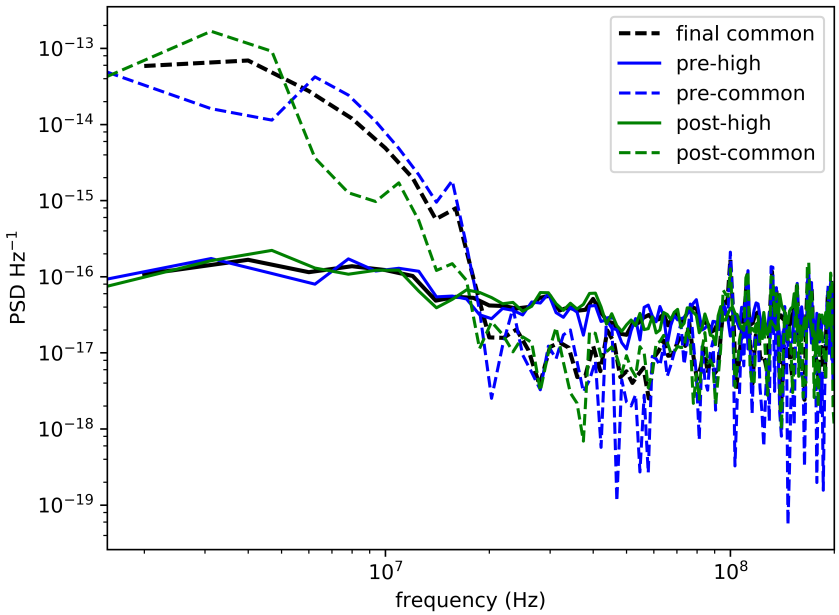

Figure 5.19: Example of PSD estimated from measurements taken on one of the fused silica samples, where pre and post indicate the region before or after the bond signal. High indicates high frequency components, common indicates the frequency components that are common to all measurements

are included in a Markov chain Monte Carlo (MCMC) analysis [162] and marginalised over, accounting for the common low-frequency noise present in multiple measurements of the same sample.

The signal model can be represented in the frequency domain by

$$\tilde{s}(f; R, \Delta t, \vec{\phi}) = \tilde{x} R i f e^{2\pi i f \Delta t} + \sum_{k=1}^{15} \frac{1}{2} \sqrt{N dt P_k^1} e^{i\phi_k} \tag{5.13}$$

where $Rif = R_{\text{bond}}$ from Equation 5.8, the discrete Fourier transform of the input pulse timeseries data is defined by $\tilde{x}$, the frequency is defined as f, time offset Δt, the timeseries sampling interval dt, and the number of samples in the input signal timeseries is N.

A uniform prior probability distribution for the parameters t_0, R_{bond}, and noise phases $\vec{\phi}$ is used with the following limits. The start time t_0 ranges between 0 and 0.5 µs, and is long enough to fully encompass the reflected pulse signal. The noise phase ranges from 0 to 2π, and R_{bond} ranges between 0 and an amplitude corresponding to the maximum allowed E_2 value. Since the bond is a silicate material it should not exceed the Young's modulus of fused silica, 72 GPa. The bond thicknesses that were measured in the SEM and the error associated with that method of imaging are interpreted as a Gaussian prior for L in which the measured value and the uncertainties represent the mean and standard deviation of the Gaussian respectively.

The likelihood function, based on a Gaussian noise model, is defined as

$$p(\tilde{b}|R,\Delta t,\vec{\phi}) = \prod_{m}\prod_{k=0}^{N-1}\frac{2}{\pi N dt P_{mk}^{w}}\exp\left(-\frac{|\tilde{b}_{mk}-\tilde{s}_{mk}|^2}{N dt P_{mk}^{w}}\right) \tag{5.14}$$

where m indices over sets of measurements for which the sample and the sample location were the same. The quantity $\tilde{b}$ is the Fourier transform of the measured reflected bond signal.

In Figure 5.20 the strength of the bond signal against the noise background can be seen in the frequency domain. The Sonatest transducer, with a centre frequency of 12 MHz noted as f_{pulse} had a perfect combination of frequency, damping, and gain properties to give a bump in SNR in the tens of MHz, seen in Figure 5.20. A time-domain example of the reflected bond signal, and the corresponding signal model and noise components are shown in Fig. 5.21. In both Figures 5.20 and 5.21 the first signal model term from Equation 5.13 is plotted in dark blue, shown with the common signal, the second term in Equation 4.11. in cyan, and combined to become the signal plus noise model, $\tilde{s}$ in black. The measured data, $\tilde{b}$ is shown here in red. The residuals in Figure 5.21 are shown in dark green. Each curve is a set of curves drawn from the posterior distribution on the unknown parameters $R, dt, \vec{\phi}$. The sum of the model and low frequency common noise component, s, matches the measured reflection signal with residuals consistent with those expected from the white noise PSD.

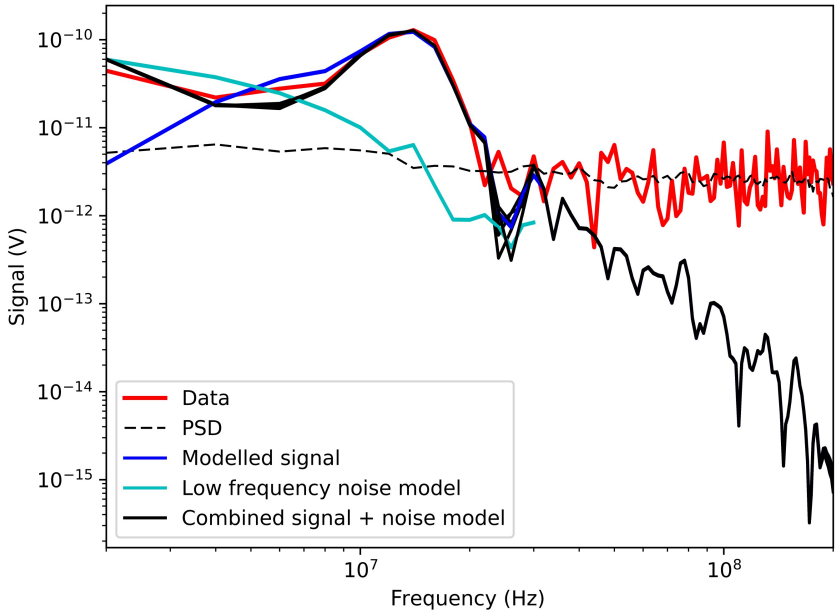

Figure 5.20: Signal data, noise background, modelled signal and combined signal model vs frequency of bonded fused silica sample data

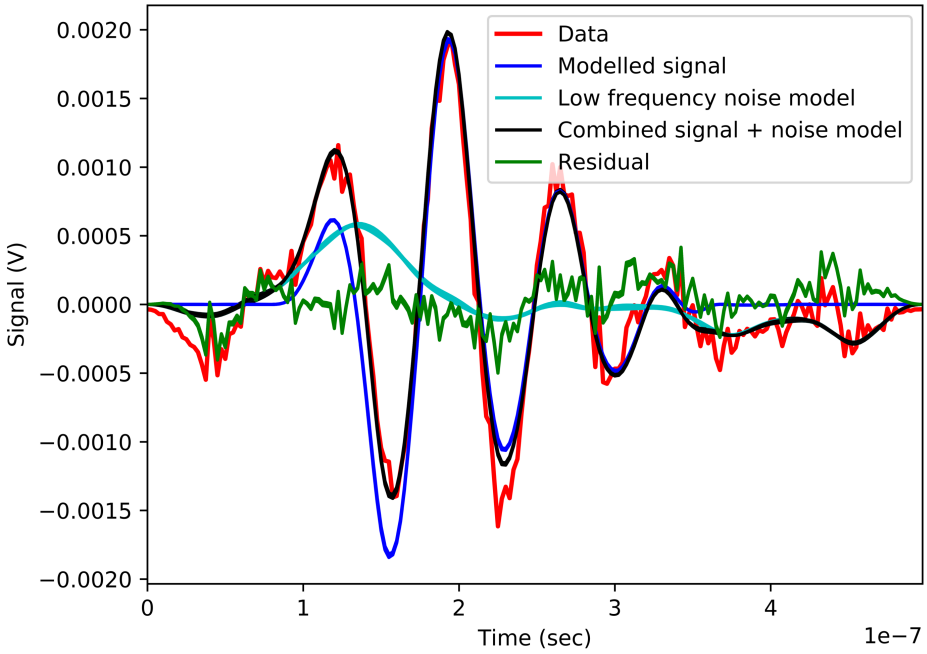

Figure 5.21: Reflected bond signal, modelled signal, noise components, combined signal model and residuals vs time of bonded fused silica sample data

An MCMC analysis is performed to obtain samples from the posterior probability distribution on the quantity R, combined with the knowledge of the bond thickness L from the SEM measurements, to generate the posterior on the Young's modulus of hydroxide catalysis bonds, E_2. This is achieved using

$$p(E_2|\tilde{b}) \propto \sum_{j}^{n} p(L = L(E_2, R_j)) \left| \frac{dL}{dE_2} \right| \tag{5.15}$$

where the sum is over posterior R samples and the derivative is the Jacobian required to transform the integral over bond thickness L into one over E_2. This derivative and the function $L(E_2, R)$ are obtained via Equation 5.8. The posterior for each measured sample is then combined and compared, as shown in the bonded fused silica results section 5.8.2.

5.8 Results and discussion

5.8.1 Pulse amplitude analysis results

The pulse amplitude based analysis described in section 5.7.1 was used to extract the Young's modulus of bonds between sapphire substrates. This analysis has a higher error associated with it when compared to the bonded fused silica data in Section 5.8.2 due to a higher and more unpredictable noise background and a larger error associated with the bond thickness

value, L. The value for L used here was not from a direct SEM measurement, rather it was based on the global peak-to-valley flatness measurements of the two sapphire substrates prior to bonding. In this case they were measured to be 106 ± 5 nm and 75 ± 55 nm. The bond thickness is thus assumed to be between the average global flatness value, 90.5 nm and a maximum value based on the added flatnesses of both substrates, 181 nm. A value of 15.3 ± 5.2 GPa was calculated for the hydroxide catalysis bonded sapphire sample measured here.

A Young's modulus value of 21.5 ± 6.6 GPa was found for the hydroxide catalysis bonds between fused silica samples analysed with the pulse amplitude approach.

Comparing the calculated Young's modulus from measurements of the thin film, 0.8 GPa, to the thin film plus foil layer, 5.9 GPa, is especially telling. The vendor supplied indium foil would be expected to behave as the bulk material, with a Young's modulus of 10 GPa. A layer consisting of the thin thermally deposited indium with a very low Young's modulus, 0.8 GPa, and the bulk indium foil would be expected to be higher than the value of the thin film on its own but not as high as bulk indium.

In this case the measured value of 5.9 GPa falls into that realistic range. Overestimating the density of the thin film would also impact this calculation, as it is assumed in the calculation that the films' density is that of bulk indium. Measuring the material properties such as the density and Young's modulus of the thermally evaporated indium layers via nano-indentation for comparison to the values found in this chapter is suggested for future studies.

5.8.2 Bayesian analysis results for bonded fused silica

The posteriors of measurements made where the transducer was positioned in the centre of the sample is shown in Figure 5.22 where the Young's modulus calculated from this combined set was $17.3 \pm^{2.3}_{2.5}$ GPa.

The posteriors of measurements made where the transducer was positioned in different positions around the same sample is shown in Figure 5.23 where the Young's modulus calculated from this combined set was $16.8 \pm^{3.8}_{3.2}$ GPa.

Interestingly, the posteriors for measurements made where the transducer was positioned in the very centre of the samples as in Figure 5.22 were narrower than those made on the same sample but with different transducer positions as in Figure 5.23, suggesting that the closer the transducer was to the edge of the bonded sample the more edge effects were seen.

Finally a combined posterior on the Young's modulus of sodium silicate hydroxide catalysis bonds, E_2, is shown for all measurements in Figure 5.24. These posteriors are statistically independent and therefore their product is used to obtain an improved result. All input posteriors are consistent and the final posterior has support from all inputs implying neg-

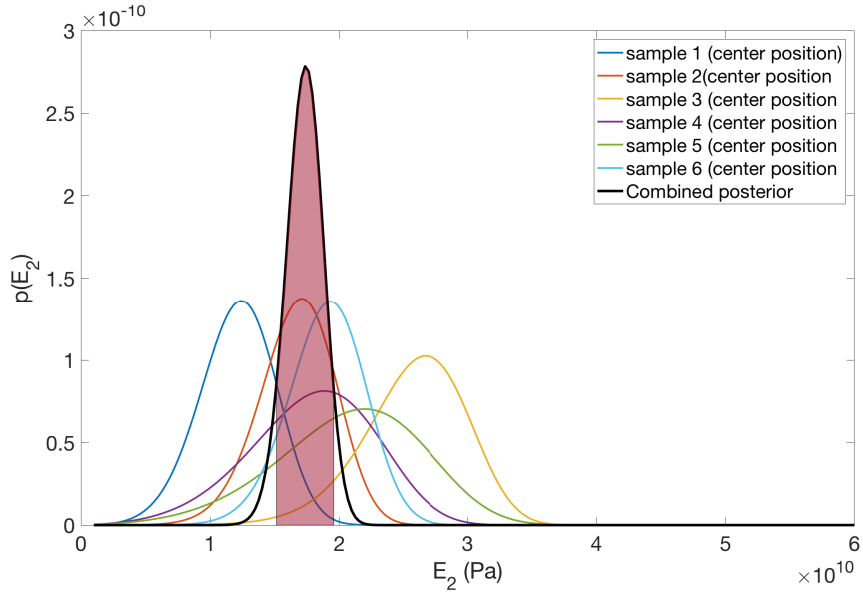

Figure 5.22: Individual E_2 posteriors of each measured fused silica sample, where the transducer was in the centre of the sample. The final combined posterior is shown in black and a 90% confidence level is shown in the light red shaded region.

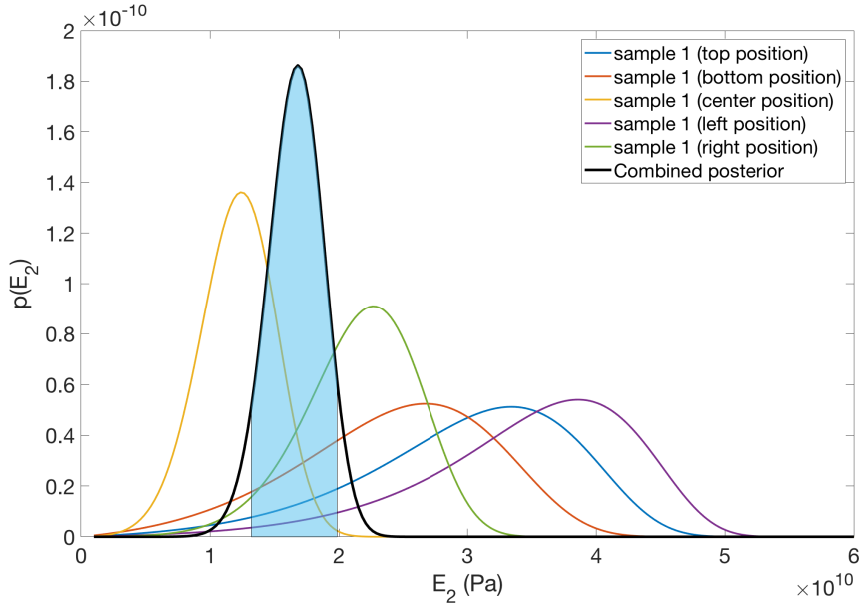

Figure 5.23: Individual E_2 posteriors of one measured fused silica sample, where the transducer was placed in five different positions. The combined posterior is shown in black and a 90% confidence level is shown in the light blue shaded region.

ligible systematic effects.

A best estimate value with a 90% confidence range of $18.5 \pm^{2.0}_{2.3}$ GPa is thus obtained for the Young's modulus of sodium silicate hydroxide catalysis bonds via Bayesian analysis. This value also agrees with the Young's modulus for the same fused silica samples analysed with the pulse amplitude approach, which was found to be 21.5 ± 6.6 GPa. The Young's

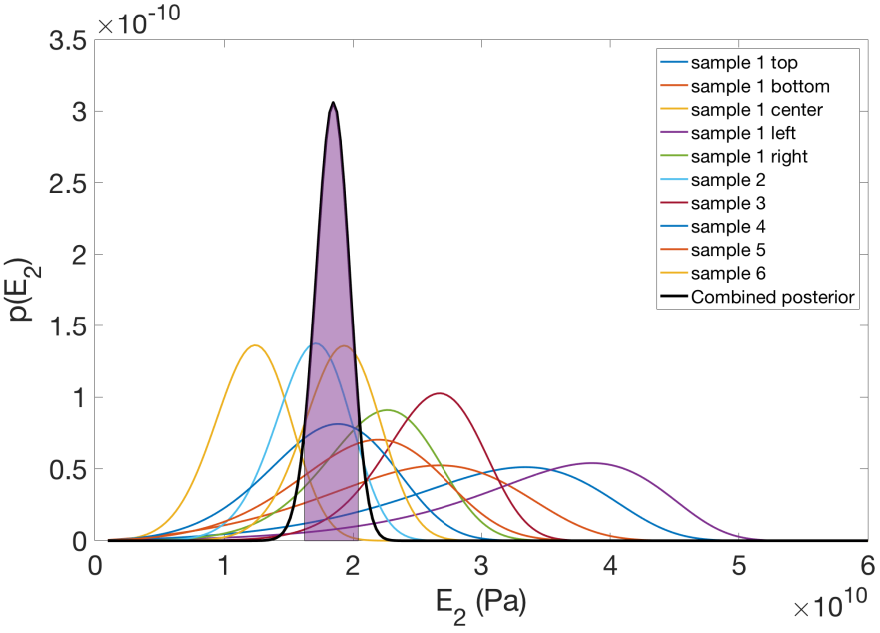

Figure 5.24: Individual E_2 posteriors of all measured fused silica samples. The final combined posterior is shown in black and a 90% confidence level is shown in the light purple shaded region.

modulus calculated here is used in Chapter 6 to evaluate the contribution to thermal noise from hydroxide catalysis bonds in finite element ANSYS models of room temperature and cryogenic detector bonded test masses.

5.9 Conclusions

A better understanding of the Young's modulus of hydroxide catalysis bonds used in GW detectors has been obtained in this study, using a non-destructive method of acoustic pulse measurement. A sophisticated Bayesian analysis model was also developed for the hydroxide catalysis bonded fused silica. The ultrasonic measurements taken on hydroxide catalysis bonded fused silica and the Bayesian analysis of them presented in this chapter were combined with FE models of a bonded aLIGO A+ upgrade test mass (explained in Section 6.7), and published as *Measurements of the Young's modulus of hydroxide catalysis bonds, and the effect on thermal noise in ground based gravitational wave detectors* in [163]. The results published in this paper are expanded and explained in greater detail in this chapter, for improved understanding of the methods involved and to offer a comparison of the bonded sapphire results with the bonded fused silica results.

Three different types of samples in total were measured in this study, hydroxide catalysis bonded fused silica, hydroxide catalysis bonded sapphire, and indium bonded fused silica. Low Young's modulus values of the indium layers with a high margin of error were calculated from these measurements due to the addition of the air and unknown thin film

properties, giving Young's modulus values of 0.8 GPa for the thin thermally evaporated film, and 5.9 GPa for a thin film plus foil layer, compared to an expected 10-13 GPa for bulk indium. The results from the pulse amplitude analysis approach found a Young's modulus value of 15.3 ± 5.2 GPa for hydroxide catalysis bonded sapphire and 21.5 ± 6.6 GPa for bonded fused silica. The larger error bars found with the pulse amplitude analysis approach are due to the complicated noise background inherent in the measurements. However, both values agree with the value found for hydroxide catalysis bonded fused silica via Bayesian analysis, which was a best estimate value of $18.5\pm^{2.0}_{2.3}$ GPa, with a 90% confidence range. All results found in this chapter are collated in Table 5.3.

Bond type	Known in the literature	Measured result
Thin film indium	none	0.8
Thin film plus foil indium	none	5.9
Bulk indium	10-13	none
hydroxide catalysis bonded fused silica	7.9	21.5 ± 6.6
Bayesian analysis of bonded fused silica	7.9	$18.5^{+2}_{-2.3}$
hydroxide catalysis bonded sapphire	none	15.3 ± 5.2

Table 5.3: Results of Young's modulus values measured in this chapter, in comparison with previously known values, where applicable. All results in units of GPa.

Chapter 6

The Young's modulus of hydroxide catalysis bonds and the thermal noise of bonded test masses

6.1 Introduction

Contributions to detector thermal noise levels come from many parts of the suspension system, as explained in Chapter 1. The faces of the test masses are the most sensitive to thermal noise contributions, as motion of this optic directly impacts the measured phase of laser light between the arms. Thus, the closer a suspension element is to this face the more stringent its noise requirement is. The contribution made by the hydroxide catalysis bonds, that join the suspension ears to the test masses, will be the focus here.

First, the calculation of the mechanical loss of hydroxide catalysis bonds will be discussed. Then, the role that the bond's Young's modulus has in thermal noise calculations is addressed, using an analytical example of a bonded rod. Finally, the mechanical loss of bonds is combined with realistic models of bonded test masses, to calculate the thermal noise contributions of bonds in several bonded test mass geometries.

Previously, the thermal noise contribution from bonds on a test mass mirror had been calculated using a Young's modulus value based on a single point of data, 7.9 GPa [124]. In this chapter ANSYS models are used to calculate the thermal noise of bonded test masses, using the new bond Young's modulus value of $18.5\pm^{2.0}_{2.3}$ GPa which was obtained in experiments described in Chapter 5. All models in this chapter are evaluated using a sodium silicate bond thickness of 61 ± 4 nm. This value is based on the average bond thickness value from previous SEM measurements of bonds between $\lambda/10$ flat fused silica substrates [77].

The thermal noise contributions from bonds on a test mass are calculated using the method outlined by Levin for the LIGO test masses [72]. This method utilises the following formula

for the spectral density of displacement thermal noise at a particular frequency, $S_x(f)$.

$$S_x(f) = \frac{2k_{\mathrm{B}}TW_{\mathrm{diss}}}{\pi^2 f^2 F_0^2}, \tag{6.1}$$

where k_B is Boltzmann constant, T is temperature, F_0 is the amplitude of a notional oscillating force incident on the test mass surface, normalised here to 1 N, and f is the frequency of oscillation of this applied force. This oscillating force can also be thought of as a pressure wave with a Gaussian profile, similar to that of the laser beam that is used to sense the displacement of the test mass. The time averaged power dissipated in the test mass, W_{diss}, can be written as

$$W_{\mathrm{diss}} = 2\pi f \int_{vol} \epsilon(x,y,z)\phi(x,y,z)dV, \tag{6.2}$$

where $\phi(x,y,z)$ is the mechanical loss angle, of the bond in this case. The other term, $\epsilon(x,y,z)$, is the strain energy stored in the bonds of a test mass when it is maximally deformed under the applied notional pressure. Finite element (FE) models created in ANSYS have been developed to allow the calculation of these two terms for bonded test masses.
There are two FE models needed for this; the first model calculates the ratio of strain energy stored in the bond to the total energy of the system, and compares it to previously measured mechanical loss values, to extract the mechanical loss angle of the bond, ϕ_{bond}. This approach will be explained in detail in Section 6.2.
The second model is used to obtain the strain energy stored in the bonds of a test mass, $\epsilon(x,y,z)$. For a system with a very simple geometry, i.e. a rod with a bond in the middle, and including only a fundamental mode of longitudinal deformation, the strain energy can be solved analytically. The derivation is shown in Appendix B, and the results are discussed in Section 6.3. For more complicated geometries and deformations including shear components, FE models must be used to solve the strain energies for loss angles at the first eight resonant frequencies, i.e. for each realistic test mass and ear geometry and material type. These models will be addressed for separate test mass geometries in this chapter.
A current aLIGO detector test mass is modelled first, followed by a prototype design for its proposed room temperature upgrade, A+. A test mass for KAGRA, a cryogenic detector currently under construction, as well as two possible test mass geometries for a future cryogenic detector, the Einstein Telescope (ET) [65], are also investigated. ET is currently still in its design phase. Unlike past detectors, it is proposed that ET be composed of two interferometer types with different characteristics that would result in a wider frequency range during operation. The ET-HF interferometer is proposed to operate at room temperature and be specialised for high frequency GW detection, while the ET-LF system would be a cryogenic interferometer focussed on low frequency GW sources [78]. Many aspects of the ET systems have not yet been fully developed, such as the type of material used for the ET-LF optics and suspension elements. However it is most likely to be either silicon

or sapphire. Therefore two initial designs for bonded test masses of silicon or sapphire of suitable geometries for ET-LF were modelled here.

6.2 Mechanical loss of bonds

FE models in combination with previous experimental measurements are used here to determine the mechanical loss angle of the hydroxide catalysis bonds. The mechanical loss angle model of a fused silica cylinder with an off-centre bond, shown in Figure 6.1, was investigated initially. The colour indicates relative deformation, where red is maximum and blue is minimum. This approach used developed modelling techniques [77, 145].

This model is used to calculate the amount of energy in each part of the sample, and the

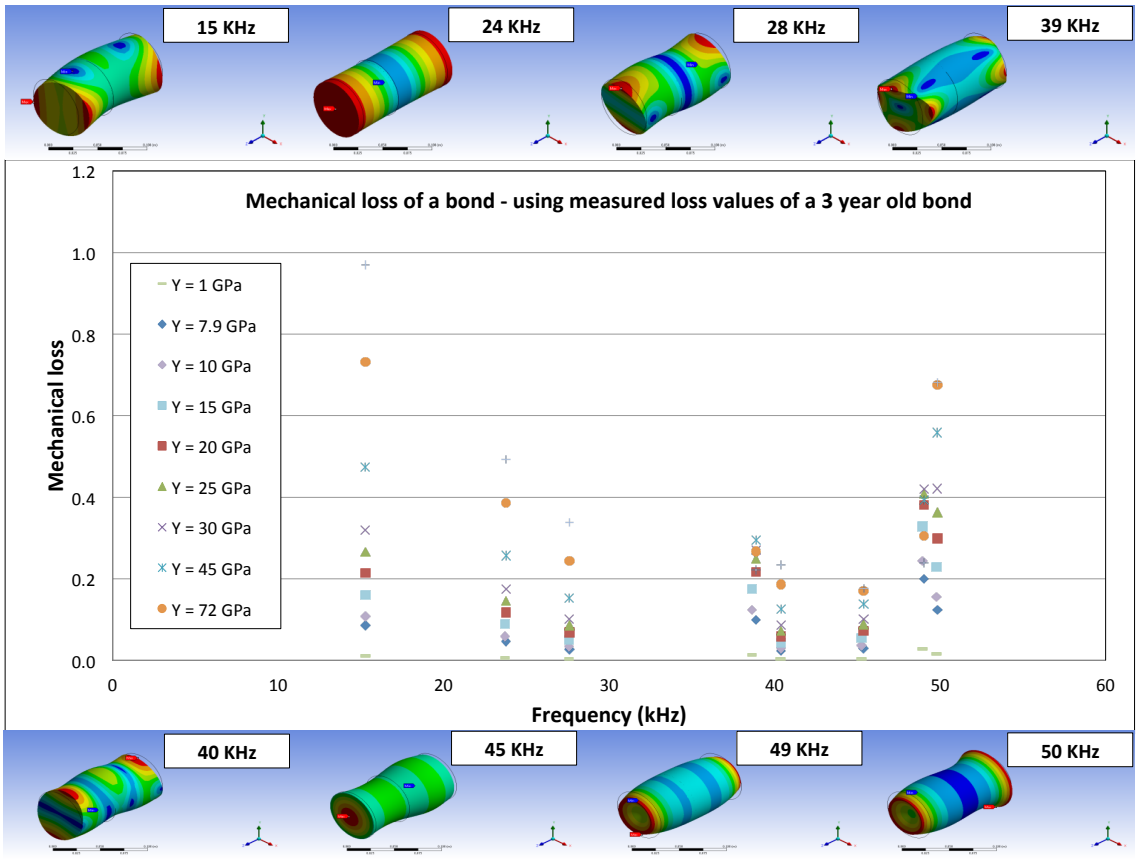

Figure 6.1: Off-centre bonded fused silica cylinder, shown at the 8 different resonant frequencies that were modelled. The colour indicates relative motion, where red is maximum and blue is minimum. The mechanical loss values are plotted at each frequency and for a range of Young's moduli [77].

ratio of energy stored in the bond to the energy stored in the total system at each resonant frequency of the cylinder can be calculated. Different loss values are associated with each resonant frequency. For modes where a large amount of the energy is stored in or near the

bond region, the effect of the bond will be amplified and a higher bond loss will be measured. In the past, two bond loss models, one frequency dependent and the other frequency independent, were analysed and from this ϕ_{bond} was determined to be most likely independent of frequency [77], thus an average value based on the first eight resonant frequencies is used.

The energy ratio assuming a bond Young's modulus of 18.5 GPa (as determined in Chapter 5) was then used along with prior mechanical loss angle measurements and model of a cylinder (of both sapphire and fused silica) with an off-centre bond to calculate $\phi_{\text{substrate}}$ [77, 164] and extract the bond loss. This is done by rearranging the equation for $\phi_{\text{bondedcylinder}}$ below

$$\phi_{\text{bondedcylinder}} = \frac{\Delta H_{\text{substrate}}}{\Delta H_{\text{total}}}\phi_{\text{substrate}} + \frac{\Delta H_{\text{bond}}}{\Delta H_{\text{total}}}\phi_{\text{bond}}, \tag{6.3}$$

where the mechanical loss angle term, $\phi_{\text{bondedcylinder}}$ is a value previously measured via experimental measurements of a fused silica cylinder with off-centre bond [77]. The other mechanical loss angle term, $\phi_{\text{substrate}}$, is calculated using a model by Penn [165].

The $\frac{\Delta H_{\text{substrate}}}{\Delta H_{\text{total}}}$ term in Equation 6.3 is approximately equal to 1, dominated by energy stored in the fused silica substrates, since the bulk cylinder is much larger in volume than the bond, and Equation 6.3 can be expressed as

$$\phi_{\text{bond}} \approx \frac{\phi_{\text{bondedcylinder}} - \phi_{\text{substrate}}}{\Delta H_{\text{bond}}/\Delta H_{\text{total}}}. \tag{6.4}$$

Finally, ϕ_{bond} can be calculated using the average $\Delta H_{\text{bond}}/\Delta H_{\text{total}}$ of the first eight resonant modes extracted from the ANSYS model.

6.3 Role of bond Young's modulus in mechanical loss and thermal noise

6.3.1 Contribution of bond Young's modulus to mechanical loss

In practice, the mechanical loss of bonds is evaluated for all resonant frequencies of bonded systems. Considering only the fundamental longitudinal mode in a rod of length L, with a bond in the middle of thickness b, the ratio of strain energies $\Delta H_{\text{bond}}/\Delta H_{\text{total}}$ can be solved analytically as

$$\frac{\Delta H_{\text{bond}}}{\Delta H_{\text{total}}} = \frac{2bE_1}{LE_2}. \tag{6.5}$$

where E_1 and ρ_1 are the Young's modulus and density of the substrate material, and E_2 and ρ_2 the same values for the bond. Equation 6.5 is derived in Appendix B. In this simplified geometry Equation 6.4 can be expressed in terms of the relative Young's moduli of the bond

and substrate material,

$$\phi_{\text{bond}} \approx (\phi_{\text{bondedcylinder}} - \phi_{\text{substrate}}) \frac{LE_2}{2bE_1}. \tag{6.6}$$

For more complicated geometries, where compression waves with shear components are included, the Poisson ratios and densities of the bond and substrate must be taken into account as well. However, it has been shown in the past that varying the bond's Poisson ratio across accepted values for silicate glasses does not have a significant effect on the loss determined from FE models [145]. Thus the Poisson ratio of hydroxide catalysis bonds are assumed to be 0.17, equal to that of fused silica.
The density of hydroxide catalysis bonds is also assumed to be roughly equal to that of fused silica. The thickness of sodium silicate bonds, given a known volume of solution and area of a $\lambda/10$ flat bond substrate, has been calculated to be about 74 nm, assuming a final bond density of 2202 kg m^{-3}, which is equal to that of fused silica [144]. The calculated value of 74 nm matches fairly well with the assumed average bond thickness of 61 ± 4 nm for bonds between $\lambda/10$ flat bond substrates, based on SEM measurements of bond thickness [77].
From Equation 6.6 it can be seen that the energy stored in the bond is proportional to its Young's modulus. To expand from this simplified example, FE models were used to find $\Delta H_{\text{bond}}/\Delta H_{\text{total}}$ at the first eight resonant frequencies, as a function of Young's modulus. As a silicate material, the Young's modulus of hydroxide catalysis bonds cannot exceed the modulus of fused silica which is 72 GPa. A value less than zero would not be possible for a physical solid. To analyse how the bond loss between fused silica substrates changes with bond Young's modulus, it was calculated for a range of 0-72 GPa, to incorporate all physically feasible values. These results, shown in Figure 6.2, do indicate an increase in the extracted bond loss as a function of the bond Young's modulus. This agrees in principle with the simplified form of Equation 6.6.

The bond loss from Figure 6.2, including previously measured $\phi_{\text{bondedcylinder}}$ values of bonded silica cylinders, cured for three years at room temperature [77, 148], gives a bond loss value of 0.17 ± 0.02 for a Young's modulus of 18.5 GPa. This bond loss value was used to extract the bond thermal noise of fused silica masses in the aLIGO and A+ upgrade sections.

6.3.2 Contribution of bond Young's modulus to thermal noise

Recalling the expression for the spectral density of displacement thermal noise at a particular frequency in Equation 6.1, it is recalled that $S_x(f)$ is proportional to the time averaged dissipated power, W_{diss}. The time averaged power dissipated in the bonds can be expressed as the product of the mechanical loss of a bond ϕ_{bond} and the strain energy stored in the bond, as in Equation 6.2. Considering the simplified case of a longitudinal mode in a bonded

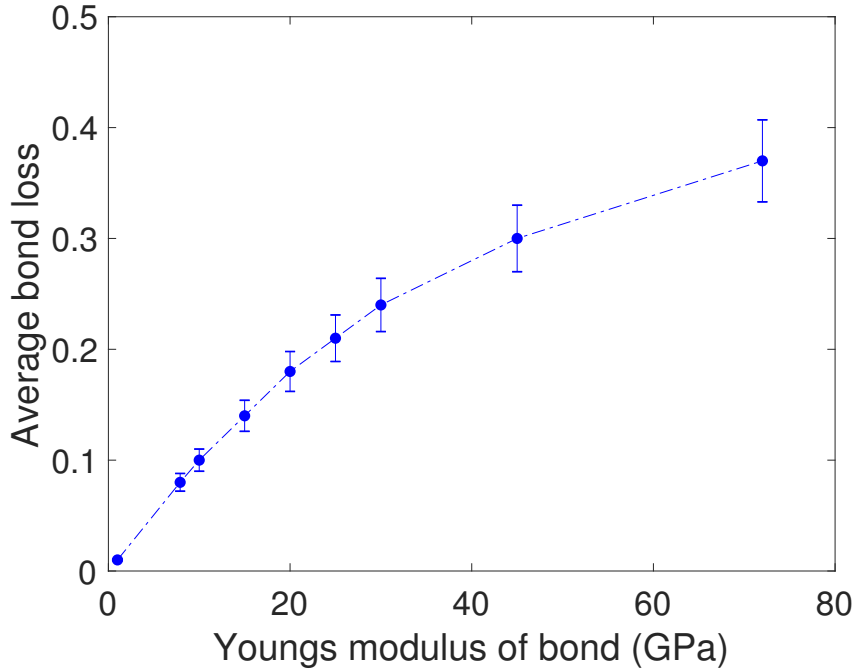

Figure 6.2: Average (of first eight resonant frequencies) bond loss values extracted from measurements and models of a bonded fused silica cylinder model, as a function of Young's modulus.

bar geometry the strain energy can be expressed as

$$\int_{vol} \epsilon(x,y,z)dV = \Delta H_{\text{bond}} = \frac{1}{4} E_2 S A_2^2 k_2^2 b, \tag{6.7}$$

where E_2 is again the bond Young's modulus, S is the cross sectional area of the bond and rod, A_2 is the amplitude of the longitudinal wave in the bond region, and k is the wave number. The quantities $A_2 = A_1 \cdot \sqrt{(E_1\rho_1)/(E_2\rho_2)}$ and $k_2 = \frac{2\pi f}{\sqrt{E_2/\rho_2}}$ are derived in Appendix B along with the Equation 6.7. Using these forms of A_2 and k_2, the strain energy can be simplified as

$$\Delta H_{\text{bond}} = \frac{1}{2}\frac{E_1}{E_2} S A_1^2 b \rho_1 (2\pi f)^2. \tag{6.8}$$

Combining Equation 6.8 with the expression for ϕ_{bond} in Equation 6.6, the following expression for W_{diss} is obtained

$$W_{\text{diss}} \approx (\phi_{\text{bondedcylinder}} - \phi_{\text{substrate}}) \cdot (A_1 \cdot 2\pi f)^2 \rho_1 L S. \tag{6.9}$$

Thus for the simplified case of a fundamental longitudinal mode in a bonded rod there is no dependence of W_{diss} on the bond Young's modulus, and thus no dependence of thermal noise on bond Young's modulus.

Of course, this is an oversimplification. In reality, $\phi_{\text{bondedcylinder}}$ is measured experimentally at the first eight resonant frequencies, and $\Delta H_{\text{bond}}/\Delta H_{\text{total}}$ is modelled at the first eight

resonant frequencies as well.
The geometry of a GW detector test mass is also much more complicated than a bonded rod with one longitudinal wave component going through the bond cross-section. In reality the laser exerts pressure waves on the face of the test mass, which is perpendicular to the bond interface. The coupling between these pressure waves and the bond interface will be much more complicated in this geometry, due in part to the addition of shear wave components. Thus FE analysis of test masses of the appropriate geometry are needed to obtain more realistic values of bond strain energy.

6.4 Bond loss values for sapphire and silicon

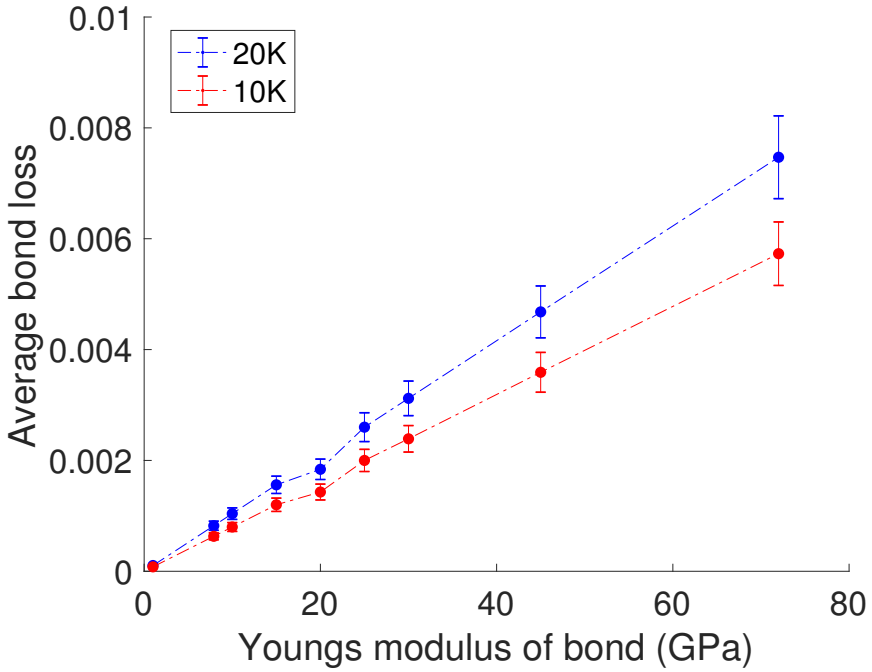

Figure 6.3: Average bond loss values extracted from measurements and models of a bonded sapphire cylinder, as a function of Young's modulus

To find the bond loss at cryogenic temperatures between sapphire, cryogenic measurements and modelling of a sapphire-to-sapphire cylinder were carried out previously using a similar technique as to the approach used for bonded fused silica [145]. Assuming a bond Young's modulus of 18.5 GPa gives bond loss values of $1.8 \pm 0.6 \times 10^{-3}$ at 20 K and $1.4 \pm 0.4 \times 10^{-3}$ at 10 K [145]. The average bond loss extracted as a function of Young's modulus is shown in Figure 6.3 [145].
These loss values are used to extract the bond thermal noise of the bonded sapphire test masses for KAGRA in Section 6.8 and for ET LF-1 in Section 6.9.
The mechanical loss of bonded silicon presented by Prokhorov et al. [166] was measured

by constructing a tuning fork out of two silicon ribbons with a silicate bond in the middle, shown in Figure 6.4. The mechanical loss of this tuning fork is $2.3 \pm 0.8 \times 10^{-3}$ at

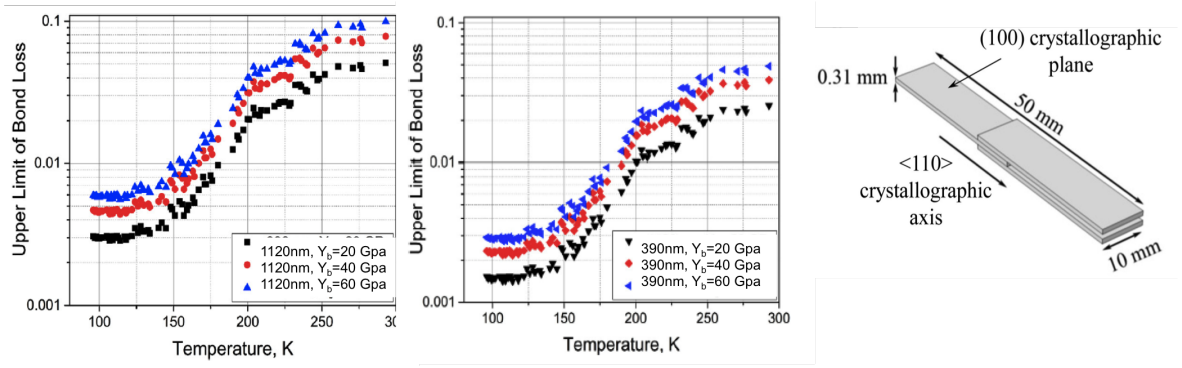

Figure 6.4: Mechanical loss values reported by Prokhorov et al. [166]. Values as a function of temperature are shown on the left and middle, at bond thickness of 390 nm and 1120 nm. The loss was calculated for three possible Y_{bond} values, with the 20 GPa values used in this study. The schematic of the bonded tuning fork used in this experiment is shown on the right side [166].

123 K, reported in [166]. This study assumed two components of the interfacial layer, the hydroxide catalysis bond and the silicon oxide layers. The addition of silicon oxide layers is necessary to joint silicon with hydroxide catalysis bond. However, it has been reported in the literature that the silicon oxide (at a total additional thickness of $\approx$ 200 nm) is the dominant source of mechanical loss in bonded silicon [166, 167]. These values are used in Section 6.10 to find the thermal noise of bonds in a silicon mass at cryogenic temperature and at room temperature. The same loss value was used for temperatures of 123 K, 20 K, and 10 K. In reality the loss is believed to decrease at lower temperatures, but it has not yet been measured below 123 K. Therefore the thermal noise at 10-20 K calculated for a bonded silicon ET test mass in Section 6.10 will be an overestimate, giving a generous upper bound on the noise.

6.5 Extracting thermal noise values from bonded test mass models

FE models are used to calculate the strain energy of the bonds, $\epsilon(x, y, z)$, in different bonded test mass systems. The test mass and ear geometry and material type are changed to suit each detector system. All assume a sodium silicate bond of thickness 61 ± 4 nm. All the bonded test mass geometries in this chapter were either based on the actual designs, as in the case of aLIGO and KAGRA, or based on the most current designs that are proposed for future systems, as in the case of the potential A+ upgrade and the ET masses. In all cases the face of the test mass optic is modelled to be deformed by a normalised incident Gaussian pressure wave with the radius of the laser beam used in the detector. The strain energy

stored in the bonds due to the test mass deformation from the laser beam is then extracted from the models.
Finally, assuming a Young's modulus of $18.5\pm^{2.0}_{2.3}$ GPa, the bond loss from the first model and the strain energy from the second model are combined. The spectral density of thermal noise, $S_x(f)$, Equation 6.1 and Equation 6.2 [72], was used to calculate the thermal noise contribution of the bond. These values were calculated at the frequency where the design sensitivity of the detectors is highest, i.e. where an increase of bond thermal noise could impact the overall detector sensitivity. Thus the thermal noise was evaluated at a frequency of 100 Hz for the aLIGO detector, the A+ upgrade, and the KAGRA detector. For the ET-LF detector whose target frequency range is lower than aLIGO or KAGRA, the design sensitivity is at a maximum around 10 Hz. Thus the bond thermal noise was evaluated at 10 Hz for the ET-LF masses.
This modelled noise is then compared to the bond's noise requirement for each GW detector. These noise requirements are based on the design sensitivity curves of each detector. Specifically the bonds have to meet a "technical noise requirement" which was defined for aLIGO as 10% of the total thermal noise budget of a test mass at 100 Hz [168–170]. The calculation of the technical noise requirement starting with detector strain sensitivity is explained in Section 6.6, using aLIGO as an example.

6.6 Thermal noise of a bonded aLIGO test mass

The total noise in strain of $4 \times 10^{-24}\ \sqrt{\text{Hz}}^{-1}$ at 100 Hz is derived from the aLIGO sensitivity curve shown in Figure 6.5.
All detector noise sources which have been categorised as technical noise sources must not exceed 10 % of the total detector target strain sensitivity across the frequency band of 10-7000 Hz as defined by the aLIGO Design Document [168]. Since the strain sensitivity of the aLIGO detector is at a maximum around 100 Hz, an increase in noise would first impact the overall detector sensitivity here. Thus thermal noise values for aLIGO are usually evaluated at this frequency.
The equivalent differential arm displacement noise limit for technical noise sources in aLIGO is 10 % of the total noise curve at 100 Hz, $4 \times 10^{-24}\ \sqrt{\text{Hz}}^{-1}$ as shown in Figure 6.5. The strain has been converted to displacement sensitivity by multiplying by the arm length of the detector, which is 4000 m for aLIGO. To calculate the displacement noise limit per test mass, now in units of $(\text{m}/\sqrt{(\text{Hz})})$, divide the total noise by the sum of the noise sources in quadrature. In this case $\sqrt{4}$ for the four test masses, giving a maximum allowable thermal noise budget of $8 \times 10^{-22}\ \text{m}\ \sqrt{\text{Hz}}^{-1}$.
Finally a room temperature fused silica aLIGO mass was modelled, shown in Figure 6.6. Each aLIGO test mass (TM) is 340 mm in diameter, 200 mm wide and weighs 40 kg. A 55 mm

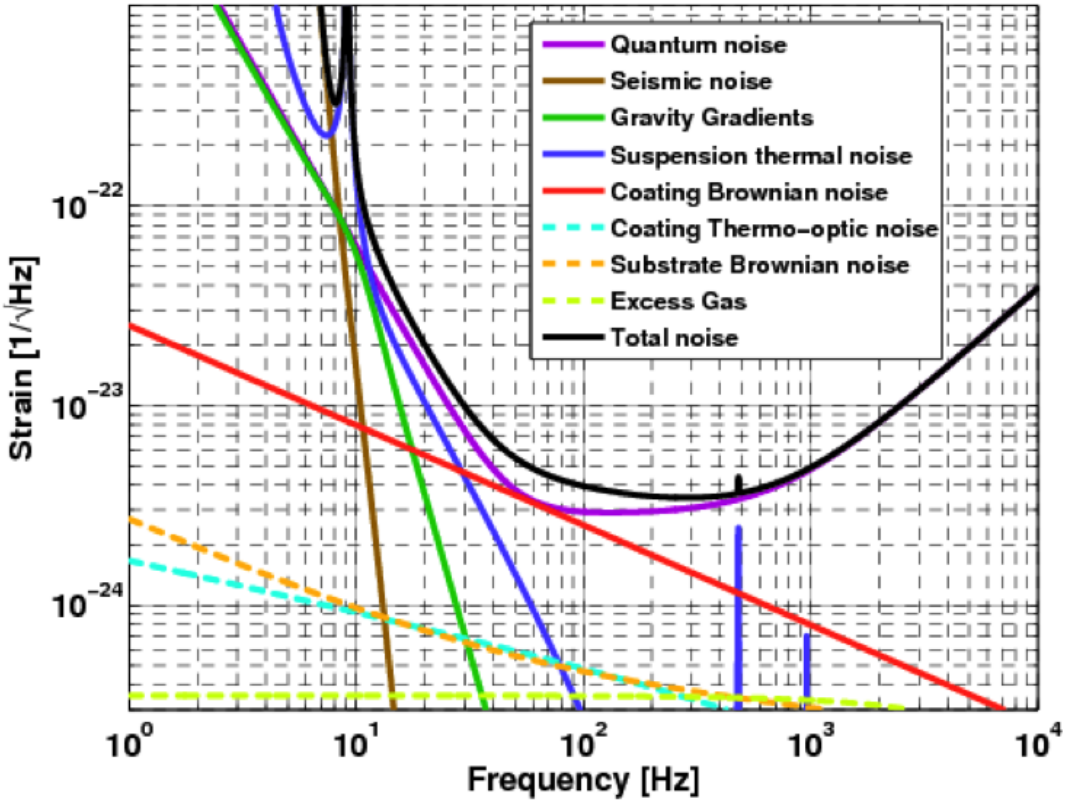

Figure 6.5: aLIGO design sensitivity curve and fundamental noise sources [171].

radius laser beam is incident upon it. There are two long ears per test mass, each one having an area of 20 mm × 60 mm for a total bond area of 2400 mm^2.

For an aLIGO mass using a loss term of 0.18 a bond thermal noise of $5.8 \pm 0.6 \times 10^{-22}$ m $\sqrt{\text{Hz}^{-1}}$ at 100 Hz was found, which meets the aLIGO thermal noise budget of 7-8 $\times 10^{-22}$ m $\sqrt{\text{Hz}^{-1}}$ at 100 Hz.

6.7 Thermal noise from the test mass bonds, for the A+ aLIGO upgrade, incorporating a newly proposed ear design

A+, an incremental upgrade to existing aLIGO detectors is currently being developed. This upgrade will make use of existing infrastructure and technologies and aims for a factor of 1.7 increase in range over aLIGO, using the binary neutron star inspirals as a benchmark [172]. In order to meet the sensitivity required for A+ a few key parameters are revisited. The coating thermal noise budget is proposed to be approximately half of aLIGO's coating thermal noise budget, utilising improvements to coating technologies. The use of

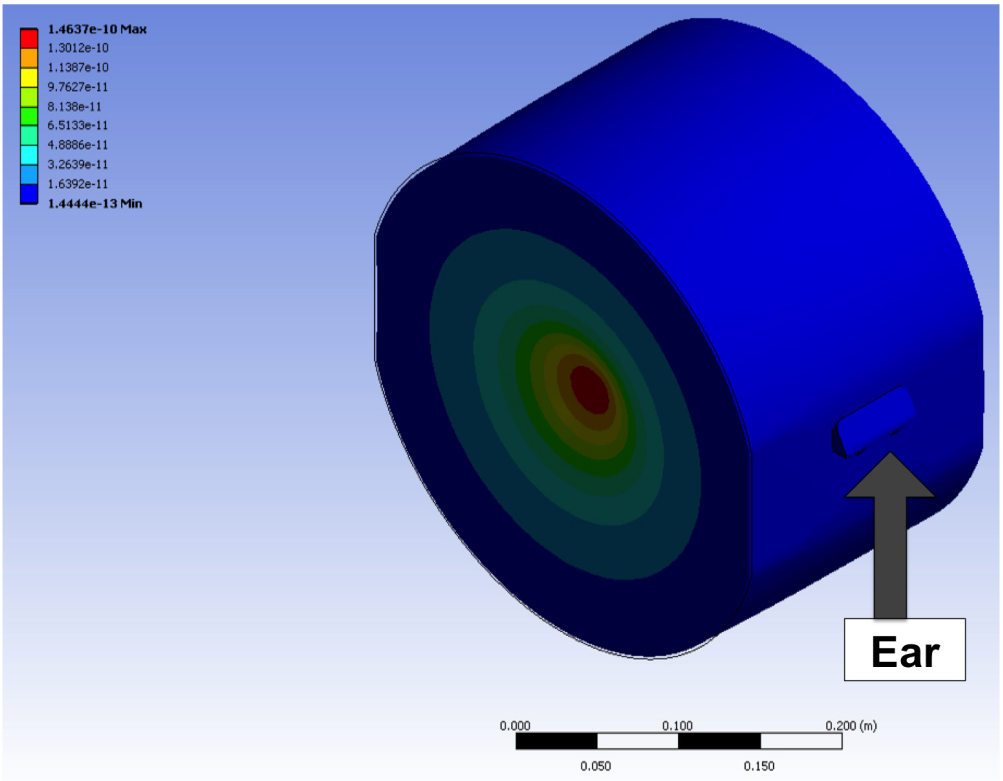

Figure 6.6: ANSYS model of aLIGO test mass model, where the colour shows the deformation of the test mass from a normalised Gaussian beam due to a laser of beam radius 55 mm. Red indicates the maximum amount of deformation and blue the minimum.

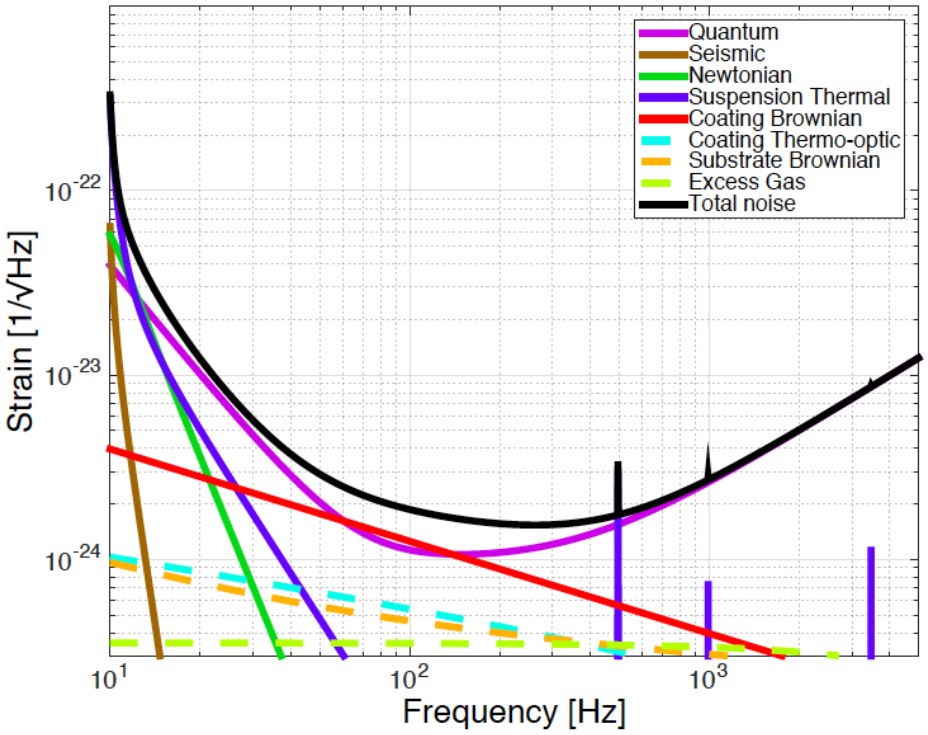

Figure 6.7: A+ upgrade design sensitivity, G1700552 [172]

frequency dependent squeezing is also proposed to lower the quantum noise level. With the successful implementation of the planned upgrades, the A+ design strain sensitivity curve, in Figure 6.7, would allow a factor of 1.7 increase in range, or 5 times increase in event rate, over the aLIGO detector.

6.7.1 A+ aLIGO upgrade ear design

The proposed increase in detector range demands a higher detector sensitivity and thus a lower bond thermal noise budget of $4 \times 10^{-22}\,\mathrm{m}\,\sqrt{\mathrm{Hz}^{-1}}$. As in the aLIGO case, this value was based on a technical noise budget of 10 % of the total thermal noise at 100 Hz from the A+ sensitivity curve. Hence an updated ear design for the A+ upgrade was investigated, with the aim of further reducing contribution of the bond to detector thermal noise, in order to meet upgrade requirements. The most straightforward method of achieving this is to reduce the surface area of the bonds by reducing the size of the ears on the masses. This can be achieved by going from two ears per mass to four ears, with a design that preserves an appropriately high stress safety factor. To achieve this, the ears must be positioned on the mass so that the horns are the same distance away from each other as they are in aLIGO, now with a space between two ears instead of a single long ear. The horn design was kept very similar to the aLIGO horn design, to keep stresses and fibre welding access the same. This and an angled ear geometry allow for a reduction in bond area of 34 % from aLIGO, down to 1580 mm^2 for one mass. This design keeps a safety factor of 3 in the bond's maximum tensile stress normal to the bond surface, a factor based on the ratio of the average tensile strength of hydroxide catalysis bonds, 16 MPa, to the maximum normal tensile stress in the bond, 5.2 MPa, taking into account a test mass load of 40 kg.
Different ear design geometries were investigated. These are shown in Figure 6.8 in comparison with the original aLIGO ear. Three new ear designs were modelled. The first was nearly square in shape, the second slightly angled at the bottom, and the third with more of an angle, wider at the top and narrower at the bottom. The stress was found to be higher in the two designs which were less angled, as stress tends to be higher in sharp square corners. The smaller, angled ear (LIGO drawing D1800010) was selected as it paired the best combination of low thermal noise, high bond strength, and safe deformation of the ear horns under load. A drawing and the FE model of the selected ear design bonded onto an A+ test mass is shown in Figure 6.9. This ear design has not yet been tested, and should undergo weld and bonding trials prior to implementation.

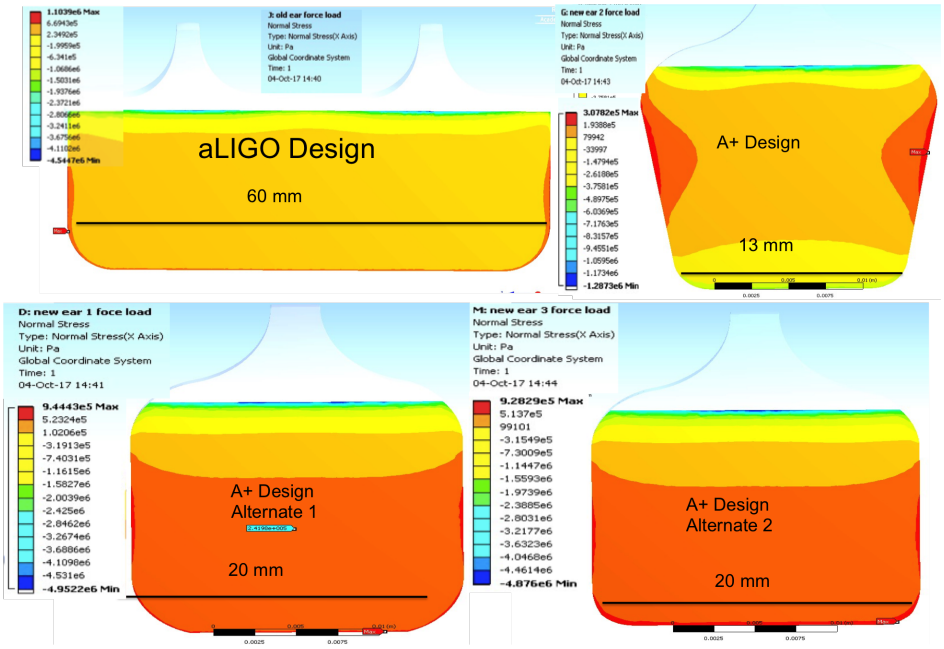

Figure 6.8: Comparisons of different ear design geometries for A+, at normal stress under force loading

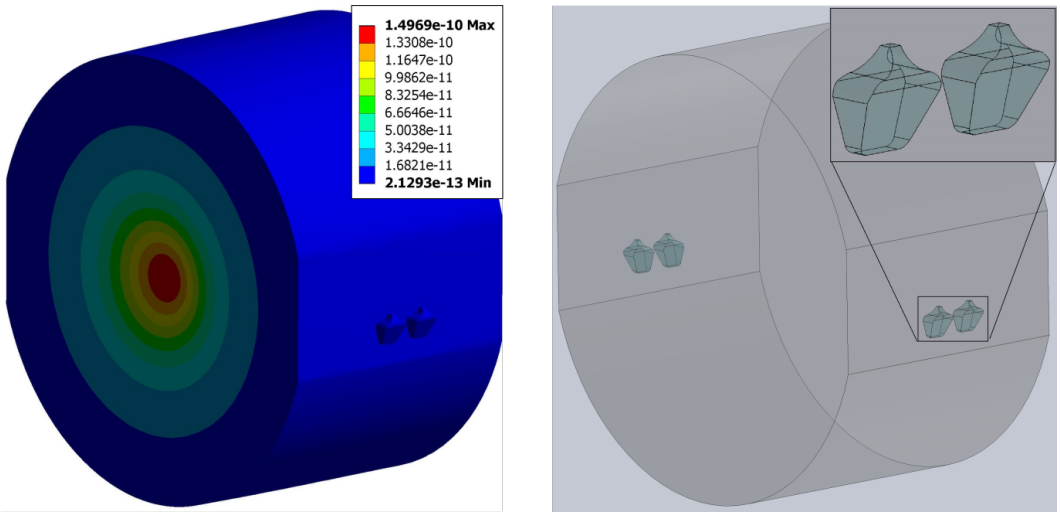

Figure 6.9: ANSYS model of an A+ bonded test mass on the left, where the colour shows the deformation of the test mass from a normalised Gaussian beam due to a laser of beam radius 60 mm. Red indicates the maximum amount of deformation and blue the minimum. A zoom-in of the new 4 ear design on the right.

6.7.2 Thermal noise of a bonded A+ mass

A comparison of the values calculated from the ANSYS models of bonded masses for aLIGO and the A+ upgrade is outlined in Table 6.1. The test mass geometry for aLIGO and the A+ upgrade is the same.

The calculated thermal noise of the new ear design modelled here, assuming the same conversion to displacement sensitivity as in the aLIGO case, is $3.8 \pm 0.4 \times 10^{-22}$ m $\sqrt{\text{Hz}^{-1}}$ at

Parameter per test mass	aLIGO	A+
Ear horn deformation under gravity (μm)	0.67	0.69
Max equivalent stress in bond under gravity (MPa)	9.2	9.3
Max tensile stress in bond, normal (MPa)	2.7	5.2
Max tensile stress in bond, shear (MPa)	±3.5	±4.8
Bond thermal noise, required ($\cdot 10^{-22}$m/$\sqrt{\text{Hz}}$)	7	4
Bond thermal noise, modelled ($\cdot 10^{-22}$m/$\sqrt{\text{Hz}}$)	5.8	3.8

Table 6.1: Comparison of aLIGO and A+ upgrade ear design parameters from FE models

100 Hz, which meets requirements stated at the beginning of this section.

6.8 Thermal noise of a bonded sapphire test mass for KAGRA

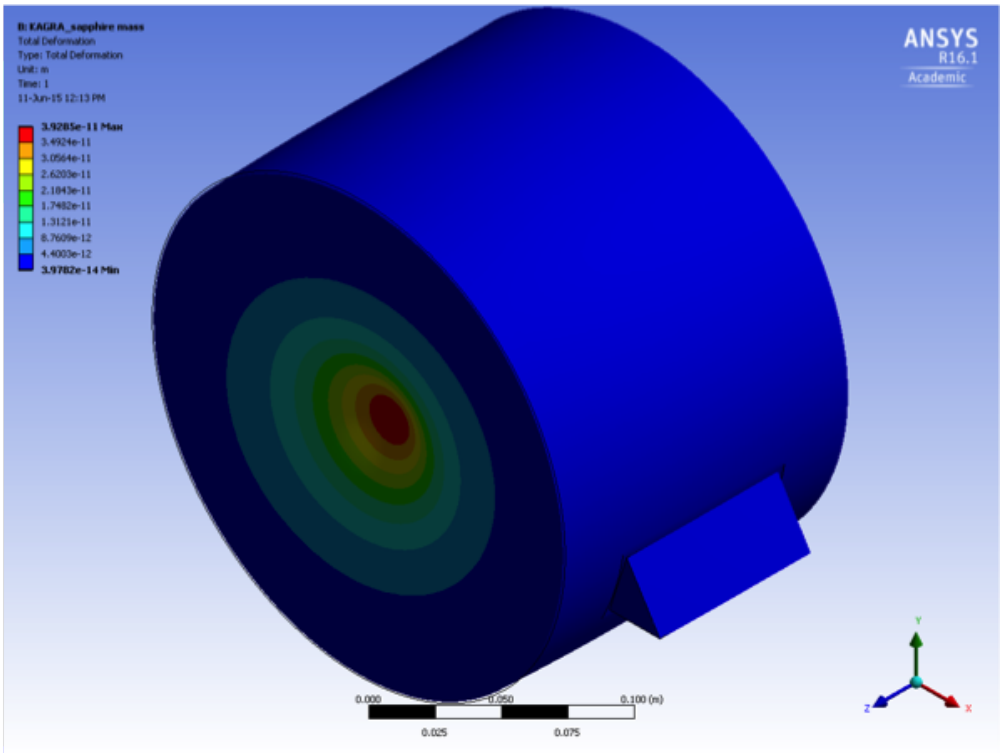

Figure 6.10: ANSYS model of KAGRA sapphire test mass and triangular ear design, where the colour shows the deformation of the test mass from a normalised Gaussian beam due to a laser of beam radius 38 mm. Red indicates the maximum amount of deformation and blue the minimum.

A cryogenic sapphire KAGRA mass was modelled here, shown in Figure 6.10. A KAGRA test mass has a 220 mm diameter, it is 153 mm wide and weighs 21 kg. A 38 mm radius laser beam is incident upon it [142]. There are two ears per test mass, on angled flats, each one having an area of 30x80 mm for a total bond area of 4800 mm^2.

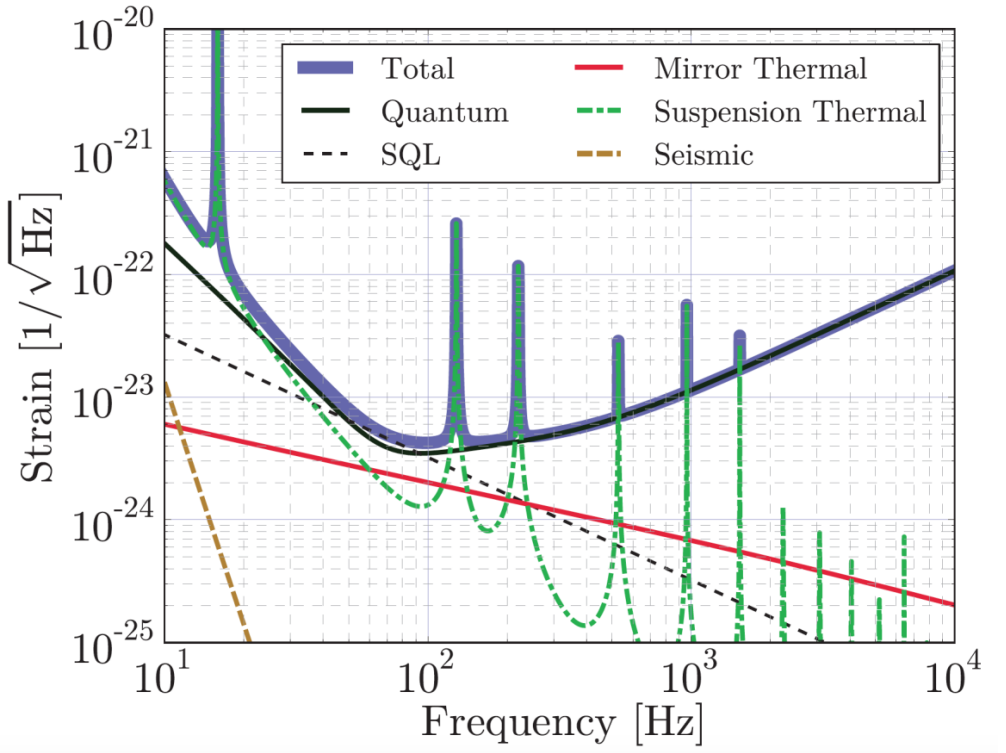

Figure 6.11: KAGRA design sensitivity curve [64]

The total detector noise at 100 Hz is roughly $4 \times 10^{-24}\ \sqrt{\text{Hz}^{-1}}$ at 100 Hz, taken from Figure 6.11. Considering an arm length of 3 km and converting to the thermal noise budget per mass, a value of $4 \times 10^{-25}\ \sqrt{\text{Hz}^{-1}} \cdot 3000\text{m}/\sqrt{4} = 6 \times 10^{-22}\ \text{m}\ \sqrt{\text{Hz}^{-1}}$ at 100 Hz is obtained as a noise limit.
The thermal noise is calculated assuming a bond loss of $1.8 \pm 0.6 \times 10^{-3}$ at 20 K and $1.4 \pm 0.4 \times 10^{-3}$ at 10 K. The bond thermal noise per mass at 100 Hz is thus calculated from this model to be $4.5 \pm 1.5 \times 10^{-23}\ \text{m}\ \sqrt{\text{Hz}^{-1}}$ at (20 K) and $2.7 \pm 0.9 \times 10^{-23}\ \text{m}\ \sqrt{\text{Hz}^{-1}}$ at (10 K), more than an order of magnitude below requirement.

6.9 Thermal noise of a bonded sapphire test mass for ET

A possible cryogenic sapphire ET mass design was modelled here, shown in Figure 6.12. This design is based on an aLIGO mass, with the bond area scaled up to a size to suspend the ET mass with a similar safety margin in tensile strength os the aLIGO masses. These numbers are estimates, as no specific test mass flat or ear designs have yet been made. This design features a 500 mm diameter, and 270 mm wide test mass weighing 211 kg. A 90 mm radius laser beam is incident upon it.
The total noise of the ET-LF detector is $1 \times 10^{-24}\ \sqrt{\text{Hz}^{-1}}$, at 10 Hz, taken from Figure 6.13. Considering a detector with a two arm right angle design and an arm length of 10 km, the

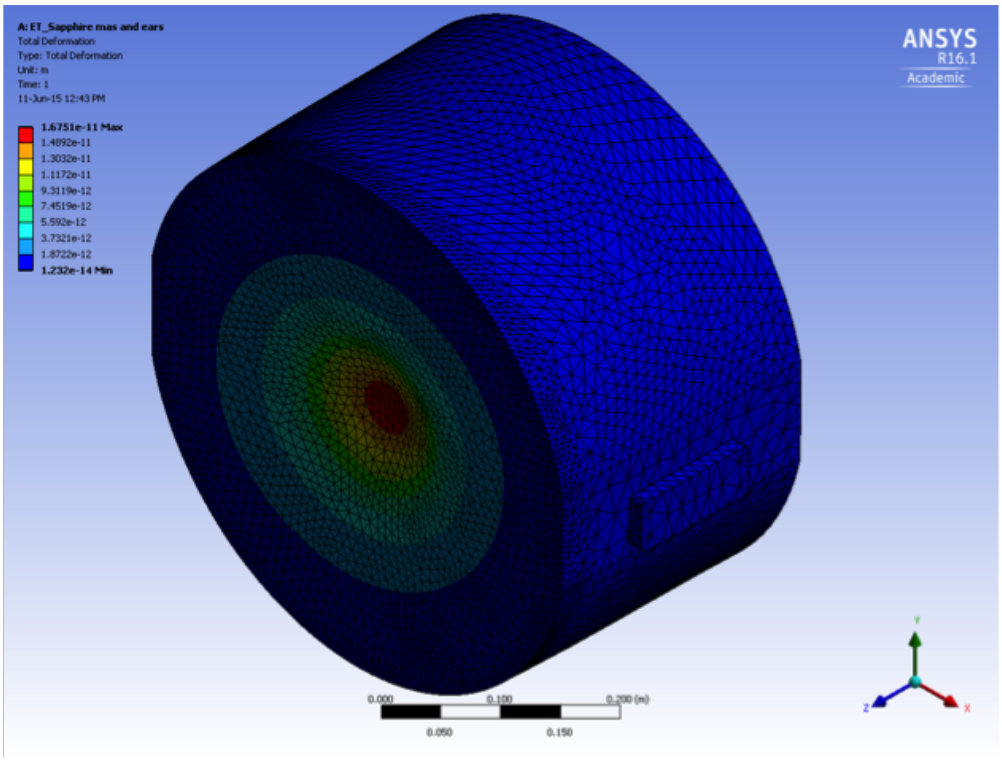

Figure 6.12: ANSYS model of ET sapphire test mass with a defined bond area but no designed ear, where the colour shows the deformation of the test mass from a normalised Gaussian beam due to a laser of beam radius 90 mm. Red indicates the maximum amount of deformation and blue the minimum.

technical noise budget per mass in m$\sqrt{\text{Hz}}$ can be calculated as 1×10^{-25} $\sqrt{\text{Hz}^{-1}}$ ·10000m/$\sqrt{4}$ =5×10^{-22} m $\sqrt{\text{Hz}^{-1}}$. The bond thermal noise per mass at 10 Hz was calculated from this model to be $3.8 \pm 1.2 \times 10^{-23}$ m $\sqrt{\text{Hz}^{-1}}$ at 10 K and $5.7 \pm 1.8 \times 10^{-23}$ m $\sqrt{\text{Hz}^{-1}}$ at 20 K, a factor of ≈10 below a technical noise requirement.

6.10 Thermal noise of a bonded silicon test mass for ET

A possible cryogenic silicon ET mass design was modelled here, shown in Figure 6.14. This design is also an estimate based loosely on an aLIGO geometry, with the bond area scaled up to a size to suspend the ET mass with a similar safety margin in tensile strength as the aLIGO masses. This mass has the same diameter as the sapphire option, 500 mm, but a different thickness of 463 mm. It also modelled to be 211 kg and have a 90 mm radius laser beam incident upon it.

In the case of bonded silicon, the total interface layer that is modelled must include both the hydroxide catalysis bond and an additional contribution from the necessary silicon oxide layers. Thus the total interface thickness used in this model is 261 nm, to fully encompass the 61 nm bond thickness plus the 200 nm total oxide layer thickness.

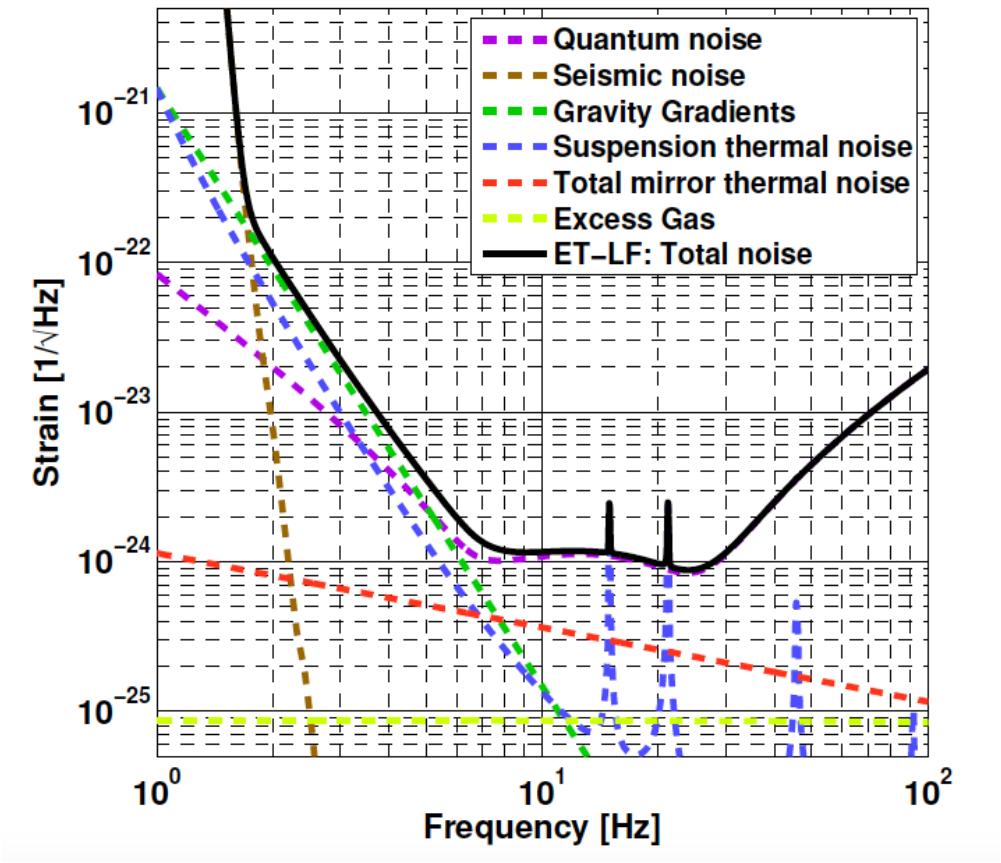

Figure 6.13: ET-LF Sensitivity curve [78]

The bond loss term reported by Prokhorov et al. [166] for bonds between silicon at 123 K, $2.3 \pm 0.8 \times 10^{-3}$, was used for this calculation. Currently there is no measured value in the literature for the bond loss below 123 K, so the same loss value found at 123 K was also used here for lower temperatures of 10 K and 20 K, giving values of $2.8 \pm 0.5 \times 10^{-22}$ m $\sqrt{\text{Hz}^{-1}}$ at 10 K and $3.9 \pm 0.6 \times 10^{-22}$ m $\sqrt{\text{Hz}^{-1}}$ at 20 K. The real bond loss at lower temperatures is probably lower, so this calculation should serve as an upper bound on the thermal noise, when compared to a technical noise budget of 5×10^{-22} m $\sqrt{\text{Hz}^{-1}}$ at 20 K taken from the total thermal noise budget at 10 Hz in Figure 6.13.

6.11 Discussion and conclusions

The thermal noise resulting from hydroxide catalysis bonds in several different bonded test mass systems was calculated here, using the Young's modulus value determined in Chapter 5, $18.5^{+2.0}_{-2.3}$ GPa. All values for aLIGO, A+, and KAGRA were calculated at a frequency of 100 Hz. Values for ET-LF were calculated at 10 Hz. An existing aLIGO model was re-analysed with the updated bond Young's modulus value, re-computing the bond mechanical loss angle and the strain energy, giving a value of 5.8×10^{-22} m $\sqrt{\text{Hz}^{-1}}$, which is under

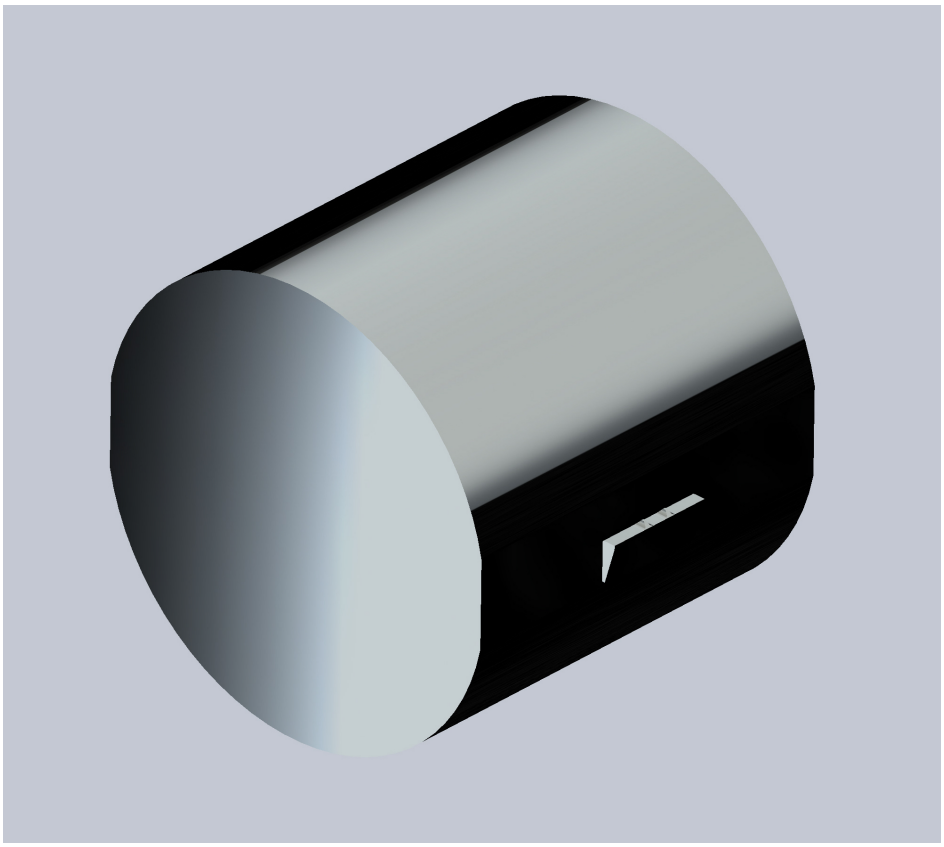

Figure 6.14: Model of ET silicon test mass, diameter 500 mm, thickness 463 mm, weight 211 kg. Modelled in ANSYS with an incident laser beam of radius 90 mm.

the aLIGO's thermal noise budget of 7×10^{-22} m $\sqrt{\text{Hz}^{-1}}$. For the next upgrade planned for aLIGO, A+, a new ear geometry was presented and the thermal noise contribution of its bond was calculated to be 3.8×10^{-22} m $\sqrt{\text{Hz}^{-1}}$, which would meet an A+ 10% technical requirement of 4×10^{-22} m $\sqrt{\text{Hz}^{-1}}$. The bond thermal noise levels of two different cryogenic sapphire masses were investigated, one with the dimensions of a KAGRA mass and the other a possible design for a sapphire mass for ET. The thermal noise contribution of the bonds to a KAGRA mass was $0.27/0.45 \times 10^{-22}$ m $\sqrt{\text{Hz}^{-1}}$ at 10/20 K which can be compared to its requirement of 6×10^{-22} m $\sqrt{\text{Hz}^{-1}}$. Similarly a value of $0.38/0.57 \times 10^{-22}$ m $\sqrt{\text{Hz}^{-1}}$ at 10/20 K was calculated for an ET sapphire mass option, compared to the same requirement of 5×10^{-22} m $\sqrt{\text{Hz}^{-1}}$.

Finally a bonded silicon mass that could be considered for the cryogenic ET-LF detector was investigated, finding a value of 2.4×10^{-22} m $\sqrt{\text{Hz}^{-1}}$ at 123 K, as well as $2.8/3.9 \times 10^{-22}$ m $\sqrt{\text{Hz}^{-1}}$ at 10/20 K compared to the proposed thermal noise limit of 5×10^{-22} m $\sqrt{\text{Hz}^{-1}}$. Here the largest contribution to bond thermal noise comes from the thicker silicon oxide layers, not the bond itself.

The system parameters and upper limits on thermal noise calculated in this chapter are summarised in Table 6.2. It should be noted, that this analysis included reasonable assumptions of bond area, but no actual ear designs for either of the ET masses. Also, the mechanical

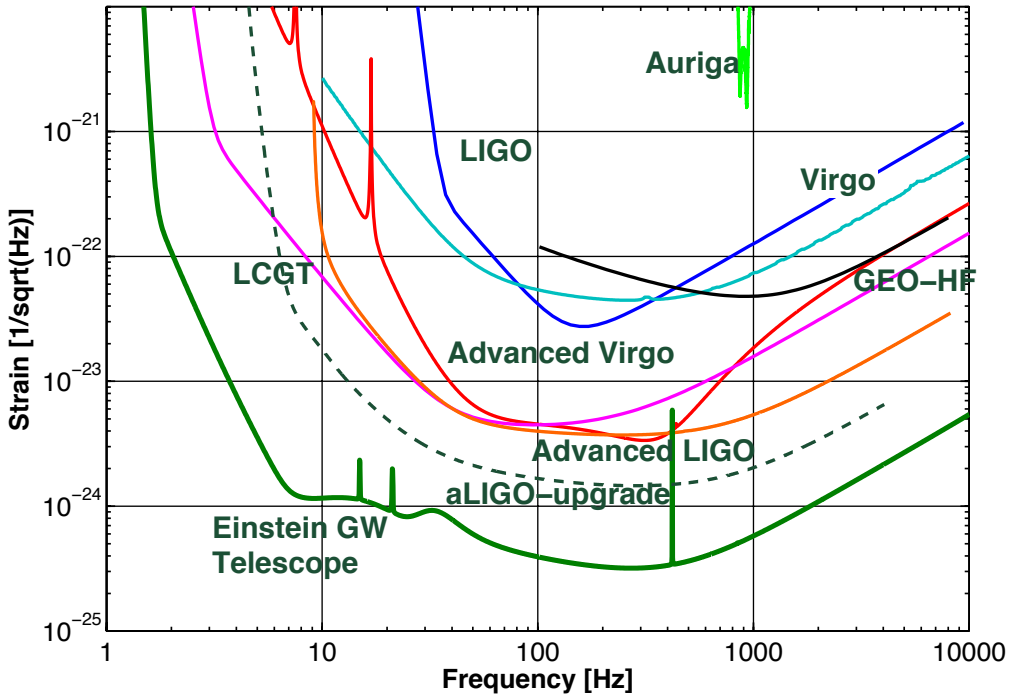

Figure 6.15: Ground-based detector design strain sensitivity curves for comparison, where LCGT has been renamed the KAGRA detector, and the Einstein GW Telescope includes both the ET-LF and ET-HF detectors [79].

loss of bonds between silicon substrates uses a value measured at 123 K, so the actual loss numbers at 20 K are expected to be lower. Future detectors such as Cosmic Explorer and Voyager were not addressed here as the suspension designs aren't yet mature enough to properly model.

In all cases investigated here the hydroxide catalysis bonds meet the thermal noise requirements of the detector's design sensitivity curves. A comparison of the detector sensitivity curves is given in Figure 6.15. This indicates that hydroxide catalysis bonds continue to be a good choice for the construction of quasi-monolithic suspensions in both room temperature and cryogenic GW detectors.

Detector	aLIGO	A+	KAGRA	ET-LF-1	ET-LF-2
TM material	fused silica	fused silica	sapphire	sapphire	silicon
TM mass (kg)	40	40	21	211	211
TM diameter (mm)	340	340	220	500	500
TM thickness (mm)	200	200	153	270	463
Ear(mmxmm)/no.	20x60/2	19.75x20/4	30x80/2	45x136/2	45x136/2
Beam radius (mm)	55	60	38	90	90
Assumed bond loss ($\times 10^{-3}$)	170±2	170±2	1.4±0.4/ 1.8±0.6	1.4±0.4/ 1.8±0.6	2.25±0.75
Operating temperature (K)	293	293	10/20	10/20	10/20
Thermal noise, required*	7	4	6	5	5
Thermal noise, modelled*	5.8±0.6	3.8±0.4	0.27±0.09/0.45±0.015	0.38±0.12/0.57±0.18	2.8±0.5/3.9±0.6

Table 6.2: Comparison of detector test mass parameters, thermal noise requirements, and modelled noise levels. *In units of ($10^{-22}\mathrm{m}/\sqrt{\mathrm{Hz}}$).

Chapter 7

Indium as a bond material in cryogenic GW detectors

7.1 Introduction

A new hybrid suspension design utilizing both indium and hydroxide catalysis bonding is being considered for current cryogenic detectors such as KAGRA [64, 173]. In this proposed design the hydroxide catalysis bonds would be used to hold the test masses to an interface piece (ear), making use of their strength under shear stress, as in room temperature detectors such as GEO600, VIRGO, and aLIGO [8, 174–176].
Indium's low shear and tensile strength means it cannot be used as a joint under shear or tensile loads. Instead it is being considered for compressive joints between the fibres and ears as well as between the fibres and blade springs in a cryogenic suspension design, a possible example of which is shown in Figure 7.1.

Indium is included in suspension design for contingency reasons, since indium can be de-bonded and re-bonded fairly easily, whereas de-bonding hydroxide catalysis bonds is more difficult. In the event of a fibre break or a test mass upgrade, the whole bonded test mass assembly could be removed by de-bonding the indium bond interface, then replaced by re-bonding it, making it a good option for future cryogenic mirror suspensions.
Some research into indium bonding of sapphire substrates in GW detectors has been done, focussing on the thermal conductivity and mechanical loss of indium [109, 110]. In this chapter the bonding of silicon substrates is focussed on, as silicon is under consideration for next generation cryogenic optic and suspension designs in the Einstein Telescope and Voyager detector [62, 78, 83].
While the suspension designs of these future detectors are not yet finalised, indium could be considered for compressive joints in these cryogenic suspensions and so repeatable indium bonding procedures that could be used in future detectors are required and significant

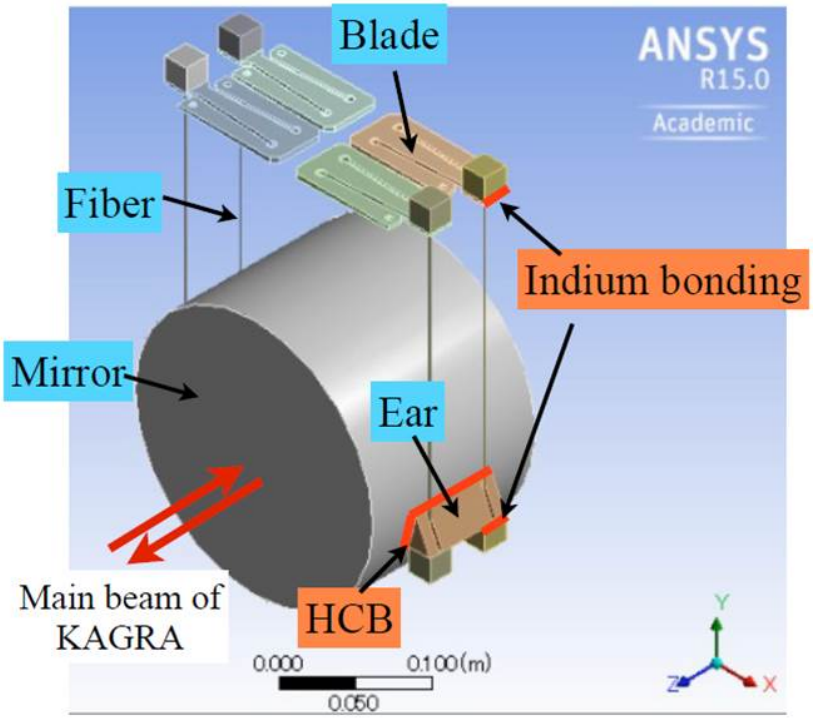

Figure 7.1: Cryogenic KAGRA suspension design with proposed indium bond placement [64]

advancements towards such procedures are presented in this chapter.

7.1.1 Aim and approach

As mentioned in Chapter 2, a few different approaches to indium bonding were considered, with techniques using indium foils or thin evaporated indium films as a layer of bond material selected as the most suitable approaches for GW detector design.
Research into the mechanical loss of indium bonds suggests that bond thicknesses of 10 µm or less are required to meet current KAGRA detector thermal noise requirements in sapphire suspensions [142, 173]. Although it is easier to create an indium bond using thicker layers of metal, unfortunately they are not suitable for use in GW detectors, as bonds that that are much thicker than 10 µm would be expected to have unacceptably high thermal noise. Instead, this chapter focusses on a two step approach to create reliable indium bonding procedures using small amounts of indium. The first step is the production and cold welding of oxide free indium layers, and the second is the application of heat and pressure to create a diffusion bond.
Different combinations of thin indium foils and thermally deposited indium coatings as well as different approaches to provide the necessary heat and pressure are explored here for feasibility as bonding techniques for cryogenic GW detectors.

Ease of installation is not the only requirement that bonds in a GW detector face. Properties such as high thermal conductivity, low contribution to thermal noise, and repeatably high quality are also very important for future generation GW detectors. Developing reliable and practical procedures for indium bonding in cryogenic mirror suspensions that retain these properties is the focus of this chapter. The results of two different approaches to achieve indium bonds of repeatable strength with thin evaporated layers and foils on silicon substrates are presented here. Full procedures for both methods can be found in Appendix A.

7.2 Preparation and cleaning of bond substrates

Silicon was chosen for use in this study, as along with sapphire it is the material most likely to be used for optical and suspension components of cryogenic GW detectors. Of the three materials most often used in GW materials research, fused silica, sapphire, and silicon, indium will bond readily to sapphire and fused silica as they are oxide materials, but less readily to silicon. Thus if these bonding approaches work for pure silicon, they should also work for oxide materials.

Most of the silicon substrates used in this study (88 of 120) were single crystal silicon from the same ShinEtsu [177] ingot. The sample dimensions were 5 mm x 10 mm x 20 mm, and they were cut and polished at Spanoptic [178]. The bond surfaces were <111> plane silicon, 5 mm x 10 mm in area.

The remaining 32 samples were 5 mm x 10 mm x 10 mmsilicon, with the bond surface in the <111> plane, and 5 mm x 10 mm in area.

In all cases, the samples were inspected for defects and the flatness measured prior to cleaning. Peak-to-valley flatness measurements were taken of each of the bond surfaces on a ZYGO GPI XP/D interferometer [129] using the same method as in Chapter 3, (Figure 3.2). The average flatness and standard deviation of all silicon samples used in the study was 60 ± 15 nm. All measured flatness values are shown in Figure 7.2.

The silicon samples were all solvent cleaned the same way prior to bonding, in an ultrasonic bath of acetone, isopropanol and methanol as explained in detail in Appendix A.

7.3 Preparing a jointing layer: thermal deposition

An Emitech K950X Evaporator[156] was used in this experiment to deposit indium onto the 5 mm x 10 mm silicon bond surfaces after they were solvent cleaned. The evaporator works by placing a small piece of metal (in this case indium) into a tungsten basket, placing

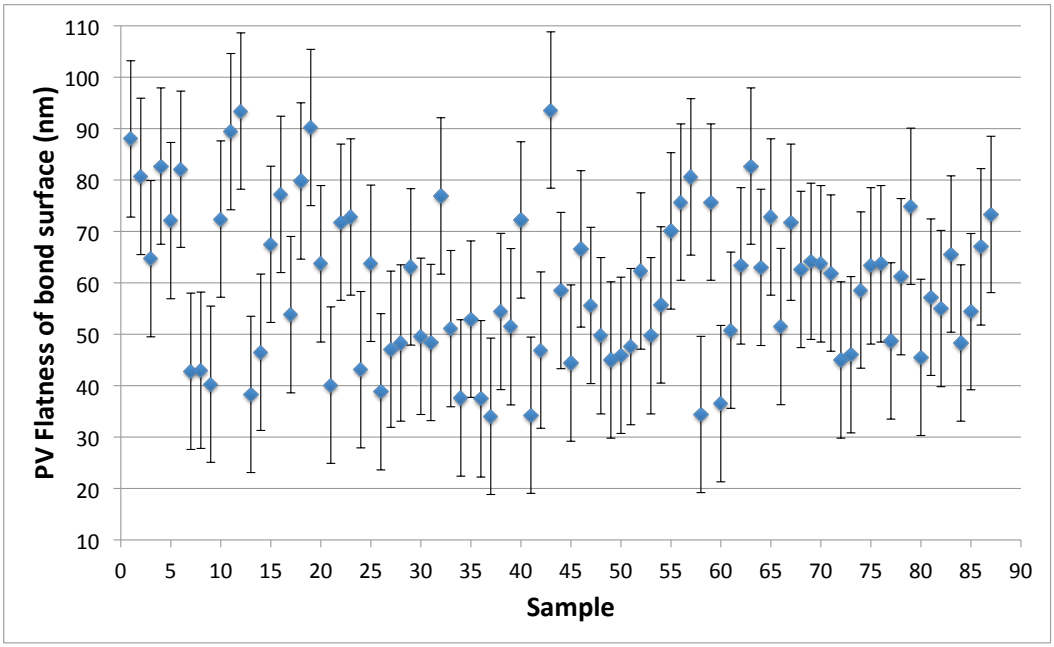

Figure 7.2: PV flatness measurements of bond surfaces of ShinEtsu silicon samples

the clean silicon samples bond side up in the base of the vacuum chamber, pumping the vacuum chamber down to 9×10^{-4}mbar and running a high current through the electrodes attached to the tungsten basket. The metal in the basket is evaporated, and coats everything inside the chamber. The thickness of the indium actually deposited on the samples is quantified via the following approach; indium pieces are weighed before loading them into the evaporator and an additional silicon sample is coated in each run. This silicon witness sample is also etched at the same time as the other samples, then the indium layer thickness is measured as explained in Section 7.3.1.

7.3.1 Thickness measurements of deposited indium layers

The Emitech evaporator [156] does not have a built in way of regulating or measuring deposited layer thickness. Initially, part of the silicon witness sample was masked with tape before coating. The tape was then removed and the step between the indium coating and the silicon substrate was measured with a Wyko NT1100 white light interferometer [131], shown in Figure 7.3.

This proved to be an unreliable measurement, due in part to the different reflectivity of the indium layer and of the silicon substrates which made it difficult for the Wyko to focus on both layers during one scan across the whole surface. Also the non-uniformity of the indium layer compared to the bare silicon substrate led to a high error, which can be seen in the differences between along the profile in the y-direction, which measured an average

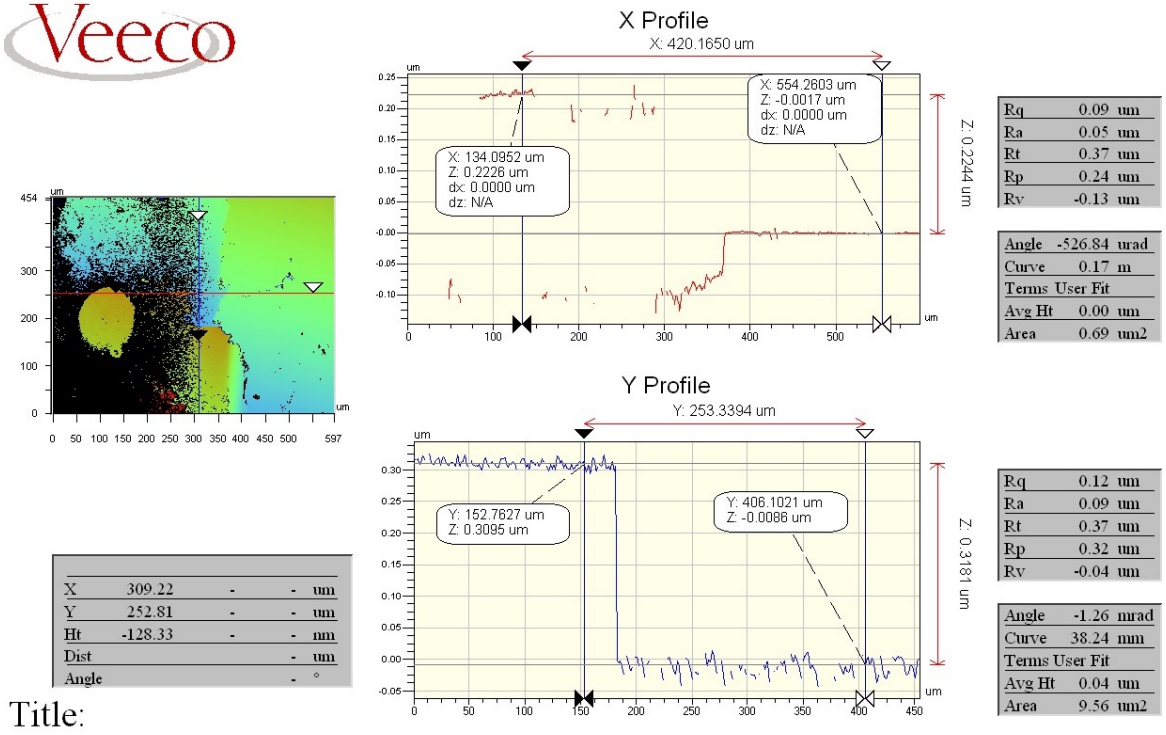

Figure 7.3: Wyko white light interferometer measurements of etched and un-etched indium foil, 50 µm.

step of 318 nm. The profile in the x-direction was also measured to be 224 nm, though it runs along the coated and un-coated edge and as such it was expected to have a higher associated error. Both measurements are shown in Figure 7.3. The error for this method was 100-200 nm in the y-direction depending on the uniformity of the indium coating.

A more repeatable and faster way of measuring indium layer thickness was to use a Shimadzu EDX-8000 Energy Dispersive X-ray Fluorescence Spectrometer (EDXRF) system [159]. The EDXRF machine performs non-destructive elemental analysis by irradiating materials placed inside it with an X-ray source and measuring the X-ray fluorescence peaks that are emitted from the material.

As the fluorescent X-ray intensity is a function of concentration, quantitative analysis is also possible by measuring the amount of X-rays at the wavelength specific to each element. Another silicon sample coated in the same run as measured in Figure 7.3 was measured in the EDXRF as well, which gave an indium layer thickness of 282 $\pm$ 10 nm as shown in Figure 7.4. This approach was used to measure the thickness of the indium layers for the rest of the study.

Using this technique the layer thickness of each indium run can be controlled by weighing each metal piece that prior to loading it into the evaporator. In practice, the maximum weight that can be used is 0.28 g. Any more than that and the indium gets too heavy and falls out when melted instead of evaporating. One basket of 0.28 g of indium equates to an evaporated layer of 200-350 nms thick, depending on what the sample height is in the

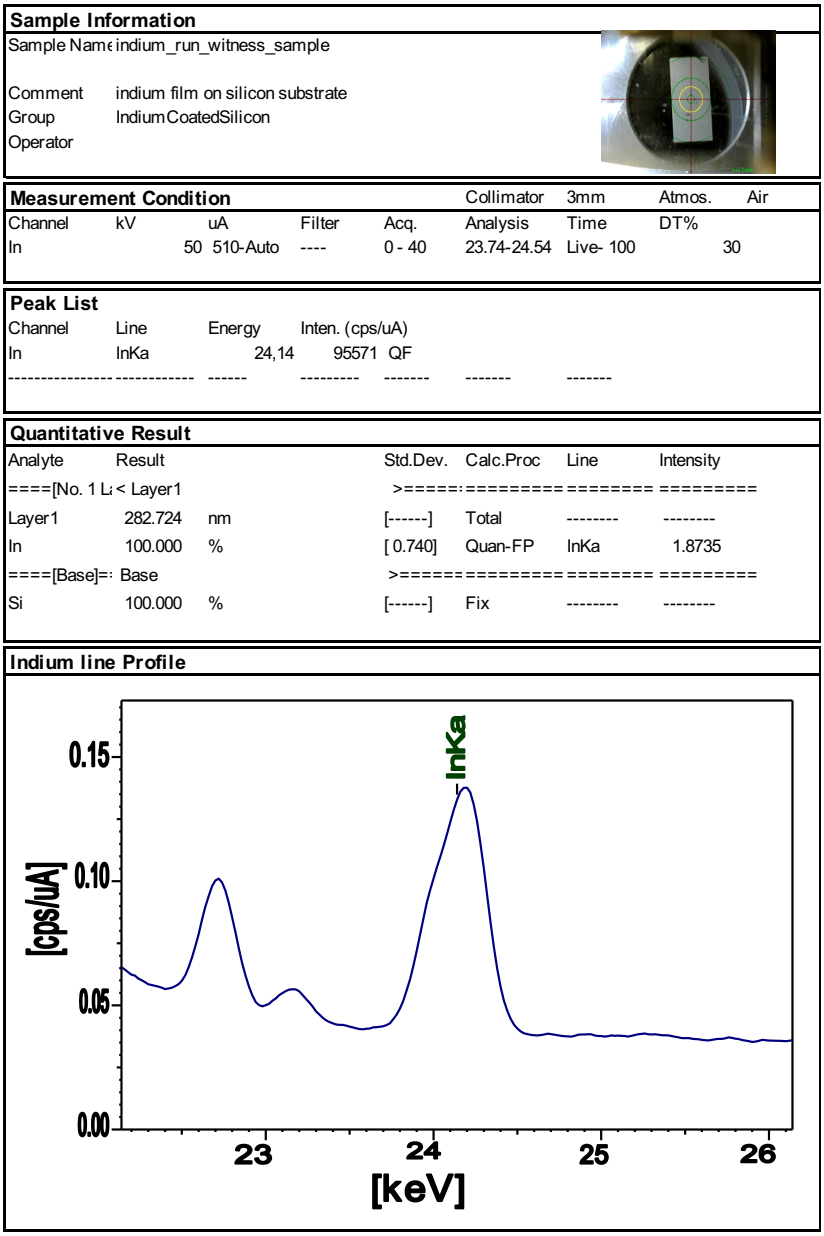

Figure 7.4: EDXRF measurement of the indium thickness on a coated silicon witness sample. The indium Kα line is seen at 24.2 keV and its integrated strength is proportional to the thickness of the indium layer deposited on the sample.

evaporation chamber, and how long the samples are allowed to be coated. The total bond thickness of the evaporated indium layer is the witness sample thickness multiplied by two, as two samples are contacted together to form each bond.

7.3.2 Structure of thermally deposited indium layers

Thin layer structure can be very different from the bulk structure for many materials, and visually there were differences in the reflectivities of the indium layers depending on their

thickness. Therefore the structure of the thin deposited layers was investigated, and compared to bulk indium which has a tetragonal crystal structure [179]. Two samples were coated with indium layers of thickness 200 nm and 500 nm as measured in the EDXRF, using fused silica as a substrate material instead of silicon, as the crystalline nature of silicon would impact measurements but the amorphous fused silica should not. The samples were measured in a Siemens/Bruker D5000 X-ray Powder Diffraction (XRD) System [180]. Results of this test are shown in Figure 7.5 and compared to diffraction peaks of bulk indium [179] which are overlaid in the upper left hand corner.

The measured diffraction peaks indicate a well defined crystal structure in both deposited

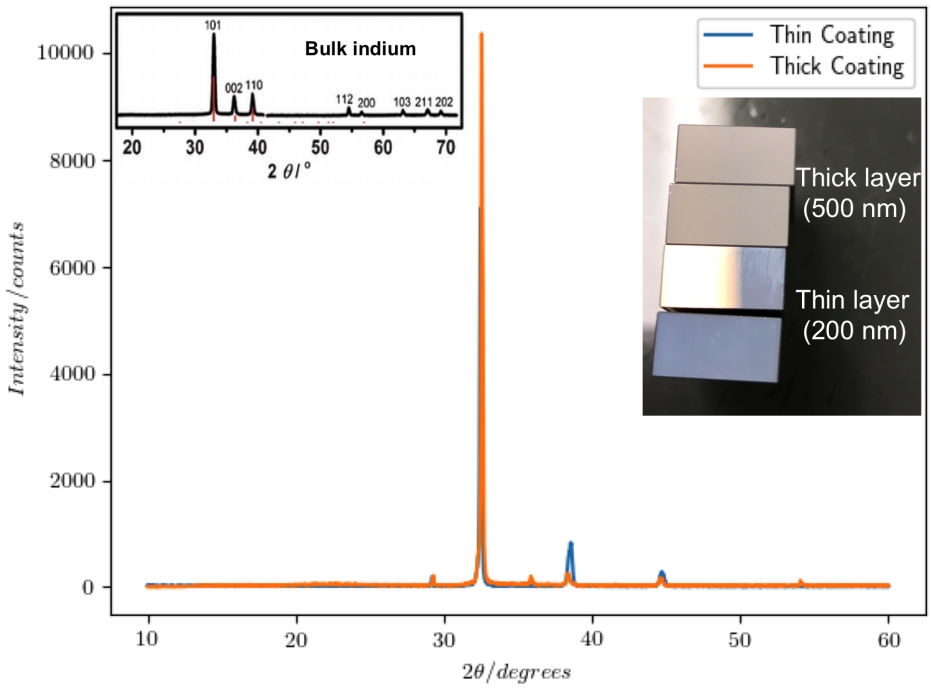

Figure 7.5: Measured diffraction peaks of thermally deposited indium, with bulk indium diffraction peaks overlaid in the top left. Both layers are imaged on the right for reflectivity comparison, where the thinner layers on the bottom two substrates are highly reflective and the thicker layers on the top are less reflective.

indium coatings, with the dominant peaks around 33 and 39 degrees matching those of bulk indium. The integral of the diffraction peak at roughly $2 \cdot \theta = 39$ degrees is larger for the thinner coating than for the thicker one, indicating that the growth mechanism favours addition to a particular crystal face first which then changes over the length of deposition time. As the layers are deposited onto the samples, they are observed to be highly reflective at the start, then get progressively cloudier as the coating gets thicker. A comparison image of this is shown on the right in Figure 7.5. The change in crystal structure as the indium layer grows thicker could account for the difference in surface roughness for different coating thicknesses.

7.4 Cold welding the joint: mitigation of indium oxide

In practice the most difficult part of using indium as a bond material is dealing with the indium oxide layer. Bonds will only occur if pure indium comes into contact with itself, other metals, or non-metallic oxides such as fused silica. However, an oxide layer forms nearly instantaneously on the indium surface as it is exposed to air, starting at 3-4 nm and passivating at 8-10 nm after 2-3 days [93]. If the pure indium stays encased in this shell of oxide, a bond cannot be created [107]. Two different oxide mitigation approaches are discussed. One approach is to prevent the oxide from forming, the other is to remove the oxide immediately before bonding.

7.4.1 Prevention of oxide formation: inert gas approach

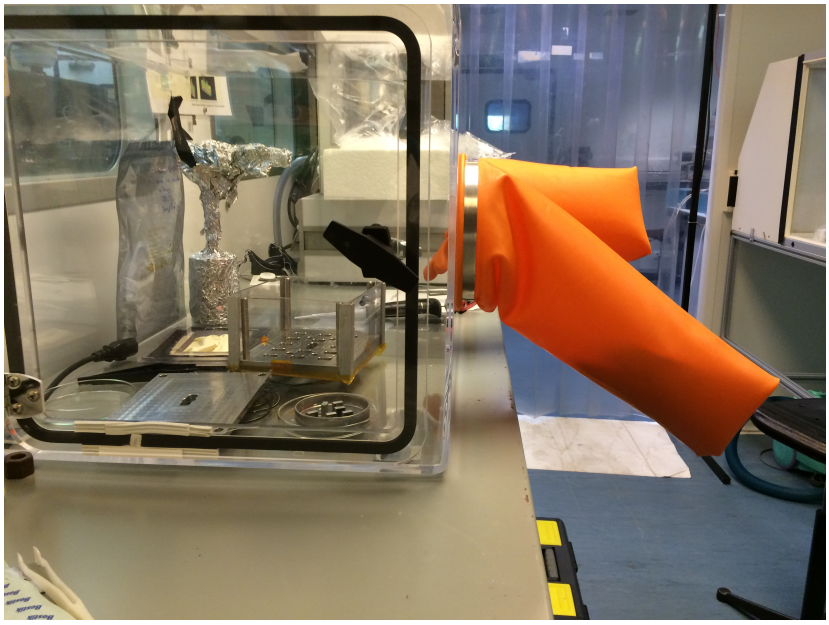

Figure 7.6: Inert gas environment for cold welding indium coated samples; glovebox filled with argon kept at positive pressure with the bonding jig and samples inside.

Here the approach of keeping the native oxide from forming was tried. The evaporator chamber was flushed with argon several times before adding the clean silicon samples. The indium deposition was carried out under vacuum, after which the coated samples were transported from the evaporator to a glovebox purged with argon, and then placed into a bonding jig which is shown in Figure 7.6. The jig was placed inside an airtight polycarbonate box and purged with argon for transport to the strength tester, which was used to apply pressure during bonding, while keeping the jig under positive pressure argon flow during the whole bonding process.

The full diffusion bonding set-up is shown in Figure 7.7, with the specific temperature and pressure values explained in Section 7.5.

7.4.2 Oxide removal: chemical etch approach

The second approach was to allow some oxide formation after the indium film deposition, and to remove it just before cold welding the indium surfaces together for bonding. This was achieved by chemically etching the oxide from the indium, drying with nitrogen gas, and immediately cold welding the samples together. A 7-10% solution of hydrochloric acid and de-ionised water was used for the chemical etch. Each indium coated silicon substrate was placed in this solution for 40 seconds, then immediately placed in clean deionised water to quench the acid. After this step the samples were submerged briefly in methanol to get rid of the remaining water. They were then dried with nitrogen and cold welded together and set in the bond jig.
The full procedure is described in Appendix A. Once the indium is cold welded together the rest of the procedure can be performed in air, as the indium surfaces are no longer in contact with air. The jig was transferred to the strength tester where the samples were heated up to 145 °C and compressed to 1 MPa for 60 minutes in an air atmosphere, using the set-up shown in Figure 7.7.

7.4.3 Comparison of oxide mitigation approaches

To see which approach led to stronger bonds, a batch of three bonds using the inert gas approach were bonded during the same week as a batch of three chemically etched bonds. Factors such as sample surface preparation, amount of indium deposited, evaporation time, and temperature and pressure during bonding were kept the same in both runs, only the oxide removal approach was changed. All samples were then tensile strength tested at the same time, as per the procedure detailed in Chapter 3. These breaking stress results are shown in Figure 7.8.

As is also seen in Figure 7.8, the chemical etch approach led to stronger bonds. If the current facilities allowed a seamless transition from evaporator to bond jig in an inert gas environment then this approach would most likely work well. Unfortunately, in practice it is very difficult to keep the samples in a fully oxygen free environment through all the steps, especially during transport from the evaporator to glovebox and during the bonding itself. The glovebox was kept at positive pressure when samples were packed into the bond jig, as was true for the transport jig box, but the possibility of air leaks was still quite high

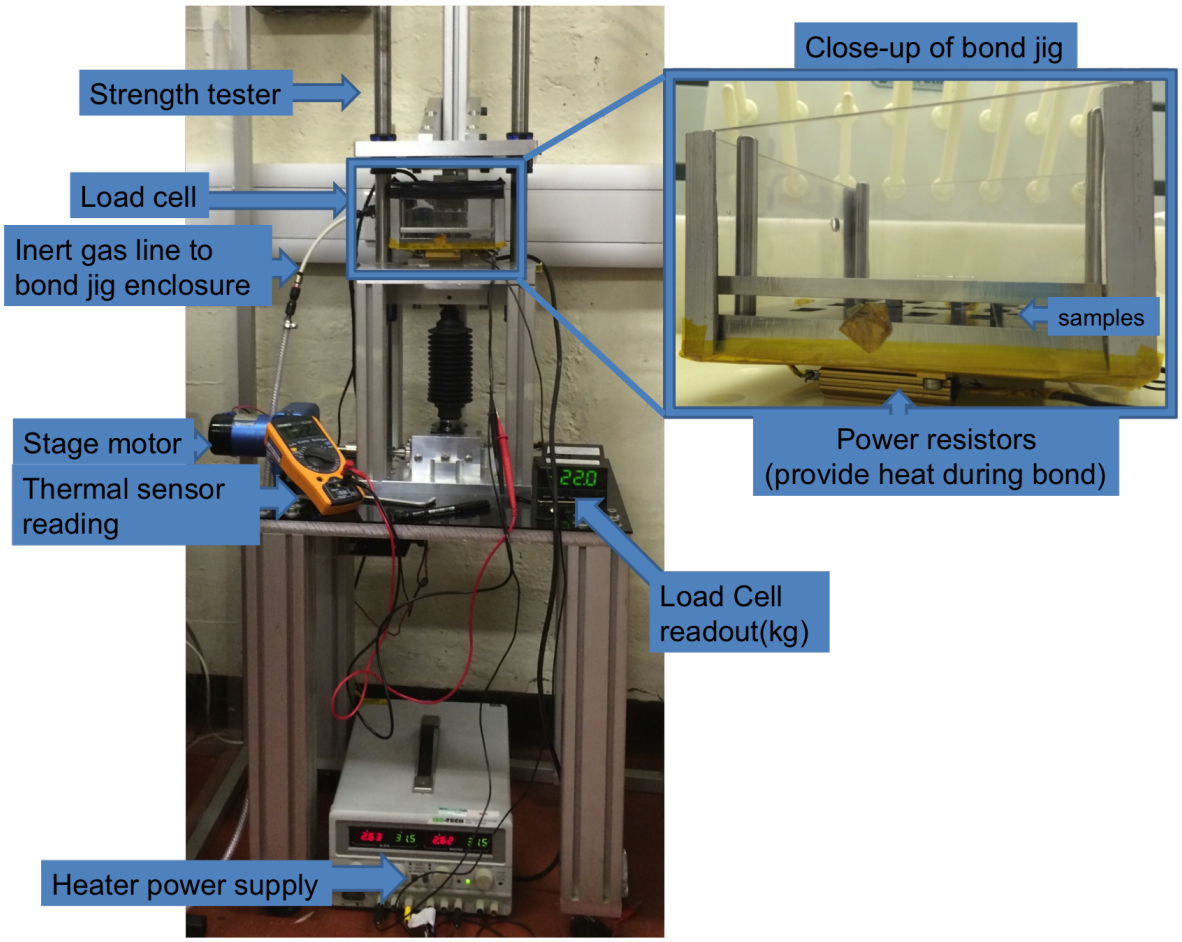

Figure 7.7: Pressure bond setup

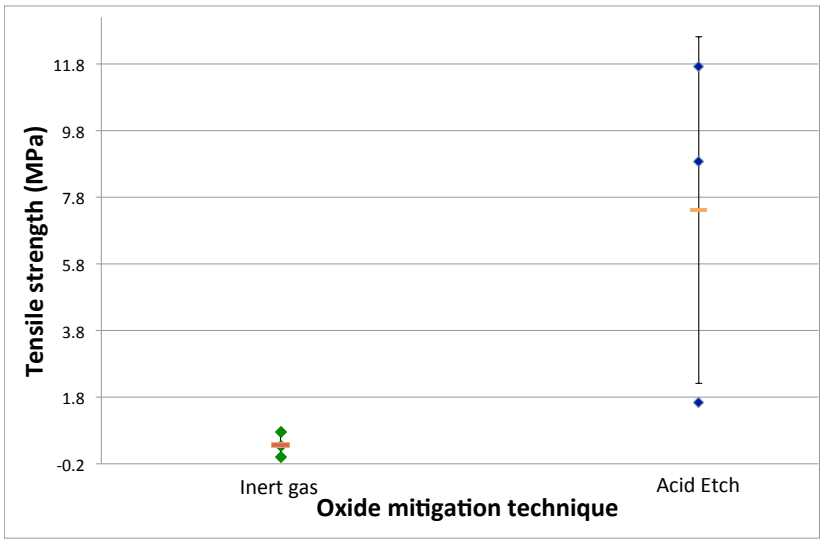

Figure 7.8: Strength test results of different oxide removal approaches

for most of the procedure. Ideally this approach should take place in a a single vacuum or inert gas chamber for the entirety of the procedure. This is not a feasible option for non-industrial labs, and indeed would be difficult in practice for detector suspension assembly procedures. Therefore the chemical etch approach was used for the remainder of the study.

7.5 Heat and pressure approach 1: diffusion bonding

The first approach to provide the necessary heat and pressure to create diffusion bonded indium was a retrofit to the MKII Strength Testing Machine at IGR [135]. While this strength tester is usually used to test the strength of fused silica fibres, it can also be used to provide the necessary calibrated pressure to samples compressed by its pressure foot. To properly do this, a custom bond jig that fits under the pressure foot was developed. This bond jig, shown in Figure 7.7 is a metal assembly with cut outs on the bottom plate where the 5x10x20 mm silicon samples sit. Two power resistors were attached to the bottom plate and hooked up to a 60 V power supply to provide heat. A PT1000 variable resistor sensing element was epoxied to the bottom metal plate equidistant to both resistors to measure the temperature of the samples and bond jig via the temperature dependant resistance of the PT1000 sensor (see Appendix A).
Six 5 mm x 1 20mm x 20 mm silicon samples had indium layers thermally deposited onto them and were cold welded together following the procedures explained in Section 7.4.2 to form three 5 mm x 1 0mm x 40 mm samples with an indium bond in the middle. Three samples of this type were placed equidistant from each other in the bonding jig to complete the bonding process. Having three samples per batch kept the distribution of pressure equal between them via a three point contact. Once they were placed into the bonding jig a flat stainless steel plate was carefully placed over the top of the samples. The jig was then placed in the retrofitted strength testing machine.
The samples were compressed and then heated up to 135 °C. The heat is created by supplying 60 V across the power resistors attached to the bond jig, while monitoring the temperature via the temperature dependent resistor (which is also attached to the bond jig plate). The retrofitted strength tester provides at least 1 MPa per sample area of compression as monitored by the load cell readout. The load cell was calibrated by hanging a 1 kg and 2 kg weight from it and verifying that the readout read 1.00 kg and 2.00 kg. The experimental setup is shown in Figure 7.7, and the full procedure is explained in detail in Appendix A.
Each bond run took about an hour, monitoring the temperature as it ramped up to 135 °C and then turned the voltage down gradually to hold the temperature steady at 135 °C for 20 minutes. Typical bond temperature ramp curves are shown in Figure 7.9. For a diffusion bond to form between indium layers an elevated temperature is required, however it is not

necessary to heat the indium up to its melting point of 157 °C [181].

Indium bonds that were created in this way were strength tested to judge bond quality

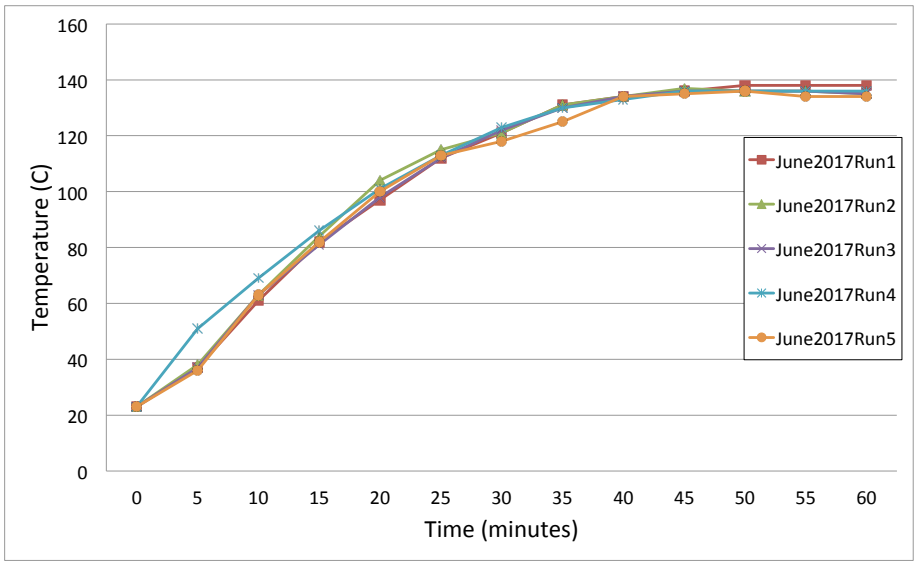

Figure 7.9: Temperature curves for June 2017 indium diffusion bond runs

using the same Zwick-Roell 200 kN machine [135], that was used to measure the tensile strength of hydroxide catalysis bonded sapphire in Chapter 3.

It should be noted that the tensile strength of hydroxide catalysis bonds is very important because they are used to bond interfaces together under high shear and tensile stress, in a situation where there is a tendency for peeling to take place. Indium will only be used in compression bonds. So while the tensile strength of the indium bonds is not as important as for hydroxide catalysis bonds, it is used here as a standard by which to judge bond quality and repeatability.

After breaking the bonds during tensile strength testing, the bond interfaces were visually inspected and photographed and then imaged under an Olympus BX51 Nomarski Microscope [160] to judge bond quality. Well bonded indium layers were visibly torn from one silicon substrate and adhered to another and there was a tell-tale "speckle pattern" as well which indicated a diffusion bond had been formed over the surface. This can be seen in Figure 7.10. Conversely, a poorly bonded surface looked very similar to a freshly deposited indium coating, or had visibly cloudy areas that indicated oxide formation had impeded cold welding in the first place as shown in Figure 7.11.

Strength testing was performed to gauge two things, the repeatability of the bonds over a statistically significant number of bond runs and also the comparison of bond strength over

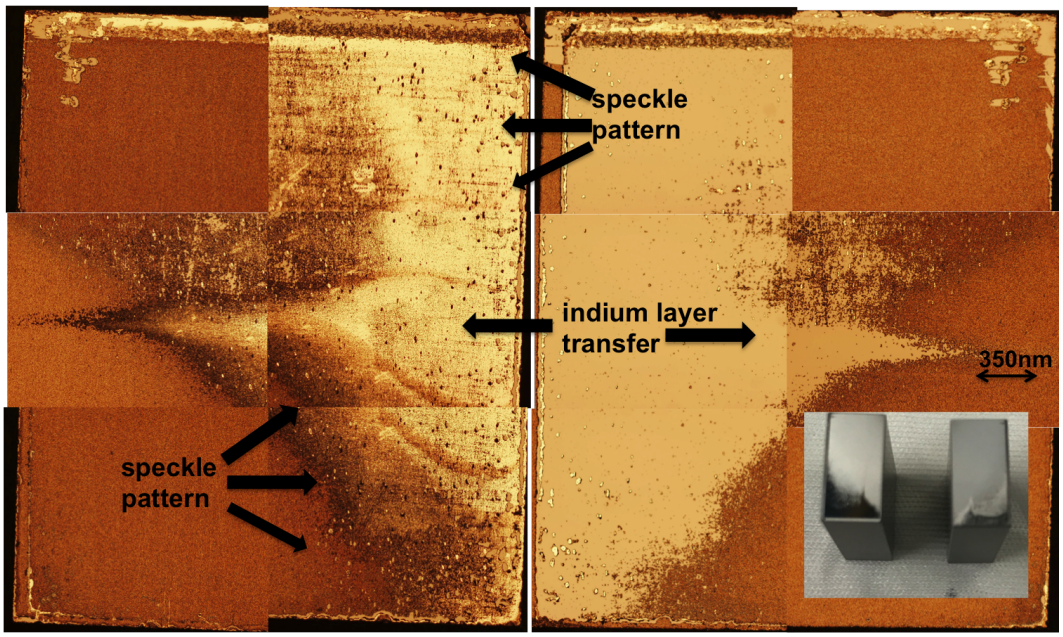

Figure 7.10: Post-break visual inspection of the two halves of a high quality indium diffusion bond between silicon. The large images show the two silicon samples that were bonded together at 5x magnification under the Nomarski microscope, with a smaller inset photo of the same surfaces. The tensile strength at break was 6.1 MPa for this sample.

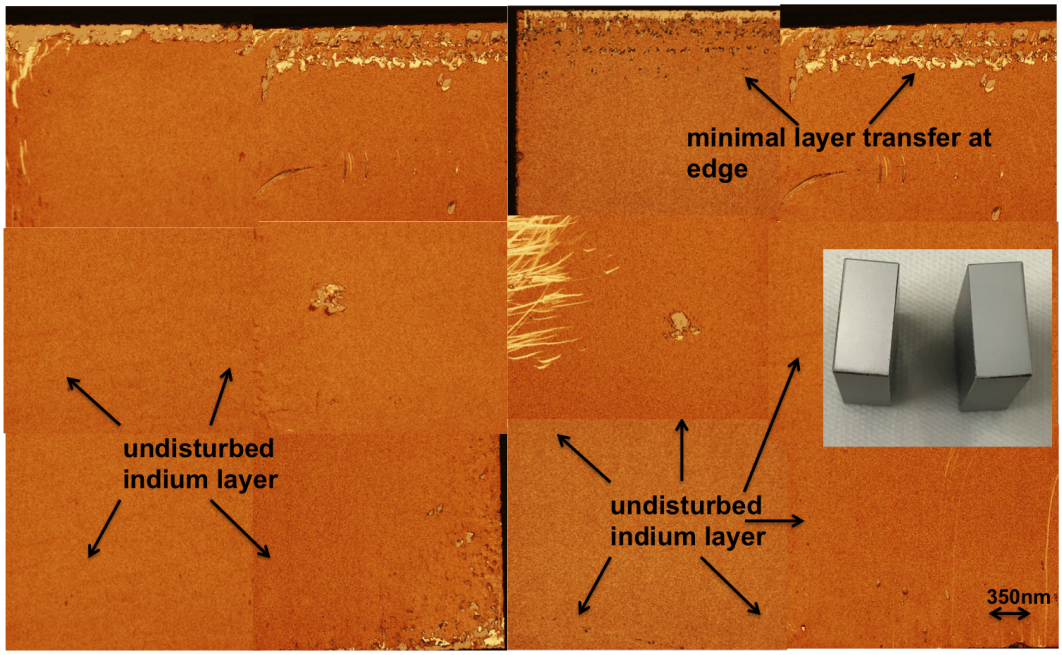

Figure 7.11: Post-break visual inspection of the two halves of a low quality indium diffusion bond between silicon. The large images show the two silicon samples that were bonded together at 5x magnification under the Nomarski microscope, with a smaller photo of the same surfaces inset at the bottom right. The tensile strength at break was 1.4 MPa for this sample.

time. Bonds of varying ages were strength tested at the same time to see if their strength changed, which could indicate indium oxide growth occurring after bonding. There was no trend in strength over time, as seen in Figure 7.12 which indicates that if the initial cold

weld of oxide-free surfaces is successful then the indium bond will remain strong over time with no oxide growth or degradation. The same strength results are plotted as a function of

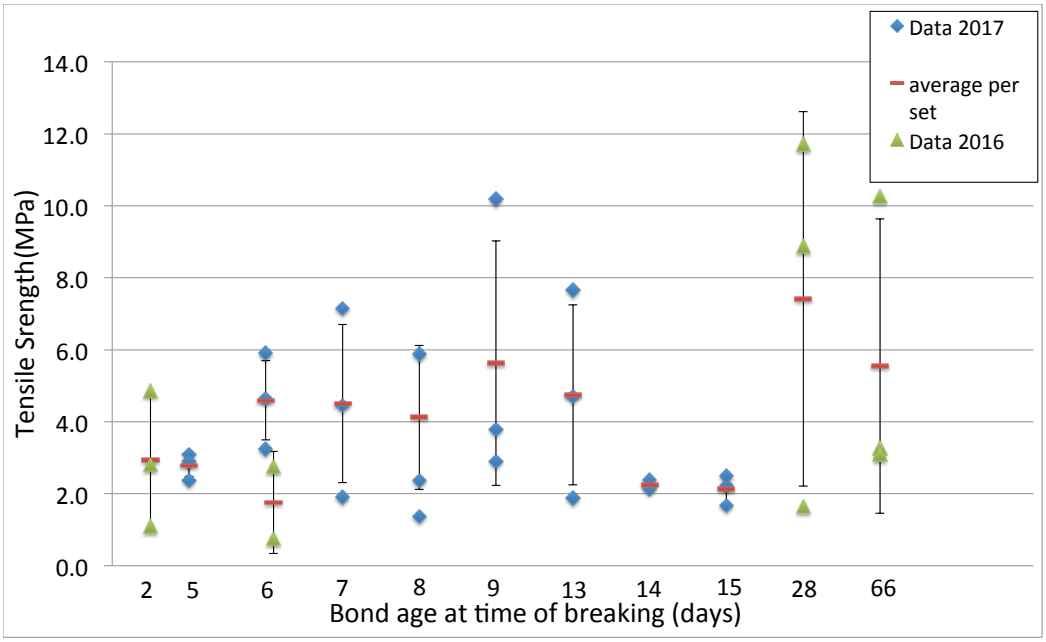

Figure 7.12: Tensile strength as a function of age, for all diffusion bonded indium.

indium layer thickness, as shown in Figure 7.13. These results show that consistently good

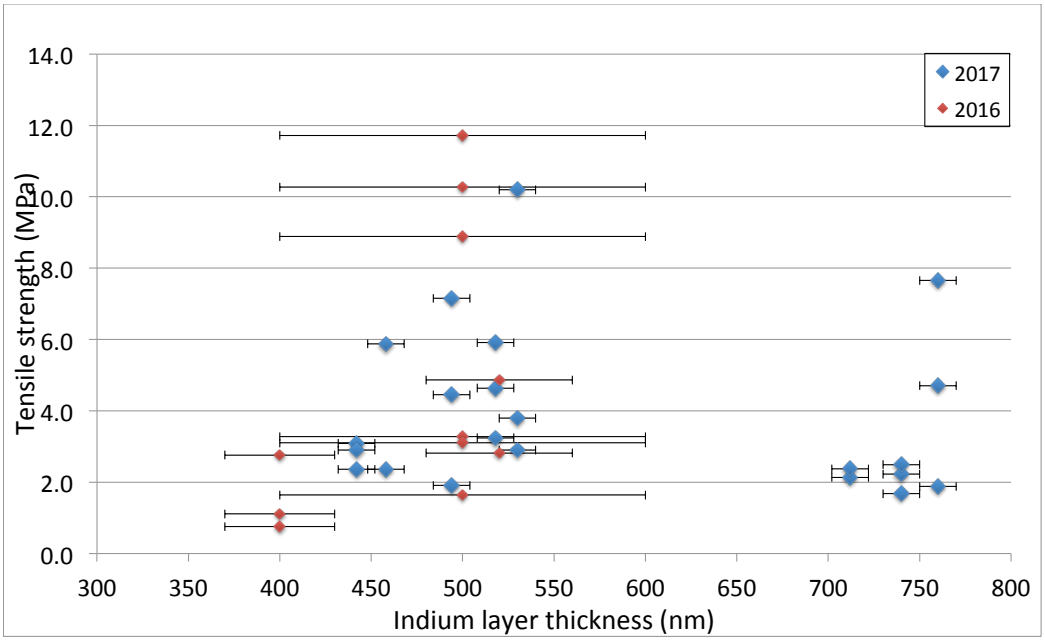

Figure 7.13: All diffusion bond strength results as a function of deposited indium layer thickness.

quality indium bonds can be achieved using 400 nm to 700 nm thick indium layers.

7.6 Heat and pressure approach 2: induction bonding

With cryogenic detectors that have indium bonds under compression in its suspension design, in-situ indium bonding procedures were considered. Due to the geometry of suspension and optic interface parts, applying direct compression and prolonged heat to the optic-suspension interface may not be feasible. Therefore, use of an induction heater was proposed as a contact-less method of creating bonds by heating the jointing material, indium, without heating the non-metallic optics or suspension components.
An induction heater is composed of a small driver circuit and a large induction coil, called working coil, that metals can be placed inside and heated. When the circuit is powered, the working coil has an alternating electric current running through it at a certain frequency defined by the coil's geometry and the circuit components. This AC current produces an electromagnetic field (EM field) in and around the working coil, which will induce an equal and opposing current according to Lenz's law in metal objects that are placed inside the coil, called an eddy current[182]. These eddy currents flow against the electrical resistivity of the metal, which generates localised heating [183]. A schematic of this is seen in Figure 7.14.
The working coil and the metal object it heats function in a similar way to a transformer,

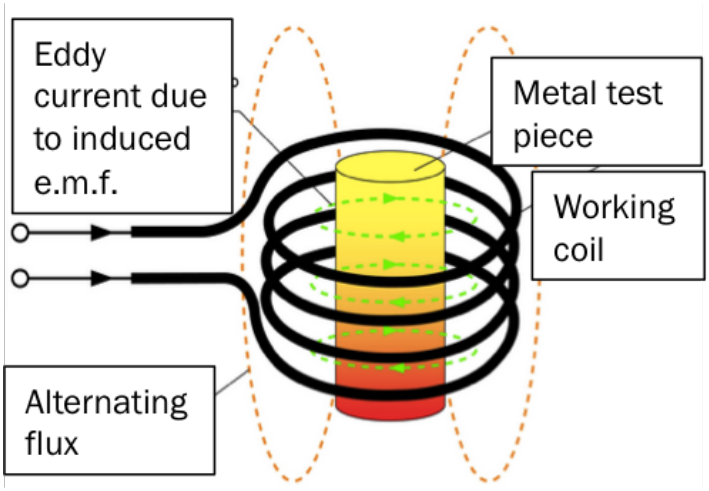

Figure 7.14: Schematic of induction heater coil and EM field lines [183].

where the working coil is the transformer primary and the metal to be heated is the transformer secondary [182]. In a true transformer resistive heating is minimised to minimise power loss, usually by making the transformer coils out of a good electrical conductor like copper, which has an electrical resistivity of 16.8 nΩ m. For an induction heater the opposite is desired, the metals that are easiest to heat have a higher resistivity and are not the best electrical conductors, iron for example has an electrical resistivity of 100 nΩ m.
Most metals can be inductively heated, but some heat much faster than others. The rate of heating of the metal is dependent on the frequency and intensity of the induced cur-

rent, as well as the properties and geometry of the metal to be heated. The specific heat, magnetic permeability, and the electrical resistivity of the metal all matter to the rate of heating [183]. Metals that have a high electrical resistance will resist the induced currents more, and heating will happen faster. Ferromagnetic metals like iron heat faster than non-magnetic metals, as there is also heat generated via magnetic hysteresis loss [183].
The "skin effect" whereby most of the eddy currents produced in the metal piece are concentrated in its outer layer, or skin, is highly dependent on the frequency of the working coil. Increasing the coil frequency will shift the induced eddy currents closer and closer to the outer layer of metal, which can be calculated as the skin depth δ_s [182]

$$\delta_s = \sqrt{\left[\frac{\rho_r}{\pi f \mu}\right]} \tag{7.1}$$

where f is the working coil frequency, μ is the permeability of the metal, and ρ_r is the electrical resistivity of the metal. Indium has an electrical resistivity of 84 nΩ m at room temperature, and 291 nΩ m at 154 °C [184]. Most conducting metals have a permeability close to the vacuum permeability, $\mu_0 = 4\pi \cdot 10^{-7}$Wb/Am. Given a volume magnetic susceptibility of $\chi_v = 7x10^{-6}$ for indium, its magnetic permeability can be calculated via

$$\mu_{\text{indium}} = \mu_0(1 + \chi_v). \tag{7.2}$$

Therefore $\mu_{\text{indium}} \approx \mu_0$ can be assumed for calculations. The resonant frequency of the induction heater can be calculated via

$$f_{\text{resonant}} = \frac{1}{2\pi\sqrt{LC}} \tag{7.3}$$

where C is the capacitance of the driver circuit capacitor and L is the inductance of the working coil. This frequency can also be measured by contacting oscilloscope leads across the coil while running the circuit and viewing the sine wave frequency on the oscilloscope. The inductance L can be calculated using the equation for a hollow core inductor, Equation 7.4, where μ_0 is again the vacuum permeability, N is the number of coil turns, A the coil area and l the coil length.

$$L = \frac{\mu_o N^2 A}{l} \tag{7.4}$$

Equation 7.1 through Equation 7.4 were used to determine the induction heater characteristics in the following sections.

7.6.1 Initial industrial induction heater tests

The first successful attempt at induction heating of indium for bonding was carried out in Glasgow using an industrial Draper induction heater [185] by melting a 25 mm diameter, 50 µm thick indium foil in between two sapphire substrates, one 25 mm diameter cylinder, one 50 mm diameter shown in Figure 7.15.

The sapphire was cleaned with methanol and the foil briefly immersed in dilute HCL to

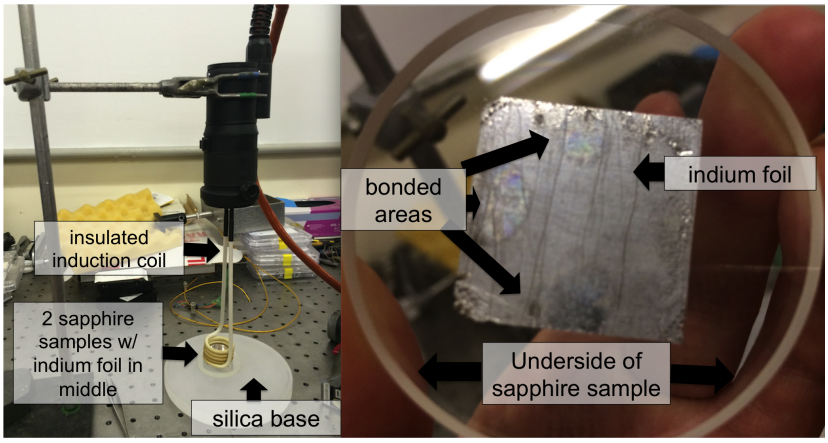

Figure 7.15: Draper induction heater coil and sample on left, bonded sample on right.

remove the indium oxide. It was rinsed in DI water, then rinsed with methanol, then dried with nitrogen gas and set in between the substrates. No heat or compression was applied at this point. A 30 mm diameter coil was set over the samples and heated for slightly over a minute before turning the heater off. The temperature of the sapphire sample at this point read 200 °C, measured with a non-contact IR gun pointed at the indium foil. After letting the sample cool it was inspected to find 30% of the indium layer had melted, with fringes visible in some of the bonded sections, seen on the right side of Figure 7.15 The sample was not strength tested with a machine, but did pass finger strength tests.

7.6.2 ELiTES project: induction bonded indium at the ICRR

Convinced that induction heating of indium in between sapphire was at least somewhat feasible, an induction heating of indium project was pursued by the author at the Institute for Cosmic Ray Research (ICRR) at the University of Tokyo in April 2016 as part of the ELiTES (ET-LCGT Telescopes: Exchange of Scientists) exchange program.

The Draper tool used in Glasgow was an industrial tool built to heat large metal parts such as M12 bolts on car wheels, and therefore had a much higher power rating (1750 W) and lower frequency (50 Hz) than was required to heat the relatively small amounts of indium used here. Here a lower power and higher frequency induction heater was built with the

aim of being better suited to the small amounts of indium metal that would be used in GW detector bonds. The circuit shown in Figure 7.16 was built and several different coil and capacitance values were experimented with in order to find an optimised design for indium heating, following recommendations on building induction heaters by RM Cybernetics [186]. Operating frequencies of 100-400 kHz range were focussed on in this test, to keep the eddy currents as close to the surface of the thin metal pieces as possible. Using an inductor frequency in this range, an electrical resistivity of 84 nΩ m, and a magnetic permeability of $\mu_{\text{indium}} \approx \mu_0$ would equate to indium skin depths of $\delta_{s1} = 461$ µm/100 kHz and $\delta_{s2} = 230$ µm/400 kHz as calculated using Equation 7.1.

The working coil in this circuit is centre tapped meaning that instead of a simple one coil

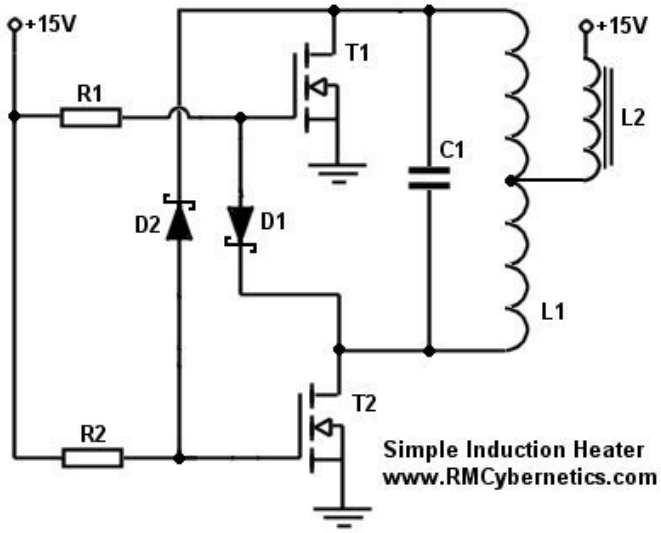

Figure 7.16: Low power induction heater circuit

solenoid, the working coil consists of two smaller coils that are joined in the middle, which can be seen in Figure 7.17. The centre of the coil is connected to the positive supply and then each end of the coil is alternately connected to ground by the transistors so that the current will flow back and forth in both directions [186].

There are voltage and current spikes during normal use of this circuit, as well as continuous operating currents of up to 10 A. Thus the components in Table 7.1 were selected to withstand high voltages and currents, as well as potentially higher temperatures due to the operating current. Additionally, the mosfets were mounted on heat sinks, thick copper wire that was specified to the operating currents was used and the temperature was carefully monitored. Also, the heater was not used continuously for more than 5 minutes, to allow the circuit components time to cool down between bonding runs.

The frequency listed in Table 7.1 was measured by hooking up a probe across the working coil during operation and viewing the sine wave output on an oscilloscope screen. The operating frequency of the circuit depends on the geometry of the working coil and the

Circuit component /characteristic	Values /part number
R1/R2	240 Ω/0.6 W
D1/D2	1N4002-E3/73 100 V/1 A
T1/T2	STP30NF10 100 V/35 A
L2	2 mH (17 turns on ferrite core)
C1	0.5 µF
L1	0.95 mH
f_{resonant}	247 kHz (4 turn copper coil 25 mm diameter)

Table 7.1: Circuit component values, part numbers, and operating frequency used in the ICRR induction heater circuit

capacitance (value C1) in the circuit. If either of these is changed the resonant frequency of the circuit will also change. The frequency can be calculated using Equation 7.1, where C is the capacitance listed in the table, and L the inductance of the working coil.
For example, using $C = 0.5\mu F$ and $L = 0.95$ µH gave an expected frequency of 231 kHz, which was measured to be 247 kHz, matching reasonably well. The working coil was hand-wound and its inductance value was not measured directly but roughly calculated using the equation for a hollow core inductor, Equation 7.2. The completed circuit required a power

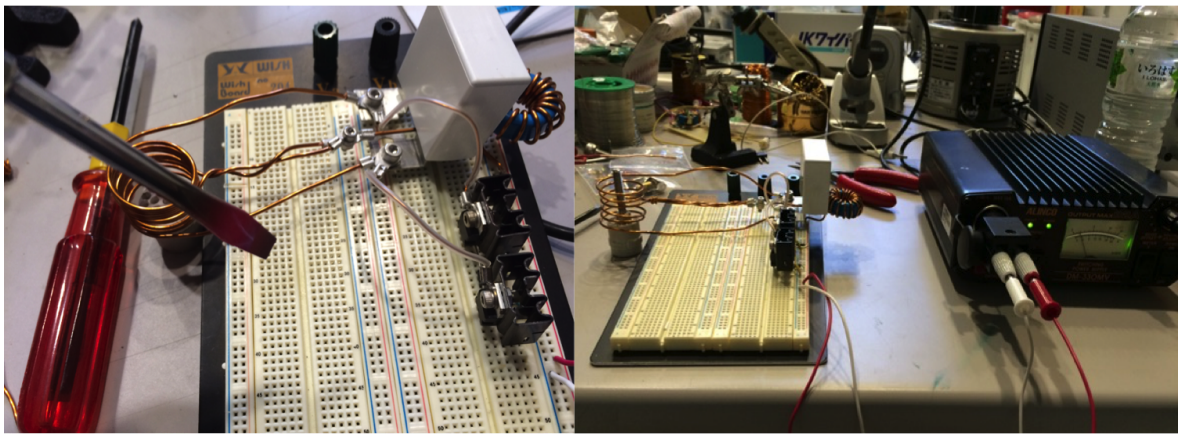

Figure 7.17: Induction heater circuit at the ICRR, on the left heating a screwdriver, on the right a sample with indium in the middle

supply unit (PSU) that can provide an immediate input voltage of 15 V DC and up to 5 A of current otherwise it will fail to resonate. If the power supply is not able to provide at least this much current and voltage to the circuit when it is switched on, the transistors in the circuit will not have a high enough voltage supply to work correctly and they will start to heat up, which risks damaging the circuit [186]. A 8 A power supply worked for this circuit. In normal operation this induction heater circuit draws 2-5 A with a supply voltage of 15 V, which gives it a maximum power rating of P = IV = 5x15 =75 Ws, much lower than the Draper tool previously used in Glasgow which had operating currents of 7.5 A, a voltage rating of 230 V, for a power of 1750 W.

A steel screwdriver tip was first inserted into the working coil to test the circuit, and it heated to red hot within 30 seconds, as seen in Figure 7.17. After the successful screwdriver test a 0.55x1 cm square piece of indium foil was inserted in the same coil. It took 2 minutes to reach its melting temperature of 157 °C.

7.6.3 IGR induction bonding procedure

A ZVS 12-48 V 20 A 1000 W induction heater circuit and a high voltage/high current power supply were procured to continue this induction heating study at the University of Glasgow. This PSU, a PeakTech 1560 switching mode power supply [187], can supply up to 32 V and 30 A. It was current limited to 15 A for safety, but in practice operating currents did not get over 10 A (with a power rating of 320 W). The wire leads between the circuit and the power supply were rated to withstand over 15 A. The circuit had six 0.33 µF capacitors as received, shown in Figure 7.18. Two of these capacitors were removed initially to increase the resonant frequency of the circuit.

A working coil was fixed tightly between two brass terminals. A selection of coil geometries, shown in Figure 7.19 was tested by putting one 50 µm indium foil topped 5 mmx10 mmx20 mm silicon sample into the centre of the working coil. Then the induction heater was powered on and the indium layer monitored for signs of melting, as shown in Figure 7.18. The temperature of the indium layer, the working coil, and the circuit were all observed with an infra-red FLIR camera [188] during these tests. The temperature of the circuit components was seen to rise at running times of longer than two minutes, so the running time of the circuit was kept to 2 minutes or less for safety reasons. Many different working coils were tried, using pure copper wire of 2 mm diameter up to 6 mm diameter copper rod. Copper rod with a diameter less than 6 mm was found to be insufficiently rated for the high levels of operating current, resulting in the working coil quickly heating up and annealing itself, as can be seen in some of the test coils on the left in Figure 7.19. Bare copper is also recommended, as most wire insulations will melt at these operating temperatures. Of the coils tested, a 4 turn, 6 mm diameter copper rod, 2.7 cm inner diameter, 3.9 cm outer diameter and 3.3 cm long working coil performed the best, melting indium foils 50 µm thick on silicon substrates after run times of under a minute.

Using Equation 7.4, a working coil inductance of 0.43 µH can be calculated, and using Equation 7.3 to calculate f_{resonant} where $C = 4 \cdot 0.33 = 1.32$ µF gives a calculated resonant frequency of $f_{\text{resonant}} = 211$ kHz. The true frequency of the circuit was measured across the working coil with a oscilloscope to be 208 kHz, agreeing well with the calculated value. Using Equation 7.1, a frequency of 208 kHz, electrical resistivity of 84 nΩ m, and a magnetic permeability of $\mu_{\text{indium}} \approx \mu_0$ a skin depth of 319 µm is calculated for indium.

The circuit diagram for Figure 7.18 was not available from the manufacturer, however it

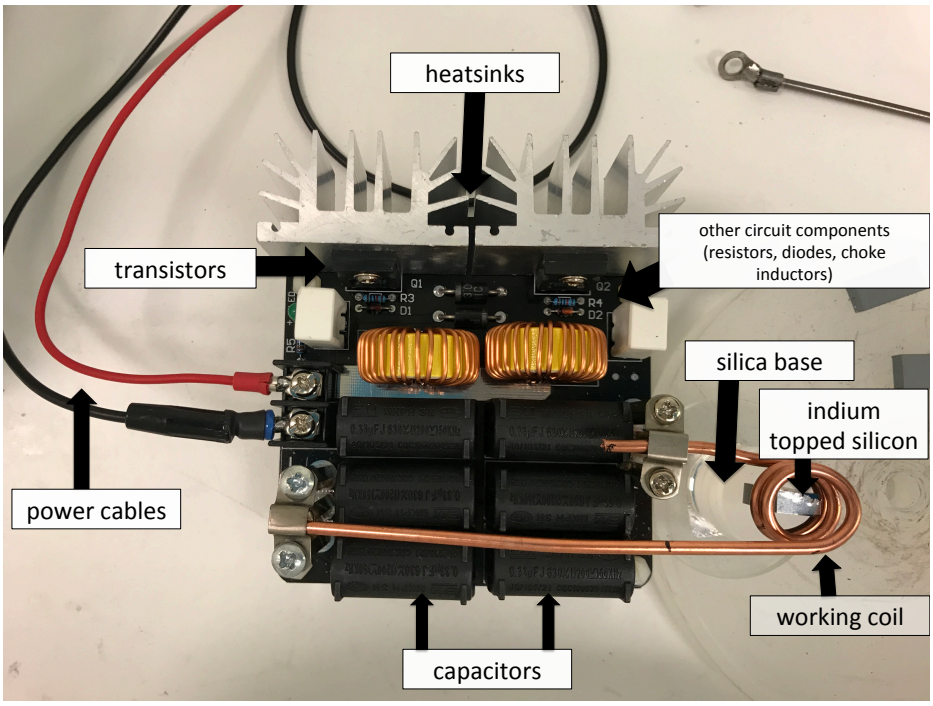

Figure 7.18: Induction heater

Figure 7.19: Induction heater test coils

was available on-line (Figure 7.20 [189]). The finished setup using this coil is shown in Figure 7.21. Silicon samples, 5 mm x 10 mm x 20 mm, were prepared by solvent cleaning and then indium coating them in an evaporator [156]. The indium oxide was removed with an acid etch, an indium foil ≈50 µm thick was added between them and the two substrates were cold welded together, as per the procedure outlined in Appendix A. The finished 5 mm x 10 mm x 40 mm samples were set upright on a silica base with the bond interface centred in the coil in x, y, and z directions for optimal and uniform heating.

The cold welded samples, three per run, were induction heated and compressed with 11.1 kg of weight, placed carefully on top of a plexiglass and metal jig. A microscope slide was fixed between the silicon samples and the plexiglass plate to shield the plexiglass from the heat

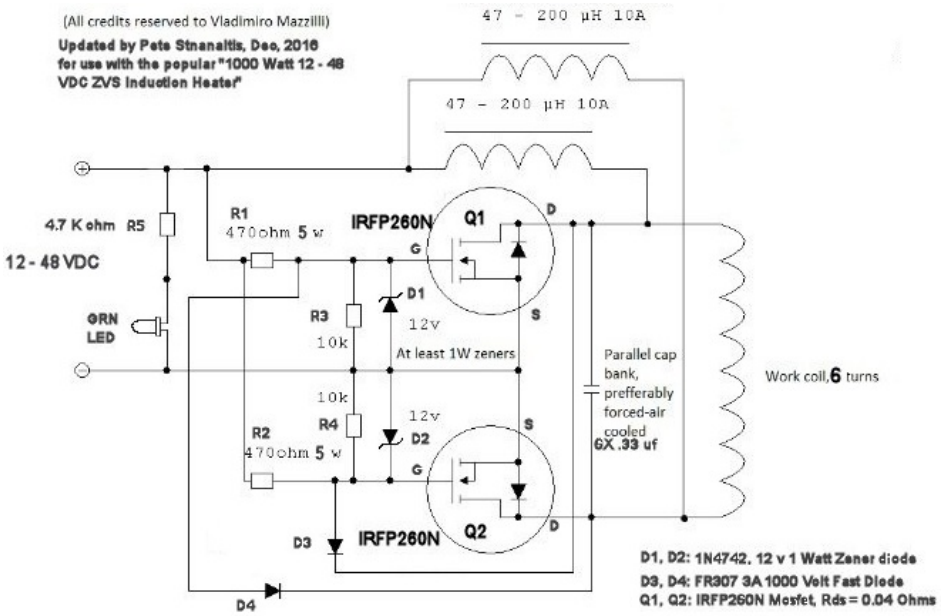

Figure 7.20: Induction heater circuit diagram

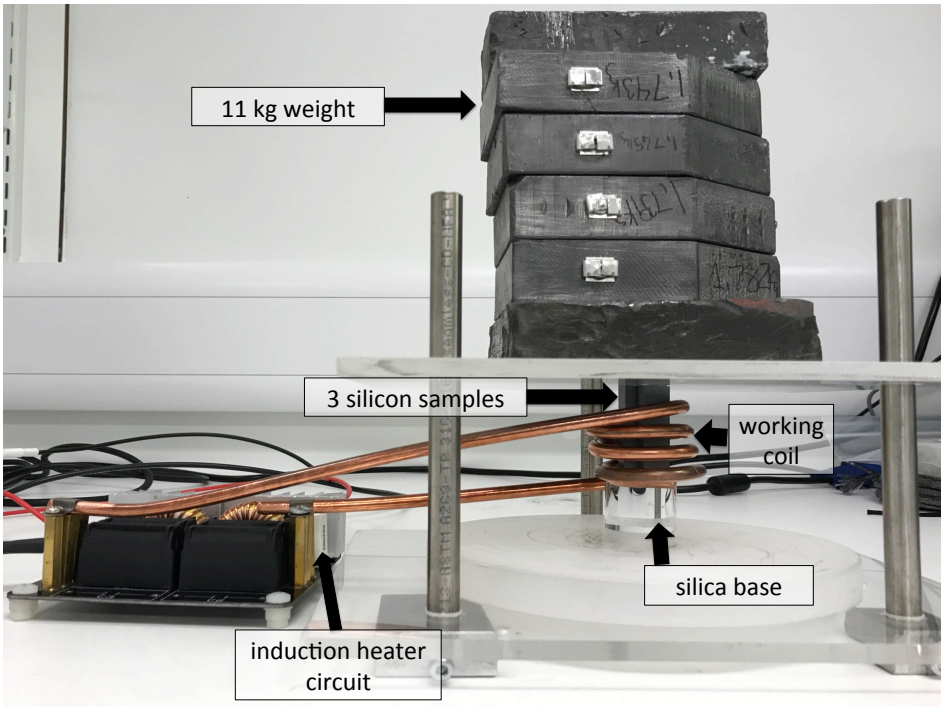

Figure 7.21: Induction bonding setup

of the inductor coil. Using $\sigma = \mathrm{F/A}$, where the area was three 4.7 mm x 9.7 mm bonds (the bond surface being chamfered down from the 5 mm x 10 mm outer dimensions) gives 0.8 MPa of pressure across the total bond area. The same weight and bond surface area was used for all induction bonds in this study. Although indium bonds are currently being considered for use in cryogenic detectors, the bond surface area per test mass and the weights of the test masses are not yet fully defined. It is possible the induction bonds in cryogenic

detectors could see higher pressures of 3 MPa. This is determined by the weight of the test mass and the geometry of the attached ears. It is possible that the quality of bonds improves at higher pressures. Ideally a pressure which simulates the weight of a real cryogenic test mass compressing indium bonds of the correct size should be investigated.

7.6.4 IGR induction bonding results

Eighteen induction bonded silicon samples with indium layers of 30-50 µm were induction bonded. With an operating time of 2 minutes the temperature of the indium layer rose above indium's melting point of 157 °C, as measured with the FLIR non-contact thermal imaging camera [188] shown in Figure 7.22. The samples were then strength tested, and

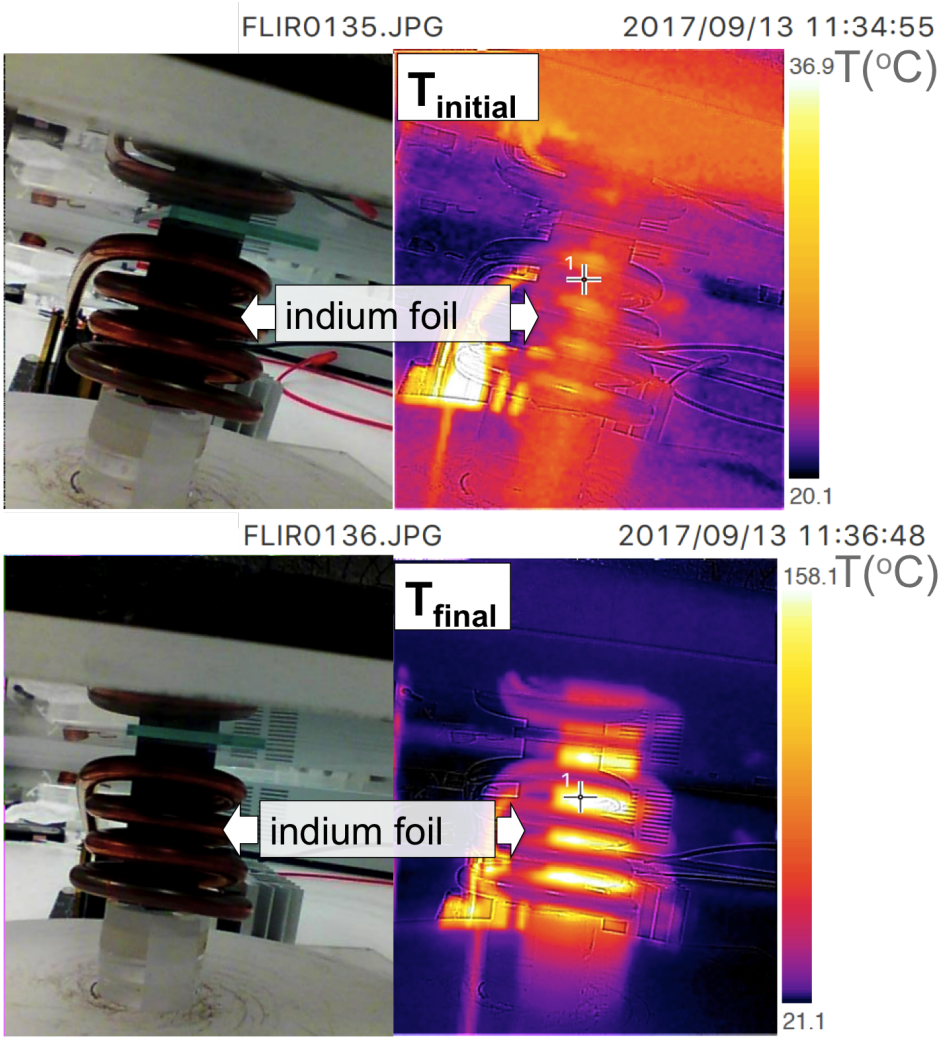

Figure 7.22: Thermal images of induction bonding indium foil between silicon substrates. The indium foil interface is in the middle of the two silicon substrates, which is not visible in this image as it is behind the induction coil.

the bond interfaces were visually inspected and photographed. They were also imaged

under an Olympus BX51 Nomarski Microscope [160] to judge bond quality. Well bonded indium layers were visibly torn off of one silicon substrate and adhered to another, as shown in Figure 7.23.

Conversely a poorly bonded surface looked very similar to a freshly deposited indium coating, or had visibly cloudy areas that indicated oxide formation had impeded cold welding in the first place as shown in Figure 7.24.

The broken samples were placed in categories based on a post-break visual examination

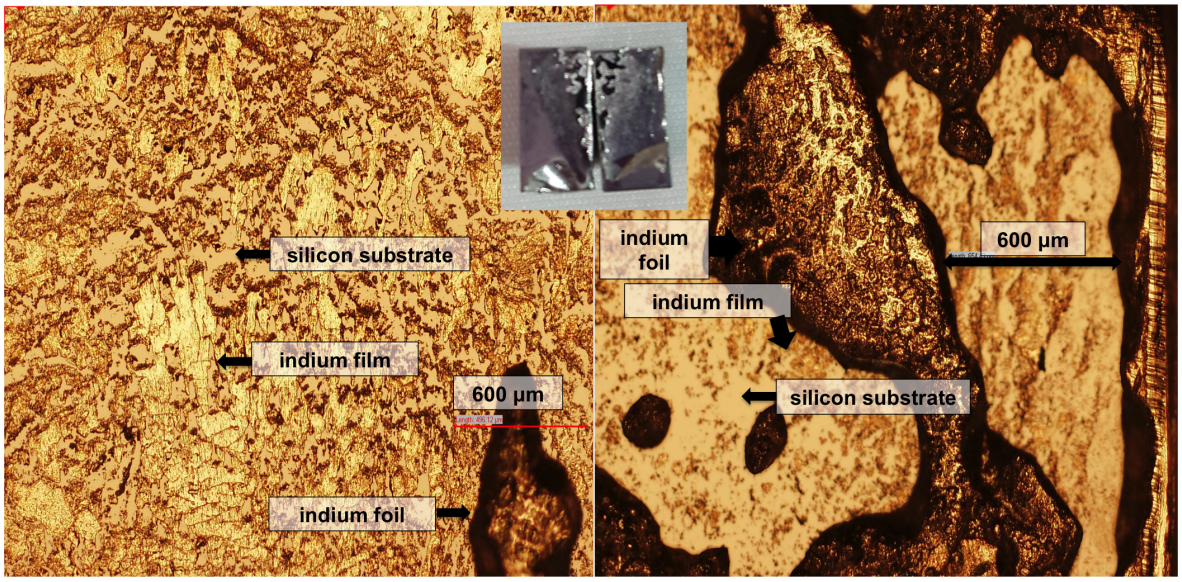

Figure 7.23: Post-break visual inspection of a high quality indium bond, photo and microscope images at 5x magnification. Tensile strength at break 11.6 MPa

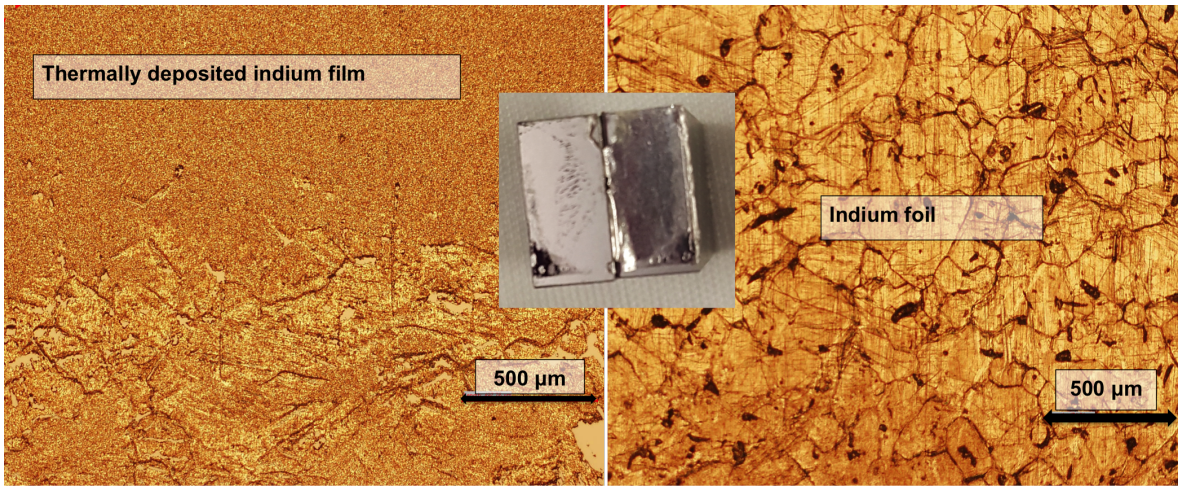

Figure 7.24: Post-break visual inspection of a low quality indium bond, photo and microscope images at 5x magnification. Tensile strength at break 0 MPa

of indium layer adhesion. The extent of adhesion in terms of the percentage of the total bond surface area as observed from the photographs and microscope images was recorded.

Three categories of bond quality were defined; one being 5% or less adhesion between indium layers, the second being 5%-29% and the third was adhesion of 30% or higher across the indium layer, as noted in Figure 7.25.
The strength testing results of these eighteen samples, separated into the three categories of extent of adhesion across the bond interface, are shown in Figure 7.25.
The amount of layer transfer and adhesion proved to be correlated to the bond strength.

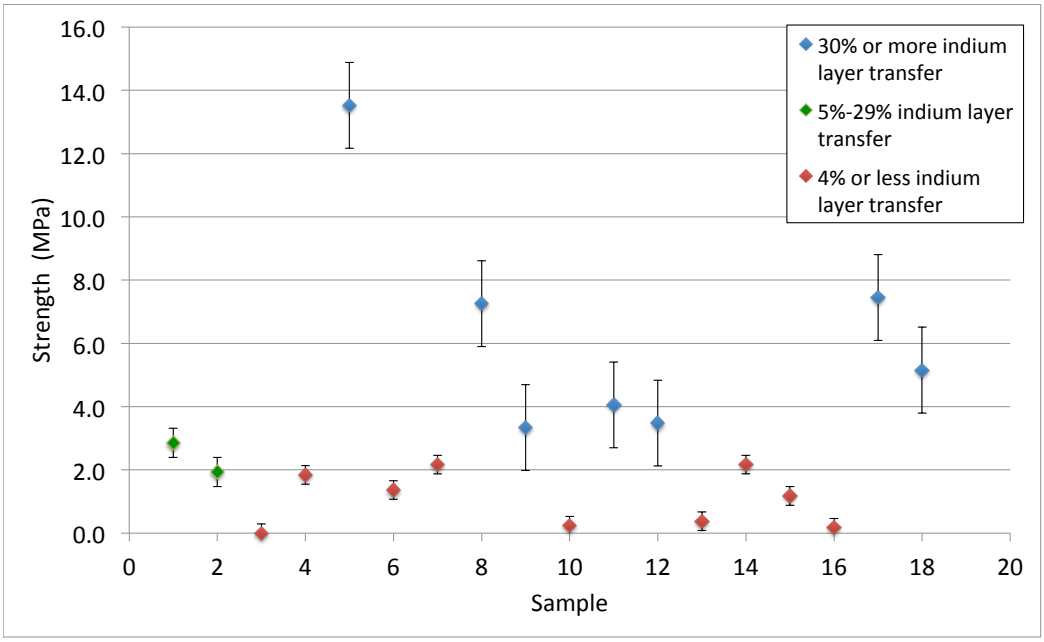

Figure 7.25: Tensile strength of induction bonded indium film and foil, 30-50 µm thick bond layers. Grouped according to amount of indium interface adhesion.

This indicates that if the initial cold weld is successful then the bond will be strong. However if the indium oxide layer is not fully removed the surfaces will not cold weld together and the bond will not form.
The amount of metal in an induction heater's working coil and the frequency of the working coil must be optimised with respect to each other to produce the ideal heating. The smaller the amount of metal there is in the coil, the more difficult this becomes. To properly heat very thin or small metal layers, the eddy currents should be concentrated at the surface of the metal as much as possible, which means minimising the skin depth. In the previous calculations for skin depth, using Equation 7.1, it can be seen that the depth the eddy currents penetrate into the metal is inversely proportional to the square root of induction heater frequency. Thus the operating frequency for small amounts of metal needs to be as high as possible.
Since a minimum of interface material is desired in GW detectors for mechanical loss reasons nine more cold welded samples were prepared. This time the indium foil was not included, only thermally deposited indium coatings of thickness < 700 nm. Since there was much less metal in these bonds compared to those containing the foil, the resonant

frequency of the induction heater was also pushed as high as possible. A third capacitor was removed and a new coil was wound, with three turns of 6 mm diameter copper rod, 2.5 cm inner diameter, 3.8 cm outer diameter and 2.5 cm long, with a calculated inductance of 0.32 µH. With $C = 3 \cdot 0.33 = 0.99$ µF this gives us a calculated resonant frequency of f_{resonant} =283 kHz. The true frequency of the circuit was measured across the working coil with a oscilloscope to be 250 kHz, which equates to a skin depth of 291 µm.
Unfortunately when the silicon samples were loaded into the coil and compressed as before, FLIR images of the induction heater as it ran showed only minimal increase in temperature, and that was mostly due to the working coil getting hotter, as shown in Figure 7.26. These nine samples were strength tested with the rest but the strength results were very

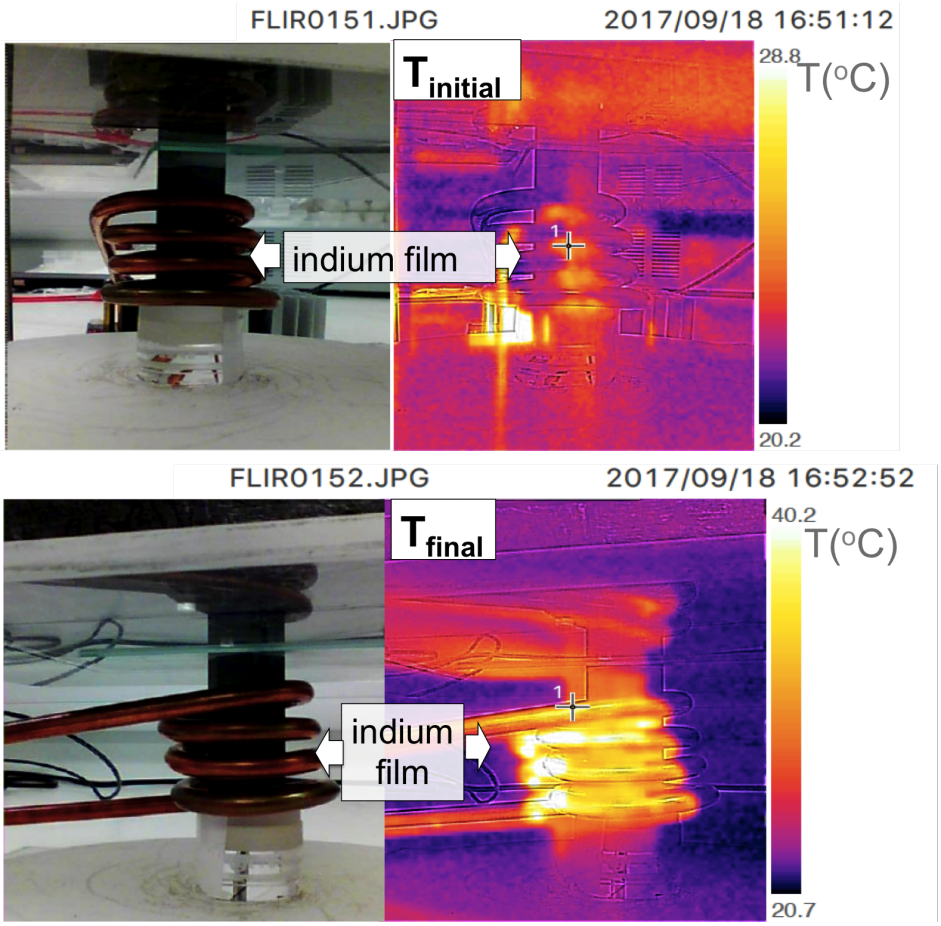

Figure 7.26: Thermal images of an attempted thin film indium bond between silicon substrates. The indium film interface is in the middle of the two silicon substrates, which is not visible in this image due as it is behind the induction coil.

low, shown in Figure 7.27 with their standard errors. The average tensile strength was 0.6±0.2 MPa. All samples exhibited 5% or less adhesion between indium layers during a post-break inspection of the interfaces.

The tensile strength results of all the induction bonded indium samples is summarised in Figure 7.28. These results indicate good quality bonds can be achieved via induction bond-

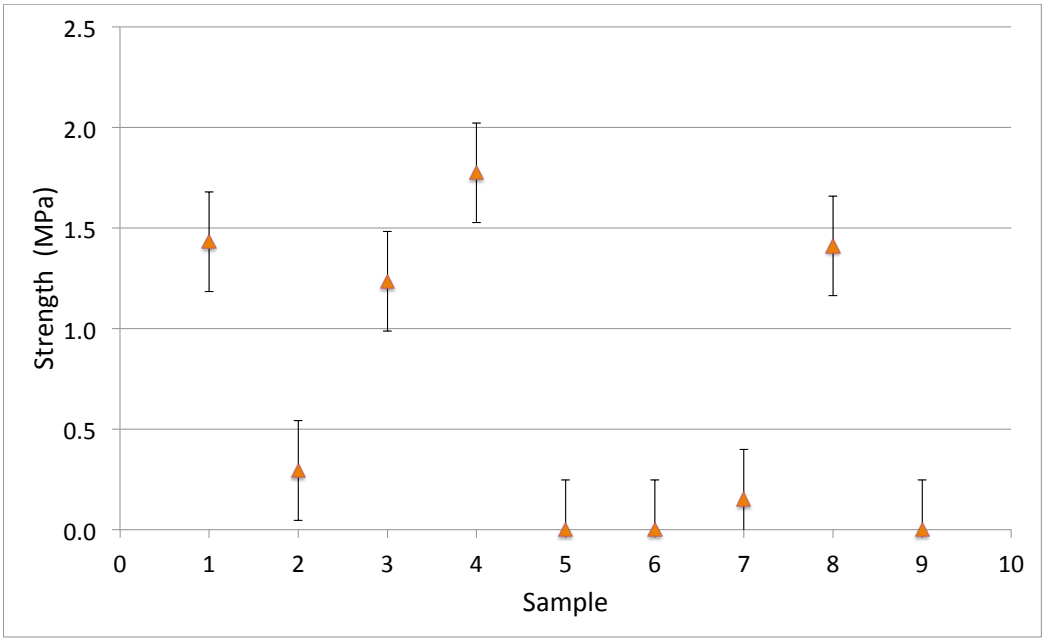

Figure 7.27: Strength of induction bonded indium film between silicon substrates, with indium layer thickness of 650 nm and 680 nm. All samples exhibited 5% or less adhesion post-break.

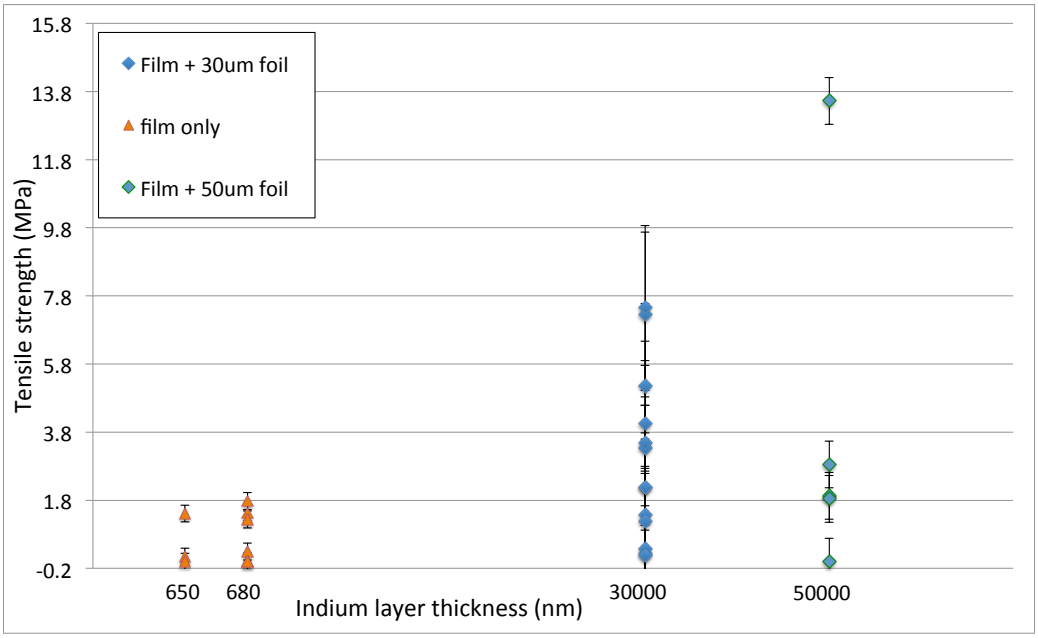

Figure 7.28: All induction bonded indium to silicon samples and calculated standard error, as a function of indium layer thickness

ing depending on the outcome of a few key factors. One, the success of the initial cold weld is essential for bond formation. Two, that the right combination of induction heater resonant frequency plus amount of indium placed into the working coil is used for optimal skin depth and heating. If there is too little metal and the the working coil frequency is too low the eddy currents are not properly induced into the layer and little heating happens.

Similarly, if the resonant frequency of the coil is too high for larger bulk metals then the sample will also not heat efficiently. Thus, better quality bonds were achieved using the addition of indium foils compared to using only thin film layers, due to the relative levels of heating.

7.7 Indium bonding results and analysis

Figures 7.29 and 7.30 show all the indium bond tensile strength results for both approaches in this study, pressure bonding and induction bonding. The strength of all of the bonds in the study ranged from 0-13.5 MPa. There was no correlation found for bond age or batch to tensile strength.

The approach that produced the weakest bonds was using the induction heater on samples

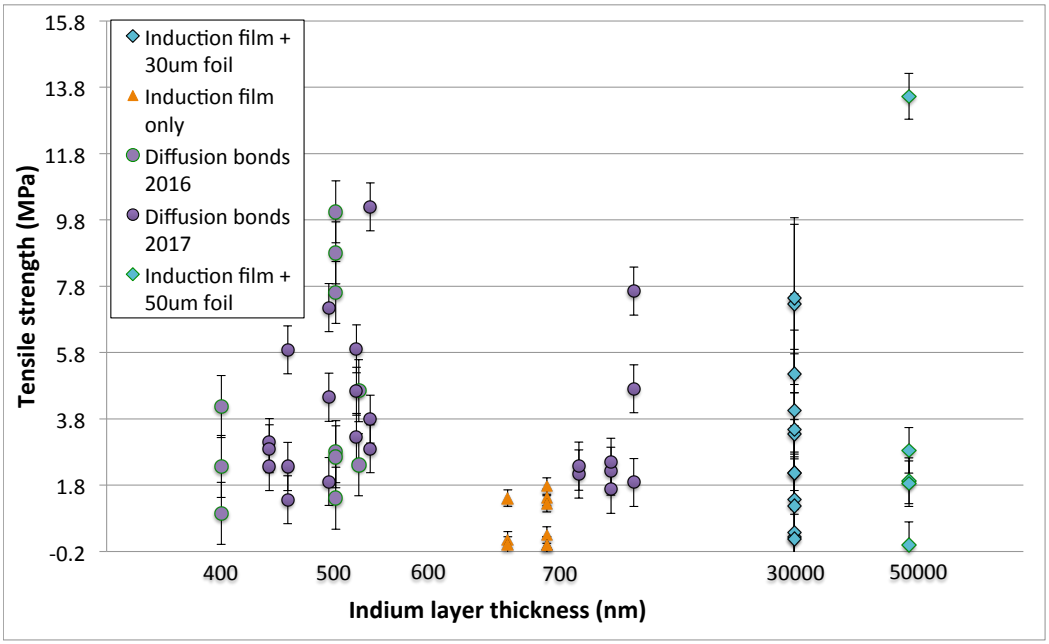

Figure 7.29: All indium bonded silicon samples with calculated standard error, as a function of indium layer thickness

with an indium layer thickness of 650 nm and 680 nm. As mentioned earlier, to take account of the smaller amount of indium in this test the operating frequency of the induction heater was increased to 240 kHz by removal of another capacitor and winding a working coil with fewer turns and slightly smaller diameter (N=3 and coil diameter=25 mm). Ideally the eddy currents would be concentrated as close as possible to the surface of the 700 nm thick indium layer, which would need an operating frequency of around 40 GHz. This far exceeds the possible operating frequency of the existing induction circuit however, and would need a new one to be designed and built in order to achieve GHz operating frequencies for nm thick indium layer heating.

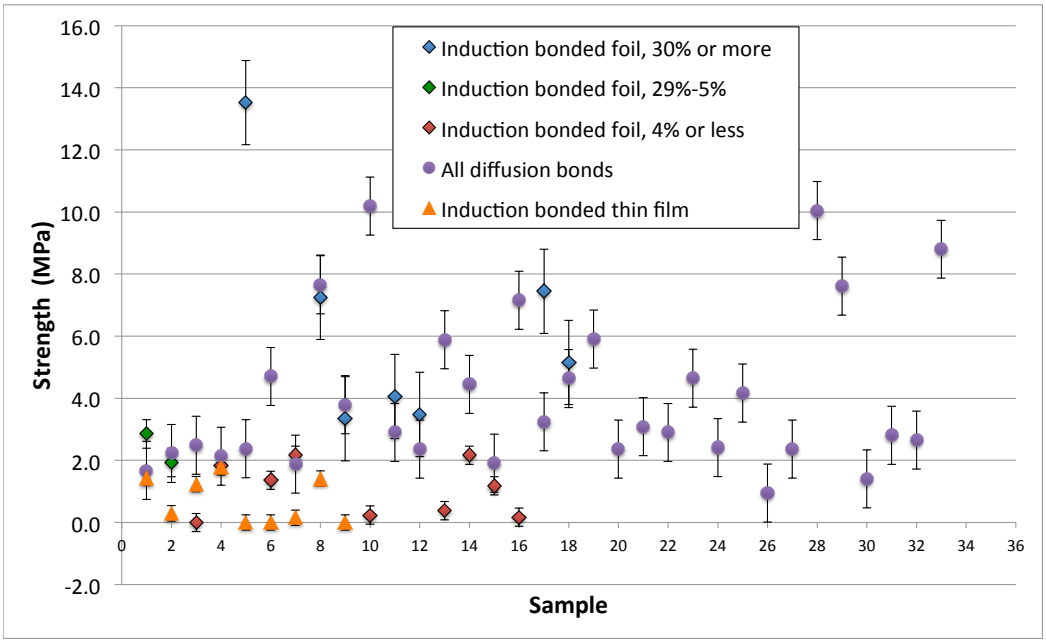

Figure 7.30: Strength comparison of all indium bonded silicon samples by bond type

The breaking stress of the induction heated thin film indium bonds was 0-1.7 MPa, with the FLIR thermal images during bonding showing only a minimal increase in temperature over a 2 minute running time, from room temperature to 40 °C.
Cold welded indium in 650-680 nm thick solder joints has been reported to have tensile strengths of up to 1.86 MPa [93]. Considering this, plus the fact that there was only a minimal increase in temperature during induction indicates that these samples were only weakly cold welded together.
When considering all of the indium bonds made with all approaches in this study, the diffusion bonded thin film indium strengths ranged from 1.4-11.7 MPa, whereas the induction bonded foils had a higher spread in strength, from 0-13.5 MPa.
It is postulated that the breaking stress of all the indium bonds created in this experiment was correlated to the initial success of the cold welding step, which can be seen for example in Figure 7.25. This effect may be enhanced due to the melting point of indium oxide being much higher than bulk indium, 1910 °C compared to 157 °C [105]. This means that if the indium interface is heated to 157 °C with an indium oxide layer still present, the bulk metal cannot break through the oxide layer and a bond will not be easily formed.

7.8 Summary and recommendations

This study has shown that two approaches, diffusion bonding and induction bonding, to produce indium bonds for gravitational wave detectors are feasible and can produce good quality bonds. All the indium bonds in this study were tensile strength tested to judge

bond quality using the same strength tester as for the hydroxide catalysis bonded sapphire in Chapter 3. It should be noted that the tensile strength of hydroxide catalysis bonds is very important because they are used to bond high tensile stress interfaces together. Indium on the other hand would only be used in compression bonds. So while the tensile strength of the indium bonds is not as important as for hydroxide catalysis bonds, it was used here as a standard by which to judge bond quality and repeatability.

There are some recommendations for further work to improve the repeatability of the induction bonded indium layers. The first would be to investigate induction bonding of thinner indium foils. Foils of 50 µm thick were the thinnest foil that could be procured in the UK, however there may be thinner ones available. From previous mechanical loss measurements of indium joints carried out by colleagues at KAGRA [142], foils of 1-10 µm thick would have acceptable loss levels for KAGRA [142], so having an induction heater that worked on them would be ideal. If a 10 µm thick foil was not available on the market, procuring a foil of 25 µm thick or so and then etching it with nitric acid until it reaches a thickness of 10 µm could be tried. Rolling the foil out to be thinner could also be tried. However, both rolling and etching of thicker foil may not give the desired layer uniformity so it is recommended to start with the thinnest available foil.

Oxide mitigation on the indium film and foil samples used in the induction tests was especially difficult. There were three indium surfaces to etch, two films and one foil, so it was difficult to keep oxide from forming on at least one of those surfaces. In the procedure that was developed here, the foil is first taken out of a methanol bath and dried with nitrogen gas. Then the first indium coated silicon sample is etched for 40-45 seconds, quenched in RO water for 10 seconds and methanol for 10 seconds and dried with nitrogen gas before cold welding it to the foil. The same etch process is then repeated as quickly as possible for the second silicon sample, and cold welded to the other side of the foil. Done this way one side of the foil is in air for a little over a minute before cold welding and the other side is in air for about 2.5 minutes. The extra time spent in air for one side of the foil could be the reason why some of the foil samples were well adhered to one side, but not to the other. When one person performs this procedure in an air atmosphere, it is difficult to get this time to be much shorter, as the samples have to be submerged in the dilute acid bath for at least 40-45 seconds to get rid of oxide. However, there could be different approaches that could improve this. If two people could etch samples at the same time, the exposure to air could easily be reduced. Also placing the samples in a small inert gas enclosure after etching could be investigated.

The FLIR camera images during induction bonding of the foils indicated temperatures of 158 °C during bonding, shown in Figure 7.22, which exceeds the melting point of indium. The samples reached indium's melting point at around one minute of operation, and the circuit was kept on for two minutes total. It was not run for longer than this because one

of the capacitors started to heat up around this time, though that may have been radiated heat from one of the working coil legs. In further tests the induction heater could be tested at longer running times and possibly air cooled with a fan, while monitoring the circuit component temperature with a thermal imaging camera.

For indium layers of 700 nm or less the diffusion bonding approach showed better results than the induction heating approach (at a frequency of 240 kHz). Increasing the thickness of the native oxide layer on the silicon substrates prior to coating them with indium could increase the bond strength, and could be attempted in future experiments via growing a thermal oxide.

Additionally, acoustic measurements with an ultrasonic transducer contacted to indium bonded samples as described in Chapter 5 could also be considered as a non-destructive method of assessing bond quality.

Chapter 8

Conclusion and Outlook

Ground-based interferometric detectors with room temperature fused silica test masses and suspension elements have proven to be sensitive enough to make the first direct detection of GWs. Binary systems of both black holes and neutron stars have been observed with these detectors. The next step for GW astrophysics is to push the boundaries of detector capabilities, in order to attain higher sensitivities necessary to increase the rate of GW detections and further the field. To do so, the observatories themselves are being redesigned and upgraded using the knowledge gained from previous generations of detectors. The sensitivity levels will be improved by controlling noise sources to a greater degree. One way of doing this is to operate the detectors at cryogenic temperatures, thereby reducing the overall thermal noise of the system.

This necessitates a change in the material chosen for use in the optics of GW detectors and their suspension elements. Fused silica exhibits a broad loss peak which is centred at 40 K. This is not a problem for room temperature operation, however it makes fused silica unsuitable for use at cryogenic temperatures. Currently the top two materials favoured by the GW community for use in the optics and suspension elements in cryogenic detectors are sapphire and silicon. Sapphire is already being implemented as a part of the KAGRA detector, while silicon is proposed for use in future detectors such as ET.

In this thesis a number of different studies of the properties of hydroxide catalysis bonds between silica or sapphire were presented. All bonds were made with sodium silicate solution. The strength of hydroxide catalysis bonds between c-plane sapphire substrates as a function of curing time were explored, with the short curing time data giving insight into the chemical process of the bonds as they develop. Knowing the strength of such bonds after longer curing times is crucial for the development of suspended sapphire optics. This provides information useful in ensuring the bonds will be strong enough to support test masses in cryogenic suspensions; by informing suspension design in deciding what area of bonded interface is sufficient.

It was found that hydroxide catalysis bonded c-plane sapphire showed an initial drop in strength, which levelled off at 15-16 MPa. These results were consistent with curing time data for sapphire obtained previously. They also agree with analysis of past bonded fused silica data at different curing times, that was gathered over many years. Bonded fused silica has been a part of GW detector suspensions since the 1990s. It is proposed that the presence of water forms additional hydrogen bonds between itself, the bonding solution, and the substrate surfaces during the early stages of bonding. The number of hydrogen bonds will decrease while the number of siloxane bonds increases and the bond cures. The decrease in hydrogen bonds as the water evaporates could account for a slight drop in strength as the hydroxide catalysis bonds stabilise.

The strength of bonds between m-m plane and a-a plane sapphire was also investigated, and found to be comparable with the strength of bonds between c-c plane sapphire.

As hydroxide catalysis bonds are currently used or planned for use in all current ground-based detectors, their material properties have to be well understood. In particular the values for density, Poisson ratio, and Young's modulus of hydroxide catalysis bonds are necessary to calculate their contribution to detector thermal noise. The density of hydroxide catalysis bonds was calculated previously, and the Poisson ratio of the bond material is inferred to be the same as fused silica. The Young's modulus proved to be challenging to characterise due to the bond being, by definition, thin and in-accessible. One measurement of a hydroxide catalysis bond Young's modulus is available in the literature, a value of 7.9 GPa. In this case a bond was altered to make it artificially thick to allow for a nano-indentation measurement. This value has historically been used to determine thermal noise arising from the bonds for aLIGO.

However, as the sensitivity of detectors improves, it is necessary to obtain more accurate values for the bond properties that directly contribute to the overall thermal noise of GW detectors. Thus a non-destructive technique for obtaining Young's modulus values of hydroxide catalysis bonds was developed and presented here, using acoustic pulse measurements. A Bayesian analysis model was also developed for the hydroxide catalysis bonded fused silica, resulting in a value of $18.5\pm^{2.0}_{2.3}$ GPa, with a 90% confidence range. This result agreed within error with the Young's modulus values found for hydroxide catalysis bonds between sapphire substrates, of 15.3 ± 5.2 GPa. For hydroxide catalysis bonds between silicon samples, it is a requirement of the bond process that the silicon is oxidised prior to bonding, otherwise a bond will not form reliably. However, the addition of oxide layers complicates acoustic measurements of the bond. Currently the analysis model is for a reflected acoustic signal from a single layer. The addition of oxide layers on either side of the bond would necessitate the development of a different and more sophisticated model. Thus it is assumed that the Young's modulus value for bonds between silicon substrates is approximately the same as those between fused silica and sapphire.

The Young's modulus value determined in this study, $18.5 \pm^{2.0}_{2.3}$ GPa, was used to model the thermal noise contributions of bonded test masses in various current and future configurations of ear and test mass and compare them to the proposed noise budgets of proposed future detectors. Two room temperature fused silica masses were modelled, representing designs for Advanced LIGO and the proposed aLIGO "A+" upgrade mass. Three different bonded cryogenic masses were also modelled, a sapphire KAGRA mass, a sapphire ET mass, and a silicon ET mass. For the cryogenic KAGRA and ET test masses the thermal noise contribution of the bonds met the proposed requirements. In all cases investigated here the hydroxide catalysis bonds meet the proposed thermal noise requirements, based on each detector's design sensitivity curves, making them appropriate for use in current and future generation detectors.

The development of indium bonding procedures for GW detectors was also studied. The possibility of new hybrid suspension designs that utilize both indium and hydroxide catalysis bonding is being considered for use in cryogenic detectors such as KAGRA or ET. It is proposed that the hydroxide catalysis bonds would be used to join the test masses to suspension interfaces. This would make use of their high strength under shear and tensile stresses, as has been used in the past for room temperature detectors such as GEO600, VIRGO, and aLIGO.

Along with hydroxide catalysis bonds, indium is proposed to be used in compressive joints such as the interface between a suspension fibre and a bladespring, or between a fibre and ear interface piece. Indium's low shear and tensile strength means it also cannot be used as a joint under shear or tensile loads. The addition of compressive indium joints would be considered for contingency reasons, since indium can be de-bonded and re-bonded relatively easily, whereas hydroxide catalysis bonds are difficult to de-bond after they are fully cured without risk of damage to the mirror substrates. In detectors with fused silica optics and suspension elements the fibres can be repaired by undoing the laser welds, as long as the ear interfaces remain intact. Currently laser weld repair is not an option for crystalline fibres such as silicon or sapphire. Thus an interface that can be de-bonded and re-bonded to replace fibres or test masses is necessary for future cryogenic mirror suspensions.

In this thesis two indium bonding approaches were investigated, diffusion bonding and induction bonding. In both cases the substrates used were polished silicon, and the indium layers between them were made of a combination of thin thermally deposited films and foils. The tensile strength and a post-break visual inspection of the indium bonds were used as standards by which to judge bond quality and repeatability. Silicon was chosen as the substrate material in this study, as it is one of the most likely choices for substrate material in future cryogenic detectors, along with sapphire.

In this thesis the first steps were taken to develop reliable bonding procedures of silicon with indium for GW detectors.

A custom bond jig that provided heat and pressure to silicon samples with indium interfaces was developed for the diffusion bonding approach. This approach provided 135 °C and 1 MPa to the bonds over ≈ 45 minutes, and achieved repeatably good quality bonds. However, applying the same amount of heat for the period of time that is necessary, 1 hour, would be difficult to do with real GW detector parts, as it would involve heating the test mass up to 135 °C for an extended period of time. This is usually avoided due to risk of damage to the optical coatings.

For the induction bonding approach, different coil geometries and operating frequencies of induction circuits were investigated. It is also a relatively fast procedure, requiring only ≈2 minutes to melt the indium at temperatures of 157 °C or more. Most importantly, the heating is localised to the indium layer, and uses no additional pressure, which makes it a practical and low stress approach for bonding GW detector test masses. For indium layers of 700 nm or less the diffusion bonding approach showed higher and more repeatable bond strengths than the induction heating approach did (at a frequency of 240 kHz). It is proposed that for future tests a higher frequency induction heater be used to improve the quality of thin bonds. For microns thick indium layers the induction bond approach was successful. It was found that the bond quality of both approaches relied on the quality of the initial cold weld, with any indium oxide in the interface preventing a cold weld and thus a bond from forming.

The results presented here demonstrate the feasibility of using indium bonds for compressive joints in GW detectors. Two procedures for preparing good quality indium bonds of various thicknesses have been developed, with enough flexibility to be customisable for bonding in-situ in GW detectors. More development to improve the repeatability of the indium bonds is needed, with some recommendations given in this thesis how to proceed. It is also recommended that the thermal conductivity of indium bonded silicon be measured prior to its inclusion in a detector.

It has also been shown that hydroxide catalysis bonds continue to be a good choice for the construction of quasi-monolithic suspensions. Their mix of high tensile strength over long term curing times, well understood material properties and low levels of thermal noise make them ideal for use in both room temperature and future cryogenic GW detectors.

Appendix A

Indium bonding procedures

The following appendix is written as a two part procedural document. The first section outlines the procedure for the induction bonding of indium between silicon substrates, and the second section outlines the pressure bond approach for indium bonded silicon. Though silicon substrates were used in this study, these procedures can also be used to bond other materials together with indium, such as fused silica and sapphire. The context, applications, and results of the indium bonding procedures investigated in this study is in . Here the separate procedures are written in full for others to follow.

A.1 Materials list for both procedures

Below is the list of items and equipment needed for the sample cleaning, preparation, indium thermal layer deposition, and cold weld steps of both indium bond procedures.

1. Access to cleanroom flowbench with sinks
2. nitrile gloves, cleanroom wipes
3. acid proof gloves, apron and eyewear
4. crossed tweezers (PEEK or teflon tips preferred)
5. clean scalpel
6. stainless steel scissors
7. small ultrasonic bath
8. scale that is sensitive to 0.01 gram

9. chemicals: reagent grade acetone, isopropanol, and methanol. Spectroscopic grade methanol. Hydrochloric acid. DI water.
10. Non-chlorinated solvents waste disposal container
11. HCL acid waste disposal container
12. indium (Bulk, wire, foil, etc.)
13. chemical spray bottles for acetone, isopropanol, and methanol.
14. beakers: 1x glass 500 ml 6x plastic 500 ml 1x plastic 50 ml
15. petri dishes: 3x large teflon petri dishes, 1x small glass and 2x large glass
16. clean nitrogen gun
17. stopwatch
18. Thermal evaporator such as Emitech K950X

A.2 Indium bond sample preparation

The samples referred to below were pieces of 5x5x10 mm single crystal silicon, procured from Spanoptic with a bond surface flatness requirement of $\lambda/10$. All samples had bond surface flatness measured on the Zygo previous to the first cleaning steps below. The full procedures are as follows, all cleaning and etching steps should be performed in a clean room to prevent contaminants from getting into the bond interface. If reverse osmosis (RO) water is not available, de-ionised (DI) water can be used.

A.2.1 Substrate cleaning procedure

1. Collect samples. Visually inspect for defects. Scribe if necessary. Always include one extra sample as a witness sample for measuring the coating thickness.
2. Set clean wipes onto the flow bench, and partially fill the ultrasonic bath with water.
3. Fill the 500 ml glass beaker with 200 ml acetone
4. Fill one of the 500 ml plastic beakers with 200 ml of isopropanol and another with methanol. Plastic beakers are used as much as possible to prevent the substrates from chipping against a glass side while in the ultrasonic. Place solvent bottles of isopropanol and high grade methanol next to the beakers of the same chemical.

5. If indium foil is being used, place it into a clean glass petri dish and press one of the samples gently onto it to give an outline to cut the foil to size. Cut carefully with clean, sharp scissors.

6. Use the crossed tweezers to handle the samples in all the following steps. Place the substrates carefully into the bottom of the glass beaker of acetone, then place the beaker in the ultrasonic and run for 9 minutes.

7. Remove the samples one by one, holding them over the surface of the acetone and spraying them with isopropanol. Place into the isopropanol beaker and run in the ultrasonic bath for 9 minutes.

8. Remove the samples one by one, holding them over the surface of the isopropanol and spraying them with methanol. Place into the methanol beaker and run in the ultrasonic bath for 9 minutes.

9. Remove the samples one by one, holding them over the surface of the methanol and rinse them with spectroscopic grade methanol.

10. Blow dry the substrates with nitrogen gas, starting with the bond surface and working downwards. Take care not to have any methanol dry on the bond surface. Do not point the nitrogen gun towards the solvents.

11. Evenly distribute the clean samples bond surface side up in the small glass petri dish. Place it in a large glass petri dish and cover with a clean dry beaker, or another petri dish that is tall enough not to touch the bond surfaces.

12. Now prepare the dilute hydrochloric acid solutions. First fill the sink with water, and fill one beaker with extra water.

13. If thin film indium and thicker indium foil are both being used, fill two pastic beakers with 200 ml of RO water. If only thin film indium is used, fill only one.

14. Label the two plastic beakers, one as 11% HCL and the other as 7% HCL.

15. Don the appropriate safety attire, acid apron over cleanroom garb, then chemical goggles/face shield and acid gloves.

16. Fill the 50 ml beaker with 40 ml of hydrochloric acid. Close acid bottle tightly and return to cupboard.

17. Pour 25 ml of acid into the beaker labelled 11% HCL and containing 200 ml of RO water, to make the 11% HCL solution.

18. Pour 15 ml of acid into into the beaker labelled 7% HCL and containing 200 ml of RO water, to make the 7% HCL solution.

19. Cover the beaker tops tightly with foil.

20. Grip the bulk indium with tweezers and dip into the 11% HCL solution for 1 minute to etch the indium oxide off.

21. Rinse the bulk indium in water, then with methanol. Dry with a cleanroom wipe.

22. Place in a clean glass petri dish. Cut a small piece of indium off the bulk with a scalpel, this will be what you load into the evaporator basket.

23. The maximum indium weight that can be held in the evaporator basket and evaporated without falling in one lump is around 0.3 grams. For this reason limit the bulk indium weights to 0.28 grams maximum.

24. Measure the weight of the small indium piece on a scale that is sensitive to 0.01 grams, placing the indium on top of a piece of cleanroom foil when weighing.

25. Repeat with a second piece, until you have two pieces of indium that don't exceed 0.28 grams individually.

26. Wrap both pieces with cleanroom foil and transport to the evaporator along with the clean samples.

A.2.2 Thermal deposition

1. Its possible that other metals in the evaporator can contaminate the indium layer during deposition. So if the evaporator has been used for thermally deposited many other metals, or if it hasn't been cleaned in a while it is necessary to disassemble and clean it before using it to deposit indium layers. This procedure makes use of an Emitech K950X Evaporator. Alternatively the indium layers could be deposited elsewhere via ion beam sputter or other approach.

2. Add two tungsen baskets to the evaporator cartridge. They should be brand new ones, or ones used only for indium.

3. Fasten the baskets securely into place and load the indium into them.

4. Place the samples in the clean petri dish onto the base inside the evaporator.

5. Close the lid, and lower the cartridge into the top and secure it.

6. Connect the electrodes to the left side, and turn the shutter to the left side too. The shutter can catch any metal splatters if the indium heats up too quickly and melts in lumps instead of evaporating.

7. Hit start and Run coating cycle.

8. Let the roughing pump start pulling vacuum for 1-2 minutes, then start the turbo pump by hitting the middle button on the turbo pump controller followed by the left button.

9. Wait until it has pumped down to "high" vacuum i.e. $< 9x10^{-4}$mbar.

10. Ramp the current slowly up to 18 amps. Stop for 3 seconds at 10 amp to let the demand catch up, then ramp up 1 amp per second from 10 amps to 18 amps.

11. Pause for a few seconds at 18 amps, then open the shutter (Usually around 9 minutes 15 seconds).

12. If the basket is visible turn the current down slowly once all the indium is gone (wearing goggles to protect eyes). If it is not visible wait until the timer reads 7 minutes 30 seconds and then turn the current down to zero.

13. Switch both electrodes over to the second basket.

14. Ramp the current up again, the same as before.

15. Again pause for a few seconds at 18 amps, then open the shutter (Usually around 6 minutes 30 seconds).

16. If the basket is visible turn the current down slowly once all the indium is gone (wearing goggles to protect eyes). If it is not visible wait until the timer reads 5 minutes and turn the current down to zero.

17. Once the current is turned down the turbo pump can start to wind down. Press the left button on the turbo pump controller then the middle button to do this.

18. Once the timer has run down to zero hit stop.

19. When pumped back up to air, remove the cartridge, set aside and remove the samples.

20. Cover samples immediately and take back to the flow bench to etch and cold weld.

A.2.3 Oxide etch and cold weld

1. Fill the flow bench sink with water and lay out three teflon petri dishes on top of new wipes. Note: this section assumes the previous steps, such as making the acid solutions, were completed.

2. Don the appropriate safety attire, acid apron over cleanroom garb, then chemical goggles/face shield and acid gloves.

3. If etching indium foil, fill the left most dish 2/3 full of 11% HCL. Fill the middle dish with RO water, and the right-most dish with a small amount of high grade methanol.

4. Pick up the first of the pre-cut indium foils with the crossed tweezers and place into the 11% HCL solution, starting the stopwatch as the foil enters the solution.

5. Gently agitate the solution with the foil, keep it submerged for 45 seconds.

6. Remove from HCL solution at 45 seconds and quench in RO water for 10 seconds, then leave it in the methanol bath.

7. Repeat for rest of foils.

8. Pour the 11% HCL from the petri dish into an HCL waste disposal bottle. Re-fill the dish with 7% HCL solution. Also empty and re-fill the RO water dish.

9. Now it is time to etch the coated substrates. Grasp the first one with tweezers and place into the 7% HCL solution, starting the stopwatch as the substrate hits the solution.

10. Keep submerged and remove at 45 seconds.

11. Quench in RO water for 10 seconds, then in methanol for 10 more.

12. Rinse the bond surface with high grade methanol as it is removed from the methanol petri dish.

13. Blow dry the substrate with nitrogen gas, starting with the bond surface and working downwards. Take care not to have any methanol dry on the bond surface. Do not point the nitrogen gun towards the solvents.

14. If using a foil, blow it dry with nitrogen also. Set the foil in the base of a clean glass petri dish and press the indium coated sample down firmly, then set it on its side.

15. Repeat the etch for one more substrate.

16. Align substrates and press firmly together. They are now cold welded and ready to be either induction bonded or pressure bonded.

17. Repeat for the rest of the samples, except for the witness sample.

18. Set aside the witness sample in a clean and covered petri dish.

19. Set aside the bonded samples in a clean and covered petri dish.

20. Measure the indium layer thickness on the silicon witness sample in the EDXRF, using the analysis group 'indium coated silicon' and following instructions in the manual[159].

A.3 Induction bond procedure

A.3.1 Materials List for induction bonding

Below is the list of items and equipment needed for the induction indium bond procedure. Figure A.1 for reference.

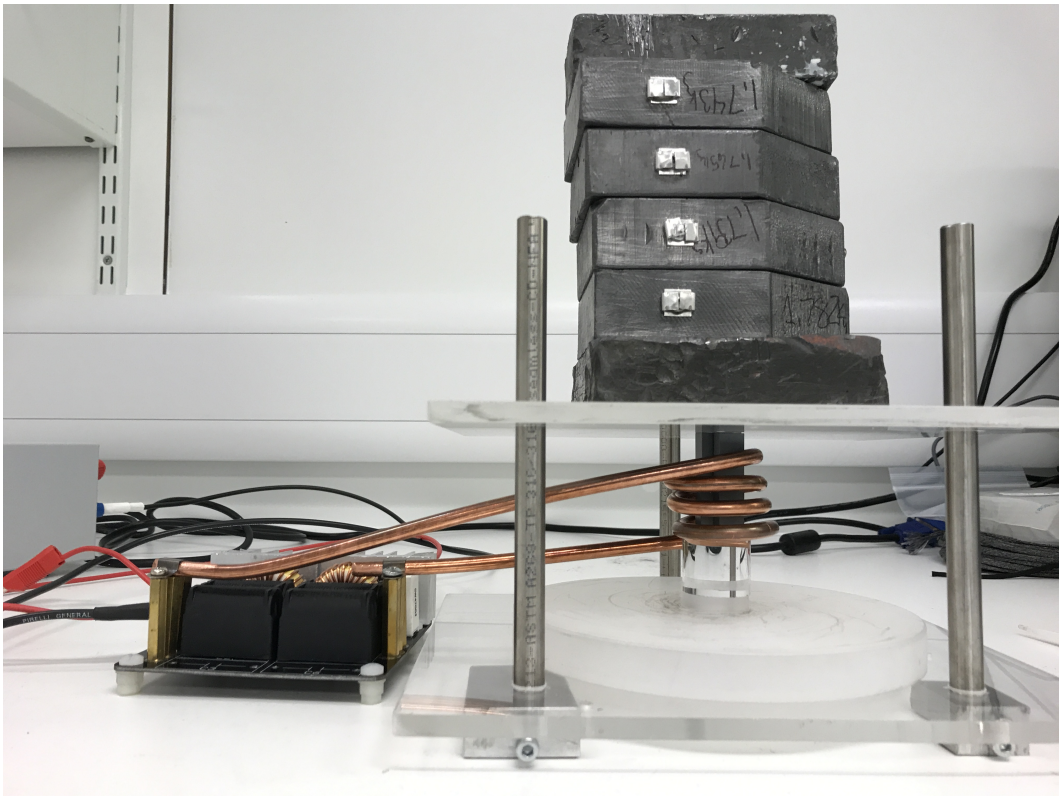

Figure A.1: IGR induction heater setup

1. Induction heater circuit with high frequency capability (custom built or bought, details in Chapter 7)
2. Un-insulated copper rod for coils, no less than 5 mm diameter
3. Non-metallic base material, such as ceramic or glass
4. High current power supply, should be able to provide at least 30 volts and 20 amps.
5. stopwatch
6. FLIR thermal imaging camera

A.3.2 Procedure

This procedure is optimised for 5x10x20 mm silicon samples, with indium bonds consisting of thermally deposited indium on each silicon substrate and indium foil in the middle. The resonant frequency of the induction heater circuit can be changed if the amount of indium changes, details of which are in Chapter 7.

1. Collect the samples that were cleaned and cold welded together following the procedures in the previous sections.
2. Set three cold welded samples equi-distant from each other on top of a 25 mm diameter glass base, which should be centered on the large glass plate, referencing the markings there.
3. Attach the appropriate working coil to the induction heater circuit and secure the leads firmly.
4. Place three of the bonded samples in a triangle equidistant from each other on top of the 25 mm glass discs.
5. Add or take away glass discs until the bond interface lines up with the middle of the coil. Then lower the coil over the samples. Visually check from all sides to see that the samples are in the middle of the coil and equi-distant apart. Make sure the metal coil is not touching the samples or the glass base. The bond interface of the samples should be in the same plane as the middle of the coil, here in between turns 2 and 3 of 4. The field is strongest here and will heat most efficiently.
6. Lower the other plexiglass plate over the samples. There is a glass microscope slide on the bottom of it that the bond samples should be centered under.

7. Carefully place the square weight onto the top of the plexiglass plate, referencing the markings to center it. Ensure a three point contact of the weighted plate to the three samples by tilting the weight slightly off axis. If it feels secure, add the rest of the weights for a total of 1 kg.

8. Check that only the black lead of the circuit is plugged into the back of the power supply unit (PSU), and turn the power supply on. If the power supply is not able to provide enough current and voltage to the circuit when it is switched on, the transistors in the circuit will not see a high enough voltage to work correctly and will start to heat up, risking damage to the circuit [186]. To avoid this, do not connect the red lead of the circuit to the power supply while the power supply is off.

9. Once the power supply has fully switched on check that the current is limited to 20 amps and the voltage to 35 volts.

10. Ready the stopwatch and turn on the FLIR camera. Check that the emissivity settings of the FLIR camera match the emissivity of objects being measured, and that the distance setting is set to match the distance that the FLIR is away from the object being measured.

11. Take a picture of the samples at room temperature with the FLIR camera, such as in Chapter 7, Figure 7.22 and Figure 7.26.

12. Now plug the red lead into the back of the powered on PSU. Hit start on the stopwatch once the circuit is drawing current.

13. Let the induction heater run for 2 minutes, taking a picture of the samples with the FLIR camera at 1 minute 30 seconds, and at two minutes. It should read a temperature of over 160 °C. Occasionally point the FLIR camera towards the heater circuit as well during operation to monitor the temperature of the circuit components. None of them should be heating up higher than 60 °C.

14. Turn the power supply off at 2 minutes, then wait an additional 5 minutes before stopping the stopwatch and slowly removing the weights.

15. Using the FLIR camera, make sure all components are cool enough to touch. Lift the working coil off and set it down away from the bonded samples.

16. Unplug the red lead from the power supply.

A.4 Pressure bond procedure

A.4.1 Materials List for pressure bond

Below is the list of items and equipment needed for the pressure indium bond procedure. Reference Figure A.2 for the pressure bond set-up.

1. Motor driven strength tester with load cell, details in Chapter 7, or equivalent set-up to provide controlled pressure
2. Bond jig to hold samples and provide heat, custom made with details in Chapter 7, or equivalent
3. Power supply
4. stopwatch
5. multimeter
6. FLIR thermal imaging camera

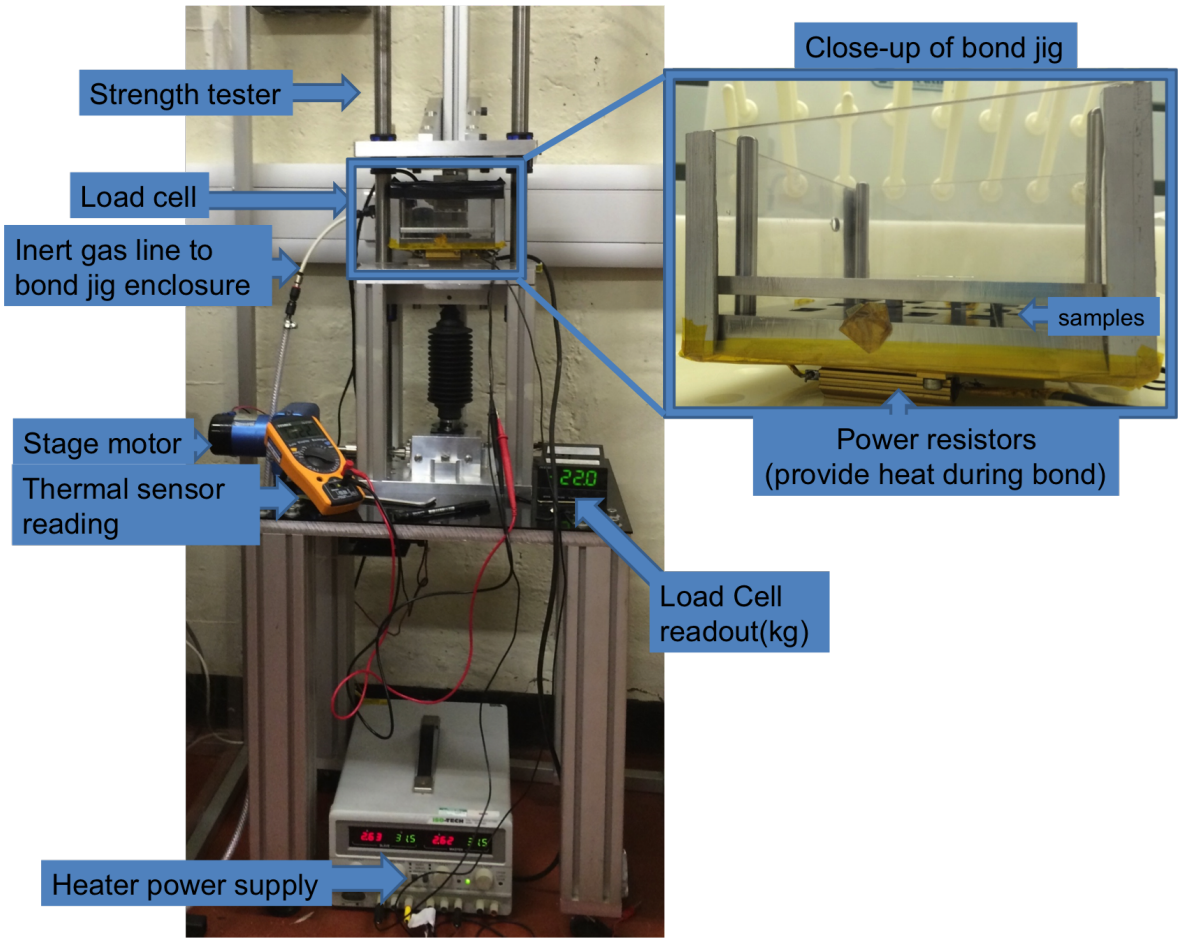

Figure A.2: Pressure bond set-up

Platinum resistance temperature sensors Pt100 (Pt1000)

KONGSBERG

Relation Temperature vs. Resistance According to IEC751 / ITS-90

°C ITS-90	0	1	2	3	4	5	6	7	8	9	10
-200	18.52										
-190	22.83	22.40	21.97	21.54	21.11	20.68	20.25	19.82	19.38	18.95	18.52
-180	27.10	26.67	26.24	25.82	25.39	24.97	24.54	24.11	23.68	23.25	22.83
-170	31.34	30.91	30.49	30.07	29.64	29.22	28.80	28.37	27.95	27.52	27.10
-160	35.54	35.12	34.70	34.28	33.86	33.44	33.02	32.60	32.18	31.76	31.34
-150	39.72	39.31	38.89	38.47	38.05	37.64	37.22	36.80	36.38	35.96	35.54
-140	43.88	43.46	43.05	42.63	42.22	41.80	41.39	40.97	40.56	40.14	39.72
-130	48.00	47.59	47.18	46.77	46.36	45.94	45.53	45.12	44.70	44.29	43.88
-120	52.11	51.70	51.29	50.88	50.47	50.06	49.65	49.24	48.83	48.42	48.00
-110	56.19	55.79	55.38	54.97	54.56	54.15	53.75	53.34	52.93	52.52	52.11
-100	60.26	59.85	59.44	59.04	58.63	58.23	57.82	57.41	57.01	56.60	56.19
-90	64.30	63.90	63.49	63.09	62.68	62.28	61.88	61.47	61.07	60.66	60.26
-80	68.33	67.92	67.52	67.12	66.72	66.31	65.91	65.51	65.11	64.70	64.30
-70	72.33	71.93	71.53	71.13	70.73	70.33	69.93	69.53	69.13	68.73	68.33
-60	76.33	75.93	75.53	75.13	74.73	74.33	73.93	73.53	73.13	72.73	72.33
-50	80.31	79.91	79.51	79.11	78.72	78.32	77.92	77.52	77.12	76.73	76.33
-40	84.27	83.87	83.48	83.08	82.69	82.29	81.89	81.50	81.10	80.70	80.31
-30	88.22	87.83	87.43	87.04	86.64	86.25	85.85	85.46	85.06	84.67	84.27
-20	92.16	91.77	91.37	90.98	90.59	90.19	89.80	89.40	89.01	88.62	88.22
-10	96.09	95.69	95.30	94.91	94.52	94.12	93.73	93.34	92.95	92.55	92.16
0	100.00	99.61	99.22	98.83	98.44	98.04	97.65	97.26	96.87	96.48	96.09
0	100.00	100.39	100.78	101.17	101.56	101.95	102.34	102.73	103.12	103.51	103.90
10	103.90	104.29	104.68	105.07	105.46	105.85	106.24	106.63	107.02	107.40	107.79
20	107.79	108.18	108.57	108.96	109.35	109.73	110.12	110.51	110.90	111.29	111.67
30	111.67	112.06	112.45	112.83	113.22	113.61	114.00	114.38	114.77	115.15	115.54
40	115.54	115.93	116.31	116.70	117.08	117.47	117.86	118.24	118.63	119.01	119.40
50	119.40	119.78	120.17	120.55	120.94	121.32	121.71	122.09	122.47	122.86	123.24
60	123.24	123.63	124.01	124.39	124.78	125.16	125.54	125.93	126.31	126.69	127.08
70	127.08	127.46	127.84	128.22	128.61	128.99	129.37	129.75	130.13	130.52	130.90
80	130.90	131.28	131.66	132.04	132.42	132.80	133.18	133.57	133.95	134.33	134.71
90	134.71	135.09	135.47	135.85	136.23	136.61	136.99	137.37	137.75	138.13	138.51
100	138.51	138.88	139.26	139.64	140.02	140.40	140.78	141.16	141.54	141.91	142.29
110	142.29	142.67	143.05	143.43	143.80	144.18	144.56	144.94	145.31	145.69	146.07
120	146.07	146.44	146.82	147.20	147.57	147.95	148.33	148.70	149.08	149.46	149.83
130	149.83	150.21	150.58	150.96	151.33	151.71	152.08	152.46	152.83	153.21	153.58
140	153.58	153.96	154.33	154.71	155.08	155.46	155.83	156.20	156.58	156.95	157.33
150	157.33	157.70	158.07	158.45	158.82	159.19	159.56	159.94	160.31	160.68	161.05
160	161.05	161.43	161.80	162.17	162.54	162.91	163.29	163.66	164.03	164.40	164.77
170	164.77	165.14	165.51	165.89	166.26	166.63	167.00	167.37	167.74	168.11	168.48
180	168.48	168.85	169.22	169.59	169.96	170.33	170.70	171.07	171.43	171.80	172.17
190	172.17	172.54	172.91	173.28	173.65	174.02	174.38	174.75	175.12	175.49	175.86

Pt1000 = Pt100 x 10

P-TSIEC751/CE 2004-11-25

Figure A.3: Resistance to temperature

A.4.2 Procedure

Below is the list of tasks to preform to complete the pressure bond procedure.
Refer to Chapter 7 for more details.

1. Collect the samples that were cleaned and cold welded together following the procedures in the previous sections.
2. Set three cold welded samples equi-distant from each other in the bond jig.
3. Lower the metal plate down until it touches the top of the samples.
4. Center the bond jig base over the large dowel pin in the bottom of the strength tester.
5. Attach the thermistor leads to a multimeter, and the power resistor leads to the power supply. The power supply should provide 60 volts.
6. Lower the load cell foot until it just touches the top of the metal jig plate.
7. Zero the load cell readout and run the strength tester motor until it reads 20 kgs of pressure on the three samples, which corresponds to 1.25 MPa for three samples each having a bond surface area of 5 mm by 10 mm.
8. As the metal jig heats up the pressure will also increase due to the thermal expansion of the metal jig. If the load cell initially reads 20 kgs, after one hour it increases to around 32 kgs. The load cell will overload at 34 kgs in compression, if it reaches this point during the bonding procedure the motor can be used to back the foot off to 32 kgs or lower.
9. Turn on the power supply.
10. The temperature will ramp up until it reaches 135C, at which point it should be held there for an additional 30 minutes to form a diffusion bond between the cold welded indium layers.
11. Record the thermistor values every five to ten minutes, turning the voltage down if necessary to keep the temperature around 135 °C. This usually takes about an hour. Typically achievable bond temperature ramp curves are shown in Chapter 7 in Figure 7.9.
12. Turn the power supply off.
13. . Leave the set-up for an hour or two to cool down while still under pressure.
14. Use the motor to lift the load cell off and away from the bond jig.
15. Lift the top plate of the bond jig and remove the bonded samples.

Appendix B

Solving the compressional wave equation in a bonded cylinder

In order to express the amount of energy stored in a hydroxide catalysis bond, the compressional wave equation is solved in this Appendix. The example of a bonded bar resonating in its fundamental longitudinal mode is used here. This bar is defined as having cross sectional area S, and total length L, with a bond layer of thickness b << L in the middle.
The origin of the x-axis is defined to be in the centre of the bond layer, as in Figure B.1. As

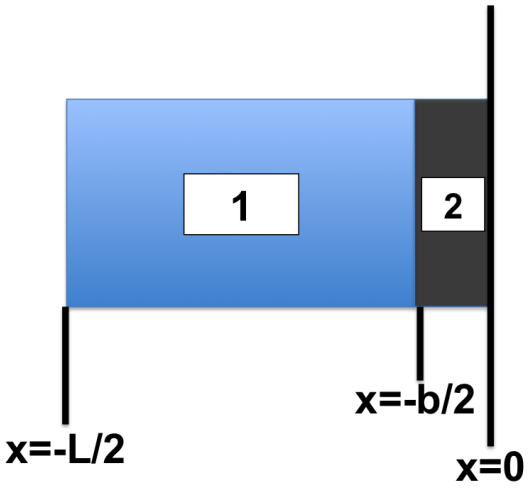

Figure B.1: Schematic of bonded bar, where region 1 is the bar and region 2 is the bond layer.

the bar resonates in its fundamental frequency it can be understood as undergoing simple harmonic motion. Thus a point on the mass at a position x can be described as undergoing displacement $\Psi(x) = A\sin(kx)$.
Displacement in the two regions defined in Figure B.1 can be expressed with the following solutions.

Possible solutions

$$\text{Region 1:} \quad \Psi_1 = A_1 \sin\left(k_1 x + \Phi\right) \tag{B.1}$$

$$\text{Region 2:} \quad \Psi_2 = A_2 \sin\left(k_2 x\right) \tag{B.2}$$

Applicable boundary conditions

A at $x = 0 \rightarrow \Psi_2 = 0$

B at $x = -\frac{L}{2} \rightarrow \frac{\partial \Psi_1}{\partial x} = 0$
$\rightarrow \frac{\partial \Psi_1}{\partial x} = A_1 k_1 \cos\left(k_1 x + \Phi\right) = 0$
$\rightarrow -k_1 \frac{L}{2} + \Phi = -\frac{\pi}{2}$ or $k_1 \frac{L}{2} - \Phi = \frac{\pi}{2}$

C at $x = -\frac{b}{2} \rightarrow \Psi_1 = \Psi_2$
$\rightarrow A_1 \sin\left(k_1 x + \Phi\right) = A_2 \sin\left(k_2 x\right)$
$\rightarrow A_1 \sin\left(-k_1 \frac{b}{2} + \Phi\right) = A_2 \sin\left(-k_2 \frac{b}{2}\right)$

D $E_1 \frac{\partial \Psi_1}{\partial x} = E_2 \frac{\partial \Psi_2}{\partial x}$
$\rightarrow E_1 A_1 k_1 \cos\left(-k_1 \frac{b}{2} + \Phi\right) = E_2 A_2 k_2 \cos\left(-k_2 \frac{b}{2}\right)$

Using boundary condition C, the relationship between the wave amplitudes A_1 and A_2 can be found, where $E_1 A_1 k_1 = E_2 A_2 k_2$. Considering the wave numbers,

$$k_1 = \frac{\omega}{v_1} \qquad \& \qquad k_2 = \frac{\omega}{v_2}, \tag{B.3}$$

with angular frequency ω and speed v_1 and v_2,

$$v_1 = \sqrt{\frac{E_1}{\rho_1}} \qquad \& \qquad v_2 = \sqrt{\frac{E_2}{\rho_2}}, \tag{B.4}$$

where E_1 and E_2 are the Young's moduli, and ρ_1 and ρ_2 are the densities of region 1 and region 2 respectively. It should be noted that since this is a compressional wave in solely the longitudinal direction, its speed depends on only the Young's modulus and density of the material. In the case where there are shear wave components, the shear modulus must be used instead of the Young's modulus. The shear modulus includes the Poisson ratio of the material, in addition to the Young's modulus.
The amplitude coefficient in the bond layer, A_2, now yields the following relationship,

$$A_2 = A_1 \frac{E_1 k_1}{E_2 k_2} \rightarrow A_2 = A_1 \frac{E_1}{E_2} \sqrt{\frac{E_2 \rho_1}{E_1 \rho_2}} = A_1 \sqrt{\frac{E_1 \rho_1}{E_2 \rho_2}}. \tag{B.5}$$

which is used in the next section.

Energy in the bond layer and the substrate

The energy , ΔH, in both regions of the bar can be calculated from

$$\Delta H = \frac{1}{2} E S \left(\frac{\partial \Psi}{\partial x}\right)^2 \delta x \tag{B.6}$$

where the bar has cross sectional area S, and the change in length of an element δx is $\frac{1}{2}\left(\frac{\partial \Psi}{\partial x}\right)^2 \delta x$. It follows that

$$\Delta H = \frac{1}{2} E_2 S A_2^2 k_2^2 \cos^2\left(k_2 x\right) \mathrm{d}x, \tag{B.7}$$

and expanding the cosine squared term using $\cos^2(kx) = \frac{1+\cos(2kx)}{2}$ gives the following form

$$\Delta H = \frac{1}{2} E_2 S A_2^2 k_2^2 \frac{1}{2}\left(1 + \cos\left(2k_2 x\right)\right) \mathrm{d}x. \tag{B.8}$$

In the bond layer region, of thickness $\frac{b}{2}$ the energy can be derived as

$$\Delta H_{\text{layer}} = \frac{1}{4} E_2 S A_2^2 k_2^2 \int_0^{\frac{b}{2}} 1 + \cos\left(2k_2 x\right) \mathrm{d}x = \frac{1}{4} E_2 S A_2^2 k_2^2 \left[x + \frac{\sin\left(2k_2 x\right)}{2k_2}\right]_0^{\frac{b}{2}}. \tag{B.9}$$

Using the approximation for small angles where $\sin(\phi) \approx \phi$, it can be seen that $\frac{\sin\left(2k_2 x\right)}{2k_2} \approx x$. Thus the following equation is derived for the amount of energy stored in a half of a bond layer of thickness b

$$\Delta H_{\text{layer}} = \frac{1}{4} E_2 S A_2^2 k_2^2 \left[2x\right]_0^{\frac{b}{2}} = \frac{1}{4} E_2 S A_2^2 k_2^2 b. \tag{B.10}$$

Analogous to the above derivation, it is possible to derive the total energy in the bar. As before it holds that

$$\Delta H_{\text{total}} = \frac{1}{4} E_1 S A_1^2 k_1^2 \int_0^{\frac{L}{2}} 1 + \cos\left(2k_1 x\right) \mathrm{d}x = \frac{1}{4} E_1 S A_1^2 k_1^2 \left[x + \frac{\sin\left(2k_1 x\right)}{2k_1}\right]_0^{\frac{L}{2}}, \tag{B.11}$$

where $L/2$ is half the bar length. As sine oscillates between -1 and 1, and the values for the wave number k_1 are usually large, it can be approximated that $\frac{\sin\left(2k_1 x\right)}{2k_1} = 0$. This gives the energy in the bar as

$$\Delta H_{\text{total}} = \frac{1}{4} E_1 S A_1^2 k_1^2 \left[x\right]_0^{\frac{L}{2}} = \frac{1}{4} E_1 S A_1^2 k_1^2 \frac{1}{2} L. \tag{B.12}$$

The ratio of energy in the bond layer to energy to the total energy in the bar can be calculated to

$$\frac{\Delta H_{\text{layer}}}{\Delta H_{\text{total}}} = \frac{\frac{1}{4}E_2 S A_2^2 k_2^2 b}{\frac{1}{4}E_1 S A_1^2 k_1^2 \frac{1}{2} L}. \tag{B.13}$$

Substituting the argument of the wave amplitude in region two, A_2, with the expression found in Eq. B.5 now yields the ratio of energy stored in a thin bonded layer of thickness b in a rod of length L as

$$\frac{\Delta H_{\text{layer}}}{\Delta H_{\text{total}}} = \frac{2bE_1}{LE_2}. \tag{B.14}$$

Bibliography

[1] A. Einstein. "Die Grundlage der allgemeinen Relativitätstheorie", *Annalen der Physik* 354.7 (1916), pp. 769–822.

[2] R. Hulse and J. Taylor. "Discovery of a pulsar in a binary system", *The Astrophysical Journal* 195.51–53 (1975).

[3] J. Weber. "Gravitational-Wave-Detector Events", *Physical Review Letters* 20 (23 1968).

[4] B. P. Abbott et al. "LIGO: the Laser Interferometer Gravitational-Wave Observatory", *Reports on Progress in Physics* 72.7 (2009).

[5] T Accadia et al. "Virgo: a laser interferometer to detect gravitational waves", *Journal of Instrumentation* 7.03 (2012).

[6] H. Grohe et al. "The GEO 600 status", *Classical and Quantum Gravity* 27.8 (2010).

[7] R. Takahashi. "Operational status of TAMA300 with the seismic attenuation system (SAS)", *Classical and Quantum Gravity* 25.11 (2008).

[8] G. M. Harry and the LIGO Scientific Collaboration. "Advanced LIGO: the next generation of gravitational wave detectors", *Classical and Quantum Gravity* 27.8 (2010).

[9] T. Accadia. "Status of the Virgo Project", *Classical and Quantum Gravity* 28.114 (2011).

[10] B. P. Abbott, R. Abbott, T. D. Abbott, M. R. Abernathy, et al. "Observation of Gravitational Waves from a Binary Black Hole Merger", *Physical Review Letters* 116 (6 2016).

[11] B. P. Abbott, others (the LIGO Scientific Collaboration, and V. Collaboration). "GW151226: Observation of gravitational waves from a 22 solar mass binary black hole coalescence", *Physical Review Letters* 116 (24 2016).

[12] B. P. Abbott, others (the LIGO Scientific Collaboration, and V. Collaboration). "GW170104: Observation of 50 solar mass binary black hole coalescence at redshift 0.2", *Physical Review Letters* 118 (22 2017).

[13] B. P. Abbott, others (the LIGO Scientific Collaboration, and V. Collaboration). "GW170814: A Three-Detector Observation of Gravitational Waves from a Binary Black Hole Coalescence", *Physical Review Letters* 119 (14 2017).

[14] B. P. Abbott, others (the LIGO Scientific Collaboration, and V. Collaboration). "GW170608: Observation of a 19-solar-mass binary black hole coalescence", *Astrophysical Journal Letters* 851 (2 2017).

[15] B. P. Abbott, others (the LIGO Scientific Collaboration, and V. Collaboration). "GW170817: Observation of Gravitational Waves from a Binary Neutron Star Inspiral", *Physical Review Letters* 119 (16 2017).

[16] P. Saulson. *Fundamentals of Interferometric Gravitational Wave Detectors*. World Scientific, 1994.

[17] A. Einstein. "Über Gravitationswellen", *Sitzungsberichte der Königlich Preußischen Akademie der Wissenschaften (Berlin), Seite 154-167.* (1918).

[18] P. Amaro-Seoane et al. "Low-frequency gravitational-wave science with eLISA/NGO", *Classical and Quantum Gravity* 29.12 (2012), p. 124016.

[19] A. W. Alsabti and P. Murdin. *Handbook of Supernovae*. Ed. by A. W. Alsabti and P. Murdin. Springer, 2017.

[20] C. D. Ott. "Probing the core-collapse supernova mechanism with gravitational waves", *Classical and Quantum Gravity* 26.20 (2009).

[21] B. F. Schutz. "Determining the Hubble constant from gravitational wave observations", *Nature* 323.310 (1986).

[22] B. P. Abbott et al. "Gravitational Waves and Gamma-Rays from a Binary Neutron Star Merger: GW170817 and GRB 170817A", *The Astrophysical Journal Letters* 848.2 (2017).

[23] V. Savchenko et al. "INTEGRAL Detection of the First Prompt Gamma-Ray Signal Coincident with the Gravitational-wave Event GW170817", *The Astrophysical Journal Letters* 848.2 (2017).

[24] T. L. S. Collaboration et al. "A gravitational wave standard siren measurement of the Hubble constant", *Nature* 551 (76 2017).

[25] I. Arcavi, G. Hosseinzadeh, D. A. Howell, C. McCully, et al. "Optical emission from a kilonova following a gravitational wave detected neutron star merger", *Nature* 551.64 (2017).

[26] G. S. Davies, M. Pitkin, and G. Woan. "A targeted spectral interpolation algorithm for the detection of continuous gravitational waves", *Classical and Quantum Gravity* 34.1 (2017).

[27] A. Hewish, S. J. Bell, J. D. H. Pilkington, P. F. Scott, and R. A. Collins. "Observation of a Rapidly Pulsating Radio Source", *Nature Physics* 217.709 (1968).

[28] B. Abbott et al. "Upper limits on gravitational wave emission from 78 radio pulsars", *Physical Review D* 76 (4 2007).

[29] B. P. Abbott et al. "First low-frequency Einstein@Home all-sky search for continuous gravitational waves in Advanced LIGO data", *Physical Review D* 96 (12 2017).

[30] R. Wagoner. "Gravitational radiation from accreting neutron stars", *Astrophysical Journal* 278 (1 1984).

[31] D. J. B. Payne, A. Melatos, and E. S. Phinney. "Gravitational waves from an accreting neutron star with a magnetic mountain", *AIP Conference Proceedings* 686.1 (2003), pp. 92–98.

[32] A. Reisenegger and A. Bonacic. "Millisecond Pulsars with r-Modes as Steady Gravitational Radiators", *Phys. Rev. Lett.* 91 (20 2003), p. 201103.

[33] M. Nayyar and B. J. Owen. "r-modes of accreting hyperon stars as persistent sources of gravitational waves", *Physical Review D* 73 (8 2006), p. 084001.

[34] L. Bildsten. "Gravitational Radiation and Rotation of Accreting Neutron Stars", *The Astrophysical Journal Letters* 501.1 (1998), p. L89.

[35] A. L. Watts, B. Krishnan, L. Bildsten, and B. F. Schutz. "Detecting gravitational wave emission from the known accreting neutron stars", *Monthly Notices of the Royal Astronomical Society* 389.2 (2008), pp. 839–868.

[36] C. Ungarelli and A. Vecchio. "High energy physics and the very early universe with LISA", *Physical Review D* 63 (6 2001), p. 064030.

[37] C. Ungarelli and A. Vecchio. "Studying the anisotropy of the gravitational wave stochastic background with LISA", *Physical Review D* 64 (12 2001), p. 121501.

[38] T. Callister et al. "Polarization-Based Tests of Gravity with the Stochastic Gravitational-Wave Background", *Physical Review X* 7 (4 2017), p. 041058.

[39] J. Weber. "Evidence for Discovery of Gravitational Radiation", *Physical Review Letters* 22 (1969).

[40] J. Weber. "Detection and Generation of Gravitational Waves", *Physical Review* 117 (1 1960).

[41] S. Rowan and J. Hough. "Gravitational Wave Detection by Interferometry (Ground and Space).", *Living Reviews in Relativity* 3.1 (2000).

[42] L. Gottardi et al. "Sensitivity of the spherical gravitational wave detector MiniGRAIL operating at 5 K", *Physical Review D* 76 (10 2007).

[43] O. D. Aguiar et al. “The status of the Brazilian spherical detector”, *Classical and Quantum Gravity* 19.7 (2002).

[44] G. E. Moss, L. R. Miller, and R. L. Forward. “Photon-Noise-Limited Laser Transducer for Gravitational Antenna”, *Applied Optics* 10.11 (1971), pp. 2495–2498.

[45] K. Danzmann and the LISA study team. “LISA: laser interferometer space antenna for gravitational wave measurements”, *Classical and Quantum Gravity* 13.11 (1996).

[46] E. Schmutzer, ed. *A gravity-wave detector using optical cavity sensing*. Vol. 306. Cambridge Press, 1983.

[47] B. J. Meers. “Recycling in laser-interferometric gravitational-wave detectors”, *Physical Review D* 38 (8 1988), pp. 2317–2326.

[48] K. A. Strain and B. J. Meers. “Experimental demonstration of dual recycling for interferometric gravitational-wave detectors”, *Physical Review Letters* 66 (11 1991).

[49] B. P. Abbott et al. “GW150914: The Advanced LIGO Detectors in the Era of First Discoveries”, *Physical Review Letters* 116 (13 2016), p. 131103.

[50] M. Pitkin, S. Reid, S. Rowan, and J. Hough. “Gravitational Wave Detection by Interferometry (Ground and Space)”, *Living Review in Relativity* (2011).

[51] J. Hough, S. Rowan, and B. S. Sathyaprakash. “The search for gravitational waves”, *Journal of Physics B: Atomic, Molecular and Optical Physics* 38.9 (2005).

[52] W. A. Edelstein, J Hough, J. R. Pugh, and W Martin. “Limits to the measurement of displacement in an interferometric gravitational radiation detector”, *Journal of Physics E: Scientific Instruments* 11.7 (1978).

[53] C. M. Caves. “Quantum-mechanical noise in an interferometer”, *Physical Review D* 23 (8 1981), pp. 1693–1708.

[54] Cella. “Underground Reduction of Gravity Gradient Noise”, *GWADW - VESF Meeting* (2011).

[55] H. B. Callen and R. F. Greene. “On a Theorem of Irreversible Thermodynamics”, *Physical Review* 86 (5 1952).

[56] M. Bassan. *Advanced Interferometer and the Search for Gravitational Waves*. Ed. by M. Bassan. Vol. 404. Springer, 2014.

[57] S. M. Aston et al. “Update on quadruple suspension design for Advanced LIGO”, *Classical and Quantum Gravity* 29.23 (2012).

[58] B. Picinbono, C. Bendjaballah, and J. Pouget. “Photoelectron Shot Noise”, *Journal of Mathematical Physics* 11.7 (1970).

[59] V. Braginsky and F. Khalili. "Gravitational wave antenna with QND speed meter", *Physics Letters A* 147 (5 1990).

[60] C. Graef et al. "Design of a speed meter interferometer proof-of-principle experiment", *Classical and Quantum Gravity* 31.21 (2014).

[61] H. Vahlbruch et al. "The GEO 600 squeezed light source", *Classical and Quantum Gravity* 27.8 (2010), p. 084027.

[62] B. P. Abbott et al. "Exploring the sensitivity of next generation gravitational wave detectors", *Classical and Quantum Gravity* 34.4 (2017).

[63] J. Harms and S. Hild. "Passive Newtonian noise suppression for gravitational wave observatories based on shaping of the local topography", *Classical Quantum Gravity* 31.18 (2014), p. 185011.

[64] Y. Aso and others (the KAGRA Collaboration). "Interferometer design of the KAGRA gravitational wave detector", *Physical Review D* 4 (88 2013).

[65] M. Punturo et al. "The Einstein Telescope: a third-generation gravitational wave observatory", *Classical and Quantum Gravity* 27.19 (2010).

[66] A. Einstein. "Investigations on the Theory of Brownian Motion", *Dover Publications, Inc.* (1956).

[67] H. B. Callen and T. A. Welton. "Irreversibility and Generalized Noise", *Physical Review 83, 34* 83.34 (1951).

[68] S. Twyford. "Developments towards low loss suspensions for laser interferometric gravitational wave detectors". PhD thesis. University of Glasgow, 1998.

[69] T. Quinn, C. Speake, R. Davis, and W. Tew. "Stress dependent damping in CuBe torsion and flexure suspensions at stresses up to 1.1 GPa", *Physics Letters A* 197.3 (1995).

[70] C. Zener. *Elasticity and anelasticity of metals*. University of Chicago Press, 1948.

[71] A. Nowick and B. Barry. *Anelastic relaxation in crystalline solids*. Ed. by N. York and London. Academic Press, 1972.

[72] Y. Levin. "Internal thermal noise in the LIGO test masses: A direct approach", *Physical Review D* 57 (2 1998).

[73] V. B. Braginsky, M. L. Gorodetsky, and S. P. Vyatchanin. "Thermodynamical fluctuations and photo-thermal shot noise in gravitational wave antennae", *Phys. Lett. A* 264.1 (1999), pp. 1–10.

[74] V. B. Braginsky, M. L. Gorodetsky, and S. P. Vyatchanin. "Thermo-refractive noise in gravitational wave antennae", *Physics Letters A* 271.5-6 (2000), pp. 303–307.

[75] M. Evans et al. “Thermo-optic noise in coated mirrors for high-precision optical measurements”, *Physical Review D* 78 (10 2008).

[76] G. Cagnoli and P. A. Willems. “Effects of nonlinear thermoelastic damping in highly stressed fibers”, *Physical Review B* 65 (17 2002).

[77] L. Cunningham et al. “Re-evaluation of the mechanical loss factor of hydroxide-catalysis bonds and its significance for the next generation of gravitational wave detectors”, *Physics Letters A* 20 (23 2010).

[78] M. Punturo et al. *Einstein Gravitational Wave Telescope Conceptual Design Study: ET-0106C-10*. Ed. by E. gravitational observatory. European gravitational observatory, 2011.

[79] S Hild. “Beyond the second generation of laser-interferometric gravitational wave observatories”, *Classical and Quantum Gravity* 29.12 (2012).

[80] A. A. van Veggel and C. J. Killow. “Hydroxide catalysis bonding for astronomical instruments”, *Advanced Optical Technologies* 3.3 (2014).

[81] V. B. Braginsky, V. P. Mitrofanov, and Panov. *Systems with Small Dissipation*. The University of Chicago Press, 1985.

[82] D. H. Gwo. “Ultra precise bonding for cryogenic fused silica optics”, *SPIE* 31.4 (1998).

[83] A. V. Cumming et al. “Silicon mirror suspensions for gravitational wave detectors”, *Classical and Quantum Gravity* 31.2 (2014).

[84] W. Andrew and S. Ebnesajjad. *Adhesives Technology Handbook (Second Edition)*. Ed. by S. Ebnesajjad. William Andrew Inc., 2008.

[85] K. Tamura et al. “Novel adhesive development for CMOS-compatible thin wafer handling”, *2010 Proceedings 60th Electronic Components and Technology Conference (ECTC)*. 2010, pp. 1239–1244.

[86] *Masterbond Epoxies*. `https://www.masterbond.com/`. Last accessed on 25/01/2018.

[87] K. Richter and R. Steiger. “Thermal Stability of Wood-Wood and Wood-FRP Bonding with Polyurethane and Epoxy Adhesives”, *Advanced Engineering Materials* 7.5 (2005), pp. 419–426. ISSN: 1527-2648.

[88] D. L. Hunston, A. J. Kinloch, and S. S. Wang. “Micromechanics of Fracture in Structural Adhesive Bonds”, *The Journal of Adhesion* 28.2-3 (1989).

[89] W. D. Bascom, R. L. Cottington, R. L. Jones, and P. Peyser. “The fracture of epoxy and elastomer-modified epoxy polymers in bulk and as adhesives”, *Journal of Applied Polymer Science* 19.9 (1975). ISSN: 1097-4628.

[90] S. Kalpakjian and S. Schmid. *Manufacturing, Engineering and Technology, seventh edition*. Pearson, 2014.

[91] K. Fletcher. *Assessment of Cold Welding between Separable Contact Surfaces due to Impact and Fretting under Vacuum*. Ed. by T. N. Contactivity bv Leiden. ESA Communication Production Office, 2009.

[92] M. R. Johnson. *The Galileo High Gain Antenna Deployment Anomaly*. Tech. rep. Jet Propulsion Laboratory, 1991.

[93] F. R. Lipsett. "Cold Welded Indium Low Temperature Window Seal", *Review of Scientific Instruments* 37.2 (1966).

[94] B. Derby and E. R. Wallach. "Theoretical model for diffusion bonding", *Metal Science* 16.1 (1982).

[95] I. E. Bottomley. "Superplastic Forming and Diffusion Bonding of Aircraft Structures", *Proceedings of the Institution of Mechanical Engineers, Part G: Journal of Aerospace Engineering* 209.3 (1995), pp. 227–231.

[96] M. Shimbo, K. Furukawa, K. Fukuda, and K. Tanzawa. "Silicon to silicon direct bonding method", *Journal of Applied Physics* 60.8 (1986), pp. 2987–2989.

[97] H. Takagi, K. Kikuchi, R. Maeda, T. R. Chung, and T. Suga. "Surface activated bonding of silicon wafers at room temperature", *Applied Physics Letters* 68.16 (1996), pp. 2222–2224.

[98] H. Saeki, J. Ikeda, and H. Ishimaru. "Optical window sealed with indium for ultrahigh vacuum", *Vacuum* 39 (6 1989).

[99] R. B. Belser. "A Technique of Soldering to Thin Metal Films", *Review of Scientific Instruments* 25.2 (1954).

[100] J. T. Klomp and A. J.C.V. D. Ven. "Parameters in solid-state bonding of metals to oxide materials and the adherence of bonds", *Journal of Materials Science* 15.10 (1980).

[101] W. M. Haynes. *CRC Handbook of Chemistry and Physics: A Ready-reference Book of Chemical and Physical Data*. Ed. by D. R. Lide. CRC Press, 2010.

[102] Y. Zhong et al. "Optical and electrical properties of indium tin oxide thin films with tilted and spiral microstructures prepared by oblique angle deposition", *Journal of Materials Research* 23.9 (2008).

[103] K. J. Bachmann. "Properties, Preparation, and Device Applications of Indium Phosphide", *Annual Review of Materials Science* 11.1 (1981).

[104] C. C. Lim. "Indium seals for low temperature and moderate pressure applications", *Review of Scientific Instruments* 57.1 (1986).

[105] R. R. Turkington and R. F. H. Lowe. "Note on the design of simple indium O ring seals", *Review of Scientific Instruments* 55.5 (1984).

[106] D. B. Fraser. "Special Indium Seal for Cryogenic Use", *Review of Scientific Instruments* 33.7 (1962).

[107] R. Straessle, Y. Petremand, D. Briand, M. Dadras, and N. F. de Rooij. "Low-temperature thin-film indium bonding for reliable wafer-level hermetic MEMS packaging", *IOP Science* 23.7 (2013).

[108] B. Abbott et al. "LIGO: the laser interferometer gravitational-wave observatory", *Reports on Progress in Physics* 72.7 (2009), p. 076901.

[109] G Hofmann et al. "Indium joints for cryogenic gravitational wave detectors", *Classical and Quantum Gravity* 32.24 (2015).

[110] P. G. Murray et al. "Low-temperature mechanical dissipation of thermally evaporated indium film for use in interferometric gravitational wave detectors", *Classical and Quantum Gravity* 32.11 (2015).

[111] K. W. MEISSNER. *Prism and Lens Making. 2nd ed. F. Twyman. London: Hilger and Watts, 1952. (U. S. distrib.: Jarrell-Ash, Boston.)* Vol. 117. 30. American Association for the Advancement of Science, 1953.

[112] R. Knechtel. "Glass frit bonding: an universal technology for wafer level encapsulation and packaging", *Microsystem Technologies* 12.1 (2005).

[113] V Greco, F Marchesini, and G Molesini. "Optical contact and van der Waals interactions: the role of the surface topography in determining the bonding strength of thick glass plates", *Journal of Optics A: Pure and Applied Optics* 3.1 (2001).

[114] R. Holt, H. Smith, and M. Gussenhoven. *Research on Optical Contact Bonding*. Tech. rep. Air Force Cambridge Research Laboratories, 1966.

[115] D. H. Gwo. "Ultra precise and reliable bonding method: US6284085B1". Pat. 6284085B1. 2001.

[116] B. Willke et al. "The GEO 600 gravitational wave detector", *Classical and Quantum Gravity* 19.7 (2002).

[117] D. H. Gwo. "Hydroxide catalyzed bonding: US6548176B1". Pat. 6548176B1. 2003.

[118] E. J. Elliffe et al. "Hydroxide-catalysis bonding for stable optical systems for space", *Classical and Quantum Gravity* 22.10 (2005).

[119] P. Amaro-Seoane, S. Aoudia, et al. "Low-frequency gravitational-wave science with eLISA/NGO", *Classical and Quantum Gravity* 29.12 (2012).

[120] R. Douglas et al. "Cryogenic and room temperature strength of sapphire jointed by hydroxide-catalysis bonding", *Classical and Quantum Gravity* 31.4 (2014).

[121] N. Beveridge et al. "Low-temperature strength tests and SEM imaging of hydroxide catalysis bonds in silicon", *Classical and Quantum Gravity* 28 (8 2011).

[122] N. Beveridge. "Characterisation of Silicon-Silicon Hydroxide Catalysis Bonds for Future Gravitational Wave Detectors". PhD thesis. Physics and Astronomy, 2012.

[123] S. Reid, G. Cagnoli, E. Elliffe, J. Faller, J. Hough, et al. "Influence of temperature and hydroxide concentration on the settling time of hydroxy-catalysis bonds", *Physics Letters A* 22.10 (2007).

[124] E. J. Elliffe. "Aspects of Thermal Noise Modeling in Ground-Based Gravitational Wave Detetors and Developments of Hydroxide Catalysis Bonding for Space-Based Gravitational Wave Detectors and other Optical Applications". PhD thesis. University of Glasgow, 2005.

[125] K. Haughian et al. "The effect of crystal orientation on the cryogenic strength of hydroxide catalysis bonded sapphire", *Classical and Quantum Gravity* 32.7 (2015).

[126] R. Douglas. "Aspects of hydroxide catalysis bonding of sapphire and silicon for use in future gravitational wave detectors". PhD thesis. University of Glasgow, 2016.

[127] M. Phelps et al. "The influence of curing time on the strength of hydroxide catalysis bonds between fused silica, sapphire, and silicon", (2018). LIGO-P1800145, manuscript in preparation.

[128] *Impex*. `http://www.impex-hightech.de/`. Last accessed on 25/01/2018.

[129] *Zygo*. `https://www.zygo.com/?/met/interferometers/`. Last accessed on 25/01/2018.

[130] *Hitachi TM 1000 tabletop Scanning Electron Microscope*. `https://www.hitachi-hightech.com`. Last accessed on 25/01/2018.

[131] *Wyko*. `https://www.eriks.co.uk/`. Last accessed on 25/01/2018.

[132] K. Green, J. Burke, and B. Oreb. "Chemical bonding for precision optical assemblies", *Optical Engineering* 50 (3 2011).

[133] A. A. van Veggel. *E050228-v4 Silicate Bonding Procedure (Hydroxide-Catalysis Bonding)*. Tech. rep. LSC, 2013.

[134] *Standard Test Method for Flexural Strength of Advanced Ceramics at Ambient Temperature-ASTM C1161 - 13*. ASTM International.

[135] *Zwick Strength tester*. `http://www.zwick.co.uk/en/products/static-materials-testing-machines/testing-machines-from-5-kn-to-250-kn.html`. Last accessed on 25/01/2018.

[136] P. Przybysz, M. Dubowik, M. A. Kucner, K. Przybysz, and K. Przybysz Buzala. "Contribution of Hydrogen Bonds to Paper Strength Properties", *Public Library of Science One* 11.5 (2016).

[137] J. Bowen et al. "Adhesion between silica surfaces due to hydrogen bonding", *Surface Topography: Metrology and Properties* 4.3 (2016).

[138] R. H. Doremus. "Diffusion in alumina", *Journal of Applied Physics 100, 101301* 100.10 (2006).

[139] S. Jenkins, K. I. Jacob, and S. Kumar. "The effect of hydrogen bonding on the physical and mechanical properties of rigid-rod polymers", *Journal of Polymer Science Part B: Polymer Physics* 38.23 (2000).

[140] H. Wakabayashi and M. Tomozawa. "Diffusion of Water into Silica Glass at low Temperature", *Journal of the American Ceramic Society, 72 1850-55* 72.18 (1989).

[141] R. H. Doremus. "Diffusion of water in silica glass", *Journal of Materials Research, Volume 10, Issue 9,* 10.9 (1995).

[142] D. Chen. "Study of a cryogenic suspension system for the gravitational wave telescope KAGRA". PhD thesis. University of Tokyo, 2014.

[143] E. R. Dobrovinskaya, L. A. Lytvynov, and V. Pishchik. *Sapphire Material, Manufacturing, Applications*. Springer Science + Business Media, LLC, 2009.

[144] K. Haughian. "Aspects of Materials Research for Advanced and Future Generations of Gravitational Wave Detectors". PhD thesis. University of Glasgow, 2011.

[145] K. Haughian et al. "Mechanical loss of a hydroxide catalysis bond between sapphire substrates and its effect on the sensitivity of future gravitational wave detectors", *Physical Review D* 94.8 (2016).

[146] W. C. Oliver and G. M. Pharr. "An improved technique for determining hardness and elastic modulus using load and displacement sensing indentation experiments", *Journal of Materials Research* 7 (6 2011).

[147] M. R. Abernathy. "Mechanical Properties of Coating Materials for Use in the Mirrors of Interferometric Gravitational Wave Detectors". PhD thesis. University of Glasgow, 2012.

[148] P. H. Sneddon et al. "The intrinsic mechanical loss factor of hydroxy-catalysis bonds for use in the mirror suspensions of gravitational wave detectors", *Classical and Quantum Gravity* 20.20 (2003).

[149] E. P. Papadakis, ed. *Ultrasonic Instruments and Devices*. Academic Press, 1999.

[150] A. I. Lavrentyev and S. I. Rokhlin. "Determination of elastic moduli, density, attenuation, and thickness of a layer using ultrasonic spectroscopy at two angles", *Acoustical Society of America* 102 (6 1997).

[151] L. Kinsler et al. *Fundamentals of Acoustics 4th Edition*. Wiley, 2000.

[152] *Sonatest*. https://sonatest.com/products/transducers. Last accessed on 25/01/2018.

[153] *JSR Ultrasonics*. http://www.jsrultrasonics.com/pr_dpr300.html. Last accessed on 25/01/2018.

[154] *ThermoFischer Scientific*. https://www.fei.com/products/dualbeam/helios-nanolab/. Last accessed on 25/01/2018.

[155] *Logitech*. https://us.store.logitech.uk.com/index.php?route=common/home. Last accessed on 25/01/2018.

[156] *Emitech Evaporator K950X*. https://www.quorumtech.com/__assets__/pdf/Manuals/K950X-Iss9.pdf. Last accessed on 25/01/2018.

[157] *Sigma Aldrich*. https://www.sigmaaldrich.com/united-kingdom.html. Last accessed on 25/01/2018.

[158] T. E. Everhart and R. F. M. Thornley. "Wide-band detector for micro-microampere low-energy electron currents", *Journal of Scientific Instruments* 37.7 (1960).

[159] Shimadzu. *EDX-7000 and EDX8000 Operation Manual-PEDX-Navi*.

[160] *Olympus Microscope*. http://cn.olympus.com/upload/accessory/20114/201147142856969394.pdf. Last accessed on 25/01/2018.

[161] M. de Lima, R. Lacerda, J. Vilcarromero, and F. Marques. "Coefficient of thermal expansion and elastic modulus of thin films", *Journal of Applied Physics* 86 (9 1999).

[162] D. L.J. G. D. Foreman-Mackey D. Hogg. "emcee: The MCMC Hammer", *Publications of the Astronomical Society of Pacific, Volume 125, Issue 925, pp. 306* (2013).

[163] M. Phelps et al. "Measurements of the Young's modulus of hydroxide catalysis bonds, and the effect on thermal noise in ground-based gravitational wave detectors", *Physical Review D* 97 (10 2018).

[164] S. Rowan, S. M. Twyford, J. Hough, D.-H. Gwo, and R. Route. "Mechanical losses associated with the technique of hydroxide-catalysis bonding of fused silica", *Physical Review Letters* 246 (1998), pp. 471–478.

[165] S. D. Penn et al. "Frequency and surface dependence of the mechanical loss in fused silica", *Physics Letters A* 352.1 (2006).

[166] L.G.Prokhorov et al. "Upper limits on the mechanical loss of silicate bonds in a silicon tuning fork oscillator", *Physics Letters A* (2017).

[167] I. W. Martin et al. "Low temperature mechanical dissipation of an ion-beam sputtered silica film", *Classical and Quantum Gravity* 31.3 (2014), p. 035019.

[168] P. Fritschel and D. Coyne. *T010075 v3 Advanced LIGO Systems Design*. Tech. rep. LIGO Laboratory, 2015.

[169] S. Kawamura, J. Hazel, and F. Raab. *LIGO-T960074 Suspension Preliminary Design*. Tech. rep. LIGO Laboratory, 1996.

[170] N. Robertson. *LIGO-G060216 Requirements and Design Breakout Presentation*. Tech. rep. LIGO Laboratory, 2006.

[171] *Gravitational wave interferometer noise calculator, v3.1*. 2016.

[172] M. Zucker. "Private Communication". talk.

[173] R Kumar et al. "Status of the cryogenic payload system for the KAGRA detector", *Journal of Physics: Conference Series* 716 (2016).

[174] H. Luck et al. "The upgrade of GEO600", *Gravitational waves. Proceedings, 8th Edoardo Amaldi Conference, Amaldi 8, New York, USA, June 22-26*. 2009.

[175] C Affeldt et al. "Advanced techniques in GEO 600", *Classical and Quantum Gravity* 27.8 (2014).

[176] F Acernese et al. "Advanced Virgo: a second-generation interferometric gravitational wave detector", *Classical and Quantum Gravity* 32.2 (2014).

[177] *Shinetsu*. `https://www.shinetsu.co.jp/en/`. Last accessed on 25/01/2018.

[178] *Gooch and Housego*. `https://goochandhousego.com/`. Last accessed on 25/01/2018.

[179] P. N. Bartlett et al. "Non-aqueous electrodeposition of metals and metalloids from halometallate salts", *RSC Advances* 3 (2013).

[180] *Bruker XRD*. `https://www.bruker.com/products/x-ray-diffraction-and-elemental-analysis/x-ray-diffraction.html`. Last accessed on 25/01/2018.

[181] R. E. Eckert and H. G. Drickamer. "Diffusion in Indium Near the Melting Point", *The Journal of Chemical Physics* 20.13 (1952).

[182] S. Lupi, M. Forzan, and A. Aliferov. *Induction and Direct Resistance Heating*. Ed. by Springer. Springer International Publishing, 2015.

[183] S. L. Semiatin. *Theory of Heating by Induction*. ASM International, 2001.

[184] A. K. Raychaudhuri, C. Egloff, and L. Rinderer. "Penetration of a weak magnetic field into superconducting indium", *Journal of Low Temperature Physics* 59.5 (1985).

[185] *500W Draper Induction Heating Tool Kit, part number IHT-15*. `https://www.drapertools.com/product/80808/Expert-Induction-Heating-Tool-Kit`. Last accessed on 25/01/2018.

[186] *DIY Induction Heater*. `http://www.rmcybernetics.com`. Last accessed on 25/01/2018.

[187] *PeakTech powersupply*. http://www.peaktech.de/productdetail/kategorie/schaltnetzteile/produkt/peaktech-1560.html. Last accessed on 25/01/2018.

[188] *Infra-red FLIR Camera*. http://www.flir.co.uk. Last accessed on 25/01/2018.

[189] *ZVS Induction heater circuit*. https://spaco.org/Blacksmithing/ZVSInductionHeater/1000WattZVSInductionHeaterNotes.htm. Last accessed on 25/01/2018.